

AD-A278 550



A SHOCK TUBE STUDY OF AERODYNAMIC
HEATING OF GAPS IN A CYLINDER SUBJECTED
TO SUPERSONIC CROSS FLOW

THESIS

Douglas D. High, Captain, USAF

AFIT/GA/ENY/94M-2

DTIC
ELECTE
APR 22 1994
S B D

DISTRIBUTION STATEMENT 1
Approved for public release
Distribution Unlimited

DEPARTMENT OF THE AIR FORCE
AIR UNIVERSITY

AIR FORCE INSTITUTE OF TECHNOLOGY

DTIC QUALITY INSPECTED 8

Wright-Patterson Air Force Base, Ohio

AFIT/GA/ENY/94M-2

A SHOCK TUBE STUDY OF AERODYNAMIC
HEATING OF GAPS IN A CYLINDER SUBJECTED
TO SUPERSONIC CROSS FLOW

THESIS

Douglas D. High, Captain, USAF

AFIT/GA/ENY/94M-2

Approved for public release; Distribution Unlimited

94-12242



94 1 22 000

A SHOCK TUBE STUDY OF AERODYNAMIC HEATING
OF GAPS IN A CYLINDER SUBJECTED
TO SUPERSONIC CROSS FLOW

THESIS

Presented to the Faculty of the Graduate School of Engineering

of the Air Force Institute of Technology

Air University

In Partial Fulfillment of the

Requirements for the Degree of

Master of Science in Astronautical Engineering

Douglas D. High, B.S.C.E.

Captain, USAF

March 1994

Accession For	
NTIS GRA&I	<input checked="checked" type="checkbox"/>
DTIC TAB	<input type="checkbox"/>
Unannounced	<input type="checkbox"/>
Justification	
By _____	
Distribution/ _____	
* Availability Codes	
Dist	Avail and/or Special
A-1	

Approved for public release; Distribution Unlimited

Preface

The purpose of this thesis was to measure the aerodynamic heating in and around expansion gaps of a body positioned in supersonic cross flow. The AFIT High Pressure Shock Tube was used to generate supersonic flow around a cylinder mounted normal to the fluid stream. Heating rates were obtained from the surface of the cylinder, from the wall of an expansion gap located on the cylinder, and from the gap floor. A comparison of Nusselt number values at each location examined the effects of different Mach numbers, changing locations on the cylinder, and variable gap widths. This research established supersonic flow data for comparison to gap heating in hypersonic cross flow.

I wish to sincerely thank the great number of people who made this thesis possible. Special thanks goes to my advisor Major Jerry Bowman, who answered a multitude of questions and provided valuable guidance. Also, thanks to Dr. Rodney Bowersox and Dr. William Elrod for providing advice and expertise in shock tube fluid flow. Mr. Dan Rioux, Mr. Jay Anderson, and Mr. Andrew Pitts at the AFIT/ENY laboratory deserve thanks for giving their assistance in equipment setup, calibration, and operation, and invaluable experience in completing shock tube testing. Additionally, I thank Jack Tiffany and the staff at the AFIT Model Fabrication shop for their prompt and precise machining work.

Finally, I wish to express a very special thanks to my wife Kim and daughter Hilary for their love, support, extreme patience throughout this research, and their sacrifices during the long hours I was gone.

Douglas High

Table of Contents

	Page
Preface	ii
List of Figures	v
List of Table	xii
List of Symbols	xiii
Abstract	xvi
 I. Introduction	 1.1
1.1 Background	1.1
1.2 Statement of the Problem	1.2
1.3 Review of Current Knowledge	1.3
1.4 Objectives and Scope	1.5
1.5 Methodology	1.6
 II. Theory	 2.1
2.1 The Shock Tube	2.1
2.2 Heat Transfer	2.5
2.3 Heat Flux Calculations	2.7
2.4 Heat Transfer at High Velocities	2.9
2.5 The Cylinder in Cross Flow	2.11
2.6 Corrections for Flow in a Restricted Channel	2.13
 III. Experimental Apparatus	 3.1
3.1 The Shock Tube	3.1
General Description	3.1
Diaphragm Section	3.2
Support Equipment	3.2
3.2 The Test Section	3.3
3.3 Instrumentation	3.3
Pressure Measuring Equipment	3.3
Temperature Measuring Equipment	3.4
3.4 Data Acquisition System	3.6

IV. Experimental Procedure	4.1
4.1 Shock Tube Set Up	4.1
Instrument Calibrations	4.1
Preparing the Shock Tube	4.2
4.2 Data Collection	4.3
4.3 Data Reduction Methods	4.5
4.4 Verification of Data Results	4.7
V. Discussion of Results	5.1
5.1 Heat Transfer Results	5.1
Error Analysis	5.1
Changes in Flow Velocity	5.2
Reference Point	5.3
Gap Wall	5.4
Gap Floor	5.5
Combined Test Results	5.5
Heat Augmentation Factors	5.6
5.2 Other Observations	5.7
Diaphragm Burst Phenomenon	5.7
VI. Conclusions and Recommendations	6.1
6.1 Conclusions	6.1
6.2 Recommendations	6.3
Appendix A: Calibration of Pressure Measuring Instruments	A.1
Appendix B: Thermocouple Voltage to Temperature Conversion	B.1
Appendix C: Surface Temperature to Heat Flux FORTRAN Program	C.1
Appendix D: Data Reduction Procedures (Sample Case)	D.1
Pressure to Temperature Worksheet	D.13
Appendix E: Shock Tube Wall Calculations/Flat Plate Calculations	E.1
Pressure to Temperature Worksheet	E.6
Empirical Model Worksheet	E.10
Appendix F: Test Run Data	F.1
Bibliography	Bib.1
Vita	Vita.1

List of Figures

Figure	Page
1.1 Wing/Cylinder Geometry	1.9
2.1 Conventional Shock Tube	2.15
2.2 (x-t) Diagram and Pressure, Temperature, Velocity Distributions at time t^* (Gaydon, 1963:1)	2.15
2.3 Gas Parameters Associated with Shock Wave Coordinate Systems	2.16
(Gaydon, 1963:14)	
(a) Laboratory Fixed Coordinates	
(b) Shock Fixed Coordinates	
2.4 Simulating a Semi-Infinite Solid with a Two-Dimensional Model	2.16
(Bonafede, 1988:61)	
2.5 Total Drag Coefficient of a Cylinder and a Sphere for Variable Re	2.17
(Žukauskas, 1987:6.7)	
2.6 Laminar and Turbulent Flow on a Cylinder	2.17
(Anderson, 1978:197)	
2.7 Local Heat Transfer From a Cylinder for Variable Re	2.18
(Žukauskas, 1987:6.9)	
3.1 Shock Tube Support Equipment	3.8
3.2(a) Instrumented Cylinder	3.9
3.2(b) Cylinder mounted in Connection Joint	3.9
3.2(c) Thermocouple Mounting in Test Cylinder	3.10
3.3 Shock Tube Instrumentation	3.11
3.4 MEDTHERM Thermocouple	3.12
4.1 Test Conditions Schematic	4.11

4.2 Data Reduction Worksheet (DADiSP)	4.12
4.3 Boundary Layer Formation Behind a Normal Shock Wave	4.13
(Eads, 1992:Fig 2.2)	
4.4 Comparison of Flat Plate Heat Transfer Correlations with Experimental Results (Incropera, 1985:367)	4.14
4.5 Local Heat Transfer From a Cylinder For Variable Re	4.15
(Žukuaskas, 1987:6.9)	
4.6 Local Heat Transfer From a Cylinder to Air in the Supercritical Flow Regime For Variable Tu (Žukuaskas, 1987:6.10)	4.15
4.7 Nusselt Numbers Obtained by Schmidt and Wenner	4.16
(Hermann, 1987:827)	
5.1 Gap Width - w/d Ratio	5.8
5.2 Nusselt vs. Theta Graphs with Means and Error Ranges	
(a) Floor Values, Mach 1.04, Gap Width 7.5mm	5.9
(b) Wall Values, Mach 1.19, Gap Width 7.5mm	5.10
(c) Floor Values, Mach 1.38, Gap Width 2.5mm	5.11
5.3 Nusselt vs. Theta Graph: Impact of Changing Flow Velocity Gap Floor Nusselt Values, Gap Width 5mm	5.12
5.4 Nusselt vs. Theta Graph, Reference Point Averages, Mach 1.04	5.13
5.5 Nusselt vs. Theta Graph, Reference Point Averages, Mach 1.19	5.14
5.6 Nusselt vs. Theta Graph, Reference Point Averages, Mach 1.38	5.15
5.7 Nusselt vs. Theta Graph, Reference Point Averages, Combined	5.16
5.8 Gap Wall Nusselt Values, Gap Width 2.5mm	5.17
5.9 Gap Wall Nusselt Values, Gap Width 5mm	5.18
5.10 Gap Wall Nusselt Values, Gap Width 7.5mm	5.19
5.11 Gap Floor Nusselt Values, Gap Width 2.5mm	5.20

5.12	Gap Floor Nusselt Values, Gap Width 7.5mm	5.21
5.13	Combined Nusselt Values, Mach 1.04, Gap Width 2.5mm	5.22
5.14	Combined Nusselt Values, Mach 1.19, Gap Width 2.5mm	5.23
5.15	Combined Nusselt Values, Mach 1.38, Gap Width 2.5mm	5.24
5.16	Combined Nusselt Values, Mach 1.04, Gap Width 5mm	5.25
5.17	Combined Nusselt Values, Mach 1.19, Gap Width 5mm	5.26
5.18	Combined Nusselt Values, Mach 1.38, Gap Width 5mm	5.27
5.19	Combined Nusselt Values, Mach 1.04, Gap Width 7.5mm	5.28
5.20	Combined Nusselt Values, Mach 1.19, Gap Width 7.5mm	5.29
5.21	Combined Nusselt Values, Mach 1.38, Gap Width 7.5mm	5.30
5.22	Gap Floor Heat Augmentation Factors, Gap Width 2.5mm	5.31
5.23	Gap Floor Heat Augmentation Factors, Gap Width 5mm	5.32
5.24	Gap Floor Heat Augmentation Factors, Gap Width 7.5mm	5.33
5.25	Gap Wall Heat Augmentation Factors, Gap Width 2.5mm	5.34
5.26	Gap Wall Heat Augmentation Factors, Gap Width 5mm	5.35
5.27	Gap Wall Heat Augmentation Factors, Gap Width 7.5mm	5.36
5.28	Pressure Gauge B, Test Run GP3MH1TH4A	5.37
5.29	Pressure Gauge B, Test Run GP3MH3TH4A	5.38
A.1	Pressure Gauge A Calibration Curve	A.3
A.2	Pressure Gauge B Calibration Curve	A.3
A.3	Pressure Gauge 4 Calibration Curve	A.4
B.1	Thermocouple Temperature vs. Output Voltage	B.3

D.1	Input Voltage Data	D.3
D.2	Gauge A Pressure History	D.4
D.3	Gauge B Pressure History	D.5
D.4	Reference Point Surface Temperature Time History	D.6
D.5	Gap Wall Surface Temperature Time History	D.7
D.6	Gap Floor Surface Temperature Time History	D.8
D.7	Extracted Reference Point Surface Temperatures	D.9
D.8	Reference Point Heat Flux	D.10
D.9	Reference Point Heat Flux with 20 Point Moving Average	D.11
D.10	Extracted P_2 Pressure History	D.12
D.11	Extracted T_2 Temperature History	D.15
D.12	Adiabatic Wall Temperatures	D.16
D.13	Reference Point Convective Heat Transfer Coefficient	D.17
D.14	Reference Point Nusselt Values	D.18
D.15	Combined Nusselt Values	D.19
E.1	Shock Tube Wall Surface Temperatures	E.3
E.2	Surface Temperatures with Instantaneous Jurup	E.4
E.3	Heat Flux, Shock Tube Wall	E.5
E.4	Extracted T_2 Temperature History	E.8
E.5	Convective Heat Transfer Coefficient	E.9
E.6	Comparison of Experimental Data with a Flat Plate Correlation	E.11
F.1	Test Run Nusselt Values, Run GP1MH4TH1A	F.8

F.2 Test Run Nusselt Values, Run GP1MH1TH1A	F.9
F.3 Test Run Nusselt Values, Run GP1MH1TH1B	F.10
F.4 Test Run Nusselt Values, Run GP1MH1TH1X	F.11
F.5 Test Run Nusselt Values, Run GP1MH1TH1Y	F.12
F.6 Test Run Nusselt Values, Run GP1MH3TH1A	F.13
F.7 Test Run Nusselt Values, Run GP1MH1TH2A	F.14
F.8 Test Run Nusselt Values, Run GP1MH2TH2A	F.15
F.9 Test Run Nusselt Values, Run GP1MH3TH2A	F.16
F.10 Test Run Nusselt Values, Run GP1MH1TH3A	F.17
F.11 Test Run Nusselt Values, Run GP1MH2TH3A	F.18
F.12 Test Run Nusselt Values, Run GP1MH3TH3A	F.19
F.13 Test Run Nusselt Values, Run GP1MH1TH4A	F.20
F.14 Test Run Nusselt Values, Run GP1MH2TH4B	F.21
F.15 Test Run Nusselt Values, Run GP1MH2TH4A	F.22
F.16 Test Run Nusselt Values, Run GP1MH3TH4A	F.23
F.17 Test Run Nusselt Values, Run GP1MH1TH5A	F.24
F.18 Test Run Nusselt Values, Run GP1MH2TH5A	F.25
F.19 Test Run Nusselt Values, Run GP1MH3TH5A	F.26
F.20 Test Run Nusselt Values, Run GP2MH1TH1A	F.27
F.21 Test Run Nusselt Values, Run GP2MH2TH1A	F.28
F.22 Test Run Nusselt Values, Run GP2MH3TH1A	F.29
F.23 Test Run Nusselt Values, Run GP2MH1TH2A	F.30

F.24	Test Run Nusselt Values, Run GP2MH2TH2A	F.31
F.25	Test Run Nusselt Values, Run GP2MH3TH2A	F.32
F.26	Test Run Nusselt Values, Run GP2MH1TH3A	F.33
F.27	Test Run Nusselt Values, Run GP2MH2TH3A	F.34
F.28	Test Run Nusselt Values, Run GP2MH3TH3A	F.35
F.29	Test Run Nusselt Values, Run GP2MH1TH4A	F.36
F.30	Test Run Nusselt Values, Run GP2MH2TH4A	F.37
F.31	Test Run Nusselt Values, Run GP2MH3TH4A	F.38
F.32	Test Run Nusselt Values, Run GP2MH1TH5A	F.39
F.33	Test Run Nusselt Values, Run GP2MH2TH5A	F.40
F.34	Test Run Nusselt Values, Run GP2MH3TH5A	F.41
F.35	Test Run Nusselt Values, Run GP3MH1TH1A	F.42
F.36	Test Run Nusselt Values, Run GP3MH2TH1A	F.43
F.37	Test Run Nusselt Values, Run GP3MH3TH1A	F.44
F.38	Test Run Nusselt Values, Run GP3MH1TH2A	F.45
F.39	Test Run Nusselt Values, Run GP3MH2TH2A	F.46
F.40	Test Run Nusselt Values, Run GP3MH3TH2A	F.47
F.41	Test Run Nusselt Values, Run GP3MH1TH3A	F.48
F.42	Test Run Nusselt Values, Run GP3MH2TH3A	F.49
F.43	Test Run Nusselt Values, Run GP3MH3TH3A	F.50
F.44	Test Run Nusselt Values, Run GP3MH1TH4A	F.51
F.45	Test Run Nusselt Values, Run GP3MH2TH4A	F.52

F.46	Test Run Nusselt Values, Run GP3MH3TH4A	F.53
F.47	Test Run Nusselt Values, Run GP3MH1TH5A	F.54
F.48	Test Run Nusselt Values, Run GP3MH2TH5A	F.55
F.49	Test Run Nusselt Values, Run GP3MH3TH5B	F.56

List of Tables

Figure	Page
4.1 Thermocouple Voltage Feedline Losses	4.2
4.2 Velocity Correction Due to Blockage Effects	4.6
4.3 Localized Heating - Reference Position	4.8
4.4 Test Run Repeatability	4.10
5.1 Gap Width - w/d Ratios	5.1
5.2 Test Run Error Analysis	5.3
B.1 NBS Polynomial Coefficients - Type K	B.2
F.1 Measured and Calculated Parameters Used in Reducing Data	F.2
F.2 Test Run Averaged Nusselt Values	F.3

List of Symbols

<i>Symbol</i>	<i>Description</i>	<i>Units</i>
a	Speed of sound	m/sec
c_p	Specific heat at constant pressure	J/kg-K
D	Diameter of cylinder test section	mm (in.)
d	Depth of gap	mm (in.)
dB	Decibels	
h	Convective heat transfer coefficient	W/m ² -K
H	Enthalpy (per unit mass)	J/kg
k	Thermal Conductivity	W/m-K
M	Mach number (u/a)	
$molwt$	Molecular weight	kg/kgmol
Nu	Nusselt number (hD/k)	
P	Pressure	Pa (psi)
Pr	Prandtl Number ($\mu c_p/k$)	
q''	Heat flux	W/m ²
r	Recovery factor	
R	Gas constant ($R_{bar}/molwt$)	J/kg-K
R_{bar}	Universal Gas Constant	J/kgmol-K
R_{block}	Blockage Ratio	
Re	Reynolds number ($\rho v_{\infty} D/\mu$)	
t	Time	sec

<i>Symbol</i>	<i>Description</i>	<i>Units</i>
w	Width of gap	mm (in)
T	Temperature	K, °C (°F)
Tu	Turbulence intensity	percent
u	Velocity, shock fixed coordinate system	m/sec
u'	Velocity fluctuation	m/sec
V	Electrical Voltage or Potential	Volt
v	Velocity, laboratory fixed coordinate system	m/sec
w	Width of gap	mm (in)
W_s	Velocity of Normal Shock Wave	m/sec
x	Distance into semi-infinite solid	m

Greek Letters

α	thermal diffusivity	m ² /sec
γ	Ratio of specific heats (c_p/c_v)	
τ	Integration variable	
μ	Dynamic viscosity	kg/s-m
ν	Kinematic viscosity	m ² /s
θ	Angle from stagnation point (cylinder)	deg
ρ	Density	kg/m ³

<i>Symbol</i>	<i>Description</i>
Subscripts	
<i>A</i>	Pressure gauge A
<i>air</i>	Air
<i>aw</i>	Adiabatic wall
<i>B</i>	Pressure gauge B
<i>bar</i>	Bar
<i>block</i>	Blockage ratio
<i>corr</i>	Corrected for blockage effects
<i>i</i>	Initial
<i>J</i>	Final value in series
<i>j</i>	Series counter
<i>ref</i>	Reference
<i>s</i>	Surface
<i>slab</i>	Model (thermocouple)
<i>sp</i>	Shock passage (time), Stagnation Point (Nusselt Number)
<i>0.1</i>	Order of time model behaves as semi-infinite slab
<i>1</i>	Shock tube driven section (before shock)
<i>2</i>	Region between shock front and contact surface, test region
<i>4</i>	Driver Section
<i>∞</i>	Free Stream (undisturbed flow)

Abstract

The effects of localized aerodynamic heating in cylinder expansion gaps positioned in cross flow were investigated in a shock tube. For this study, Mach number and Reynolds number were varied from 1.04 to 1.38 and 5×10^5 to 9×10^5 , respectively. The cylinder was instrumented with quick response time thermocouples positioned on the surface of the cylinder, the wall of the gap, and the gap floor. Gap aspect ratios varied from 1.23 to 3.69. Pressure gauges were used to measure wave shock speeds, pressure ratios, and transient pressure conditions. Surface temperatures were measured and converted to heat fluxes using a one-dimensional semi-infinite slab model. Adiabatic wall temperatures were obtained from pressure measurements and ideal gas law relationships. Local nondimensional heat transfer coefficients, Nusselt numbers, were calculated from experimental surface and adiabatic wall temperatures. The present study found a direct dependence on Nusselt number values with Mach number. Peak heating inside the gap was determined to be a function of gap width and location on the cylinder. As gap width was reduced, the location of peak heating on the cylinder varied and Nusselt number values on the floor of the gap dominated.

A SHOCK TUBE STUDY OF AERODYNAMIC HEATING OF GAPS IN A CYLINDER SUBJECTED TO SUPERSONIC CROSS FLOW

I. Introduction

1.1 Background

The desire to develop a fully reusable orbital vehicle to replace the space shuttle in carrying payloads into orbit gave birth to the National Aerospace Plane (NASP). NASP is designed to be a hypersonic vehicle capable of lifting large payloads into orbit as well as providing a suborbital platform which could span large distances in a small amount of time. NASP relies heavily on the development and implementation of advanced technologies in air-breathing engines, fuels, and innovative structural and material designs.

In order to achieve orbit, NASP must be able to operate effectively in the hypersonic regime and withstand the harsh environmental conditions imposed on the vehicle. Of particular interest is the aerodynamic heating that occurs on NASP surfaces. In designing structural components, consideration must be given to the expansion gaps and interface joints required between surface segments and panels. Expansion gaps located on the leading edge of the NASP wing encounter some of the highest heating loads; however, heat transfer investigations must also address gaps positioned in all areas of the aircraft's structure. Additionally, insufficient experimental data exists on the heating effects encountered in and around expansion

gaps. A better understanding of the heat transfer fluxes that occur in gaps is necessary.

Increasing our knowledge of heating loads in gaps aids in reducing uncertainty in the design process. One method used in finding heating loads can be obtained through the use of heat augmentation factors. These augmentation factors are used by engineers to calculate peak heating loads and identify where "hot spots" will occur on surfaces. Using augmentation factors, engineers can pick the proper materials and design structural components to withstand these severe conditions.

1.2 Statement of the Problem

More information is needed to predict aerodynamic heating in the expansion gaps located on the leading edge of blunt-nosed axisymmetric bodies. Experimental research has investigated heat loads in lateral gaps (90° to airflow), the heat loads in off-axis gaps (diagonal to flow), and the heating effects in longitudinal gaps using flat plate models. Since the leading edge of an airfoil is normally the location of extreme heat loads, it continues to be an area of considerable interest.

In order to find a way to measure peak heating in gaps on airfoils, the leading edge of a NASP wing is modeled by using a cylinder situated in cross flow. Experimental techniques are used to collect data. This is normally the preferred method due to the complexities of heat transfer around a cylinder. At various Reynolds numbers the boundary layer on the front portion of the cylinder is laminar. In this region theoretical methods for calculating local heat transfer may be applied. The rear section of the cylinder experiences an area of complicated vortical flow.

Theoretical calculations in this area become exceedingly difficult (Žukauskas, 1970:116). Additionally, heat transfer at the front stagnation point and at the boundary layer separation point also exhibits peculiar features. Because of these complexities, experimental research is used to analyze the phenomena. This approach is typical for many heat transfer problems.

To understand the effects of aerodynamic heating in hypersonic flow, it is necessary to first examine what occurs in supersonic flow. Understanding the flow characteristics and heat transfer effects in this regime is essential before expanding research to hypersonic Mach numbers. A thorough investigation provides the basis on which hypersonic heating effects can be compared.

1.3 Review of Current Knowledge

In an investigation of expansion gap heating, the results of previous experimental research was examined to determine which factors influenced heat transfer. Various types of gaps (or slots) and their orientation to free stream airflow were studied.

Bertin and Goodrich (1980:12) conducted extensive testing into the aerodynamic heating of gaps inside laminar and transitional boundary layers using instrumented gaps etched in flat-plate models. For the range of conditions studied (Reynolds numbers 2.57×10^6 to 8.11×10^6) several trends were clearly evident. Narrow transverse gaps had very little effect on the laminar boundary layer. Local heating increases were small and the transition location changed only slightly. For transitional boundary layers, locally high heating rates were observed near the upper tangent point of the recompression surface once the gap width exceeded a minimum value. Heating

increased as the gap width-to-depth (w/d) ratio increased. None of these values exceeded the heat transfer rates calculated for a fully turbulent boundary layer.

In similar research conducted by Charwat et. al. and reported by Bertin (1980:1), supersonic flow over transverse cavities produced two distinct configurations. First is a closed cavity condition where the w/d ratio is sufficiently large to allow the flow to reattach to the cavity floor. Closed cavities have higher heating rates, due to the reattachment region, and increased heating in the downstream compression corner. In an open cavity condition, w/d is small enough to allow the flow to bridge the gap. This causes relatively low heating rates over much of the gap floor, with an increase in floor heating values at locations near the downstream end. The critical w/d ratio which separates open from closed cavity flow is about 10 to 12, for a local Mach number range of 2 to 4 (Nestler and others, 1968:7).

Bertin and Goodrich (1980:9) also obtained information on heating rates measured along the length of longitudinal slots parallel to the free stream flow. Locally high heating rates were discovered along the length of these slots. They found heating rates to be higher for slots that were of greater depth. Heating is greatest at the upper tangent point (i.e., at the corner of the gap with the flat surface). The mechanism creating this heating condition is a consequence of the slot's orientation to the free stream flow. As the flow spills into the gap, this thins the boundary layer on the flat surface, creating a corresponding increase in local heating. Finally, they found that the level of heating increases as the distance from the beginning of the slot is increased.

Research into the aerothermal environment of a generic NASP wing segment was conducted experimentally using a swept delta wing as the test model. Expansion slots

were notched into the leading edge of the wing and orientated so they were offset 70° to the free stream flow (Savage, 1991:2). Information obtained from testing was used as input data in conducting detailed temperature analysis of NASP leading edge seal concepts.

With this configuration, heating on the slot floor was found to be less than for a smooth body leading edge. Heating on the windward wall of the slot was higher than the smooth body heating rates. One unexpected result occurred near the wing leading edge tangent line (where the leading edge interfaces with the top and bottom surfaces of the wing). The leeward face indicated heating rates greater, sometimes by a large margin, than on the windward face. No data was available for the wing's surface; however, the report recommends using values obtained at the leading edge tangent line as a way of estimating their values (Savage, 1991:2).

1.4 Objectives and Scope

The main objective of this study was to compare local heat transfer rates in and around a cylinder gap with heat transfer rates of a similar smooth body surface. Heat augmentation factors were calculated using the ratio of both values. These augmentation factors were then used to find peak heating loads at the leading edge of the airfoil.

A cylinder was selected to model the NASP airfoil. Its geometry matches the radius of curvature of the leading edge of a NASP wing up through an angle of 90° (see Figure 1.1). Additionally, previous research has investigated localized heating

around smooth cylinders (without gaps). Information obtained from these sources will prove useful in evaluating the accuracy of experimental results.

The experiment investigated the effects of varying Mach number and gap width on heat transfer rates around the cylinder. Three Mach numbers and three gap widths were studied. Temperature on the cylinder surface was measured at five different locations starting at the stagnation point (0°) and moving back in 30° segments (until 120° from stagnation point). Theta (θ) was used to measure angle from stagnation point and temperature sensors on the test section were rotated together in unison as theta was changed.

One factor kept constant was the orientation of gap axis with the free-stream fluid flow. The gap was aligned in a longitudinal orientation, parallel to the flow. This orientation was chosen, since limited experimental data is available for such gaps located on the front face of a cylinder (or the leading edge of an airfoil). Off axis testing was not attempted and is beyond the scope of this study.

Finally, testing was limited to an investigation of supersonic flows. It is a logical first step to gather data in this regime before increasing the free stream velocity upward towards hypersonic Mach numbers. Facility constraints prevented any testing at hypersonic Mach numbers.

1.5 Methodology

The shock tube driver section was increased in pressure opposite the driven or unpressurized portion of the tube. A diaphragm separating the two sections was ruptured generating a shock wave which propagated down the tube. The shock wave

was followed by a small region of high speed air. For appropriate diaphragm pressure ratios, this region travels at supersonic speeds and exhibits conditions of known constant pressure, temperature, density, and flow velocity. These conditions were used to simulate a very short duration steady-state condition. As the region passed around the test section, it induced a sudden temperature rise causing energy, in the form of heat, to be transferred to the surface of the cylinder.

The transient nature of the shock tube creates problems in collecting data. Since flow conditions last for only a fraction of a second, the use of the shock tube as a tool in fluid mechanics and heat transfer relies heavily on the availability of high frequency instrumentation. Advantages of short duration tests include eliminating the need for environmental cooling required of hot tunnel facilities (Eads, 1992:1.8).

To measure cylinder surface temperatures, MEDTHERM high frequency response coaxial thermocouples were used. These thermocouples were mounted on the cylinder surface, gap wall, and gap floor.

Endevco pressure transducers provided short response time pressure measurements in the shock tube. These transducers measured initial tube pressures, used in shock tube calculations, and a pressure history of the transient flow condition. The velocity of the generated shock wave is measured by comparing the time of shock passage at two non-collocated sensors.

Surface temperatures, from each thermocouple, were converted to localized heat fluxes through the use of a concise numerical technique developed by Vidal (1955) and described by Jones (1959), Cook and Felderman (1965), Kendall and Dixon (1966), and Bonafede (1988). A heat flux time history was obtained for each location.

Local heat transfer coefficients (h) were calculated for each location using heat flux values, surface temperatures, and region flow properties (temperature, density, and velocity). These heat transfer coefficients were nondimensionalized as Nusselt numbers.

Finally, the Nusselt number values at each location were compared versus Mach number and Reynolds number. Velocity corrections were included in both Mach number and Reynolds number to account for blockage effects experienced inside the shock tube. Nusselt number values measured on the gap wall and gap floor are compared to smooth body Nusselt numbers (measured at the reference position). From these comparisons, augmentation factors were calculated and used to relate heating in the gap to smooth body heat loads.

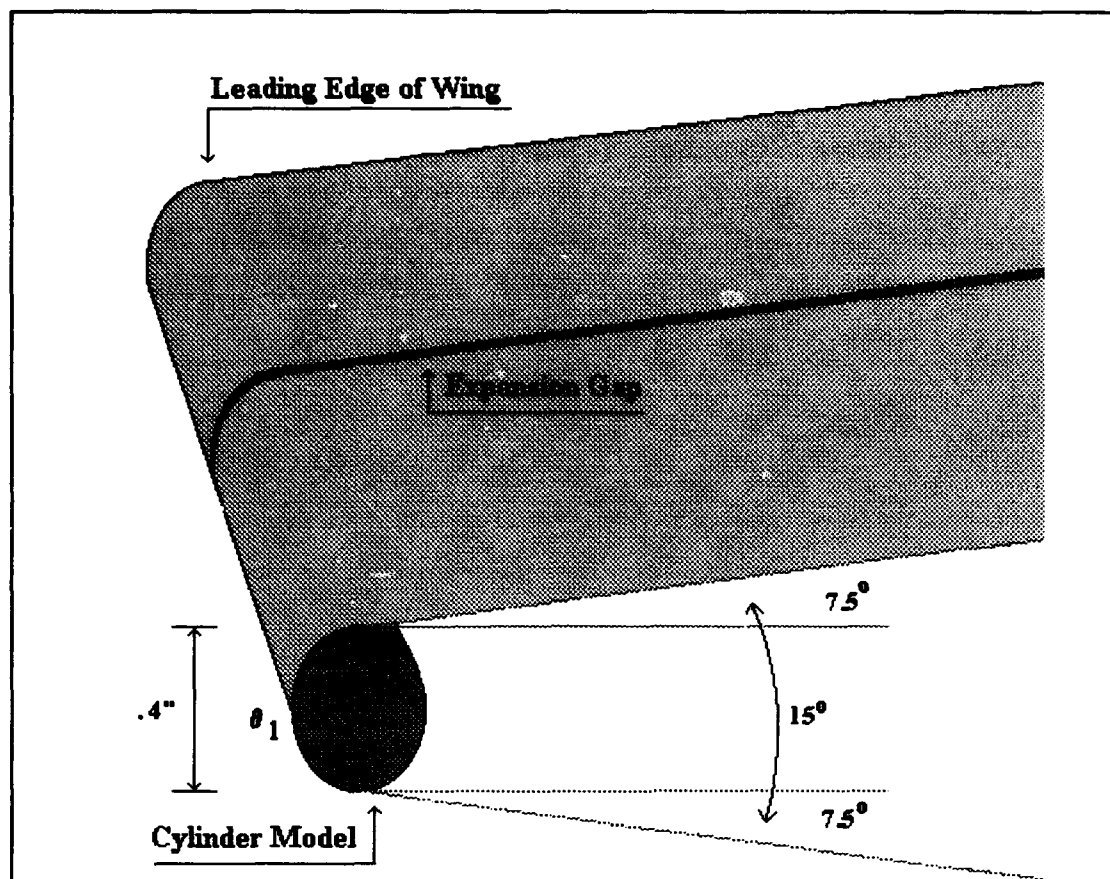


Figure 1.1. Wing/Cylinder Geometry

II. Theory

2.1 The Shock Tube

The shock tube is an apparatus used to generate a plane shock wave by the sudden bursting of a diaphragm that separates a gas at high pressure from one at lower pressure. The simplest form of a shock tube consists of a high pressure segment called the driver section and a low pressure segment called the driven section. Between these segments is a diaphragm consisting of either metal or mylar which will burst at a known pressure. Figure 2.1 shows a simple shock tube.

A normal shock wave is generated by first creating a pressure differential between the driver gas and the experimental gas in the driven section. Rupturing the diaphragm produces a compression wave in the low pressure gas which forms rapidly into a shock front. An expansion wave (or rarefaction fan) is created simultaneously and moves back into the high pressure gas. The strength and speed of the normal shock wave will depend on the initial pressure difference between driver and driven sections, and properties of the corresponding driver and experimental gases. After diaphragm rupture, conditions in the shock tube can be separated into various regions (Gaydon and Hurle, 1963:2). It is customary to denote these conditions with the following reference system:

Region 1 - Undisturbed low-pressure experimental gas. Initial pressure and temperature in this region are designated P_1 and T_1 .

Region 2 - The region between the shock front and where the experimental gas and the driver gas make contact (contact surface). Temperature and pressure in this region are labeled T_2 and P_2 . This region moves rapidly behind the shock front with velocity v_2 .

Region 3 - Region between the contact surface and the expansion wave.

Region 4 - Initial conditions at the high pressure side of the shock tube. P_4 is greater than P_1 , but normally T_4 will equal T_1 .

Region 5 - Area present if the shock wave is allowed to undergo reflection at the end of the tube.

Referring to Figure 2.2, these regions are illustrated diagrammatically by use of a location versus time depiction showing progress of the shock wave, the rarefaction fan, and contact surface separating driver and experimental gases. Pressure, temperature, and velocity distributions associated with a shock wave located at time t^* are also presented.

Region 2 is of prime interest as it establishes the conditions of test for this investigation. Region 2 is characterized by the almost instantaneous rise of temperature to a known and controlled value. Temperature and pressure are held steady as the region follows the shock wave down the tube. Test time is defined as the time it takes this region to pass through the test section. Test time depends on the location of the test section in the tube, shock wave velocity (W_s), and the velocity of the contact surface (v_2). Test time may be shortened if the reflected or rarefaction waves reach the test section before the contact surface can pass.

Using notation defined above it is possible to derive a series of basic relations for a shock wave propagating into a tube of uniform cross-section. Gaydon and Hurle (1963:14) used a comparison of laboratory-fixed coordinates (shock tube at rest) and shock-fixed coordinates (shock front at rest) to define a frame of reference from which conservation of mass, momentum, and energy properties could be applied. Figure 2.3 presents gas parameters associated with a shock wave in both coordinate systems. Using conservation of mass, momentum, and energy across a normal shock in an ideal gas, the following relationships are found:

$$\rho_1 u_1 = \rho_2 u_2 \quad (2.1)$$

$$P_1 + \rho_1 u_1^2 = P_2 + \rho_2 u_2^2 \quad (2.2)$$

$$H_1 + \frac{1}{2} u_1^2 = H_2 + \frac{1}{2} u_2^2 \quad (2.3)$$

ρ is defined as region density, u equals velocity, and H is enthalpy. The derivation of equations for pressure, temperature, and velocity in each region is straight forward. From Gaydon and Hurle (1963:20), Anderson (1990:237) and Hall(1958:142), shock velocity can be obtained knowing the initial pressure ratio across the diaphragm.

$$\frac{P_4}{P_1} = \frac{2\gamma_1 M_1^2 - (\gamma_1 - 1)}{\gamma_1 + 1} \left[1 - \frac{\gamma_4 - 1}{\gamma_1 + 1} \frac{a_1}{a_4} \left(M_1 - \frac{1}{M_1} \right) \right]^{-\left(\frac{2\gamma_4}{\gamma_4 - 1} \right)} \quad (2.4)$$

where M_1 is the shock wave Mach number (W_s/a_1) and is equal to the upstream Mach number in the shock fixed coordinate system ($v_1 = 0$). γ is the ratio of specific heats and a is the speed of sound ($[\gamma RT]^{1/2}$) for both driver and experimental gases. R is the gas constant and T is region temperature.

Actual values of M_1 will vary due to real gas effects, viscous wall interaction, and imperfect diaphragm ruptures. Gaydon and Hurle (1963), Glass (1958), and Hall (1958) all examine these effects in-depth.

The strength of the shock wave is a function of pressure ratio, gas characteristics, and initial gas temperature. Higher pressure ratios between driver and driven gases correspond to increases in shock speed and strength. Gas composition and temperature effect the speed of sound ratio (a_1/a_2), and influence shock strength. The lower the density of the driver gas ($a_1=[\gamma_1 P_1/\rho_1]^{1/2}$), the higher a_1 will be, and the stronger the shock. A driver gas with a high specific heat ratio (γ_1) will also yield a stronger shock. Finally, the higher the temperature of driver gas ($a_1=[\gamma_1 R T_1]^{1/2}$), the higher a_1 will be, and the stronger the shock.

Knowing M_1 , initial driven gas pressure P_1 , and temperature T_1 , it is possible to calculate Region 2 pressure P_2 , temperature T_2 , and velocity v_2 through use of the Rankine-Hugoniot Equations (Rankine, 1870), (Hugoniot, 1887). From Gaydon (1963:160), Hill and Peterson (1992:84), and Anderson (1990:212) test section pressure is

$$P_2 = P_1 \left[\frac{2\gamma_1 M_1^2 - (\gamma_1 - 1)}{\gamma_1 + 1} \right] \quad (2.5)$$

For temperature, Gaydon (1963:17) defines

$$T_2 = T_1 \left[\frac{(\gamma_1 M_1^2 - \frac{\gamma_1 - 1}{2}) (\frac{\gamma_1 - 1}{2} M_1^2 + 1)}{(\frac{\gamma_1 + 1}{2})^2 M_1^2} \right] \quad (2.6)$$

or from Anderson (1990:211)

$$\frac{T_2}{T_1} = \frac{P_2}{P_1} \left[\frac{\frac{\gamma+1}{\gamma-1} + \frac{P_2}{P_1}}{1 + \frac{\gamma+1}{\gamma-1} \frac{P_2}{P_1}} \right] \quad (2.7)$$

For velocity, Gaydon (1963:25) gives

$$v_2 = \frac{2a_1}{\gamma_1+1} \left(M_1 - \frac{1}{M_1} \right) \quad (2.8)$$

Note that $u_2 = (W_s - v_2)$ and $M_2 = u_2/a_2$ (see Figure 2.3). Density relationships can also be obtained through use of the ideal gas law $P_2 = \rho_2 R_1 T_1$.

2.2 Heat Transfer

Heat transfer is an energy exchange (or energy rate) due to a difference in temperature. Whenever there exists a temperature gradient in a medium or between media some form of heat transfer must take place. The mode of heat transfer that occurs between a moving fluid and a surface, both at different temperatures, is called convection.

A consequence of this fluid-surface interaction is the development of a region where the velocity of the fluid varies from zero at the surface, to a velocity equal to the undisturbed flow (u_∞). This region is called the velocity boundary layer. Similarly, there is a region in the fluid where temperature varies from surface

temperature (T_s) to the temperature of the undisturbed flow (T_∞). This region is called the thermal boundary layer. Knowledge of boundary layer phenomena is essential in understanding convection heat transfer, and the discipline of fluid mechanics plays a vital role in its analysis (Incropera, 1990:7).

A detailed discussion of convection heat transfer can be found in Incropera and other heat transfer texts. The appropriate rate equation, known as *Newton's law of cooling*, is of the form

$$q'' = h(T_\infty - T_s) \quad (2.9)$$

where q'' , heat flux, is proportional to the difference between surface and fluid temperatures, T_s and T_∞ . The heat flux is positive, in this form of the equation, if heat is transferred to the surface ($T_\infty > T_s$).

For this work T_s in equation 2.9 was obtained by measuring surface temperatures at each point of interest on the test section. Thermocouples were used to obtain a temperature history for each location. Values of q'' were calculated from T_s through a numerical approach which will be discussed later. T_∞ was measured experimentally leaving h , the convective heat transfer coefficient, as the only unknown variable.

Finding values of h at various positions on the cylinder and cylinder gap was key to this research. The value of h was then non-dimensionalized by converting it into a Nusselt number (Nu) by the following

$$Nu = \frac{hD}{k} \quad (2.10)$$

where, D is cylinder diameter and k is the thermal conductivity constant. The Nusselt

numbers determined for the gap floor and wall of the gap were compared with smooth body values to find local influence coefficients.

2.3 Heat Flux Calculations

Surface temperatures were measured with thin-film chromel-alumel coaxial thermocouples. A one-dimensional semi-infinite slab model of the thermocouple was used to derive surface heat flux from these temperatures (see Figure 2.4). The model assumes the slab extends to infinity in all but one direction. It is characterized by a single surface where transient, one-dimensional conduction occurs within the solid. This idealization is useful for early portions of a transient condition, where temperatures in the slab interior (removed from the thermocouple's surface) are uninfluenced by a change in surface conditions (Incropera, 1990:259).

The governing equation for temperature in a semi-infinite solid becomes

$$\frac{\partial^2 T}{\partial x^2} = \frac{1}{\alpha} \frac{\partial T}{\partial t} \quad (2.11)$$

where x is defined as distance into the slab and α is thermal diffusivity. The initial condition and boundary conditions for an initially isothermal, large x , semi-infinite slab are:

$$q''(0, t) = -k \frac{\partial T}{\partial x} \Big|_{x=0} \quad (2.12)$$

$$T(x, 0) = 0 \quad (2.13)$$

$$T(\infty, t) = 0 \quad (2.14)$$

$$q''(\infty, t) = 0 \quad (2.15)$$

Solutions to this problem have been derived by several sources. Vidal (1955) was the first to propose a solution using an expression in the form of an integration over time of the surface temperature. Cook and Felderman (1965:561) also derived an expression for surface heat flux using surface temperature. The integral expression, modified slightly in terms of basic properties by Bonafede (1988:41) and converted in terms of temperature surface history, is

$$q_s''(t) = \frac{k}{\pi^{1/2} \alpha^{1/2}} \left[\frac{T_s(t) - T_s(t_i)}{t^{1/2}} + \frac{1}{2} \int_{\tau=0}^{\tau=t} \frac{T_s(t) - T_s(\tau)}{(t-\tau)^{3/2}} d\tau \right] \quad (2.16)$$

where k is the thermal conductivity of the thermocouple substrate. Vidal (1956:24-26) used an alternate form of this equation as did Jones (1959:6) and Kendall (1966:4).

Cook and Felderman approximated the integral solution for surface heat flux through modeling the surface temperature function as a piecewise linear function of time. Surface heat flux is now calculated using a series summation of surface temperatures with discrete values of time. The integral in Equation 2.16 can now be performed exactly. The accuracy of the expression is limited only by the amount to which the surface temperature function is approximated by the piecewise linear

expression. Cook and Felderman's series solution, again modified by Bonafede and written in terms of temperature surface history, is

$$q_s''(t_J) = \frac{2k}{\pi^{1/2}\alpha^{1/2}} \left[\frac{T(t_0) - T_s(t_1)}{2t_J^{1/2}} + \sum_{j=1}^J \frac{T_s(t_j) - T_s(t_{j-1})}{(t_J - t_j)^{1/2} + (t_J - t_{j-1})^{1/2}} \right] \quad (2.17)$$

Cook and Felderman tested the series solution for cases where the analytical solution was known for heat flux into a semi-infinite solid. For exact values of surface temperature, the series solution behaved well and was fairly accurate. The series solution improves in accuracy when smaller time intervals are used.

An important constraint in this model is the order of time the thermocouple behaves as a semi-infinite slab. One rule of thumb discussed by Kendall and Dixon (1966:4) permits this time to be calculated as

$$t_{0.1} = 0.1 \frac{(X_{slab})^2}{\alpha} \quad (2.18)$$

where X_{slab} is the slab thickness. For times shorter than $t_{0.1}$, the temperature rise at the back of the slab is insignificant.

2.4 Heat Transfer at High Velocities

With high velocity flows it is necessary to consider the effects of compressibility and viscous energy dissipation. Convection at these velocities involves essentially two different phenomena: the conversion of mechanical energy into thermal energy which creates temperature variations in the fluid, and a variation of fluid properties as a result of these temperature variations. Extremely high velocities which lead to dissociation, mass concentration gradients, and mass diffusion will not be discussed.

This restricts the fluid flow to Mach numbers less than 5 and temperatures no greater than 2000 K.

Özişik (1985:397) recommends calculating heat transfer in high speed mediums by replacing the fluid free stream temperature (T_{∞}) in Equation 2.9 with adiabatic wall temperature (T_{aw}). Adiabatic wall temperature measures the steady state balance between viscous energy dissipation and heat conduction at the surface of the exposed body. T_{aw} is obtained from Equation 2.19.

$$T_{aw} = T_{\infty} + r \frac{v_{\infty}^2}{2c_p} \quad (2.19)$$

v_{∞} is free stream velocity, c_p is specific heat at constant pressure, and the parameter r is called the recovery factor. The value r is related to Prandtl number (Pr) and for air $r \approx Pr^{1/2}$ (Kays and Crawford, 1993:380).

Another correction for high-speed flow is used in calculating reference temperature. Reference temperature is used in determining values for different properties of the fluid. For low-speed fluids the reference temperature is normally an average of the difference between free stream and surface temperatures. Temperature gradients in high-speed fluids are generally very large and properties of the fluid will also vary significantly with temperature. The variation of these properties in a boundary layer can be included into heat transfer equations by evaluating them at the following reference temperature (Özişik, 1985:398).

$$T_{ref} = T_{\infty} + 0.5 (T_s - T_{\infty}) + 0.22 (T_{aw} - T_{\infty}) \quad (2.20)$$

This temperature correlates solutions within a few percent for Mach numbers up to 20 over a wide range of free-stream and surface temperatures.

2.5 The Cylinder in Cross Flow

A cylinder positioned in cross flow was picked to model the effects of aerodynamic heating experienced on the leading edge of a blunt-nosed axisymmetric body. A great deal of information exists about the aerodynamics of cylinders and the localized heat transfer around them. A brief examination of this information is given to provide an understanding of the different processes influencing cylindrical heating.

Heat transfer around a cylinder in cross flow is a function of many different variables. These include free stream velocity, turbulence level, physical properties of fluid, thermal load, heat flux direction, geometry of the body, and other factors. A number of authors cover these areas in detail. They include: Žukauskas (1987), Incropera (1990), Özişik (1985), and Žukauskas (1972) to name a few.

Fluid dynamics and heat transfer around curvilinear bodies are very complex processes. They are mainly dependent on fluid type and Reynolds number (Re)

$$Re = \frac{\rho v_{\infty} D}{\mu} \quad (2.21)$$

D is cylinder diameter, v_{∞} is free stream fluid velocity, ρ is fluid density, and μ is dynamic viscosity. Drag forces on a cylinder, created by surface shear stresses and pressure differentials in the flow direction, vary with changing Re number. Figure 2.5 shows the drag coefficient for a circular cylinder as a function of Re . The variation of

drag coefficient (and fluid flow) in Figure 2.5 is a result of drag being dominated by flow separation on the rear face of the cylinder. Regions of different Re and fluid flow include: (1) laminar, (2) subcritical, (3) critical, and (4) supercritical. These variations are caused by the different contributions of skin friction at low Re , and laminar and turbulent boundary layers on flow separation at higher Re (Anderson, 1978:195). Figure 2.6 sketches laminar and turbulent flow around a cylinder.

Variation in fluid flow over a cylinder gives rise to similar variations in local heat transfer (see Figure 2.7). In real fluids, because of viscosity effects, a laminar boundary layer forms on the front part of the cylinder. Its thickness increases downstream until an adverse pressure gradient on the cylinder forces boundary layer separation. This separation is strongly influenced by the occurrence of boundary layer transition which is dependent on Re number.

For $Re \leq 10^5$, Nu near the stagnation point decreases with increasing θ (angle from stagnation point). This is due to the growth of the laminar boundary layer. A minimum is reached at $\theta \approx 80^\circ$ at which point separation occurs. Nu then increases with θ due to mixing associated with vortex formation in the wake (Incropera, 1990).

At $Re = 2 \times 10^5$, two heat transfer minima are observed in the critical flow regime. The first minimum is again due to laminar boundary layer development. A sharp increase in Nu occurs at $\theta \approx 80^\circ - 100^\circ$ and is caused by boundary layer transition to turbulence. The second minimum is at the separation point of the turbulent boundary layer, $\theta \approx 140^\circ$, and Nu increases again with the formation of the wake region.

In the supercritical flow region ($Re = 2 \times 10^6$) the first heat transfer minimum

moves forward on the cylinder to around $\theta \approx 30^\circ$. This shift is caused by an increase in turbulence level which acts to narrow the laminar boundary layer. Higher turbulence levels also create heat transfer increases on the front part of the cylinder. The effects of higher turbulence levels are generally insignificant in the rear part of the cylinder (Žukauskas, 1987:6.7-6.9).

2.6 Corrections for Flow in a Restricted Channel

Consideration must be given to the effects of placing a cylindrical model in flows restricted by walls and experiencing considerable blockage of the cross section. Blockage is defined to be the ratio of the model's projected area with the cross section area of the channel.

$$R_{block} = \frac{A_{projected}}{A_{tube}} \quad (2.22)$$

As blockage ratio (R_{block}) increases, velocity outside the boundary layer surrounding the cylinder will increase. This changes both the pressure and velocity distributions of the fluid passing the model.

Žukauskas (1972) defines an average value of velocity which is obtained by integrating over the cylinder surface

$$V_{corr} = V_{\infty} \left(1 - \frac{\pi}{4} R_{block} \right)^{-1} \quad (2.23)$$

This value is used to take into account the blockage ratio in technical calculations of drag and heat transfer. Equation 2.22 is valid for all blockage ratios less than 0.8.

Heat transfer also changes with an increase of channel blockage on the flow pattern. Heat transfer on the front portion of the tube increases as the blockage ratio is increased. These influences are taken into account by substituting v_{corr} for free stream flow (v_∞) in the calculation of Mach and Reynolds numbers (Žukauskas, 1972:105,133).

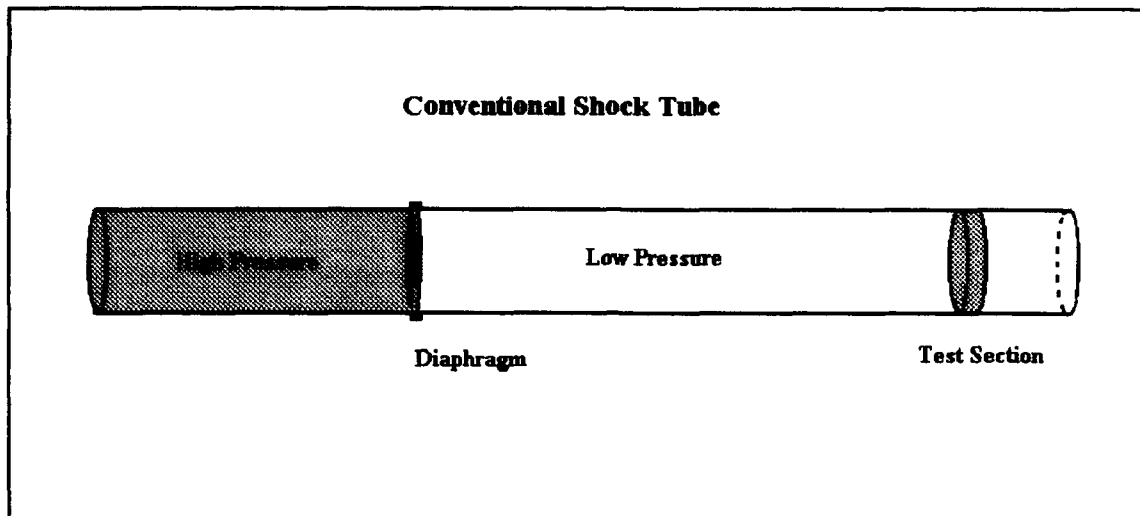


Figure 2.1. Conventional Shock Tube

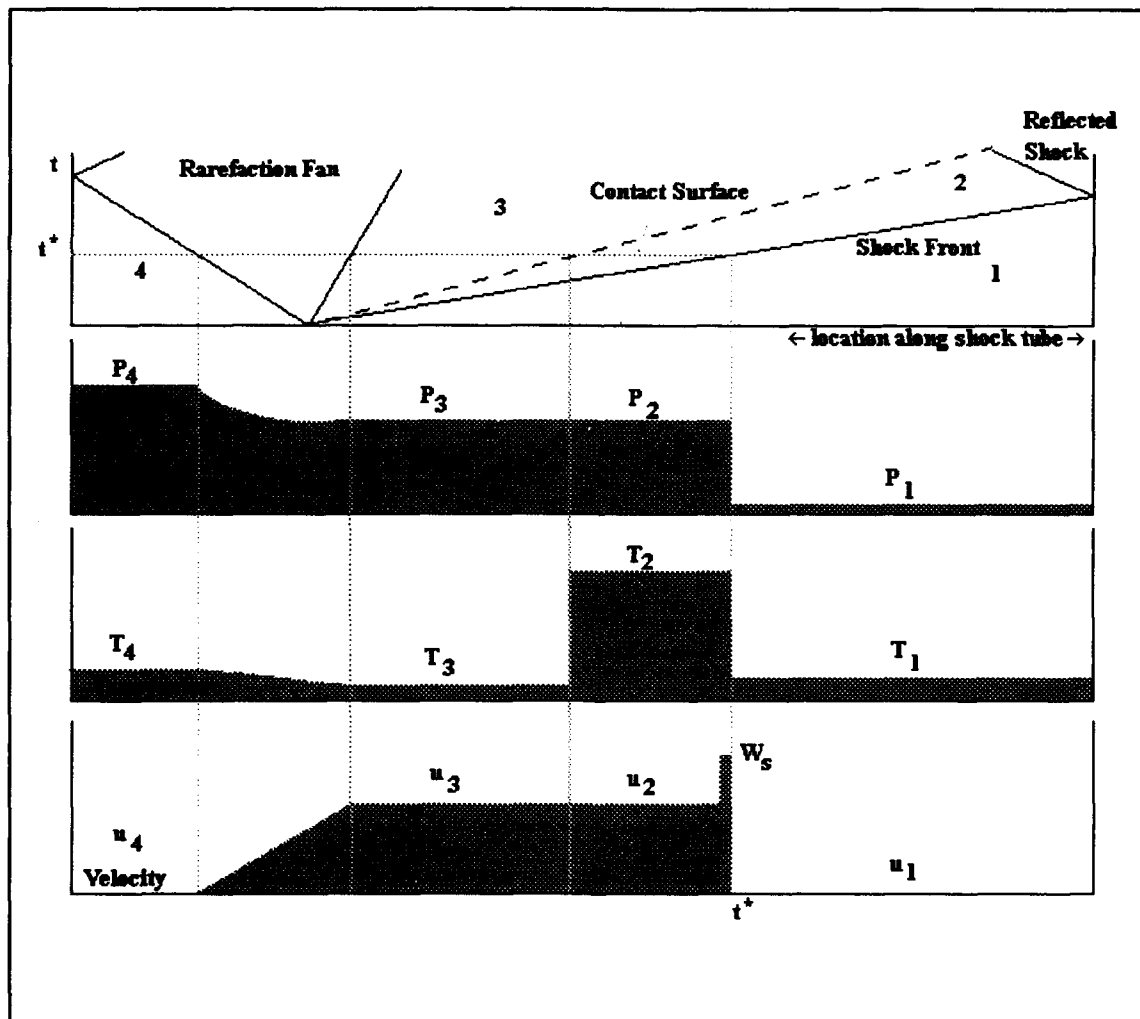


Figure 2.2. (x-t) Diagram and Pressure, Temperature, Velocity Distributions at time t^*
2.15

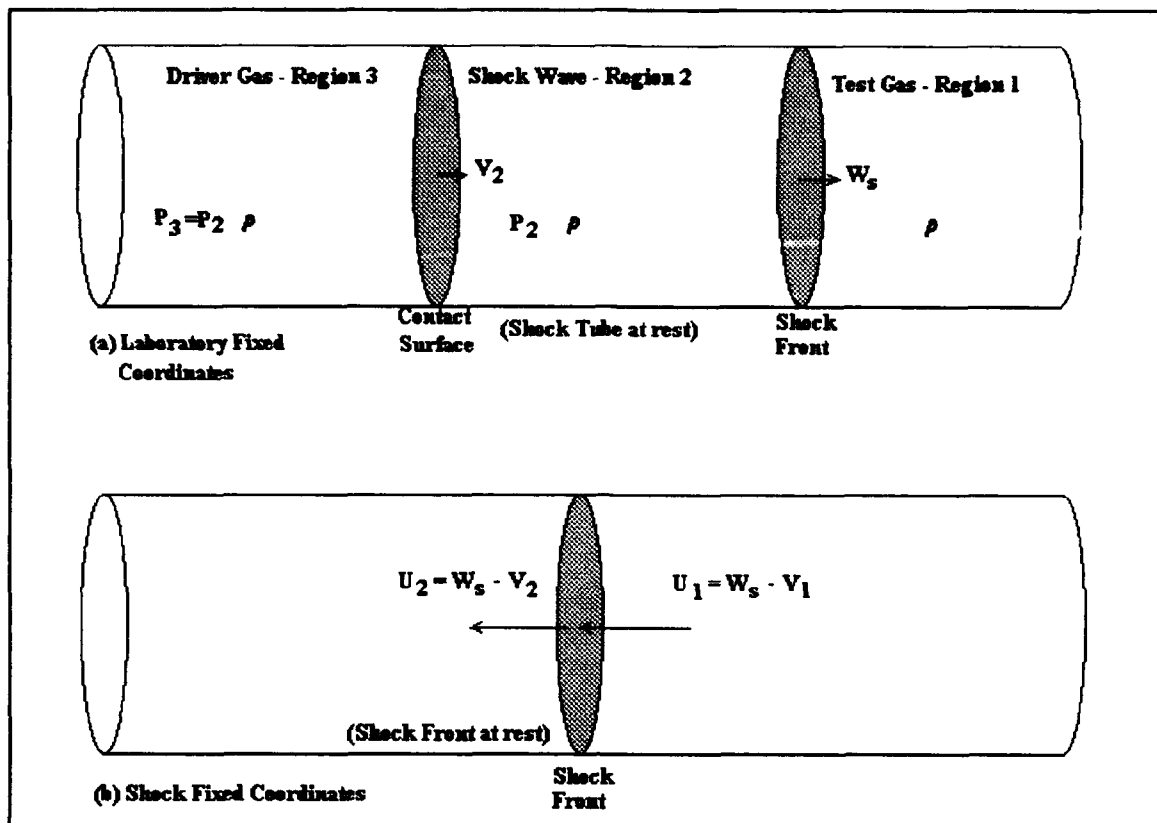


Figure 2.3. Gas Parameters Associated with Shock Wave Coordinate Systems
(Gaydon, 1963:14)

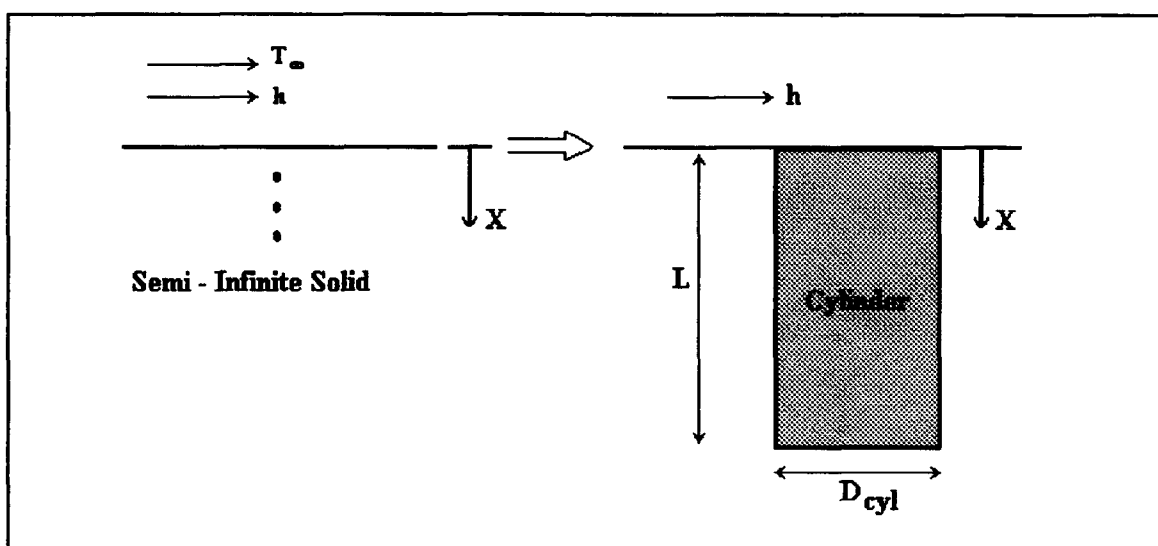


Figure 2.4. Simulating a Semi-Infinite Solid with a Two-Dimensional Model
(Bonafede, 1988:61)

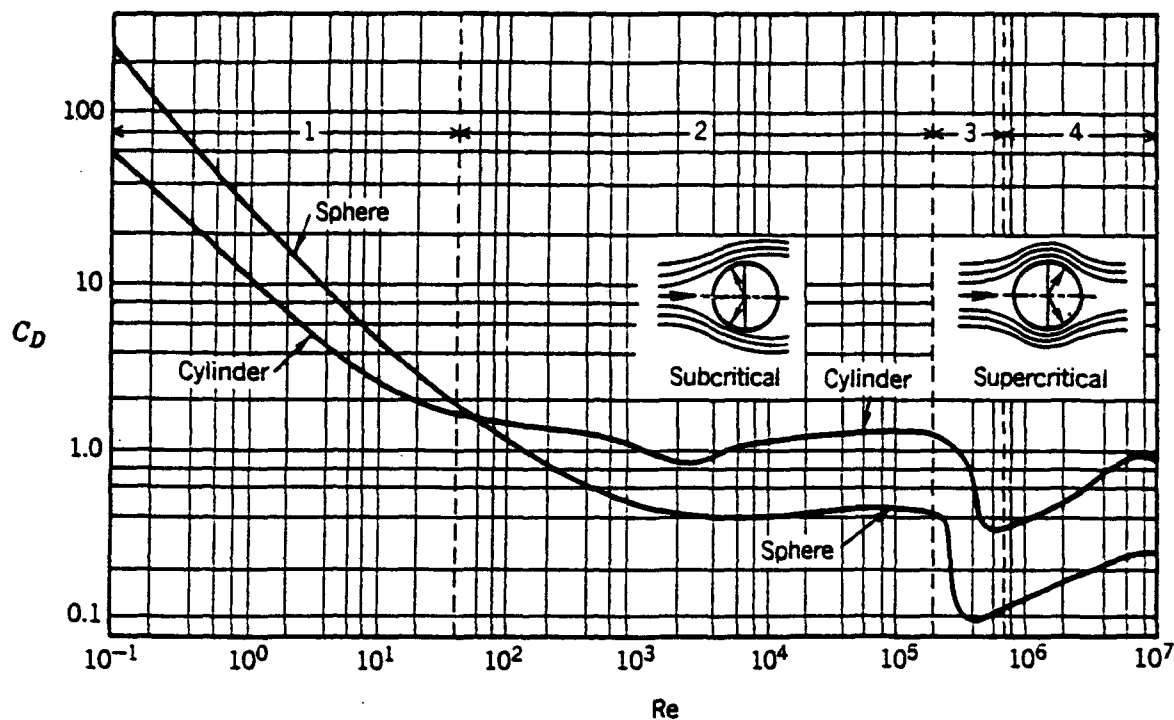


Figure 2.5. Total Drag on a Cylinder and a Sphere for Variable Re
(Žukauskas, 1987:6.7)

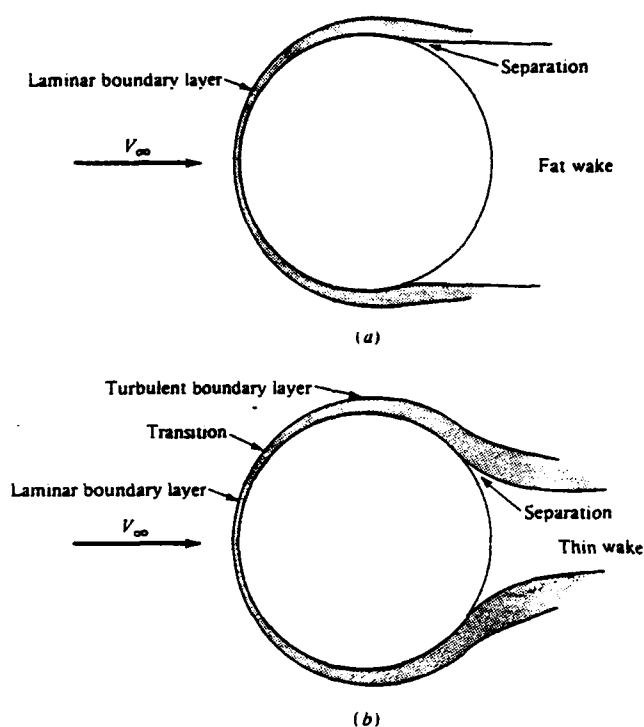


Figure 2.6. Laminar and Turbulent Flow Around a Cylinder
(Anderson, 1978:197)

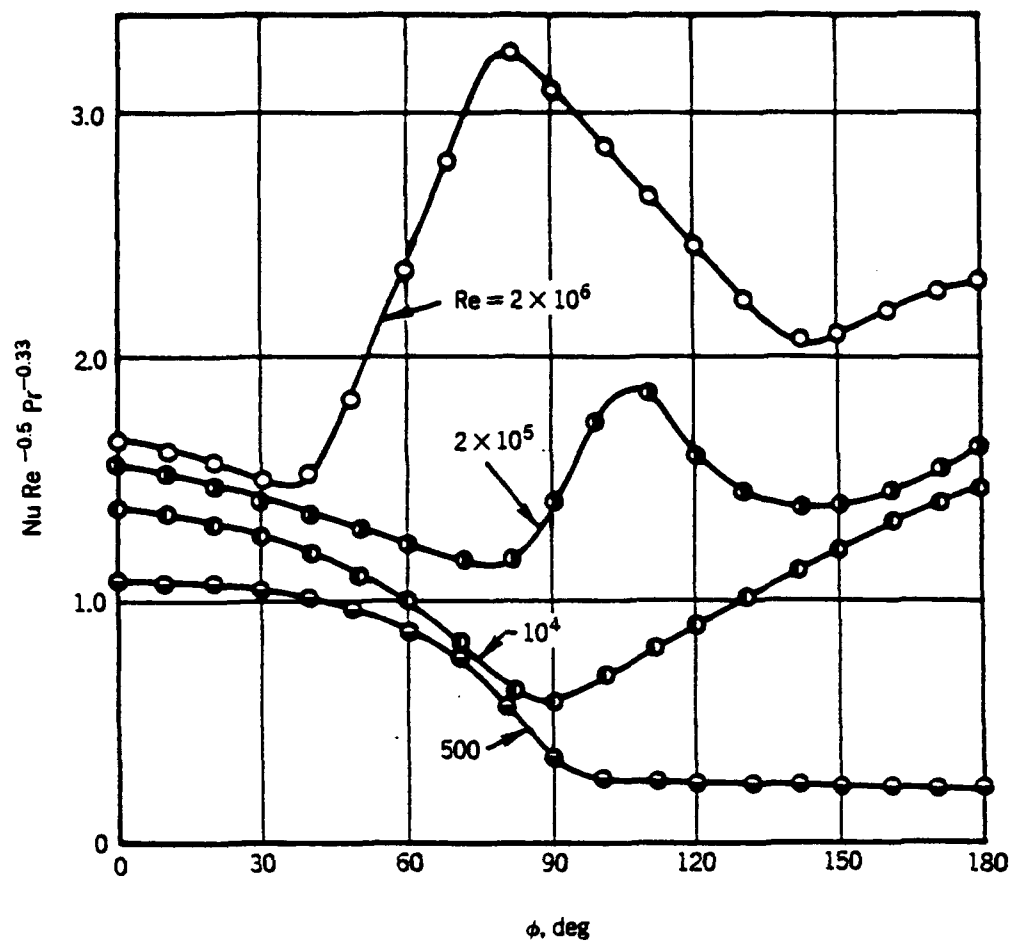


Figure 2.7. Local Heat Transfer From a Cylinder for Variable Re
(Žukauskas, 1987:6.9)

III. Experimental Apparatus

3.1 The Shock Tube

General Description. The shock tube used for this study is constructed of type-321 stainless steel tubing. Its cross-section is circular in shape with an inside diameter of 2.069 inches. Tube walls are one inch thick. Each section of tubing is five feet long and the modular construction permits the user to vary the length of the driver sections, driven sections, and location of the test section to meet the specific needs of the test (McQueen, 1984:6). To gain easy access in changing diaphragms between firings, an electrically actuated pneumatic piston/cylinder is installed to roll the driver section away from the rest of the shock tube. For this study, the length of the driver section was five feet while the length of the driven section was 25 feet. The test section was placed before the last five foot segment of the driven section, 20 feet downstream from the diaphragm. Figure 3.1 shows the shock tube driver and driven sections.

Dry air was utilized for both the driver and driven gas. Supply pressures up to 2500 psig were available to pressurize the driver section for different diaphragm pressure ratios. Air pressure in the driven section (P_1) was left at atmospheric for all tests.

Diaphragm Section. Diaphragms were constructed using stainless steel or aluminum. Diaphragms were .032" thick with scribe depths ranging from .021" to .026" for stainless steel and .017" to .019" for aluminum.

The double diaphragm assembly in the shock tube is a device designed to operate with either one or two diaphragms, depending on the operating mode selected. In the single diaphragm mode, the driver gas pressure (P_d) is raised to the burst pressure of a given diaphragm material. Rupture pressure depends on diaphragm thickness and scribe depth. Although adequate in producing shocks, this method is problematic (e.g. poor predictability due to the variations found in diaphragm strength).

The double diaphragm mode is more useful in predicting shock strength and when diaphragm failure takes place. In this mode, two diaphragms are placed between the driver and driven sections. Pressure is increased in the driver section and region between the two diaphragms to one-half the desired pressure ratio. Both diaphragms must be able to withstand this pressure. The region between the diaphragms is sealed off by closing a valve, and the driver section is pressurized to the desired (P_d/P_t) pressure ratio. Diaphragm rupture is activated by venting the region between diaphragms, creating a high pressure differential between the upstream diaphragm and driver section. This induces a failure in the upstream diaphragm followed by rupture of the downstream diaphragm (McQueen, 1984:10).

Support Equipment. Several items of equipment are required to operate the shock tube. A control panel was used to open and close pressure valves during system pressurization, firing, and venting. A remote camera was used to monitor driver pressure during the pressurization process and also to confirm diaphragm rupture. Finally, a pressure regulator was used to control the flow of high pressure air (2500 psig) into the driver section. A schematic of control devices is shown in Figure 3.1.

3.2 The Test Section

The test section consisted of a stainless steel cylinder mounted in a shock tube connection joint. The test section was mounted 20 feet downstream from the tube diaphragm and five feet from the end of the driven section between the last two segments of tubing. Stainless steel was used to construct the model because of its known values of thermal diffusivity (α) and thermal conductivity (k). Additionally, these values closely match the thermophysical properties of thermocouple probe material selected for the experiment.

The test cylinder consisted of an instrumented cylinder, an instrumented sleeve, a simple sleeve, and three thermocouples (see Figures 3.2a, 3.2b, and 3.2c). The instrumented cylinder was inserted inside both sleeves to create a larger cylinder having a diameter of 10.16 mm. The test section spanned the inside of the shock tube connection joint and was 52 mm in length. The instrumented sleeve provided access for both reference and wall thermocouples. The simple sleeve was mounted opposite the instrumented sleeve leaving a gap exposing the floor thermocouple. Gap depth equaled 2.03 mm. The simple sleeve was adjusted to vary the width of the gap. The entire assembly rotated inside the connection joint and was used to place thermocouples at various angles (θ) from the stagnation point.

3.3 Instrumentation

Pressure Measuring Equipment Two Endevco 8510B-500 (0-500 psig) pressure transducers were used to obtain pressure information inside the shock tube. These sensors were placed in the driven section and are located five feet and 15 feet

downstream from the shock tube diaphragm (Figure 3.3). A Viatran, model 104, pressure transducer was mounted in the driver section to record Region 4 pressures (P_4). The Viatran operates in a pressure range of 0 to 2000 psig. Additionally, driver pressure was displayed via an Ashcroft pressure gauge. This gauge monitors driver pressurization during test runs and verifies diaphragm rupture during shock initiation.

Each pressure transducer voltage output was fed into an Endevco model 4423 signal conditioner for signal processing, filtering, and amplification. Information was then fed into the DL1200 datalab for recording and processing. Information on pressure transducer calibration procedures and calibration graphs is contained in Appendix A.

Temperature Measuring Equipment. Temperature measurements were obtained using MEDTHERM coaxial thermocouple probes. These probes offer microsecond response times and the ability to measure rapid temperature variations in metal wall surfaces. MEDTHERM thermocouples have operated successfully inside combustion chambers, gun barrels (MEDTHERM TN-371, 1977), bearings, and in laser heating applications (Lowder, Mooney, and O'Neil, 1974).

"Through the wall" mounting techniques used in model construction allows measurement of wall surface temperatures without disturbing the surface geometry. The thermal junction is formed within a one to two micron thickness at the end of the thermocouple, allowing for very accurate positioning of the junction. The probe is inserted through an accurately drilled hole in the model so the junction forms a continuous part of the test surface. In order for the probe surface temperature to be the same as the wall surface temperature, the probe materials were selected so as to

have values of thermal diffusivity and thermal conductivity which closely match the corresponding model wall properties (MEDTHERM Bulletin 500). Advantages of the probe include:

Response Time: The small mass of the thermal junction allows for a nominal response time of 10 microseconds for a slivered junction.

Accuracy: Conduction losses are minimized because the thermocouple materials are actually part of the wall.

No Surface Protuberance: Convective flow over the surface is undisturbed.

Three thermocouples were installed into the test section using the procedures detailed above. All were type: **TCS-015-K-.375-CR-TG6-0-0**. Type K thermocouples (Chromel P, Alumel) were picked due to similarities with stainless steel in material thermal diffusivity and conductivity. Construction consists of the substrate element (a tube of Chromel P) swaged over the second element (a wire of Alumel) with .0005 inch thick insulation between elements (see Figure 3.4). A contact is made on the end of probe by dragging emery paper across the face in one direction. This cold welds slivers of the tube metal and center wire together at the probe surface forming a "sliver" junction (Jones, 1993).

Hardware compensation was used to find equivalent voltage from each thermocouple. Three battery powered Miniature Electronic Ice Points (Omega model MCJ) provide type K voltage calibration. Output voltage from each Ice Point Reference was noise filtered and amplified using a Pacific Instruments Differential Data Amplifier (60A-2,A17,B6,F412-G1). Amplified voltage was sent, via 50' coaxial cables, to the DL1200 datalab for recording and processing. Thermocouple voltage to

temperature conversions were accomplished using a non-linear transformation equation. Appendix B details the procedures used in converting thermocouple voltage into units Kelvin.

3.4 Data Acquisition System

The Datalab DL1200 Multichannel Waveform Recorder is a high-speed, analog-to-digital instrument used to capture voltage signals from pressure and temperature sensors. Up to eight analog channel inputs can be received simultaneously. After capture, the signals are digitally transferred, stored, and analyzed using Data Analysis and Display Software (DADiSP, version 3.01C). This software runs on a COMPAQ 80386-25 computer with Windows 3.1. DL1200 instrument parameters are controlled remotely through the DADiSP program using a macro incorporating IEEE-488 (GP-IB) interfaces (DL1200,1984:1). Additionally, a Dynascan, model 1570A, Dual Time Base Oscilloscope and a Hewlett Packard 3456A Digital Voltmeter are used for fault detection and signal amplification calibration.

Data was acquired by triggering the DL1200, which stored each channel signal as a number of equally spaced points representing the waveform amplitude at discrete moments in time. Triggering, trigger setup, sample interval, and channel setup were all controlled by DADiSP. After recording a data series, digitized signal information was transferred from the DL1200 into the DADiSP Worksheet environment. The DADiSP Worksheet uses the form and power of a spreadsheet in displaying, manipulating, and analyzing complex scientific and technical data. A Worksheet consists of a number of graphic windows (similar to cells in a traditional spreadsheet).

Each window displays a series of data (pressure series, temperature series, etc.). These windows contain either a raw data series or the mathematical transformation of data appearing in other windows. As many as 100 graphic windows may be contained in a single Worksheet (DADiSP, 1992:3-2).

During data reduction, it was necessary to integrate surface temperature data to calculate the corresponding surface heat flux (see Section 2.3). A FORTRAN program was written using the series solution mentioned in Chapter 2. This program was imbedded within the DADiSP program, and data series information was marked, input, and retrieved using the Worksheet window format. Appendix C contains the FORTRAN temperature to heat flux conversion program.

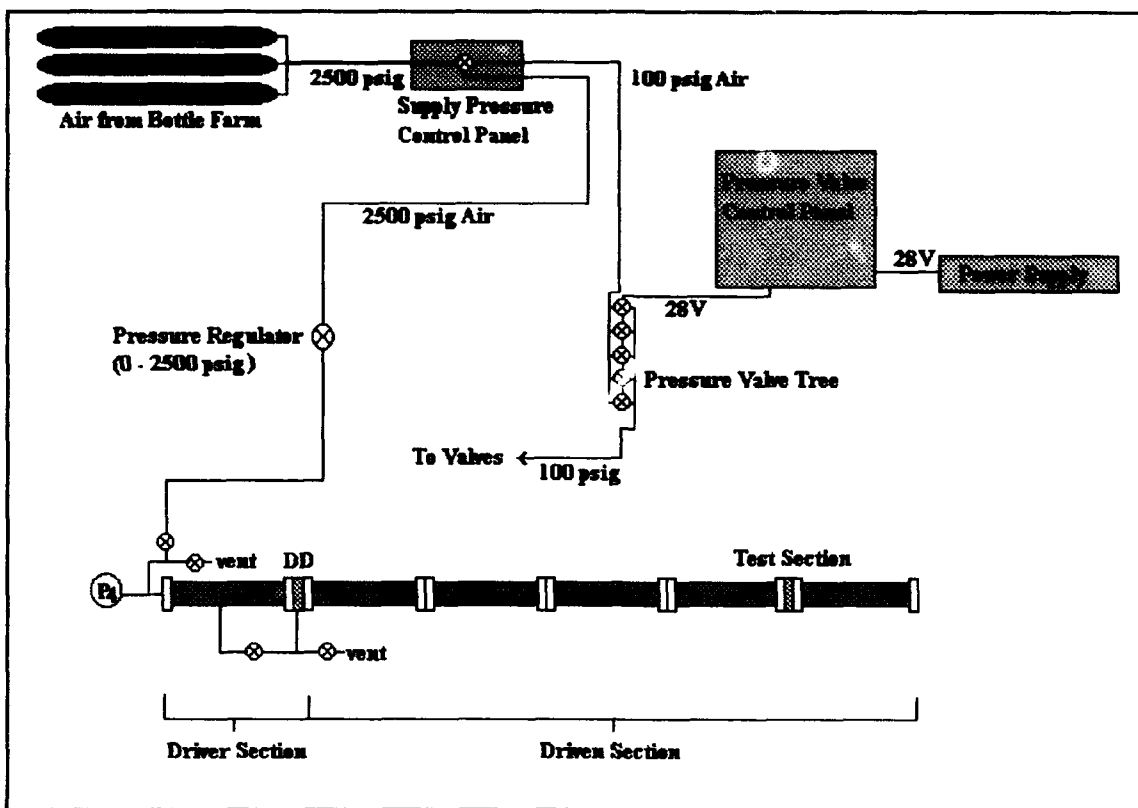


Figure 3.1. Shock Tube and Support Equipment

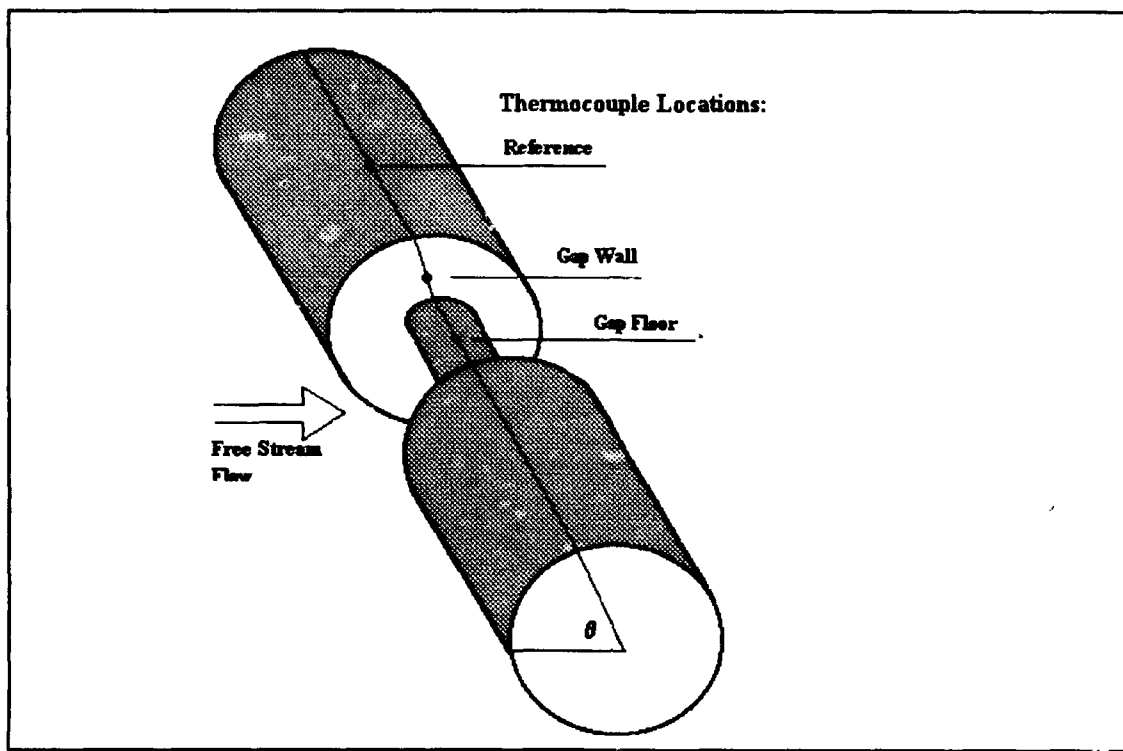


Figure 3.2 (a). Instrumented Cylinder

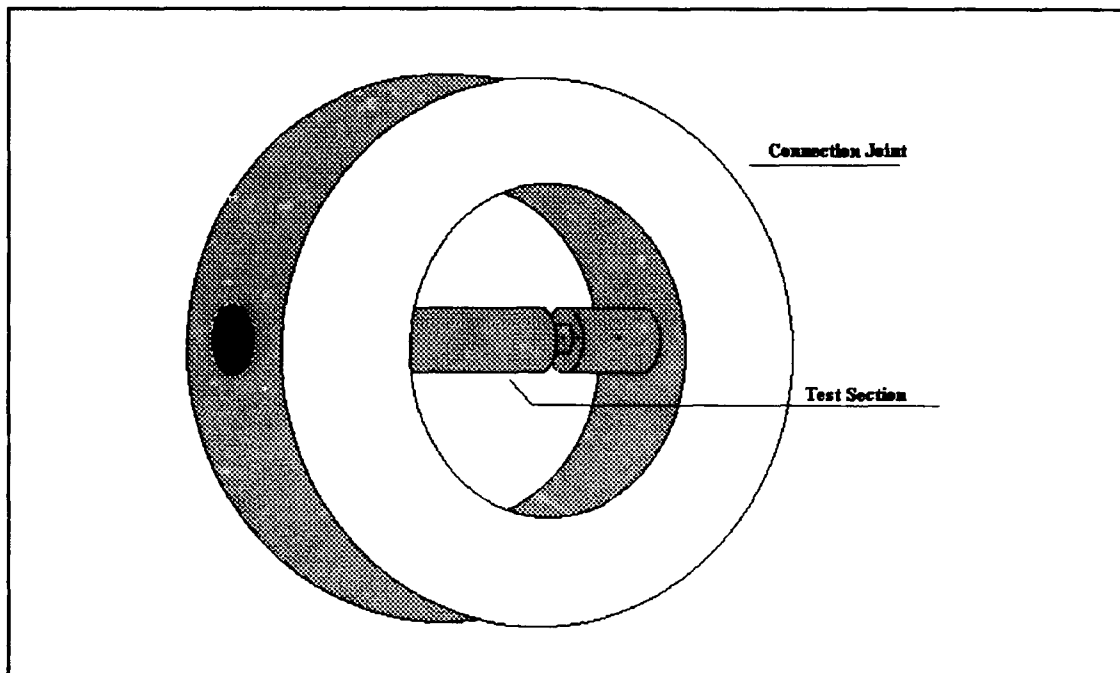


Figure 3.2 (b). Cylinder Mounted in Connection Joint

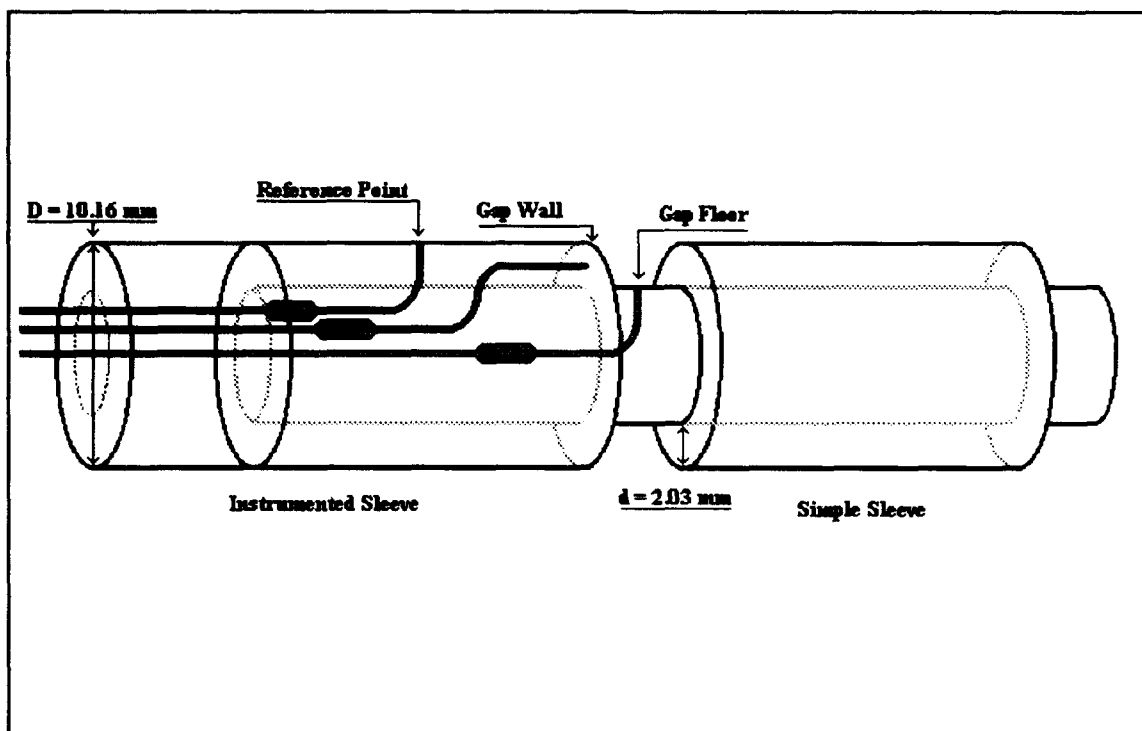


Figure 3.2 (c). Thermocouple Mounting in Test Cylinder

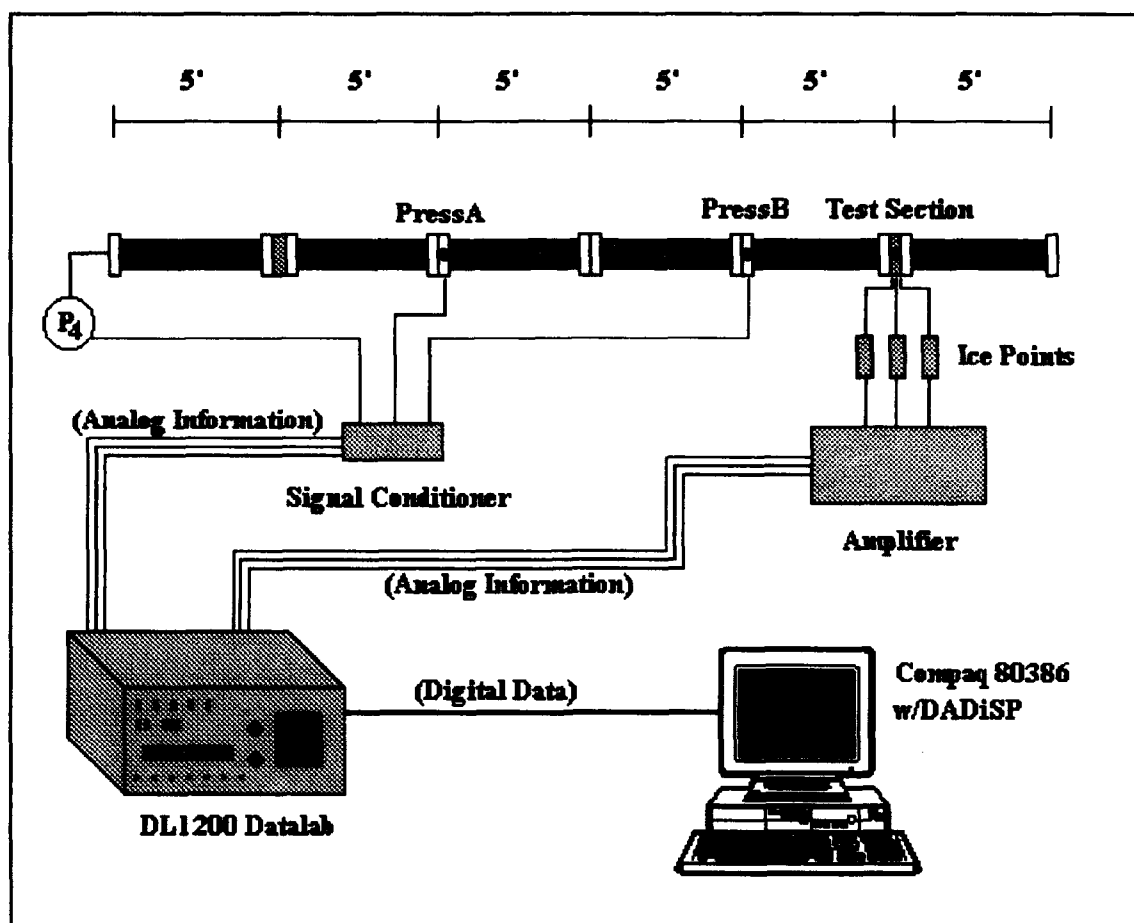


Figure 3.3. Shock Tube Instrumentation

Thermocouple Model:
TCS-015-K-375-CR-TG6-0-0

TCS - Probe Model Number

015 - Probe Diameter (in)

**K - ISA Calibration Code
(Chromel-Alumel)**

375 - Probe Length (in)

**CR - Function Plating Material
(Chromium)**

**TG - Lead Wire Insulation
(Teflon Fiberglass)**

6 - Length of Lead (ft)

0 - No Transition Piece

**0 - No Mounting Configuration
Selected**

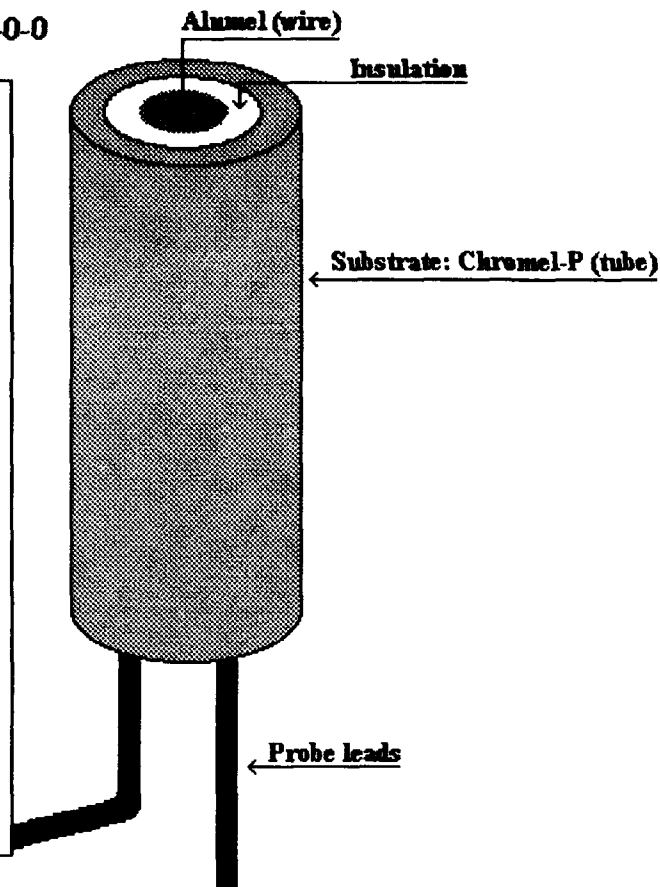


Figure 3.4. Medtherm Thermocouple

IV. Experimental Procedure

4.1 Shock Tube Set Up

Instrument Calibrations. To assure accuracy in obtaining data, calibrations were performed on sensors and amplification devices (see Appendices A and B). All electronic equipment was turned on at least 30 minutes prior to recording any data. The Pacific Instruments, Differential Data Amplifier proved especially sensitive to temperature fluctuations; however, after a sufficient warm up period the amplifier worked normally. Voltages at each Ice Point Reference were recorded using a Hewlett Packard digital voltmeter. Voltage signals were fed through the Differential Data Amplifier where each signal was filtered and amplified by a gain of 100 (40 dB). Voltages were checked again using the voltmeter. Fine gain adjustments on the amplifier were used to calibrated voltage gains and ensure accuracy was met. In order to reduce the amount of high frequency noise sent to the DL1200, the signals were also passed through a 1kHz bandwidth, four pole Butterworth filter. This filter was chosen due to its flat amplitude response (Pacific, 1987:1.8). Thermocouple voltages were measured a third time at the DADiSP data output display and compared with the initial thermocouple voltage readings. Voltage differences between the two measurements reflect feed line losses (50' coaxial cables) and varying equipment sensitivities. Table 4.1 records the percent change in thermocouple voltage due to these losses.

Table 4.1

Thermocouple Voltage Feedline Losses

Date	Thermocouple #1	Thermocouple #2	Thermocouple #3
27 Aug 93	0.093 %	2.376 %	0.835 %
2 Sep 93	0.896 %	1.515 %	1.093 %
9 Sep 93	2.547 %	0.575 %	1.440 %
5 Oct 93	2.796 %	0.270 %	2.384 %
12 Oct 93	2.740 %	1.399 %	2.189 %
Avg Voltage Loss	1.81 %	1.23 %	1.59 %

Pressure gauges were referenced to ambient absolute pressure before performing shock runs. An ambient pressure of 14.43 psia was used to reflect the elevation of the laboratory above sea level. Barometric pressure changes were assumed to be negligible. Voltage to pressure conversions were accomplished with calibration slope information calculated in Appendix A.

Preparing the Shock Tube. The test section was set up using gap width and the angle from stagnation point (θ) as variables. The cylinder was assembled with the three thermocouples aligned and the simple sleeve positioned to the desired gap width (2.5mm, 5mm, 7.5mm). The cylinder was then installed into the shock tube connection joint and rotated to the proper theta for data collection. Three runs are performed at this position (at different velocities) after which the cylinder was rotated to the next angle of interest. Data was collected at five different angles, starting at the stagnation point ($\theta = 0^\circ$) and then in 30° increments until $\theta = 120^\circ$. The cylinder was then removed and adjusted to the next gap width.

The shock tube was readied for use once the test section was installed and positioned. The driver section pressure was increased to a pressure ratio corresponding to desired flow velocity for a particular run. The driven section was left at ambient pressure and temperature (P_1 and T_1). Once the desired pressure ratio was achieved between driver and driven sections, a shock wave was generated using the double diaphragm technique mentioned in Section 3.1. Measurements of the test condition occurred after passage of the incident shock through the test section. Reflected shock conditions were not recorded.

Obtaining repeatable flow conditions was essential in comparing data runs. Precise control and measurement of driver and driven pressures played a major role in repeatability, since P_2/P_1 determines the resultant shock strength, and in turn, flow velocity (Eads, 1992:4.8). Burst characteristics of the diaphragm also have a major impact on repeatability. Improper diaphragm rupture can lead to shock strengthening and inconsistent shock wave formation. This may yield different shock wave velocities from the same pressure ratio. Pressure time history graphs from each pressure transducer were checked for instantaneous increases of pressure during normal shock wave passage (step impulse). Shock runs which displayed step pressure rises at each transducer were assumed to have valid normal shocks.

4.2 Data Collection

Before shock wave generation, the DL1200 was armed and awaited a trigger signal to begin recording information. The trigger was selected to key off channel 1 which receives information from pressure gauge A. Trigger threshold level was set to

begin recording when a 10 % change in the channel input level and a positive slope change were observed (going from smaller to larger voltages through the trigger level). Trigger information was filtered, using a slow AC connection (ACS) technique, to remove high frequency noise and cut down on erroneous trigger signals. Trigger pulse and subsequent data collection were initiated when a shock wave passed the first pressure sensor (PressA).

After a trigger signal was received, the DL1200 recording data from each channel at a rate and manner defined in timebase setup. The DL1200 was equipped with two separate timebases to provide flexibility in recording sampled data. Timebase A was used for the first portion of the record. It was equipped with pre-delays and post-delays which define the percentage of samples captured before and after the trigger pulse. It sampled the analog signal at time rate A. Timebase B followed A and sampled at rate B until memory was filled. Both timebases were set to sample every 5 μ sec with a pre-delay containing 10 % of the total record. No post-delay was set.

A total of 4,095 data samples was collected per channel for each test run. Each channel had a time length of 20.5 msec to capture pressure and temperature changes during the test before memory buffers were filled. DL1200 channel gain was set to capture optimum signal coverage and resolution. Channels collecting thermocouple signals measured voltages in the range of -.5V to .5V and had an amplitude resolution of .24 mV. Pressures were measured at a range of -1V to 1V and amplitude resolution was .49 mV. Each signal was recorded as a data series of equally spaced points representing waveform amplitude at discrete moments in time. Collected data series (from each sensor) were transferred into the DADiSP program for processing.

4.3 Data Reduction Methods

All data was reduced using the DADiSP worksheet format described in Section 3.4. Figure 4.1 displays test section variables and parameters of interest used during data reduction.

Voltage information from each channel was first converted to either pressure or temperature using transformations calculated in Appendices A and B. Relevant surface temperatures were extracted from each thermocouple data series (normally 1800-2000 data points) and input into the FORTRAN program for calculation of surface heat fluxes. Random fluctuations in each curve were smoothed using a 20-point moving average around each point in the data series. Test times ranged from 3 to 5 msec depending on the strength of the normal shock.

Free stream temperature (T_∞) was obtained from Region 2 temperatures. T_2 was assumed equal to T_∞ during the shock tube test time discussed in Section 2.1. T_2 was calculated using the perfect gas law and Region 2 pressure (P_2). Since there was no pressure gauge collocated at the test section, pressure gauge B was used in calculating P_2 . Pressure gauge B was located five feet in front of the test section; however, it was assumed P_2 did not change dramatically in this distance. Pressure data was extracted, converted to T_2 , and matched to coincide with surface temperature data. T_2 was converted to T_{aw} , to correct for high velocity fluid flows (Section 2.4), and combined with surface temperature and surface heat flux to calculate heat transfer coefficients.

Free stream velocity (v_∞) was assumed to equal v_2 (Figure 4.1) and v_2 was calculated using M_1 and Equation 2.8. M_1 was calculated using the time difference

between shock passage between pressure gauges A and B. The value v_2 was used in intermediate calculations to find T_2 and reference temperature (T_{ref}). Finally, v_∞ was corrected for blockage effects (Section 2.6) and v_{corr} was used to calculate Mach and Reynolds numbers for flow velocities (note: the speed of sound (a_2) was assumed constant while calculating M_{corr} and RE_{corr} ($M_{corr} = v_{corr}/a_2$)). Table 4.2 lists blockage corrections for the three different flow velocities investigated.

Table 4.2
Velocity Correction Due to Blockage Effects

Velocity Setting	$v_\infty = v_2$ (m/s)	M_2	a_2 (m/s)	v_{corr} (m/s)	M_{corr}	RE_{corr}
Vel #1	352	0.84	420.4	436	1.04	5.6×10^5
Vel #2	425	0.96	441.3	527	1.19	7.1×10^5
Vel #3	528	1.11	474.0	655	1.38	9.4×10^5

Nusselt number values at each gap location were found using Equation 2.10 along with heat transfer coefficients, cylinder diameter, and the fluid's thermal conductivity constant (k). The value k was found using the reference temperature (Equation 2.20) and values listed in Table A.4 of Incropera (1985:A15). Figure 4.2 is a representative example of the worksheets used in reducing data.

Graphs containing Nusselt number values calculated from each test run were presented in Appendix F. Values for gap floor, gap wall, and reference location were overlaid to display the differences in heat transfer between them. This was accomplished for each test. Nusselt number values were averaged and this information, along with data from each test run, was consolidated to examine Nusselt

number dependence on flow velocity, gap location, gap width, and angle from stagnation point.

4.4 Verification of Data Results

The validity of experimental procedures, quality of data, and data reduction techniques were verified using a test run configured with the thermocouple mounted flush against the side of the shock tube wall. A flat plate geometry was assumed since the exposed probe face of the thermocouple was much smaller than the radius of curvature of the tube wall. The known characteristics of convective heat transfer along a flat plate were used to validate experimental results.

Localized heat transfer on a flat plate was simulated using a transformation between shock wave velocity and distance along the plate. At the time when the shock wave reaches the thermocouple's position, velocity and thermal boundary layers have not yet formed. This is similar to the leading edge position on a flat plate at $x = 0$. As the time after shock passage increases, both boundary layers begin to grow, similar to the boundary layers which form along the length of a flat plate. The value x (distance along the plate) is represented by $v_2 t_{sp}$. The value t_{sp} is time after shock passage (see Figure 4.3). Temperature data was collected and reduced in a manner similar to procedures described earlier in this section. Results were compared to an empirical correlation found in Incropera (1985:367) and Özışık (1985:316). Equation 4.1 was used to find localized Nusselt numbers in turbulent flow.

$$Nu_x = 0.0296 Re_x^{4/5} Pr^{1/3} \quad 0.6 < Pr < 60 \quad (4.1)$$

Experimental results were plotted with the empirical model and compared together in

Figure 4.4. Due to similarities observed between values of both curves, data reduction techniques were assumed to be valid in predicting heat transfer coefficients from surface temperature data. Appendix E details both flat plate correlations and shock tube wall calculations.

Heating values at the cylinder reference position were examined to obtain an estimate of the quality of data recorded during test runs. Heat measurements from the cylinder surface were compared with data from existing heat transfer literature on cylinders in cross flow. Data was selected from sixteen test runs. Thirteen runs were acquired using a M_{corr} equal to 1.04. Test runs were collected at each theta setting ($\theta = 0^\circ$ thru $\theta = 120^\circ$). Three additional tests were performed at a M_{corr} of 1.38.

Žukauskas (1987:6.9-6.10) used a nondimensional relationship between Nusselt, Reynolds, and Prandtl numbers to measure localized heating ($Nu Re^{-.5} Pr^{.33}$). This value was calculated for each test run using velocities which were corrected for blockage effects (v_{corr}). Results at each angle were averaged and presented in Table 4.3 and plotted in Figure 4.5.

Table 4.3

Localized Heating - Reference Position

Shock Mach No.	M_{corr}	θ (deg)	$Nu Re^{-.5} Pr^{.33}$
1.8	1.04	0	1.67
1.8	1.04	30	1.62
1.8	1.04	60	1.63
1.8	1.04	90	0.75
1.8	1.04	120	0.44
2.3	1.38	0	3.43

Data in Table 4.3 was compared to localized heat transfer graphs presented by Žukauskas. Figure 4.5 shows the variation of localized heat transfer as a function of angle from stagnation point. Figure 4.6 shows the effects of turbulence level (Tu) on localized heating.

At lower M_{corr} test runs ($Re = 5 \times 10^5$), localized heat transfer at the reference point appears consistent with data obtained by Žukauskas (up to $\theta = 90^\circ$). At angles of θ greater than 90° , experimental heating rates drop off to values lower than predicted (Figure 4.5). Instead of displaying two heat transfer minima (as predicted by Žukauskas) only one is observed at $\theta \approx 120^\circ$.

At the higher M_{corr} equal to 1.38 ($Re = 9 \times 10^5$), experimental data was evaluated only at the stagnation point. Heating rates observed were significantly higher than values predicted by Žukauskas (Figure 4.5). This may be caused by an increase in the freestream turbulence level. In the supercritical flow regime, an increase in turbulence level causes a shift in the first heat transfer minimum. This narrows the laminar boundary layer creating an increase in localized heat transfer on the front part of the cylinder (Žukauskas, 1987:6.9). Figure 4.6 shows that 15 % increase in turbulence level (Tu) increases stagnation point heating by 57 % ($Re = 7.7 \times 10^5$). Experimental Tu values were not measured during test runs.

Experimental data was also compared with Nusselt numbers obtained by Schmidt and Wenner, and reported in Hermann (1987:827). Heat transfer data was plotted versus contours of Re numbers. Again, localized heat transfer at the reference point matches values obtained by Schmidt and Wenner (adjusting for the higher Re number)

except at angles greater than 90°. At these angles, heating rates drop off to values lower than predicted (see Figure 4.7).

Another check of test results was accomplished to determine if one dimensional flow assumptions were valid. Ideally, temperature measurements would be obtained across the flow channel (horizontal axis) to verify that temperature is one dimensional. Due to model constraints, thermocouples on the test section could only be moved 5 mm horizontally. Measurements were gathered at both extremes of cylinder movement (± 5 mm). Values appeared to drop slightly between the two positions; however, results were inconclusive due to an unwanted drop in shock wave strength between test runs.

Finally, data was compared to determine the repeatability of test runs with similar configurations. Table 4.3 displays a representative sample of similarly configured test runs and Nu values measured.

Table 4.3
Test Run Repeatability

Test Run	Shock Mach Number	Reference (Nu)	Gap Wall (Nu)	Gap Floor (Nu)
GP1MH4TH1A	1.80	900	1000	1200
GP1MH1TH1Y	1.90	950	750	1300
GP1MH1TH1A	2.06	1500	1200	1500
GP1MH1TH1B	2.06	1500	1150	1450
GP1MH1TH3A	2.00	1200	1500	600
GP1MH2TH3A	2.01	1000	1600	500

Throughout the entire testing sequence the repeatability of similar configured test runs was excellent.

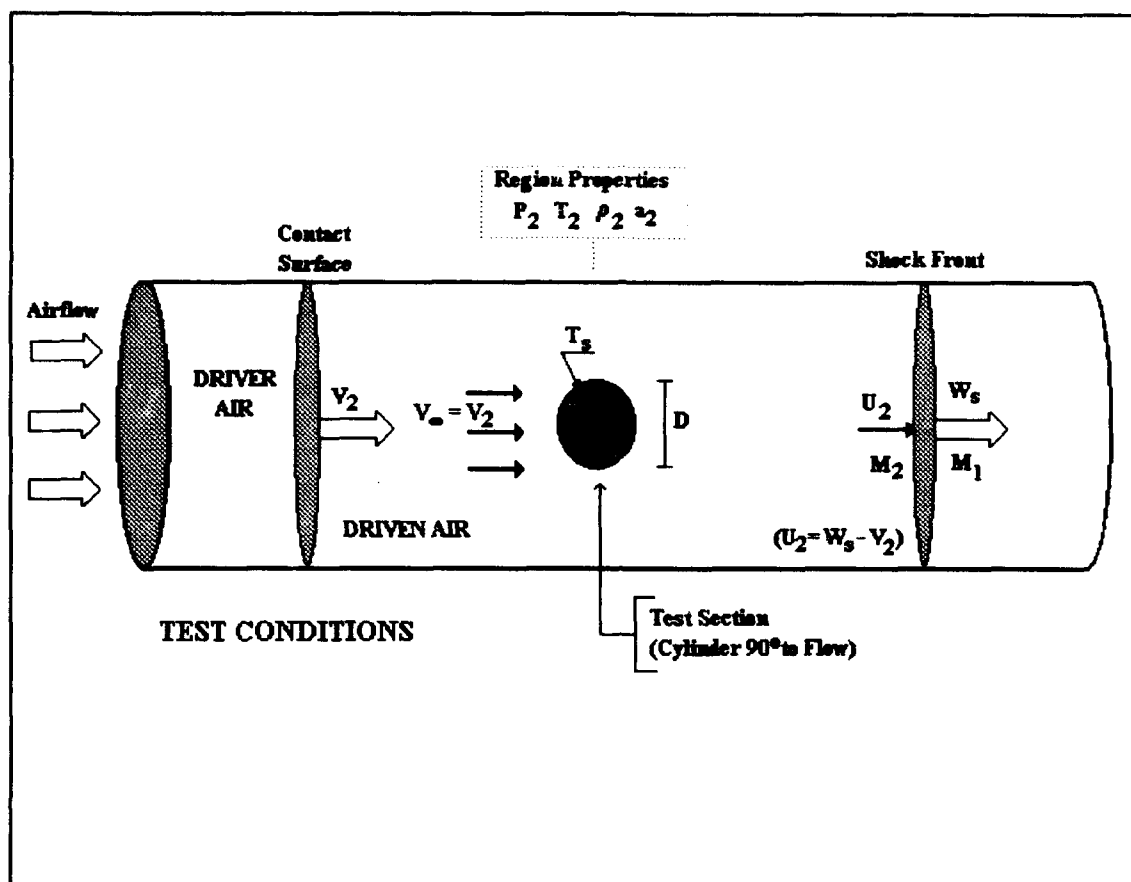


Figure 4.1. Test Conditions Schematic

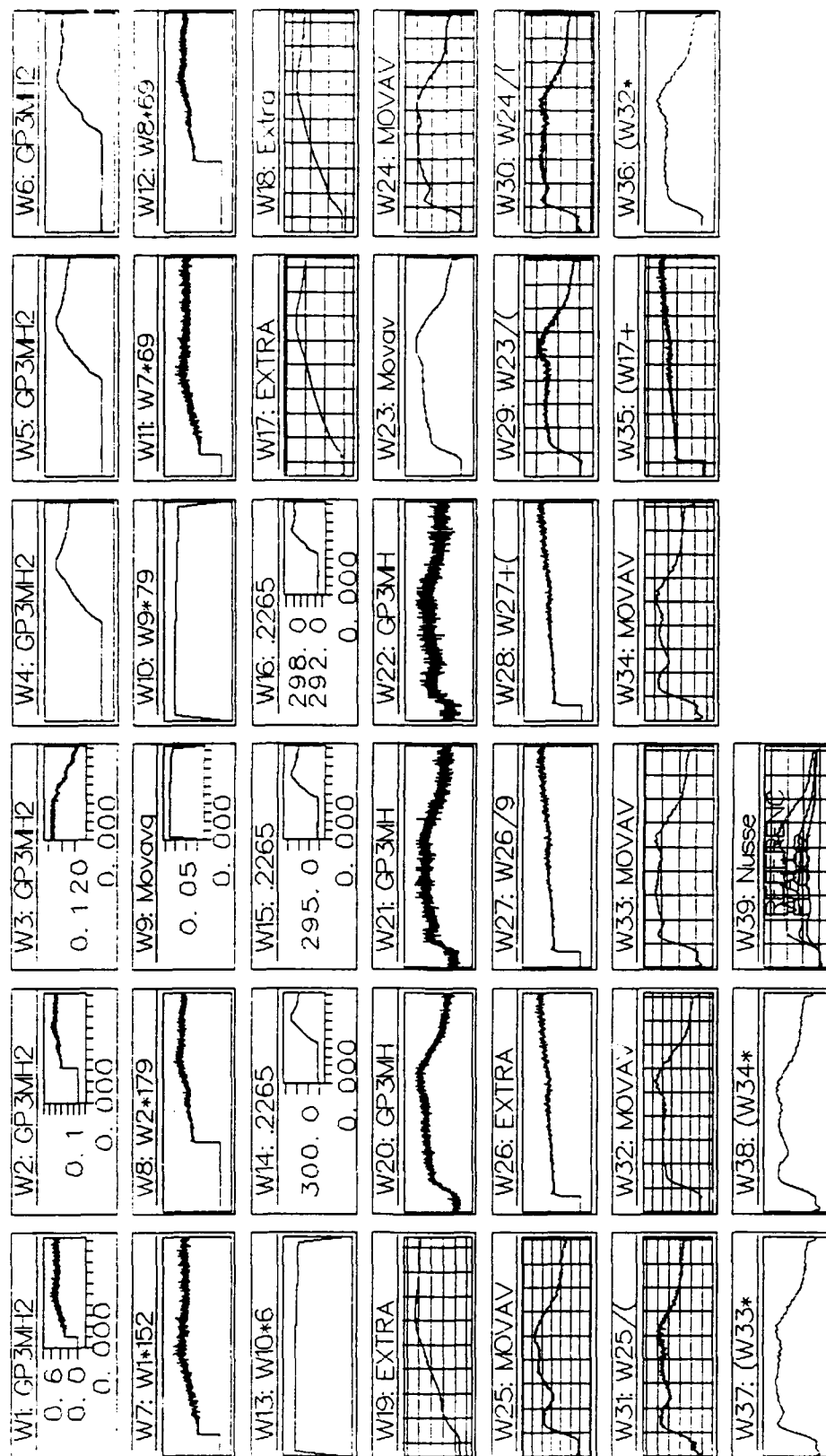


Figure 4.2. Data Reduction Worksheet (DADiSP)

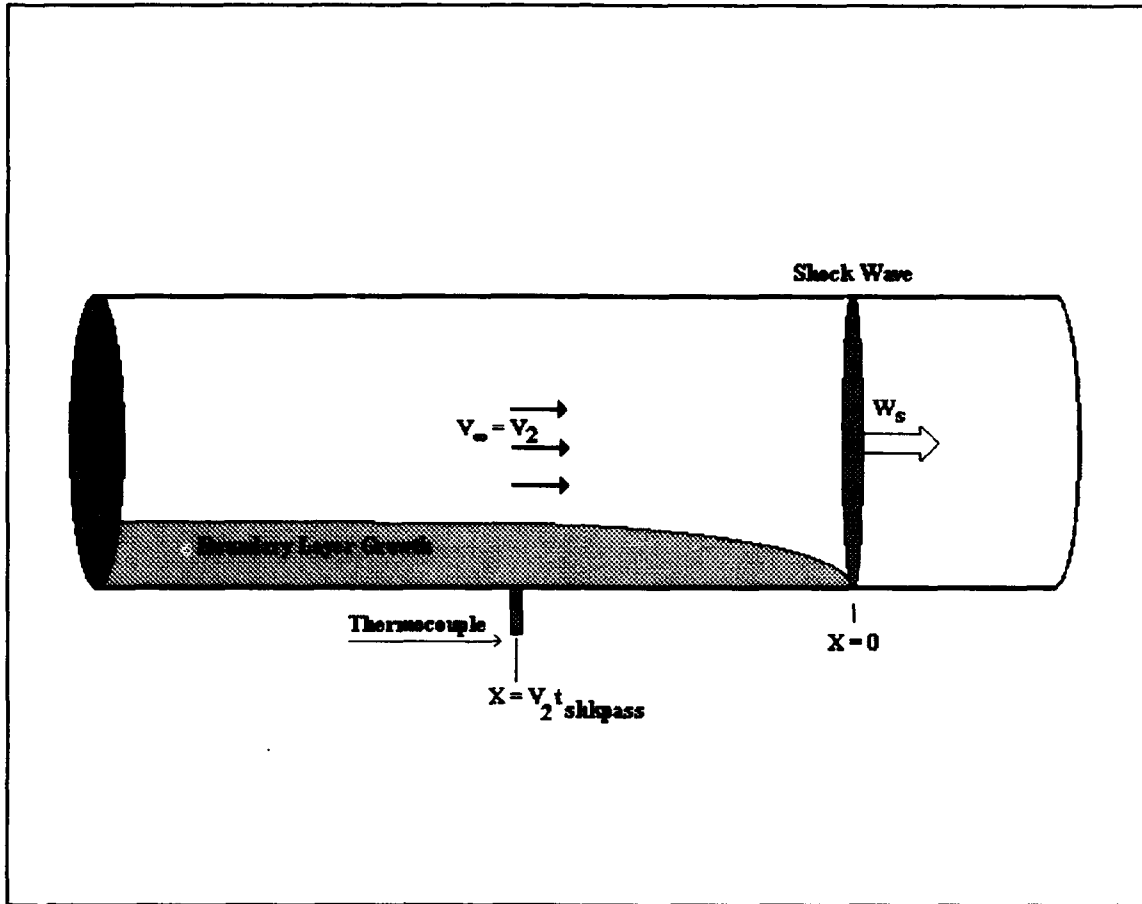


Figure 4.3. Boundary Layer Formation Behind a Normal Shock Wave
(Eads, 1992:Fig.4)

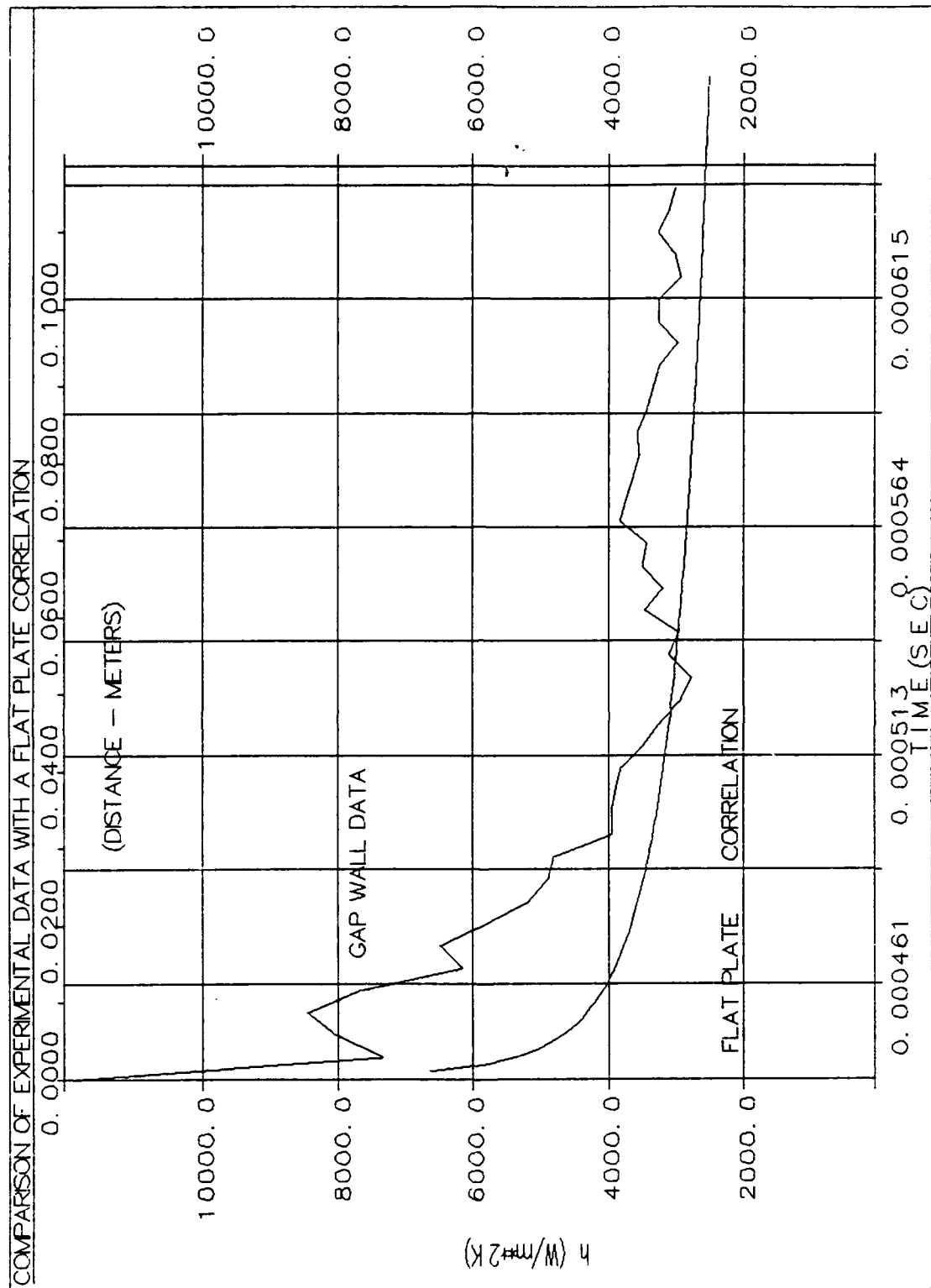


Figure 4.4. Comparison of Experimental Data with a Flat Plate Correlation
(Incropera, 1985:367)

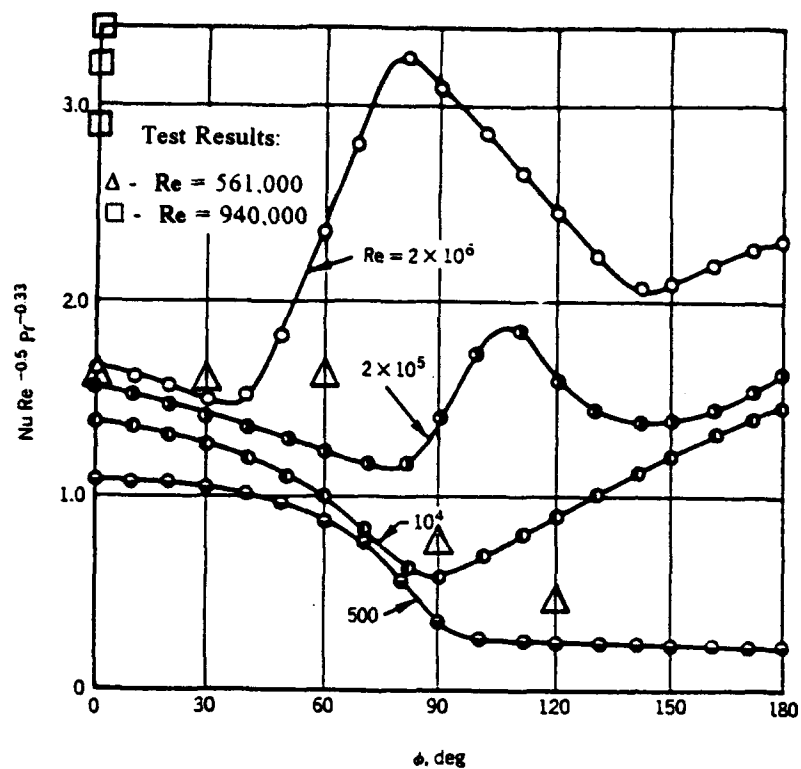


Figure 4.5. Local Heat Transfer From a Cylinder for Variable Re
 (Žukuakas, 1987:6.9)

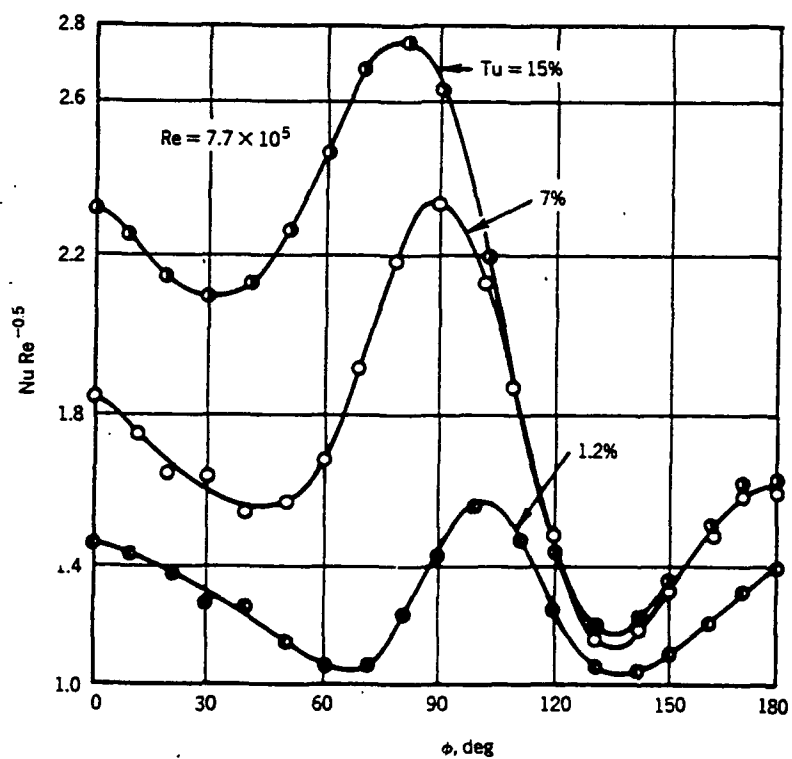


Figure 4.6 Local Heat Transfer from a Cylinder to Air in the Supercritical Flow Regime for Variable Tu
 (Žukuakas, 1987:6.10)

Reference Point Test Results

$\Delta - Re = 561,000$

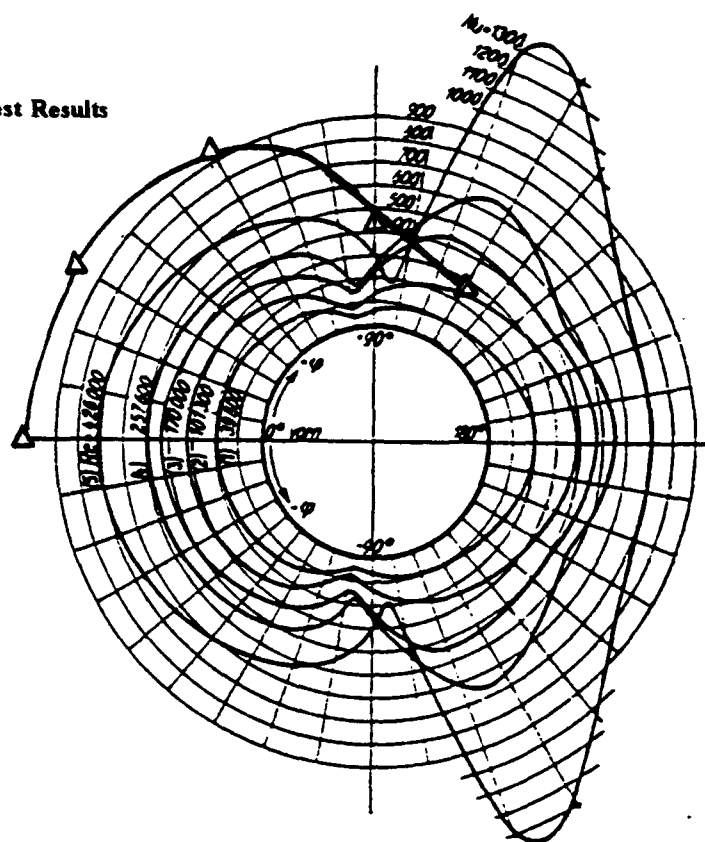


Figure 4.7. Nusselt Numbers Obtained by Schmidt and Wenner
(Hermann, 1987:827)

V. Discussion of Results

5.1 Heat Transfer Results

Test run data collected at each sensor location was consolidated to show heat transfer dependence on flow velocity, angle from stagnation point, and changing gap width. Gap width was represented by the width to depth ratio (w/d) shown in Figure 5.1. Table 5.1 lists w/d ratios for each gap width tested.

Table 5.1

Gap Width - w/d Ratios

Gap Width	2.5 mm	5.0 mm	7.5 mm
w/d	1.23	2.46	3.69

Averaged Nusselt values were obtained from each sensor position and plotted versus angle from stagnation point (θ). Cubic spline interpolation was used to curve fit plotted data. The curves were constructed from a series of cubic equations, each connecting one point to the next (MathSoft, 1993:225). Figure 5.2a shows a typical Nusselt number (Nu) vs. theta graph for values collected at a freestream Mach of 1.04 and gap width of 7.5mm. Solid triangles represent the averaged Nu values obtained from a particular run (these are left off subsequent graphs).

Error Analysis. An error analysis was accomplished to account for experimental uncertainties, tolerances in calibrations, and the fluctuations of measuring equipment. Nu mean and standard deviation data was extracted from a representa

sample of all test runs. Standard deviation was calculated for each run and provides a measure of the dispersion of observations about the mean. Standard deviation characterizes the uncertainties associated with experimental attempts to determine "true" Nu values (Bevington, 1969:15). Figure 5.2a shows a sample Nu vs theta curve with standard deviations and means plotted.

In order to compare deviations at different points on the graph, each standard deviation was divided by its mean to convert it to a percentage of the mean. These values were averaged together to find the overall percentage of uncertainty for each graph. For example, data presented in Figure 5.2a can vary $\pm 13\%$ from values on the curve and still remain within one standard deviation of accuracy.

The five test runs evaluated in Figure 5.2a represent 10% of data collected at Mach 1.04. Standard deviations, calculated and presented in Figure 5.2a, were assumed to statistically represent data collected at Mach 1.04. Similar analyses were performed on Mach 1.19 (Figure 5.2b) and Mach 1.38 (Figure 5.2c) test groups. Results are tabulated in Table 5.2.

Changes in Flow Velocity. As the freestream Mach number increases, all sensor locations experienced a rise in local Nu values. Increases in flow velocity appear to change the magnitude of Nu values; however, Nu vs. theta curves maintain similar shapes. Figure 5.3 shows data on heat transfer rates from three different flow velocities on the floor of the cylinder gap (gap width = 5mm). As the flow was increased from Mach 1.04 to Mach 1.38, Nu curves increased in magnitude, exhibiting maximum heat transfer rates at $\theta \approx 30^\circ$. This graph was representative of the behavior at all sensor locations undergoing changes in freestream velocity.

Table 5.2

Test Run Error Analysis

Test Run	Sensor Location	M_{corr}	Nu Means	Nu Standard Deviation
GP3MH1TH1A	Floor	1.04	1048	127.3
GP3MH1TH2A	Floor	1.04	860	65.7
GP3MH1TH3A	Floor	1.04	550	37.3
GP3MH1TH4A	Floor	1.04	172	43.8
GP3MH1TH5A	Floor	1.04	336	43.2
GP3MH2TH1A	Wall	1.19	1506	122.9
GP3MH2TH2A	Wall	1.19	1358	88.4
GP3MH2TH3A	Wall	1.19	1226	70.9
GP3MH2TH4A	Wall	1.19	977	107
GP3MH2TH5A	Wall	1.19	500	30.5
GP2MH3TH1A	Floor	1.38	2606	56.3
GP2MH3TH2A	Floor	1.38	3380	126
GP2MH3TH3A	Floor	1.38	3470	219.3
GP2MH3TH4A	Floor	1.38	354	205.6
GP2MH3TH5A	Floor	1.38	201	38.4

Reference Point. Reference location heat transfer data was consolidated and presented for each flow velocity investigated. Since reference point heat transfer rates were independent of gap width, test runs having similar flow velocities and different gap widths were averaged together to form one graph. Figures 5.4 thru 5.6 display reference point heat transfer data for each Mach number investigated. Mean and standard deviation information (obtained from different gap widths) was included on

each graph. All three graphs show a local maximum at the stagnation point and another local maximum around the 50° point (Figure 5.7). As mentioned earlier in Section 4.4, Nu values matched data presented by Schmidt and Wenner up through $\theta \leq 90^\circ$ (Figure 4.7).

Nu values at the reference location were compared with floor and wall heat transfer rates to calculate heat transfer augmentation factors. These factors can then be used to estimate heat transfer rates inside gaps when only smooth body or stagnation point heat transfer rates are known.

Gap Wall. Maximum heat transfer in the gap wall was a function of flow velocity, θ , and w/d . As mentioned earlier, flow velocity influenced only the magnitude of the heat transfer curve (higher Mach number causes an increase in heat transfer). The value w/d was important in determining the angle θ at which peak heat transfer occurs. For a w/d of 1.23 (gap width = 2.5mm), Nu values peaked at values of $\theta \approx 50^\circ$ (Figure 5.8). When w/d was increased to 2.46 (gap width = 5mm), Nu values increased to a maximum at $\theta \approx 30^\circ$, then maintained a constant heat transfer rate through $\theta \approx 80^\circ$, after which values fell off with increasing θ (Figure 5.9). Increasing the w/d to 3.69 (gap width = 7.5mm), Nu values were greatest at the stagnation point and then fell off in magnitude with increasing θ (Figure 5.10).

Examining the dependence of Nu with changing w/d , several observations were noted. Increasing w/d reduces the intensity and spreads out the location of maximum heat transfer. If w/d was large enough, peak heat transfer occurred at the stagnation point. Narrowing the width of the gap (decreasing w/d) generated a large heat transfer rate for a small range of θ . Peak wall heating (hot spots) occurred in gaps with

small w/d . These hot spots were confined to a small portion of the cylinder (around $\theta = 50^\circ$).

Gap Floor. Flow velocity, theta, and w/d influence heat transfer in the floor of the gap. The size of the w/d ratio again determined the location (theta) where peak heat transfer occurred. For a w/d of 1.23, Figure 5.11 revealed that Nusselt values peak at $\theta \approx 50^\circ$ (same angle as gap wall peak values). As w/d was increased to 2.46, the peak heat transfer location shifted forward to $\theta \approx 30^\circ$ (refer back to Figure 5.3). At a w/d of 3.69, peak heat transfer occurred at the stagnation point and Nusselt values fell off as theta increased (Figure 5.12).

Increasing w/d influences the location of peak Nu values to move forward on the cylinder towards the stagnation point. Peak heating was observed to occur over a small region of theta given any w/d . If w/d was large enough, peak heat transfer occurred at the stagnation point.

Combined Test Results. Figures 5.13 thru 5.21 present gap floor, gap wall, and reference location Nusselt values overlayed together for each flow velocity and gap width. Three different flow velocities and three w/d settings were tested. For w/d settings of 1.23 and 2.46, gap floor heat transfer rates predominated over gap wall and reference locations (except at Mach 1.04 and $w/d = 1.23$; wall Nu values were larger). For a w/d ratio of 3.69, reference point heat transfer rates were larger than both wall and floor locations.

Another finding involved the relationship between peak heating locations observed in the wall and floor of the gap. For a w/d ratio equal to 1.23, peak Nu values on the wall and floor occurred at the same location ($\theta \approx 50^\circ$). At w/d ratios equal to 2.46,

there was no apparent correlation. Finally, at a w/d ratio of 3.69, heat transfer in the wall and floor of the gap peaked at the stagnation point.

Heat Augmentation Factors. Heat augmentation factor graphs are presented in Figures 5.22 thru 5.27. Graphs were plotted for both floor and wall locations and at each gap width investigated. Curves were obtained by dividing floor and wall Nu data by the reference Nu value recorded at stagnation point.

Each gap floor graph showed that the maximum value for each factor occurred at a similar theta independent of flow velocity. As w/d was increased from 1.23 to 2.46, the location of the maximum value moved forward on the cylinder. Additionally, the maximum value of the augmentation factor remains unchanged as the curve shifts forward. For example, at Mach 1.19 the maximum augmentation factor has a value of 1.5 and occurs at $\theta \approx 50^\circ$ ($w/d = 1.23$). At a w/d equal to 2.46 the maximum augmentation factor at Mach 1.19 still equals 1.5, but now the maximum occurs at $\theta \approx 30^\circ$.

As w/d was increased to 3.69, reference location heat transfer rates on the cylinder dominate wall and gap effects. A large gap width does not create a "hot spot." The walls of the gap were far enough away that the gap floor acts in a manner similar to a smooth cylinder. Wall heat transfer effects become negligible.

Gap wall graphs have augmentation factors which, in most cases, were less than corresponding floor factors. At the smallest w/d , wall maximum values were concentrated at $\theta \approx 50^\circ$ with a range of 1.1 to 1.35. As w/d was increased, the augmentation factors lose value, compared to floor values, and a maximum location was not clearly defined.

5.2 Other Observations

Diaphragm Burst Phenomenon. A problem discovered during shock tube testing influenced both the speed and formation of the shock. Test runs collected at lower Mach numbers displayed normal Region 2 pressure versus time curves (P_2 vs. time). As the shock wave passed the sensor location, pressure readings jumped to Region 2 pressures and maintained these values until the rarefaction wave passed. Ideally the curve should look like a square wave with P_2 remaining constant throughout data collection. Figure 5.28 shows a P_2 time history curve obtained at a lower Mach run. Figure 5.29 shows a P_2 time history curve obtained at a higher Mach setting. At higher Mach runs, the pressure curve did not remain constant. Instead, it builds intensity until the rarefaction wave passed.

Possible causes may be the diaphragm rupture process and/or diaphragm composition. For lower Mach runs aluminum diaphragms were used. Post shock inspections showed normal petalling of the diaphragms. For higher Mach runs stainless steel diaphragms were used. Inspections of these diaphragms showed varied results. Some diaphragm petals were partially ripped or torn, and some were petalled multiple times. Other diaphragms were only partially petalled. It is believed that these results indicate a complicated diaphragm rupture sequence which serves to slow down and change the formation of the normal shock wave. This rupture process may also cause a series of secondary shocks which results in shock strengthening and a rise in P_2 pressure as test time progresses (Elrod, 1993).

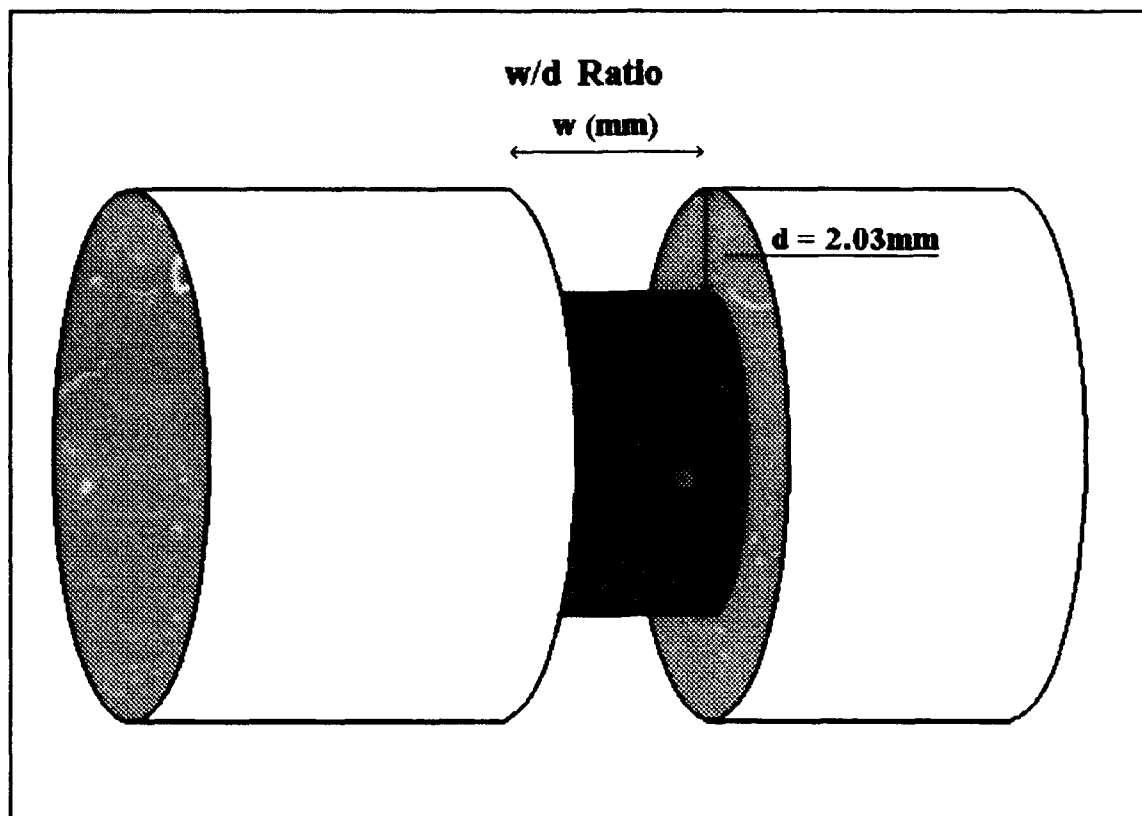


Figure 5.1. Gap Width - w/d Ratio

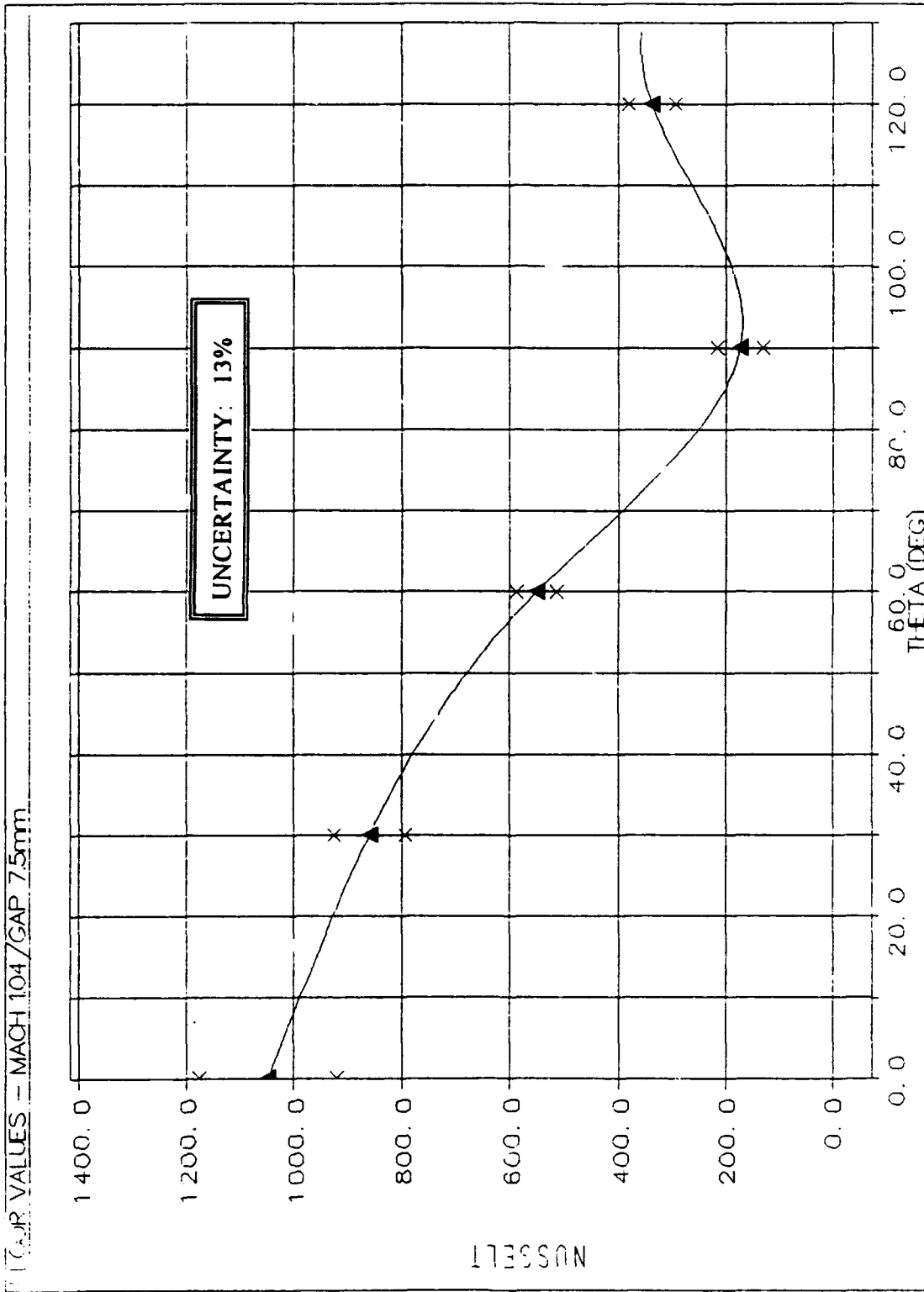


Figure 5.2. Nusselt vs. Theta Graphs with Means and Error Ranges
(a). Floor Values, Mach 1.04, Gap Width 7.5mm

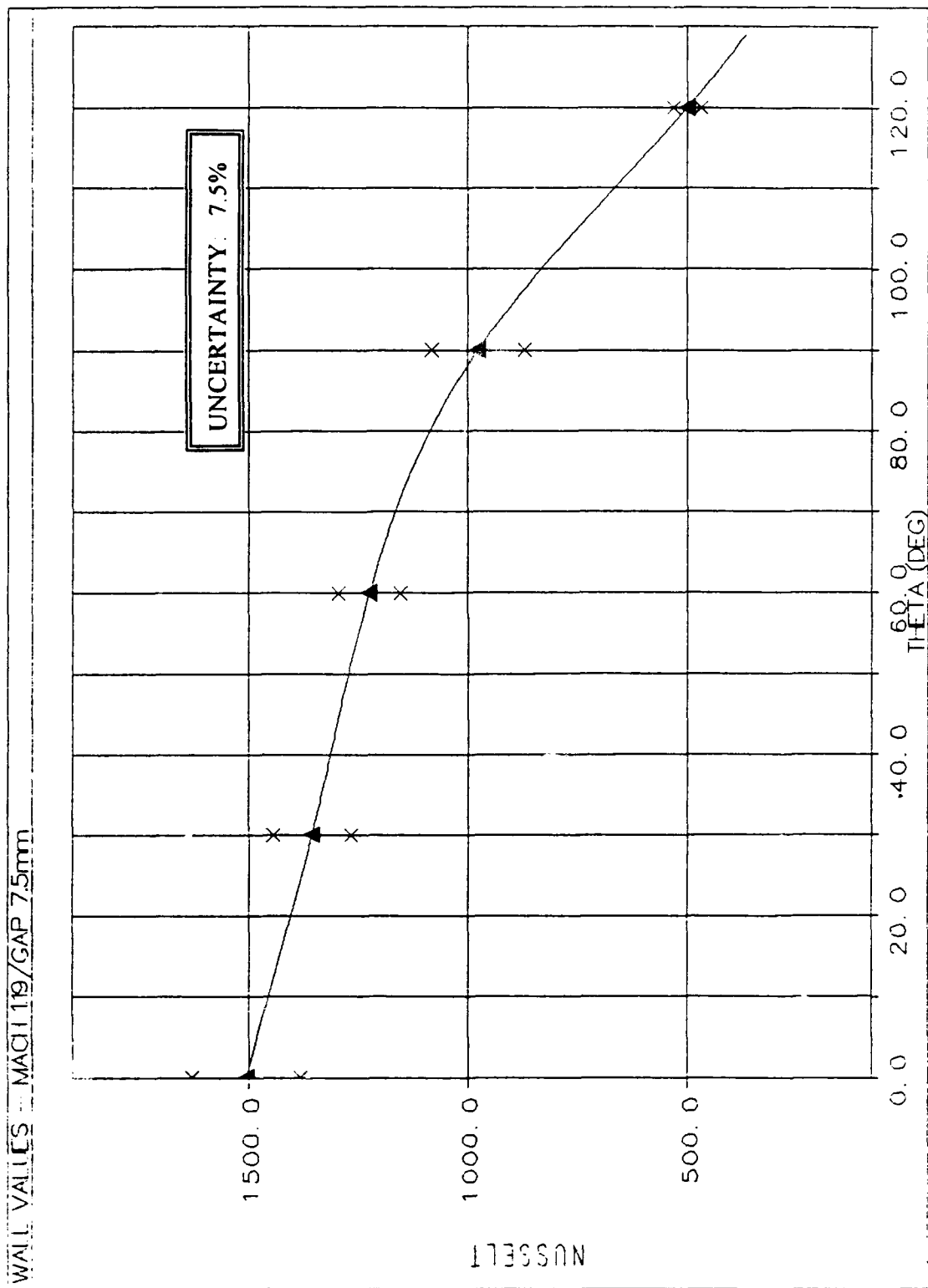


Figure 5.2 (b). Wall Values, Mach 1.19, Gap Width 7.5mm

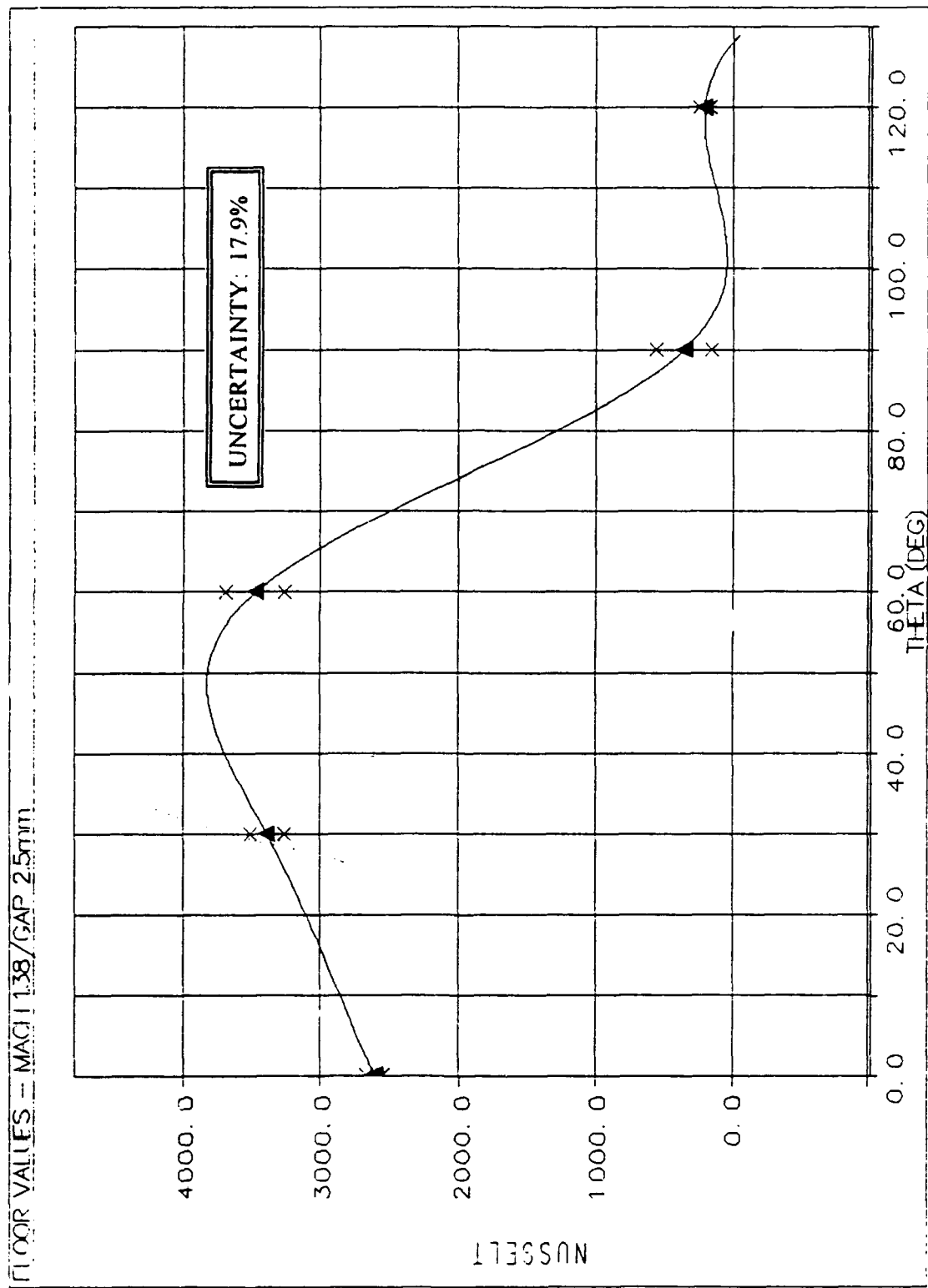


Figure 5.2 (c). Floor Values, Mach 1.38, Gap Width 2.5mm

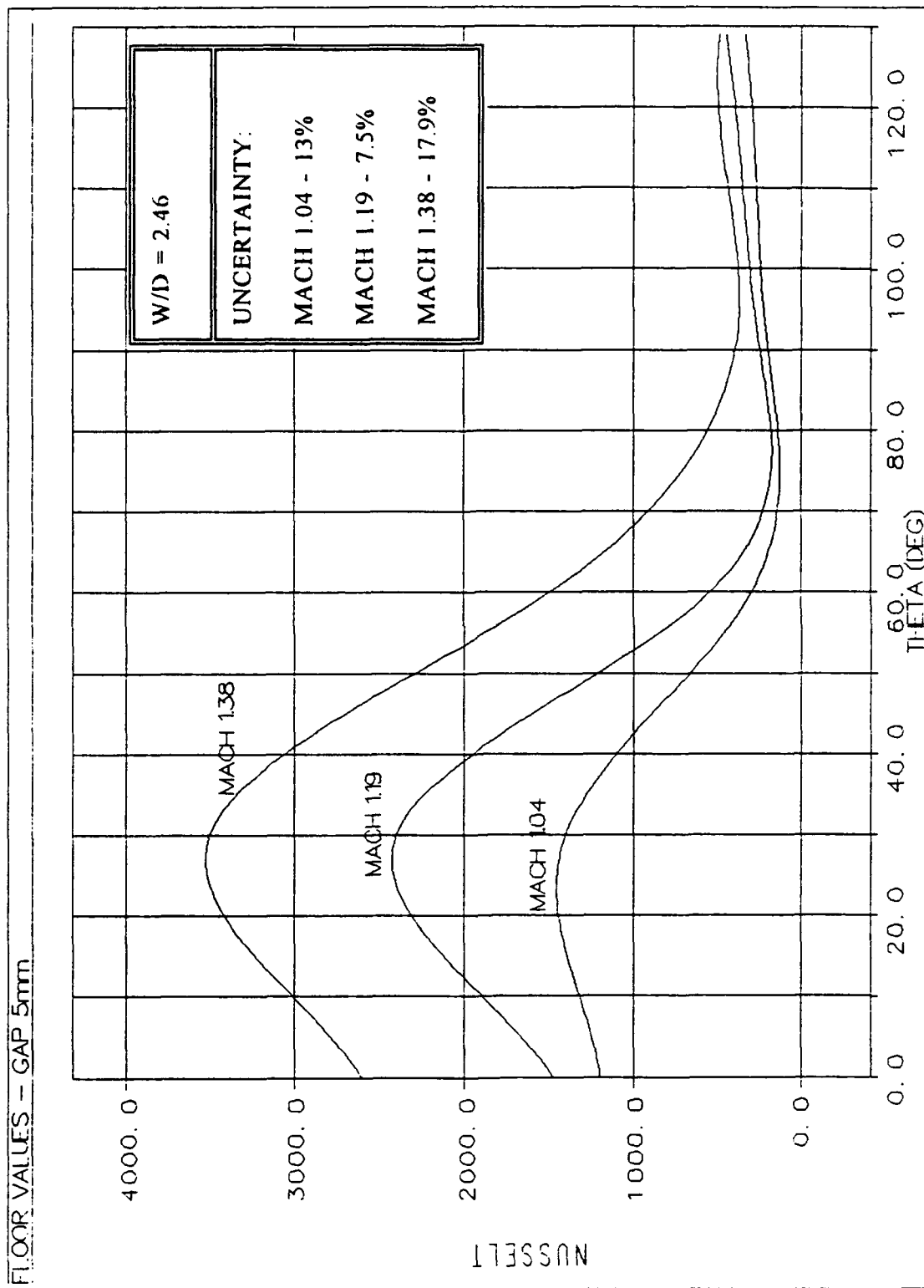


Figure 5.3. Nusselt vs. Theta Graph. Impact of Changing Flow Velocity
(Gap Floor Nusselt Values, Gap Width 5mm)

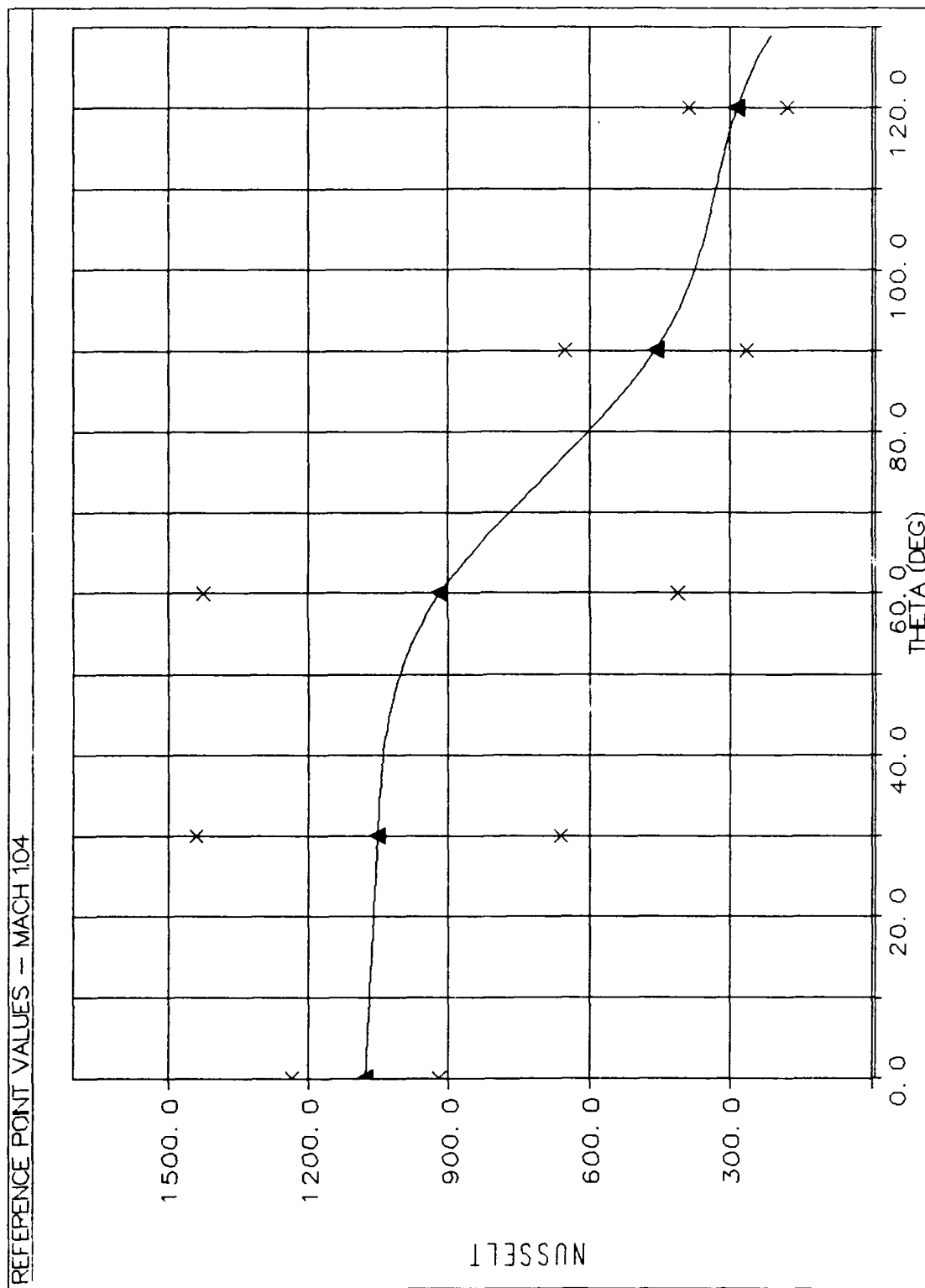


Figure 5.4. Nusselt vs. Theta Graph, Reference Point Averages, Mach 1.04

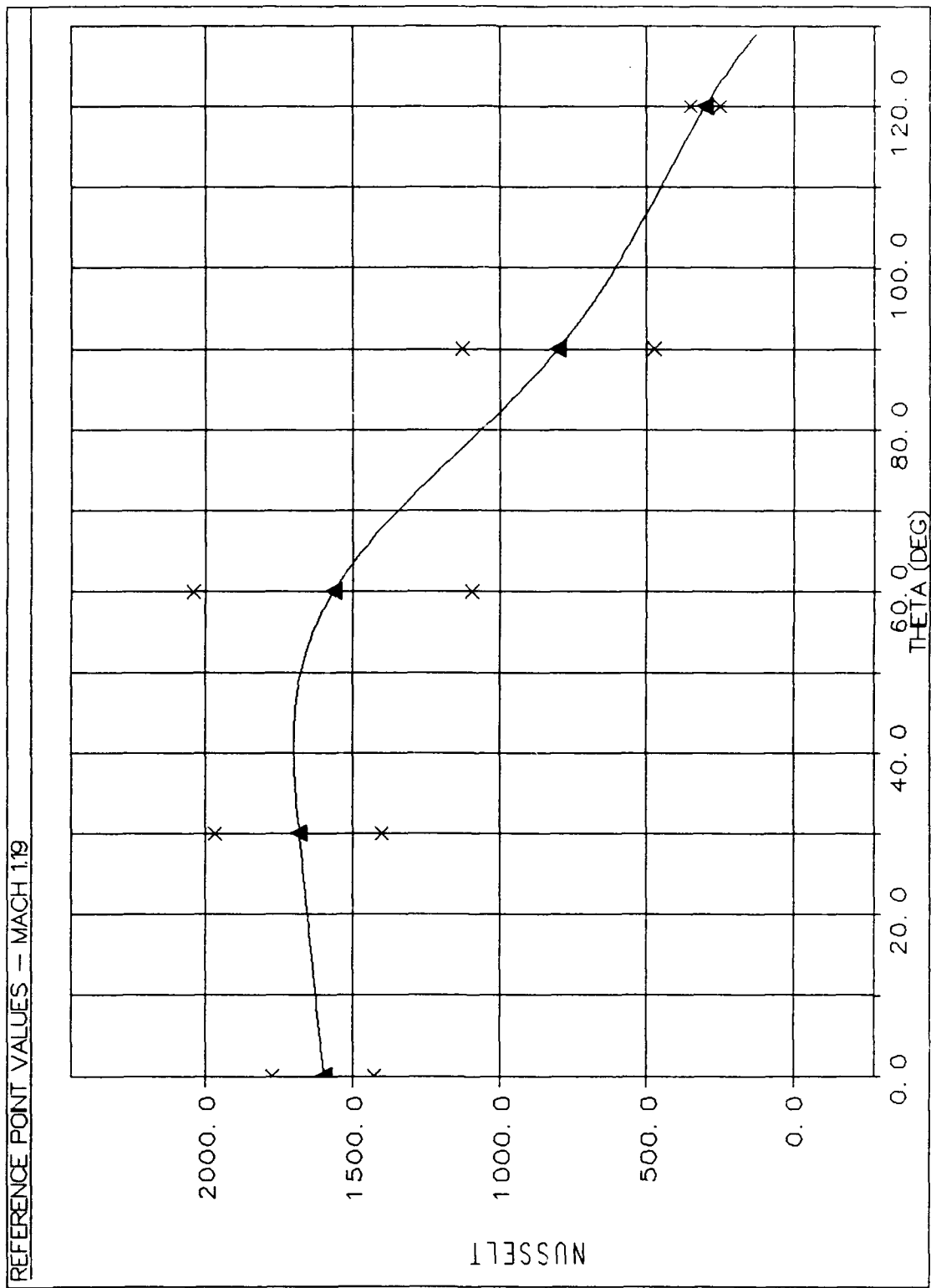


Figure 5.5. Nusselt vs. Theta Graph, Reference Point Averages, Mach 1.19

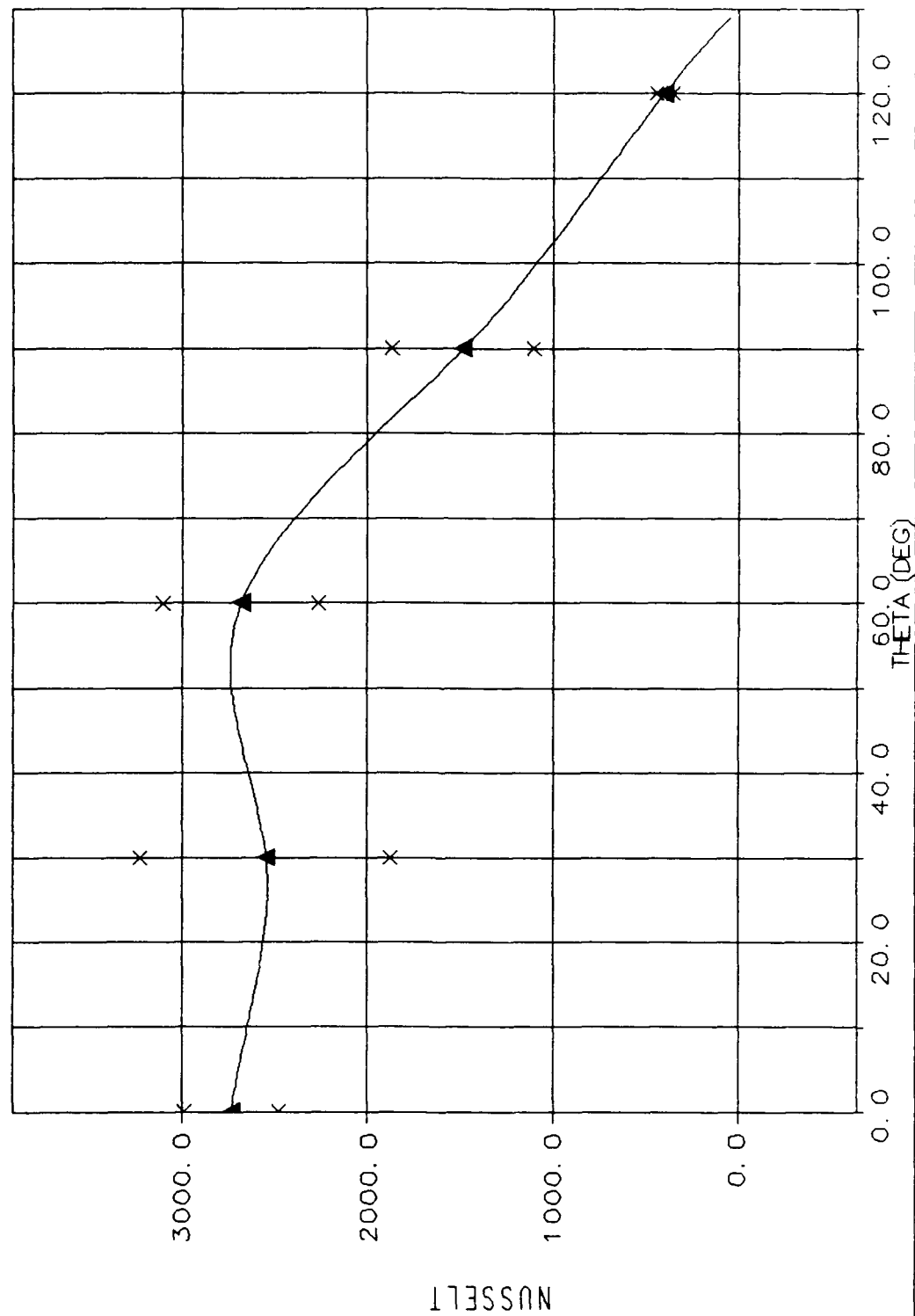


Figure 5.6. Nusselt vs. Theta Graph, Reference Point Averages, Mach 1.38

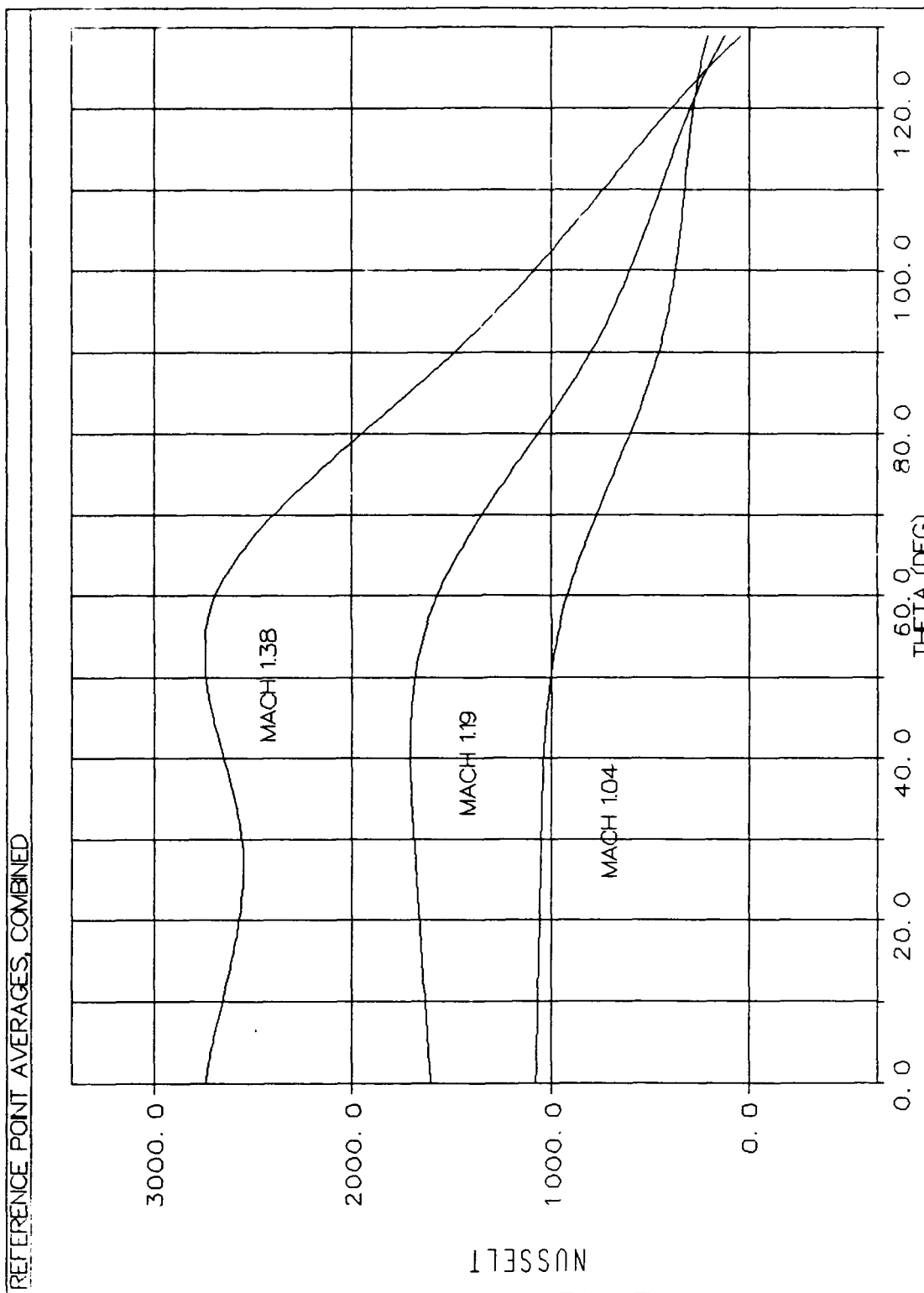


Figure 5.7. Nusselt vs. Theta Graph, Reference Point Averages, Combined

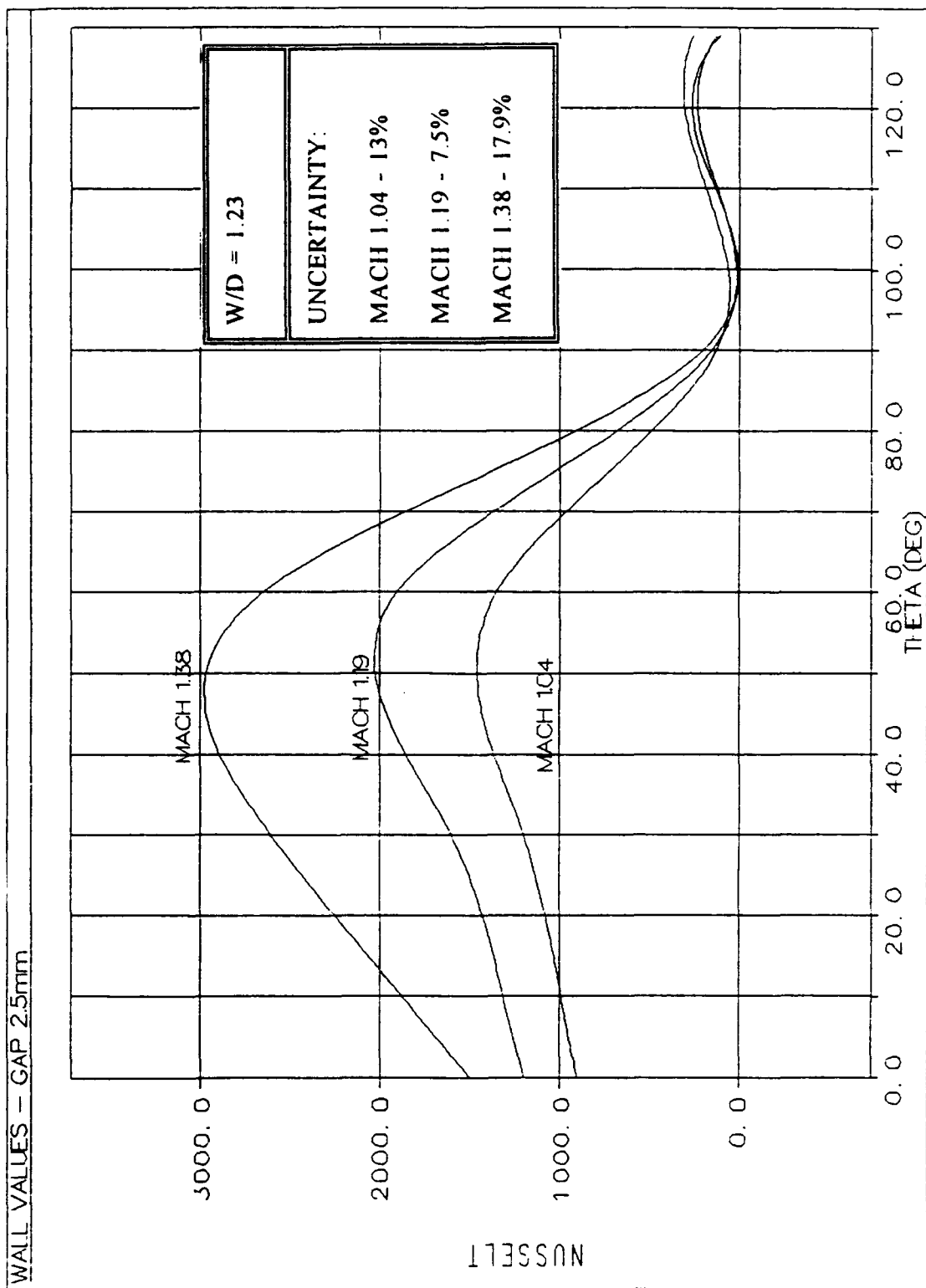


Figure 5.8. Gap Wall Nusselt Values, Gap Width 2.5mm

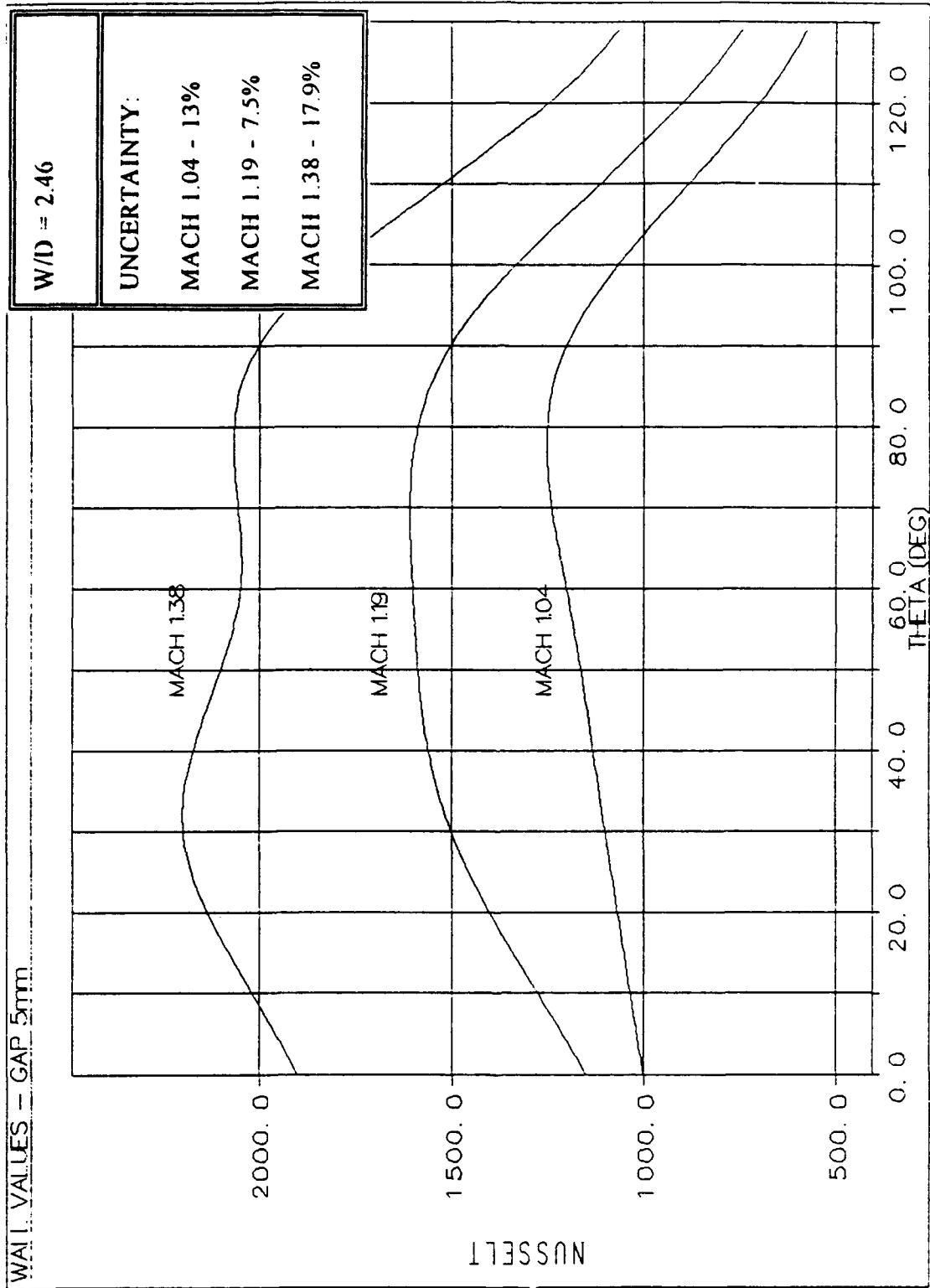


Figure 5.9. Gap Wall Nusselt Values, Gap Width 5mm

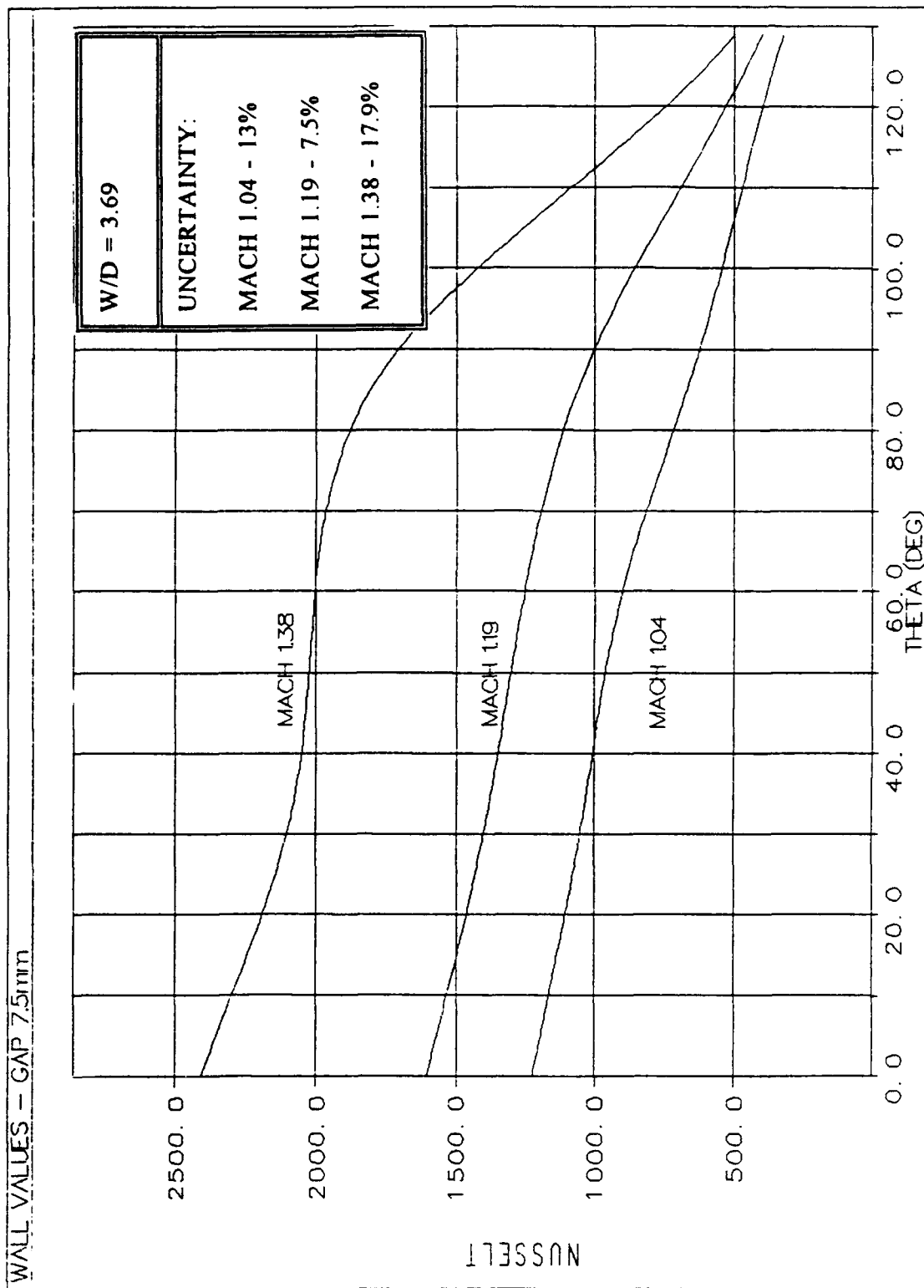


Figure 5.10. Gap Wall Nusselt Values, Gap Width 7.5mm

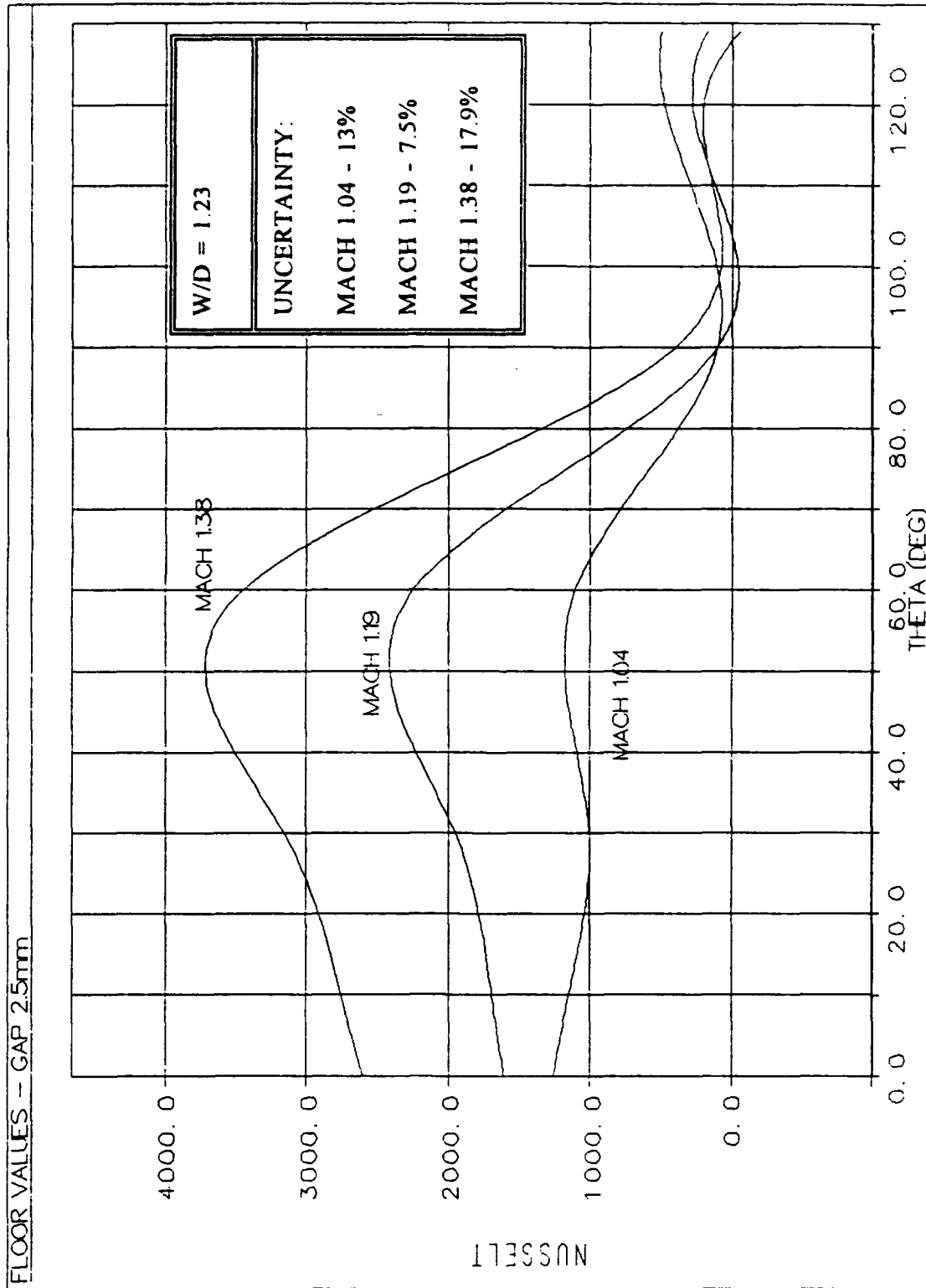


Figure 5.11. Gap Floor Nusselt Values, Gap Width 2.5mm

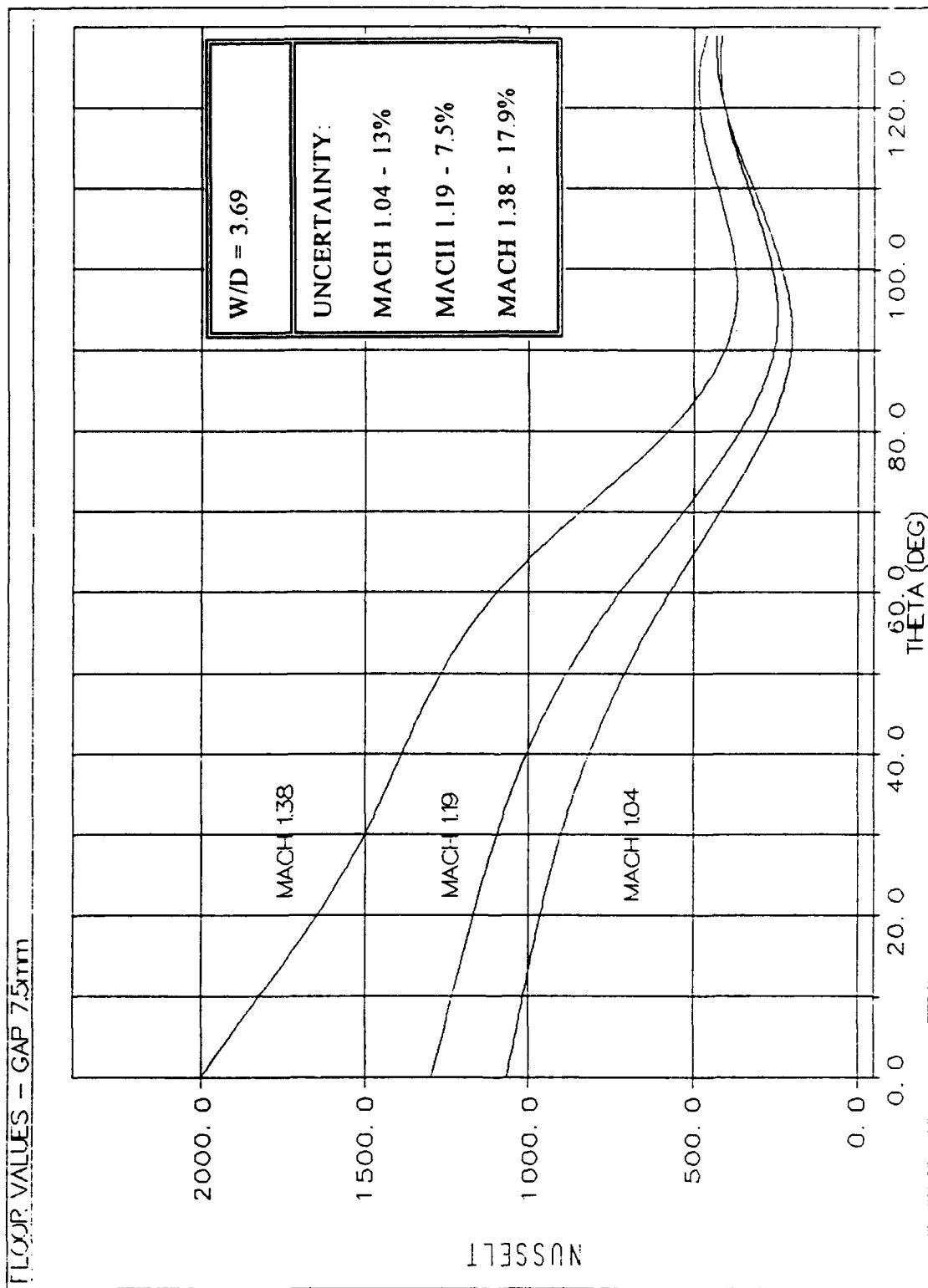


Figure 5.12. Gap Floor Nusselt Values. Gap Width 7.5mm

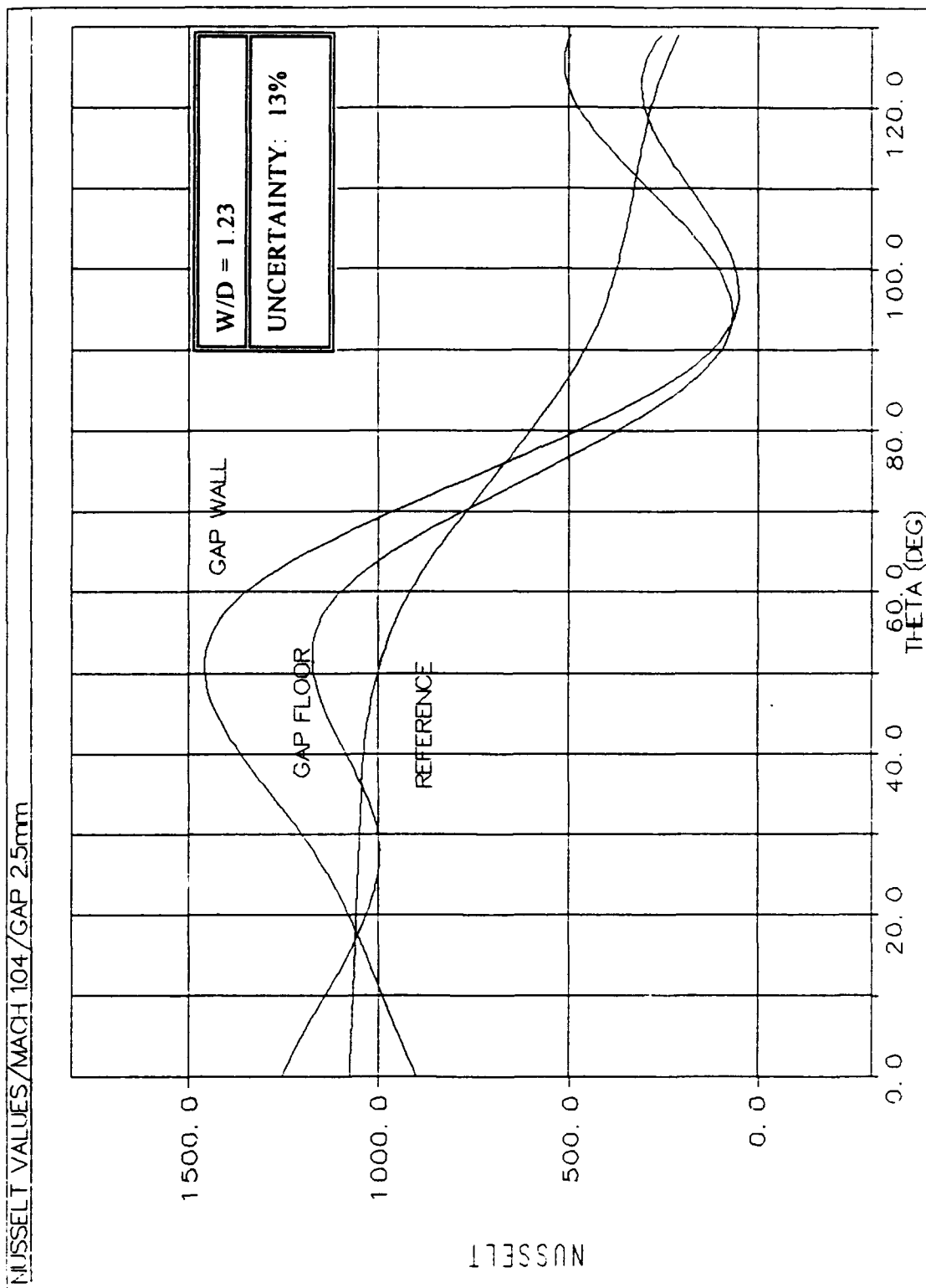


Figure 5.13. Combined Nusselt Values, Mach 1.04, Gap Width 2.5mm

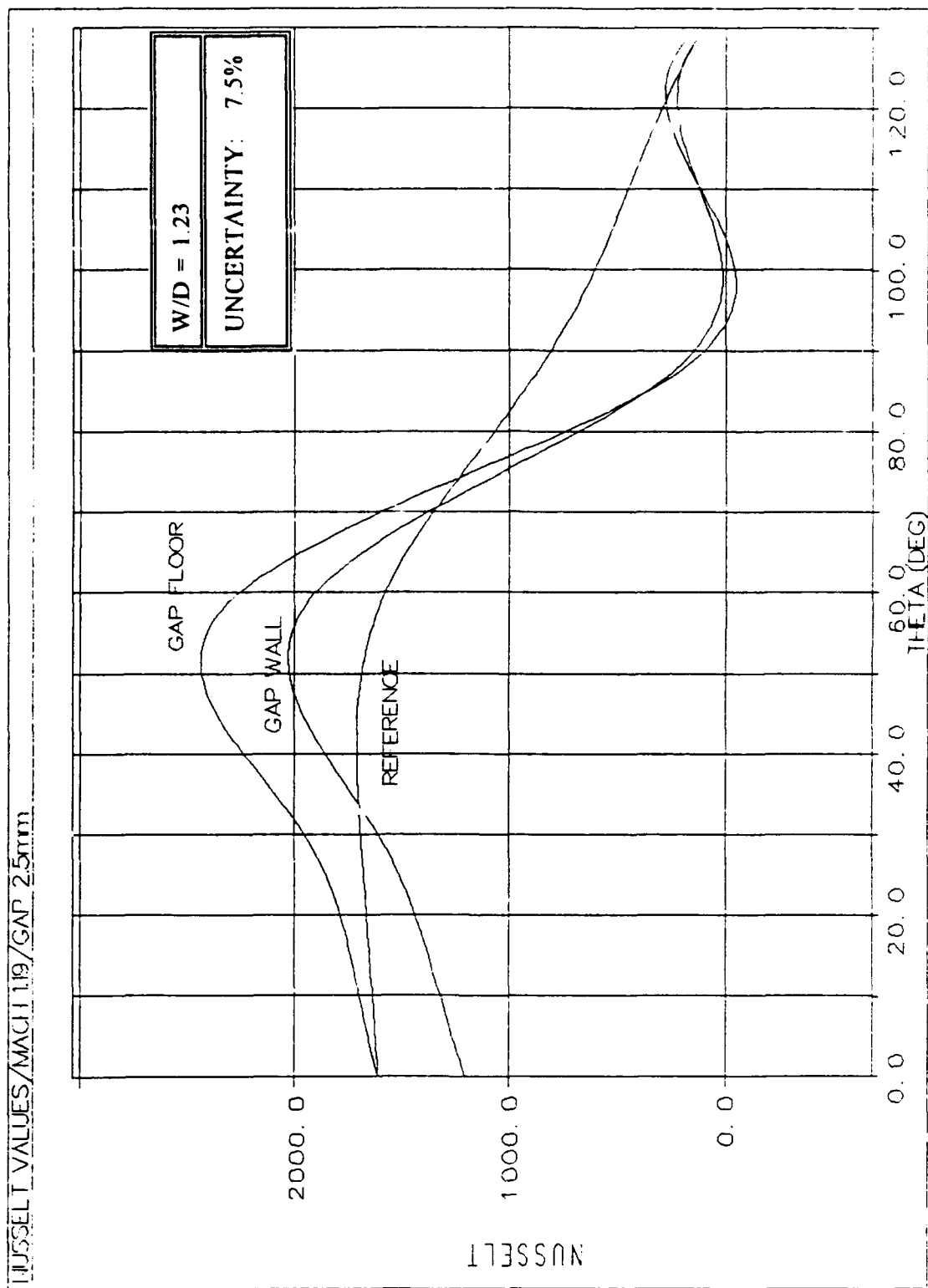


Figure 5.14. Combined Nusselt Values, Mach 1.19, Gap Width 2.5mm

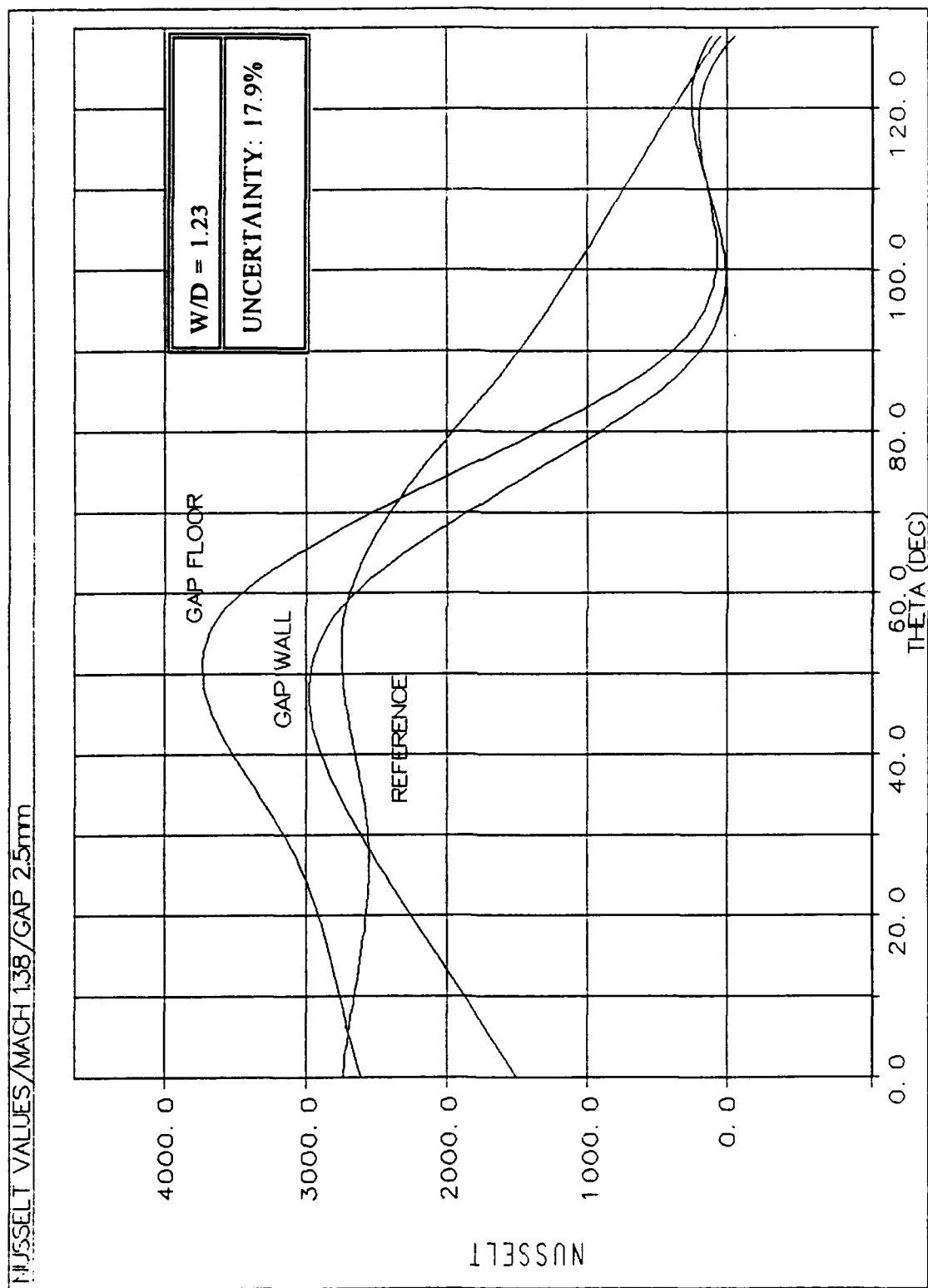


Figure 5.15. Combined Nusselt Values, Mach 1.38, Gap Width 2.5mm

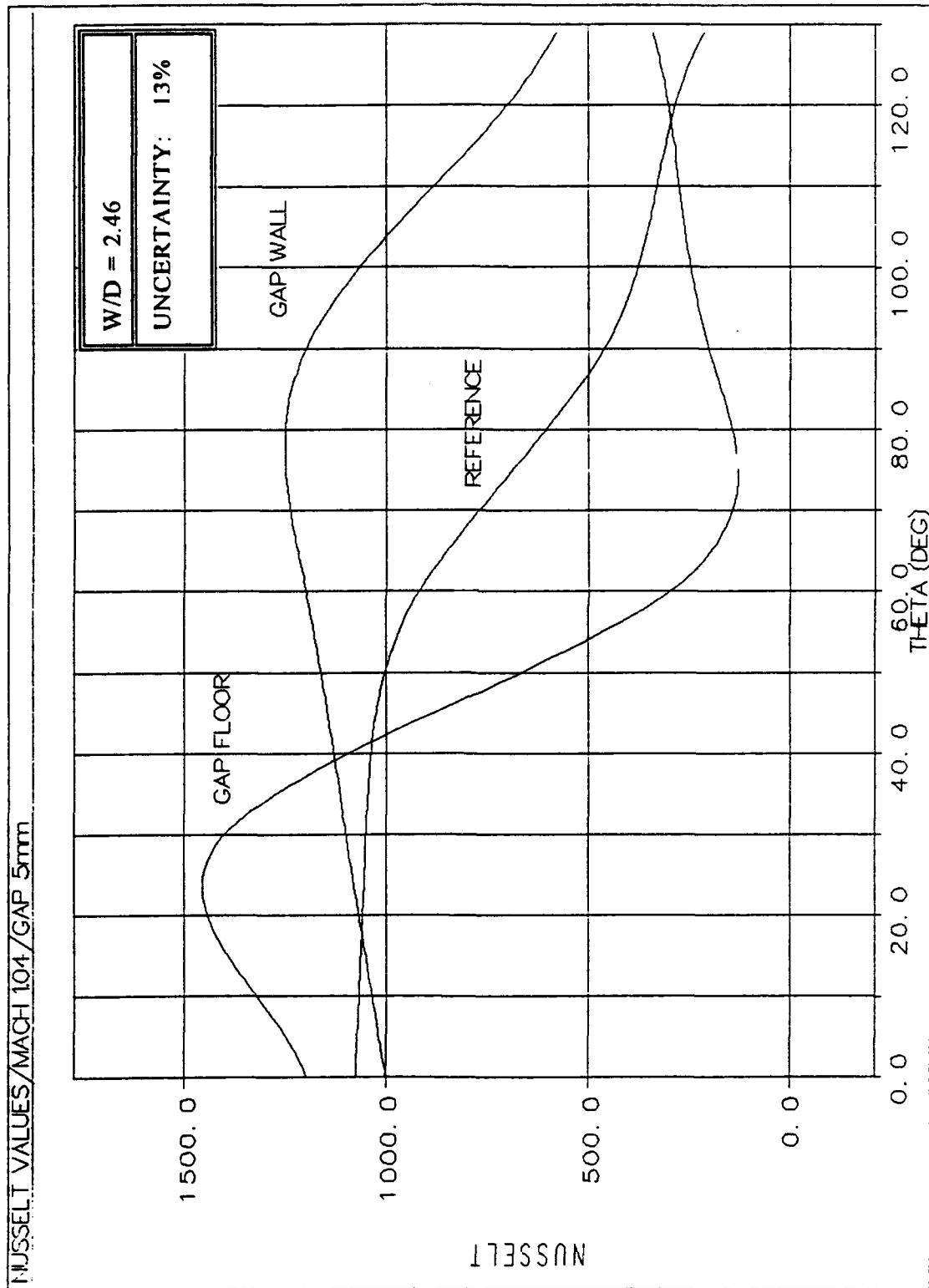


Figure 5.16. Combined Nusselt Values, Mach 1.04, Gap Width 5mm

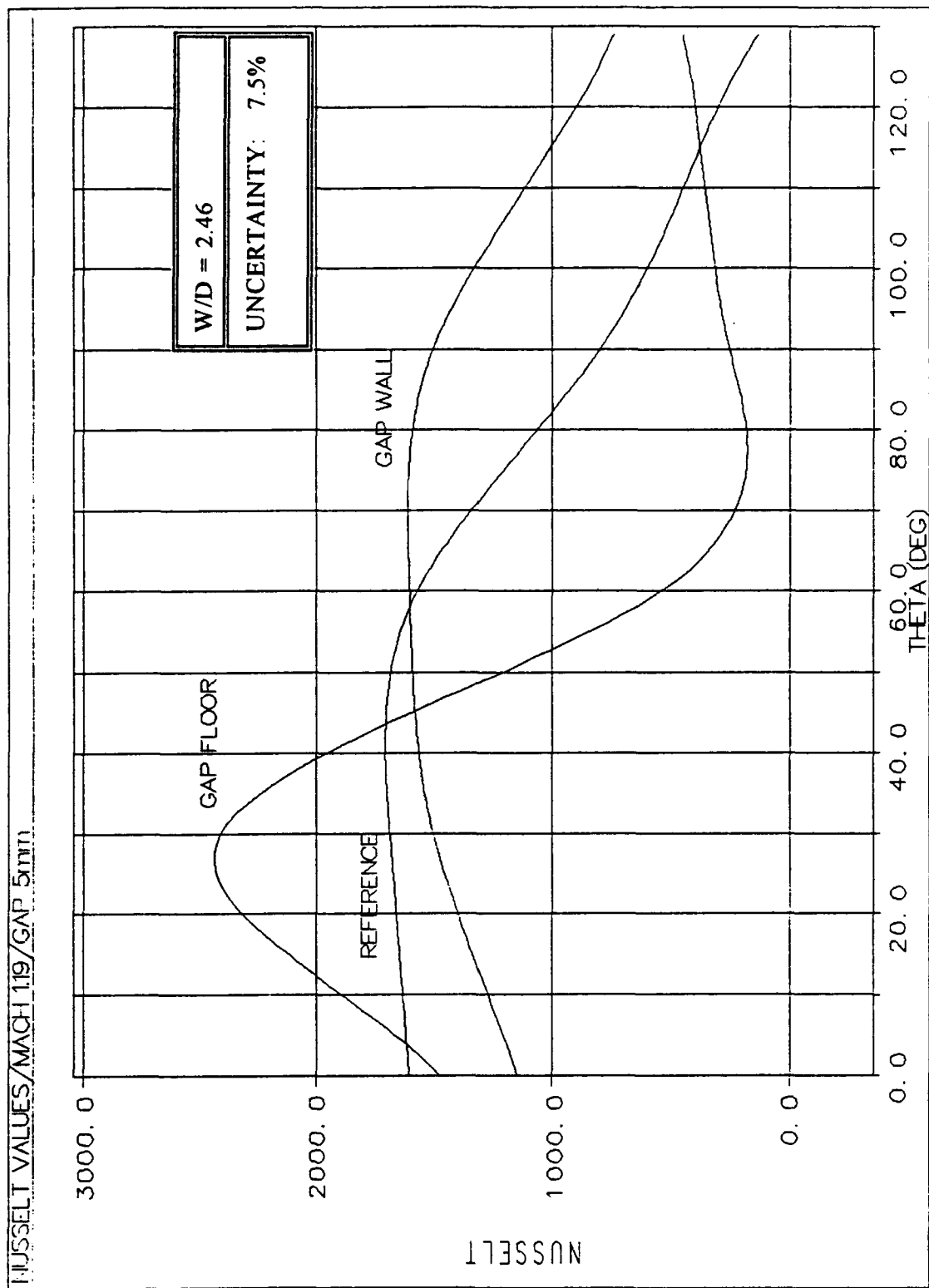


Figure 5.17. Combined Nusselt Values, Mach 1.19, Gap Width 5mm

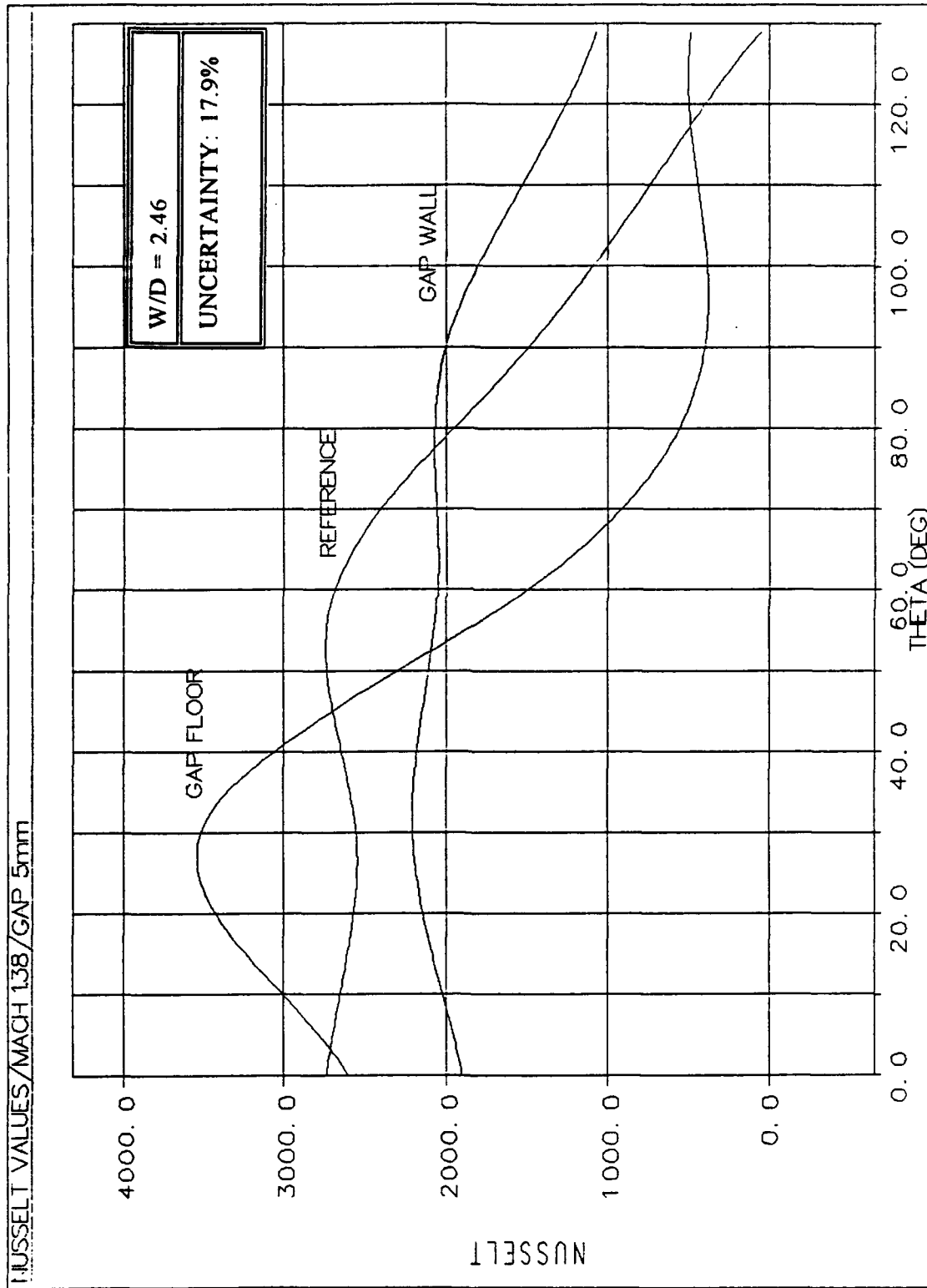


Figure 5.18. Combined Nusselt Values, Mach 1.38, Gap Width 5mm

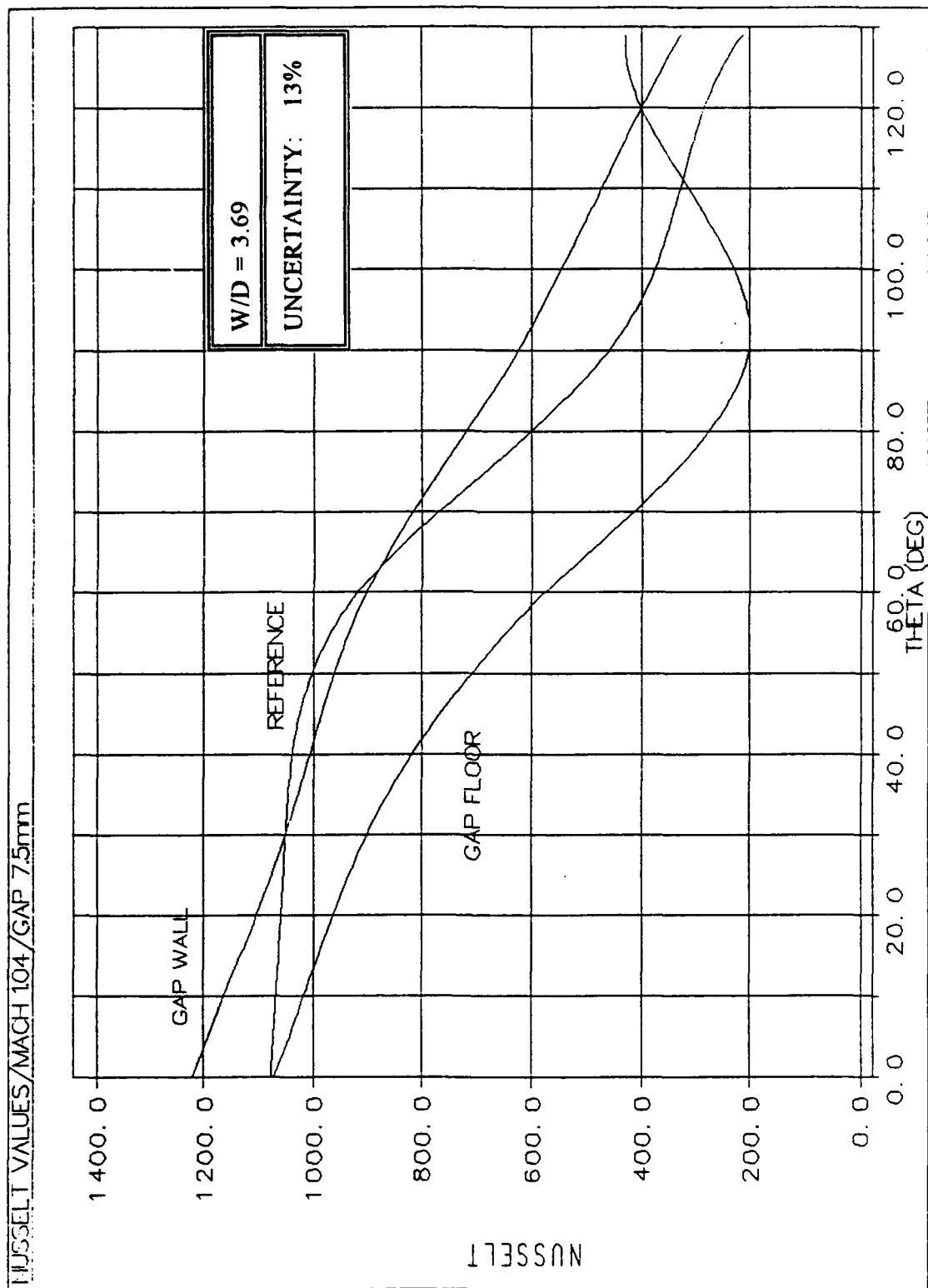


Figure 5.19. Combined Nusselt Values, Mach 1.04, Gap Width 7.5mm

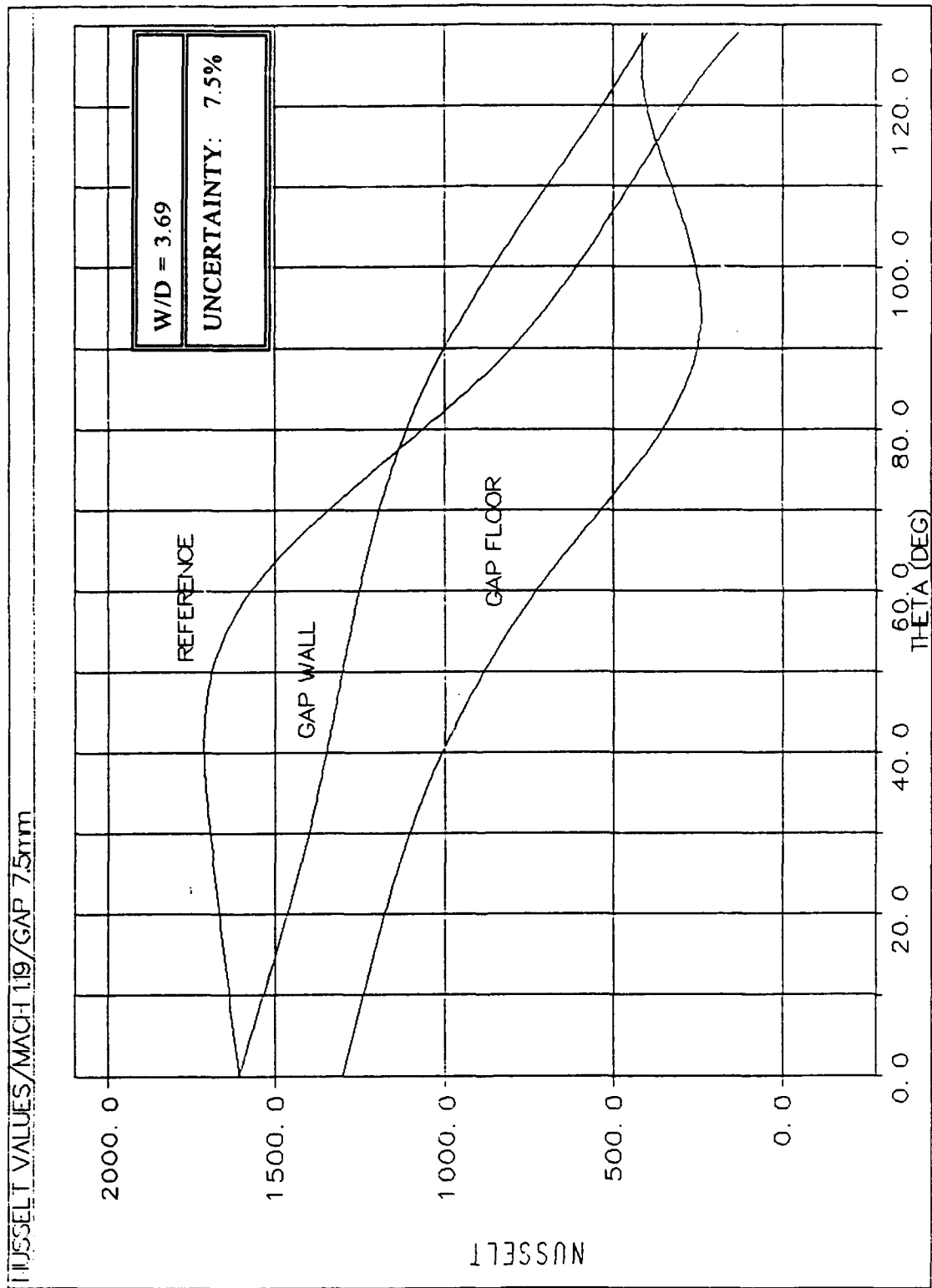


Figure 5.20. Combined Nusselt Values, Mach 1.19, Gap Width 7.5mm

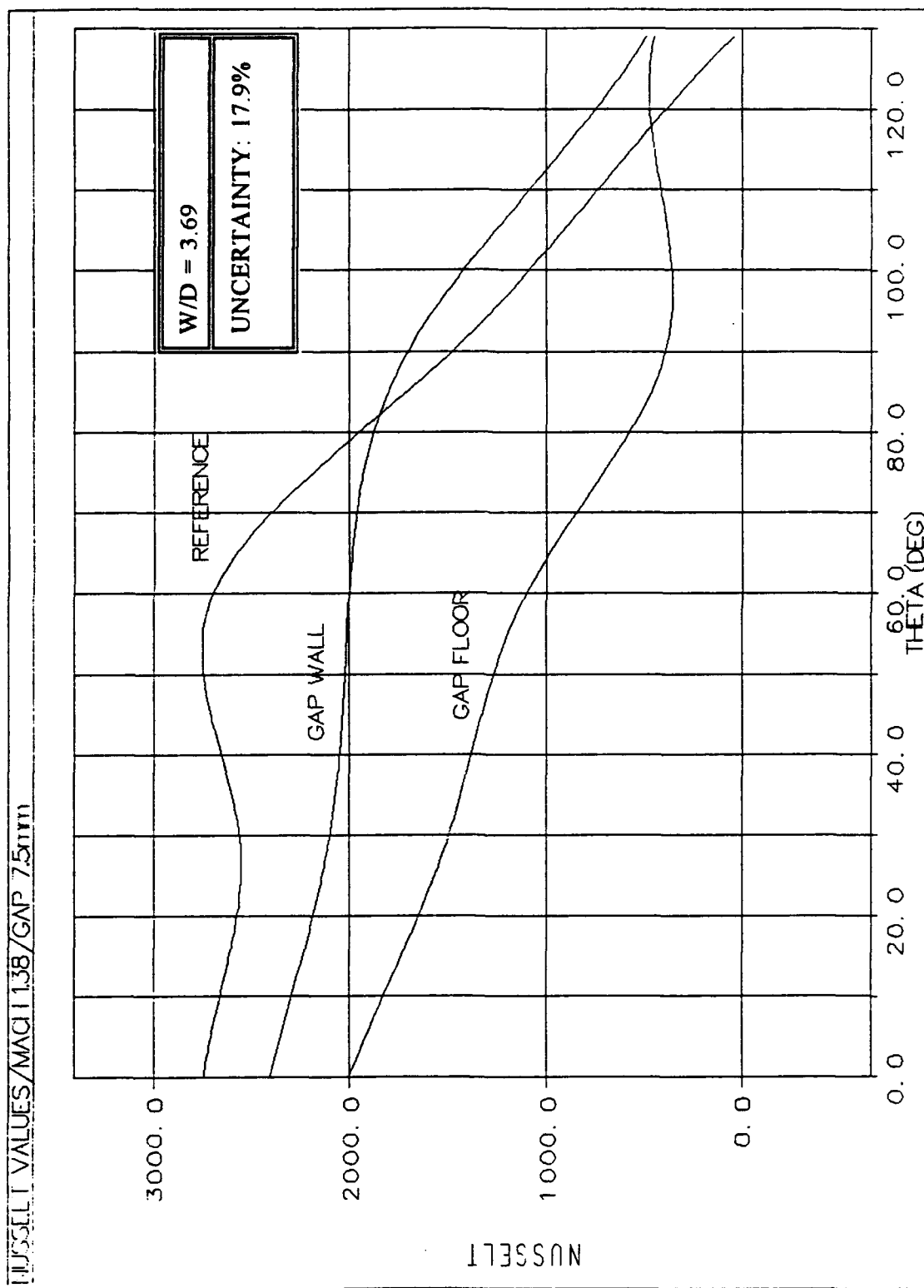


Figure 5.21. Combined Nusselt Values, Mach 1.38, Gap Width 7.5mm

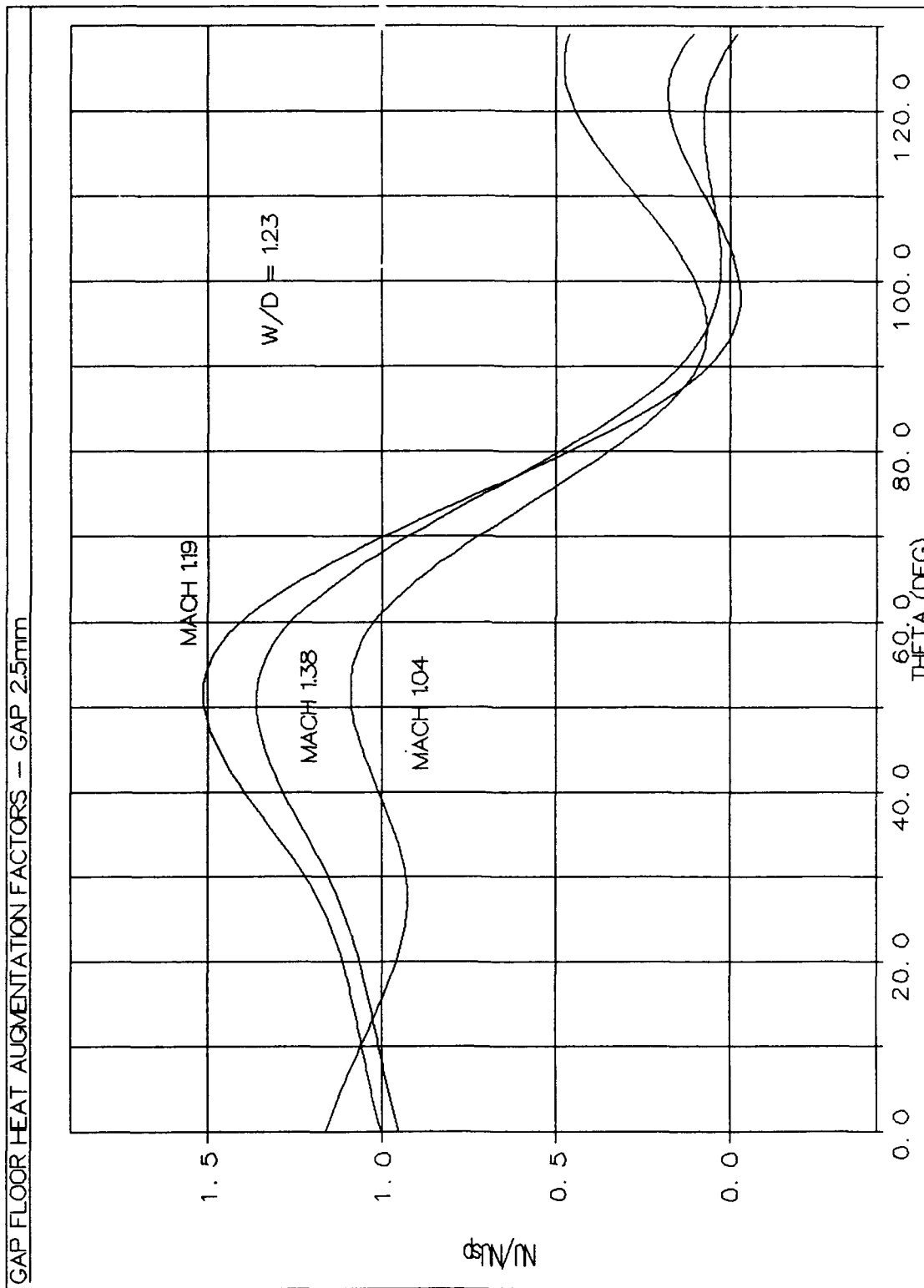


Figure 5.22. Gap Floor Heat Augmentation Factors, Gap Width 2.5mm

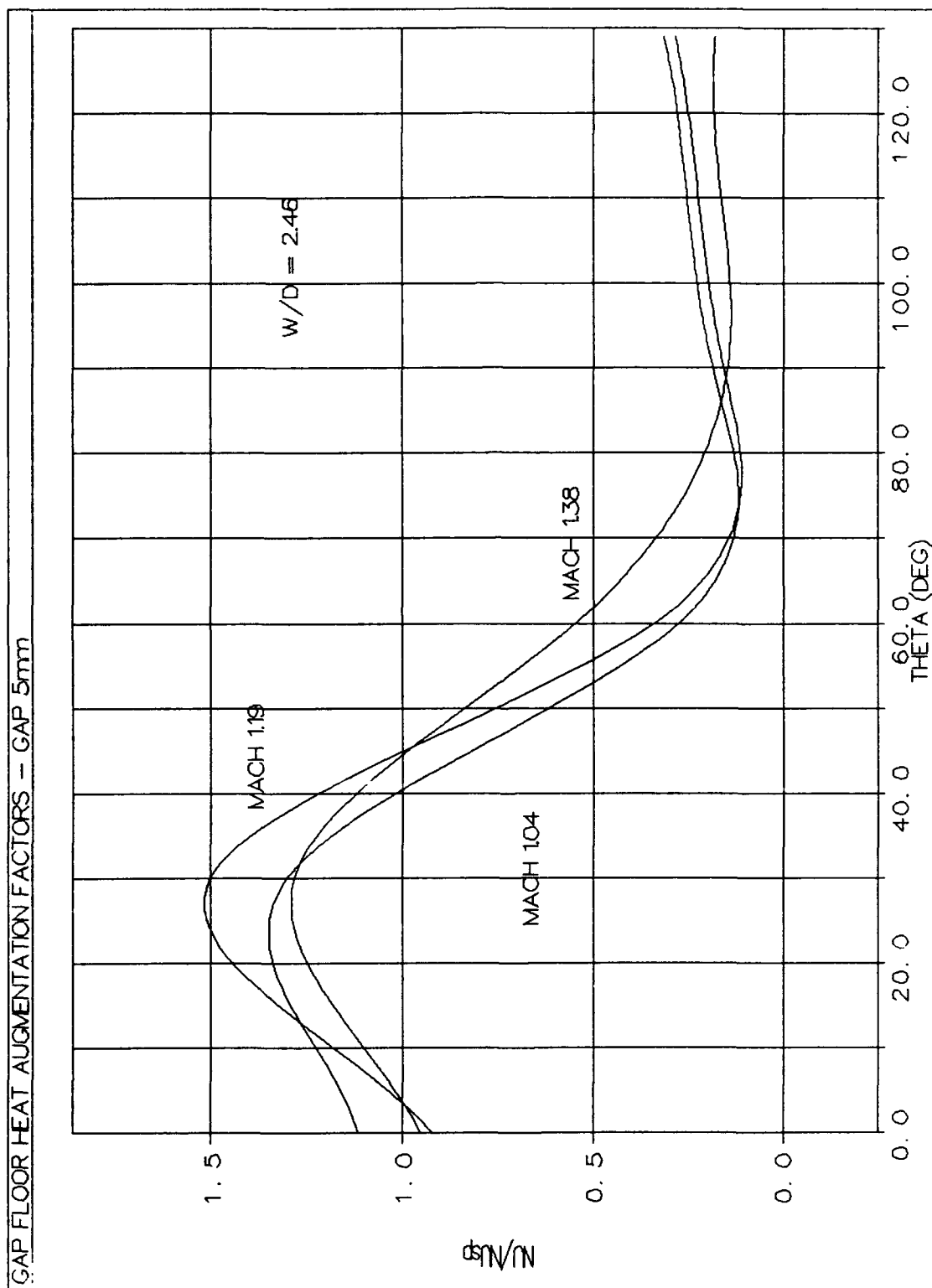


Figure 5.23. Gap Floor Heat Augmentation Factors, Gap Width 5mm

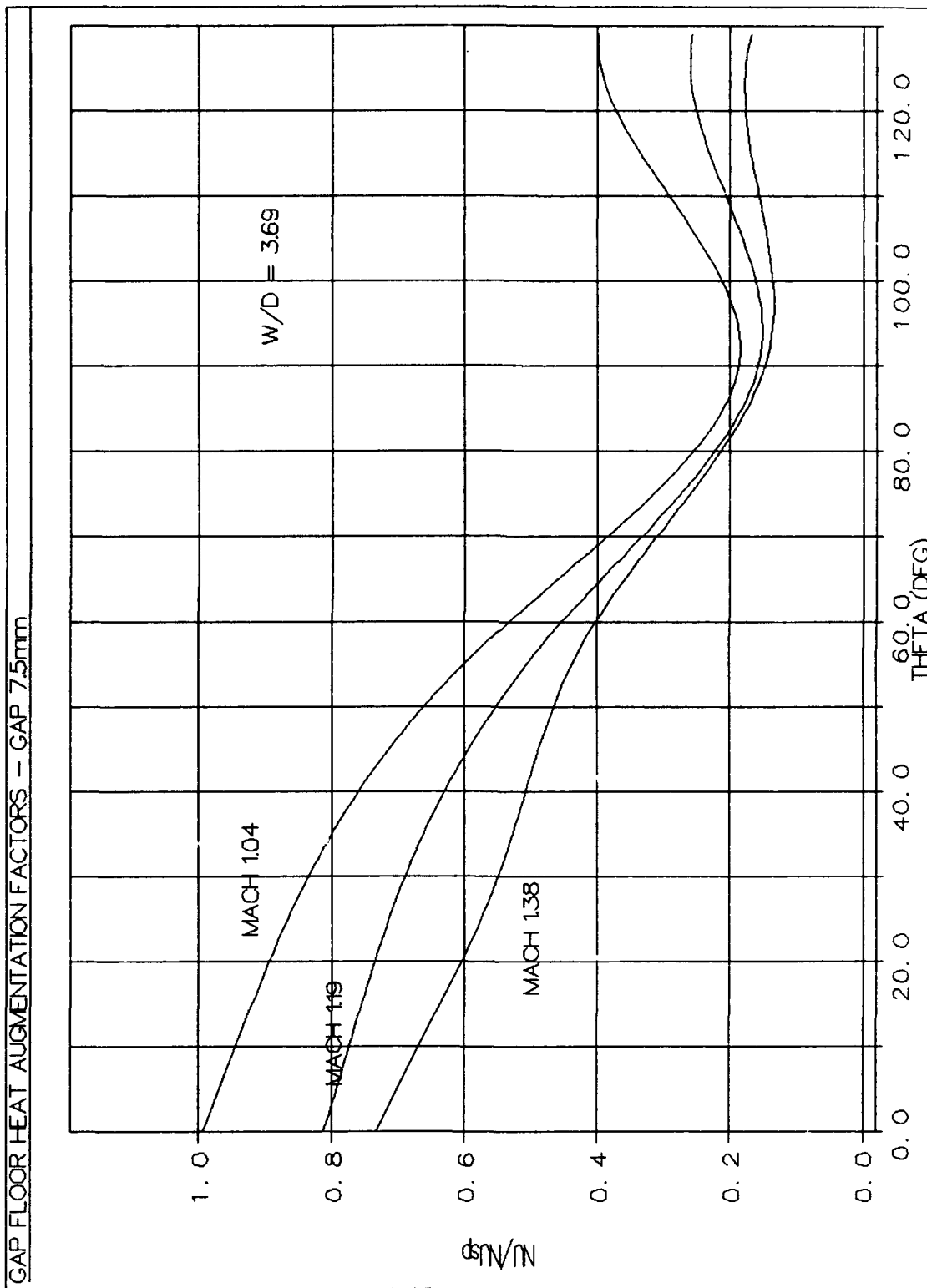


Figure 5.24. Gap Floor Heat Augmentation Factors, Gap Width 7.5mm

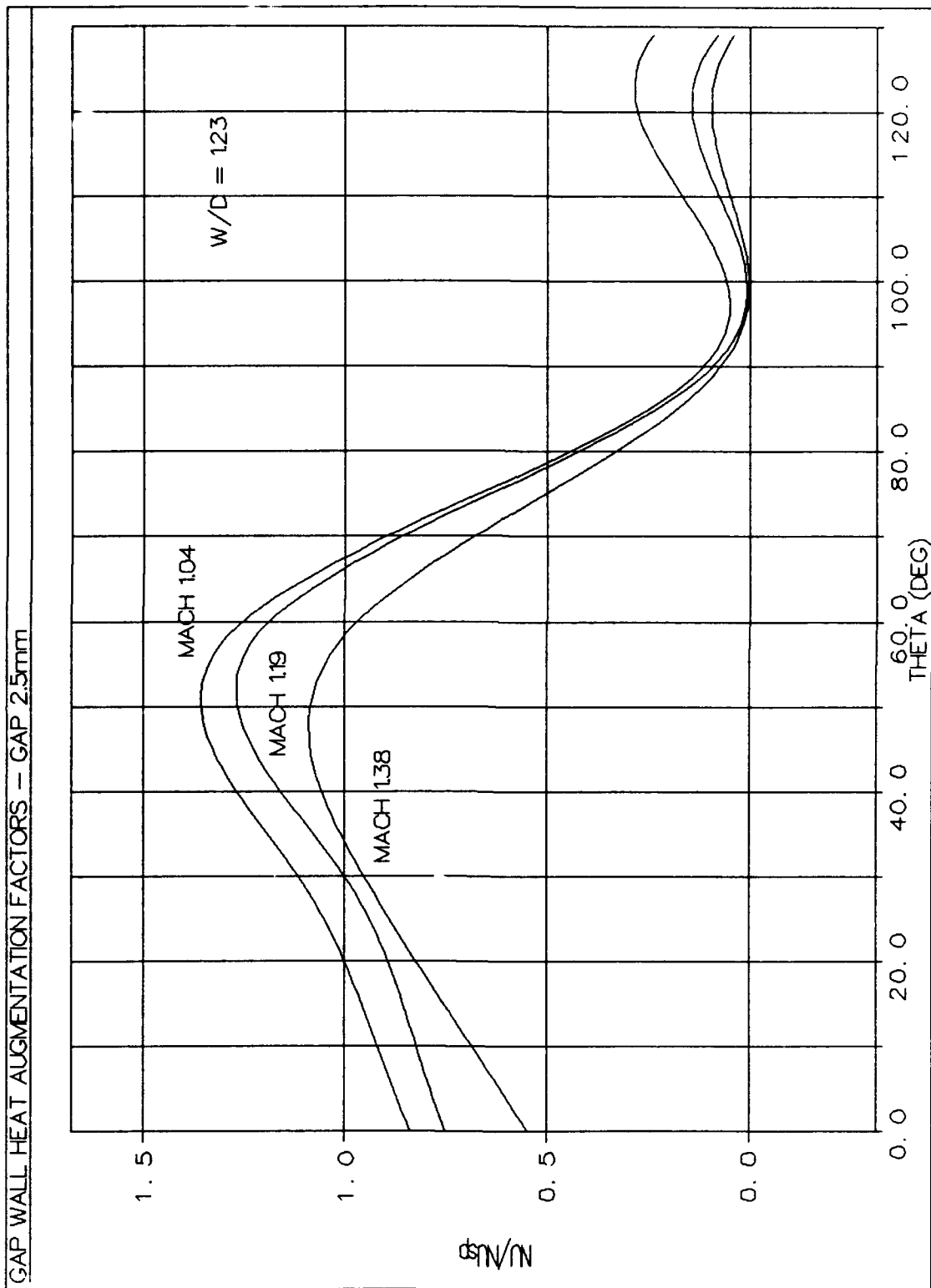


Figure 5.25. Gap Wall Heat Augmentation Factors, Gap Width 2.5mm

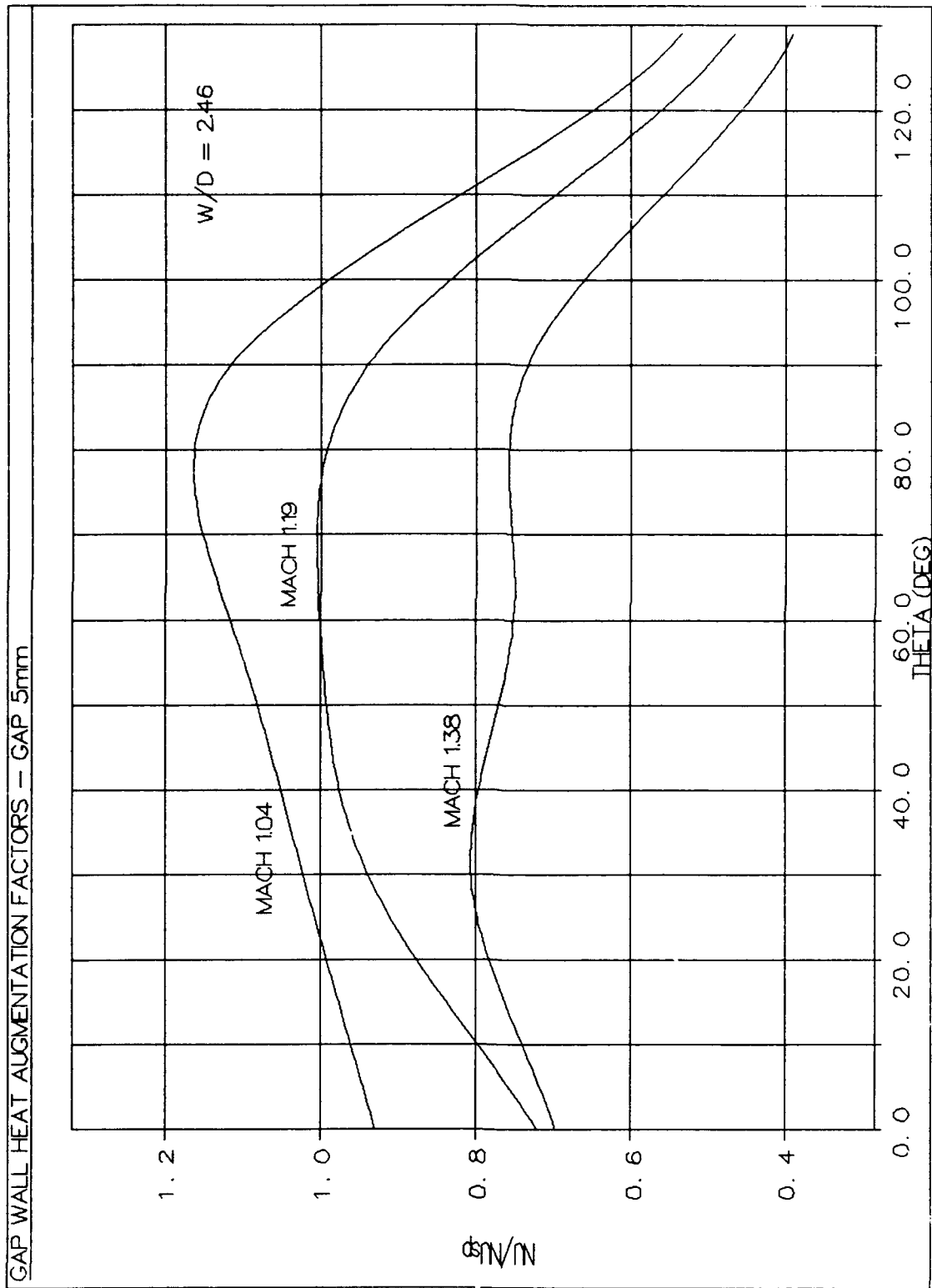


Figure 5.26. Gap Wall Heat Augmentation Factors, Gap Width 5mm

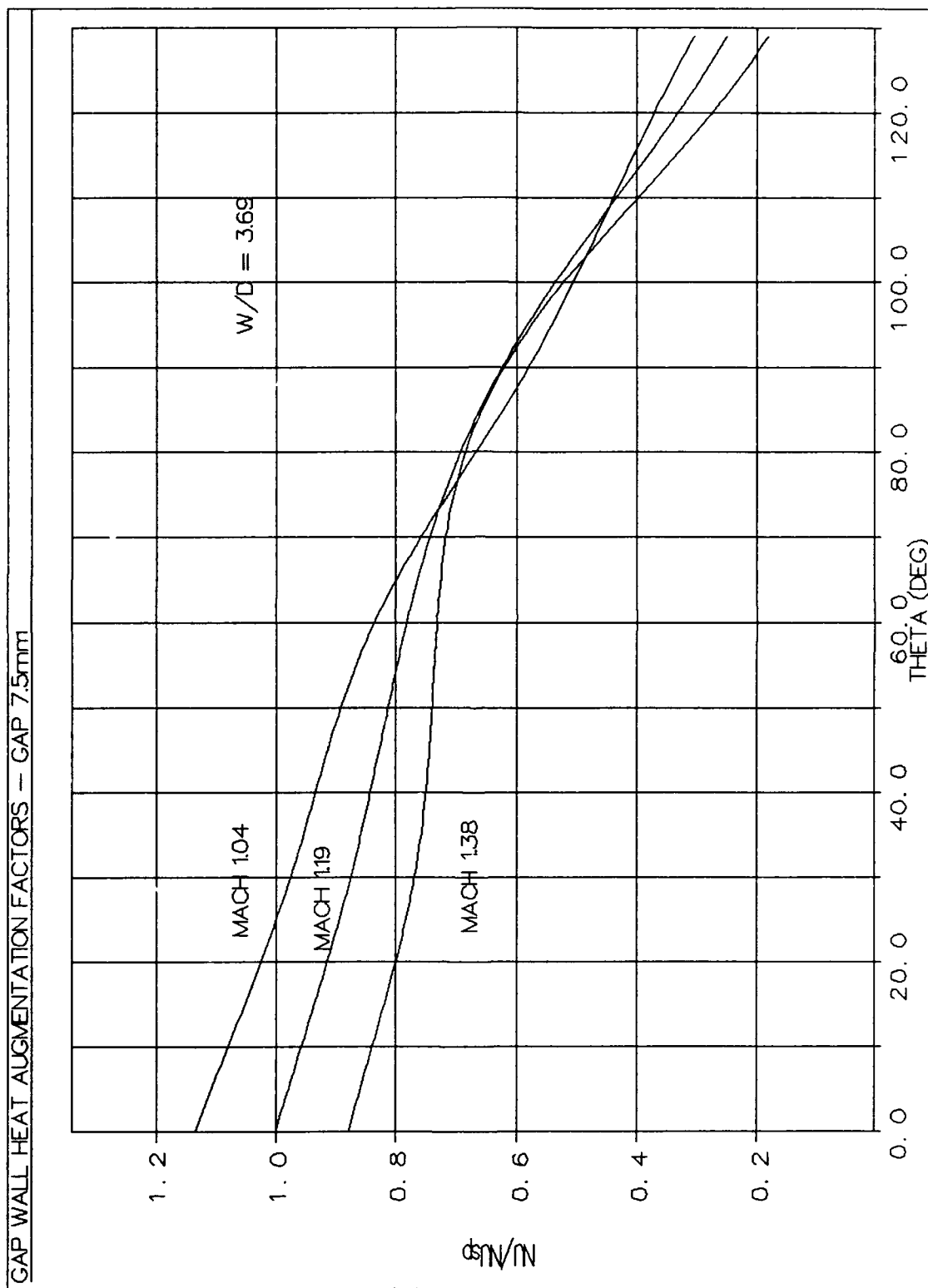


Figure 5.27. Gap Wall Heat Augmentation Factors, Gap Width 7.5mm

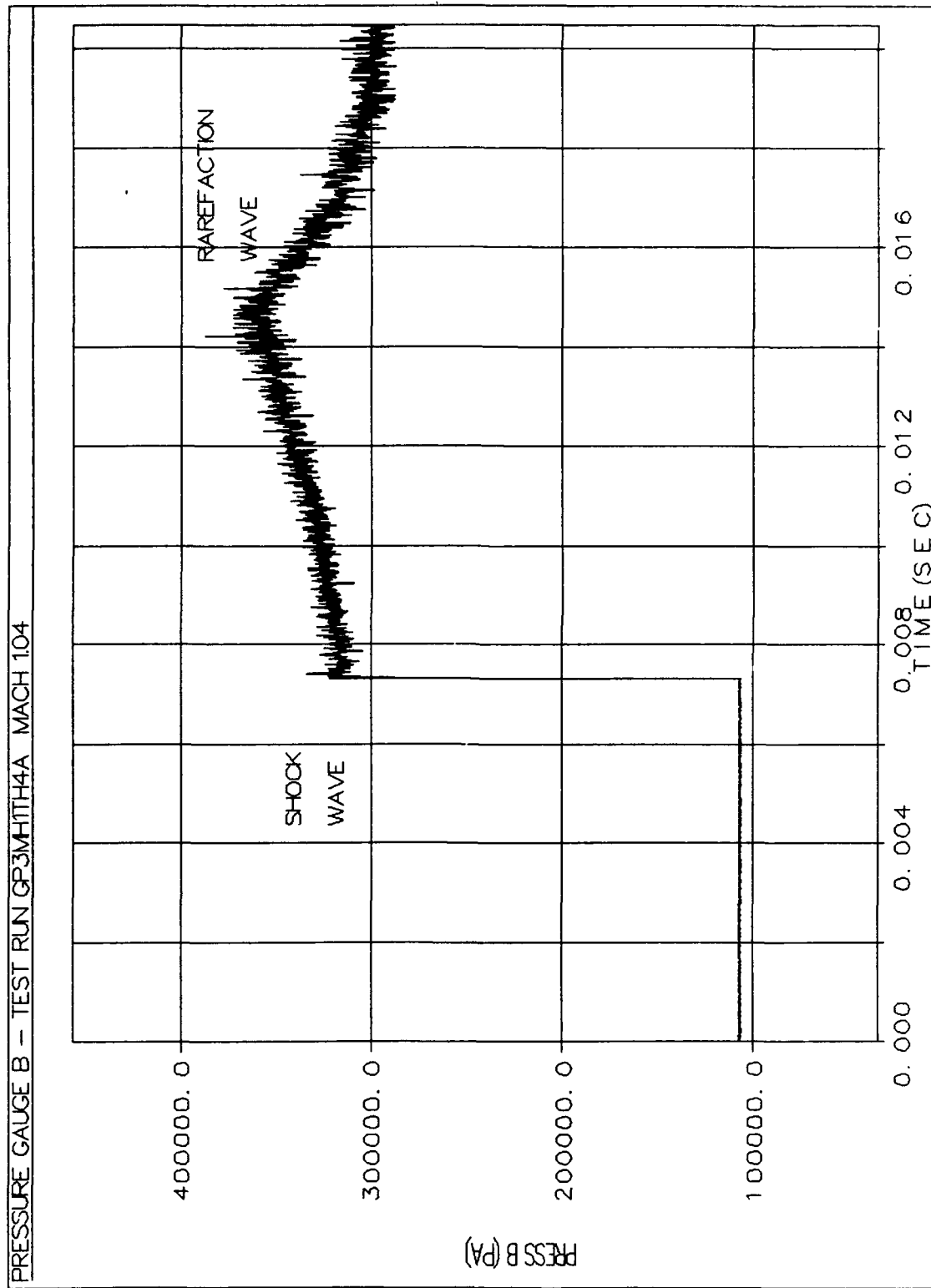


Figure 5.28. Pressure Gauge B, Test Run GP3MH1TH4A

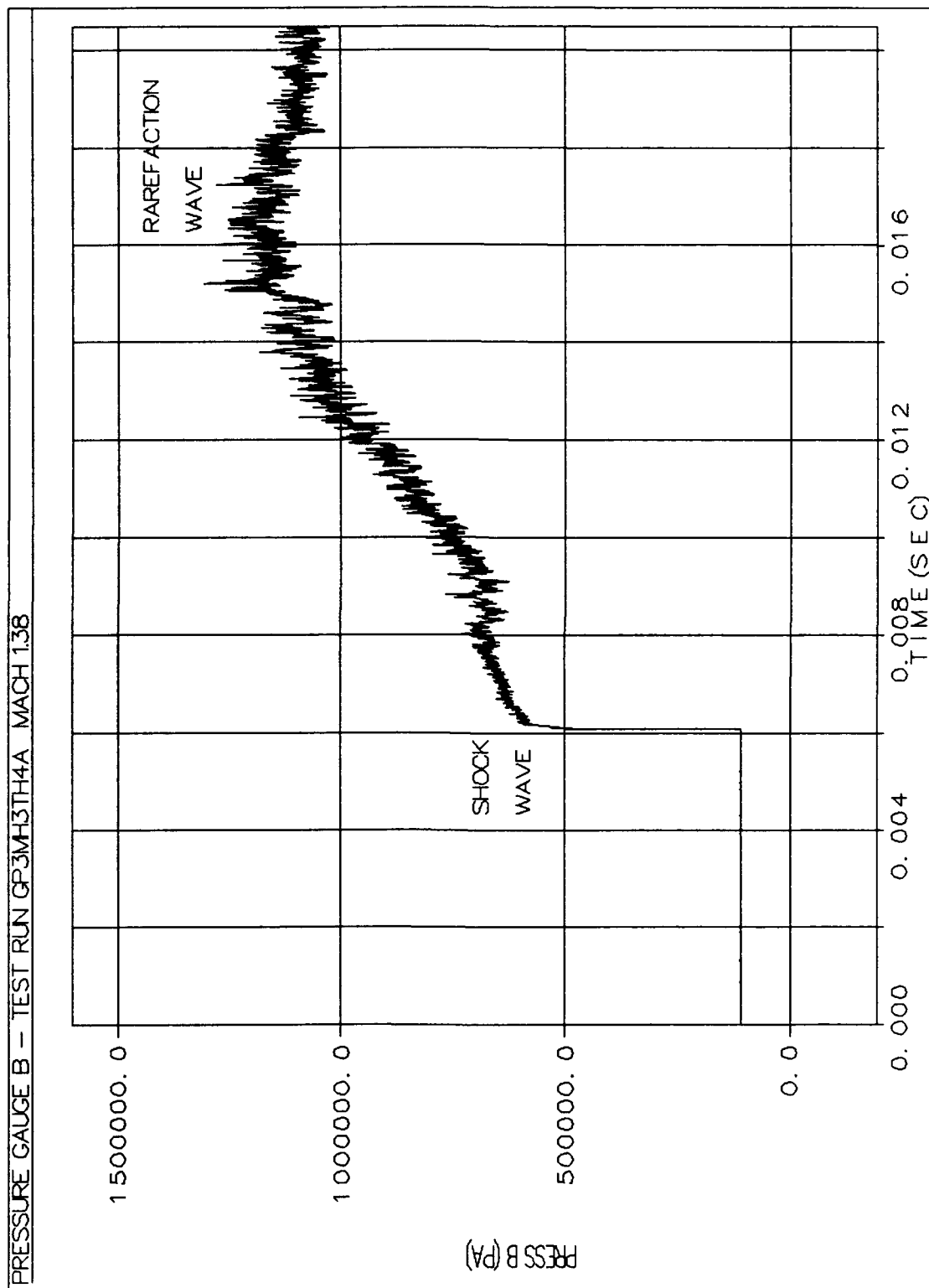


Figure 5.29. Pressure Gauge B, Test Run GP3MH3TH4A

VI. Conclusions and Recommendations

6.1 Conclusions

This study endeavored to investigate aerodynamic heating in expansion gaps. A cylinder, notched with a gap, was positioned 90° to the freestream flow with the gap aligned parallel to the flow. Gap width, free-stream Mach number, and angle from stagnation point were varied to determine influences on heat transfer rates. Based on results obtained from this study, a number of conclusions were drawn.

First, there exists a direct dependence between Nusselt number and Mach number. Nusselt number increases with an increase in free-stream velocity and occurs at all sensor locations investigated. An increase in flow velocity, within the range of Mach numbers investigated, did not vary the location of peak heating on the cylinder. Once flow around a cylinder was within a specific flow regime (i.e. the supercritical regime), changes in flow velocity appear to change the magnitudes of peak heat transfer, not location.

Second, peak heating inside the gap was a function of w/d (gap width to depth ratio) and angle from stagnation point. Due to the complexities of fluid flow around a cylinder, localized heat transfer rates vary with changing theta. These heat transfer rates were in turn influenced by changes in gap width (w/d). For large values of w/d , peak heat transfer rates occur at the stagnation point. At this w/d , reference point heat transfer rates were larger than both the gap wall and floor locations. As w/d was

reduced, peak gap wall and floor Nu values move aft, away from the stagnation point (at $w/d = 2.46$, $\theta \approx 30^\circ$; at $w/d = 1.23$, $\theta \approx 50^\circ$).

Third, in cylinders having longitudinal gaps exposed to supersonic cross flow, gap floor heat transfer rates predominate over the gap wall and reference locations. Experimental test data corroborates this finding for small values of w/d ($w/d \leq 2.46$). Large values of w/d ($w/d \geq 3.69$) result in reference point heat transfer being dominant with peak heat transfer values occurring at the stagnation point.

Several factors influence heat transfer effects. One hypothesis, as the supersonic fluid flows around the cylinder, it spills into the gap (as a consequence of its orientation to the free stream). This may cause a thinning of the boundary layer and a corresponding increase in heating. This thinning is influenced by the proximity of the gap walls to each other. As the width of the gap narrows, walls will influence the thickness of the boundary layer on the floor of the gap and the point where the flow transitions from laminar to turbulent. Maximum heat transfer takes place where the transition to turbulent flow develops on the gap floor.

Fourth, heat augmentation factors were used to predict maximum heat transfer rates. Augmentation curves were obtained by dividing localized Nu values by the smooth body Nu value (reference point) measured at the stagnation point. These curves normalize the different Mach numbers used during test runs. Although location of maximum heat transfer moves as a function of w/d , results suggest the value of the augmentation factor remains constant. There was also a trend that indicated heat augmentation factors might remain constant for changes in Mach number. This finding was inconclusive due to limits in data collected.

The largest heat augmentation factor occurred on the floor of the gap for w/d ratios of 1.23 and 2.46. The augmentation factor was measured at 1.5 for Mach numbers equal to 1.19. Location of the maximum augmentation factor was a function of gap width. At $w/d = 1.23$ a maximum was observed at $\theta = 50^\circ$; at $w/d = 2.46$, the maximum was at $\theta = 30^\circ$.

6.2 Recommendations

Based on the results of this study, the following recommendations were made.

First, similar tests should be conducted using smaller increments in theta spacing. This would capture possible gaps in existing data. Testing should be expanded to the higher Mach numbers to find heat augmentation factors at higher flow velocities. A comparison with existing test results would identify if trends in w/d and flow velocity are still valid at higher Mach numbers.

Second, off-axis orientations of the gap to the free-stream flow (ie. changing wing sweep) is an area not addressed in this study. Further investigation into the effects of changing the gap sweep angle is warranted.

The following recommendations are suggested in the use of laboratory equipment and test planning.

Continue to use MEDTHERM thermocouples for collecting surface temperature data. Sensors have a high frequency response time and are excellent in capturing temperature changes during shock tube test runs. Care must be given to the installation of thermocouples into the test section and their extended operation once installed. A number of thermocouples were broken during model fabrication (due to

tight fit tolerances of the test section). Thermocouple probe leads also fatigued and broke after multiple test runs. This was caused by vibrations in the shock tube created during shock generation. Bolting down the driven section of the shock tube will reduce vibrations in the driven section, cutting fatigue wear on the thermocouple wires, and increasing tube alignment accuracy.

Collocate a pressure sensor at the test section to record the Region 2 pressure history. This will reduce uncertainties caused by using pressure data collected at locations away from the test section. It will also make the process of data reduction simpler.

Use different driver gases (Helium) which could yield stronger shocks at lower relative pressure differentials. Also, further testing of diaphragms will be required to determine which diaphragm material and pressure ratios will provide the best normal shock formation (flat P_2 curve), and reduce the effects of shock strengthening. Finally, modify the test section cylinder to accommodate more thermocouples. Additional thermocouples could be used to examine areas of possible interest (gap lip, floor corner), and be used to verify one dimensional flow around the cylinder. Using a cylinder with a larger diameter would raise the effective Reynolds number and provide room for additional sensors.

Appendix A: Calibration of Pressure Measuring Instruments

Two Endevco model 8510B-500 pressure transducers and one Viatran model 104 pressure transducer were calibrated using an Ameter model PK II, pneumatic dead weight tester. The tester uses compressed air and calibrated weights to supply known pressures to a chamber where the transducer was attached. Misalignment and friction effects were reduced by spinning the calibration weights (Eads, 1992:C.1).

Each transducer was calibrated while connected to its designated Endevco model 4423 Signal Conditioner. Both components were kept together for experimental measurements. Gain was set to provide an acceptable voltage range for measurements during calibration. Output of the signal conditioner was read using a HP model 3466A Digital Voltmeter.

Both Endevco transducers were calibrated over their entire operating range (0 - 500 psig). The Viatran transducer was calibrated up to 500 psig which was the calibration limit of the tester. Output voltage was recorded as a function of input gauge pressure (psig). Endevco output voltages were recorded for 11 pressures, and Viatran output voltages were recorded for 10. Data points for each transducer were plotted in Figures A.1, A.2, and A.3.

Using calibration curve slope data, three voltage-to-pressure conversion equations were obtained. The y-intercepts were measured during test run setup and were used to convert gauge pressure to absolute pressure.

Forward Pressure Transducer (PressA), Gain = 10

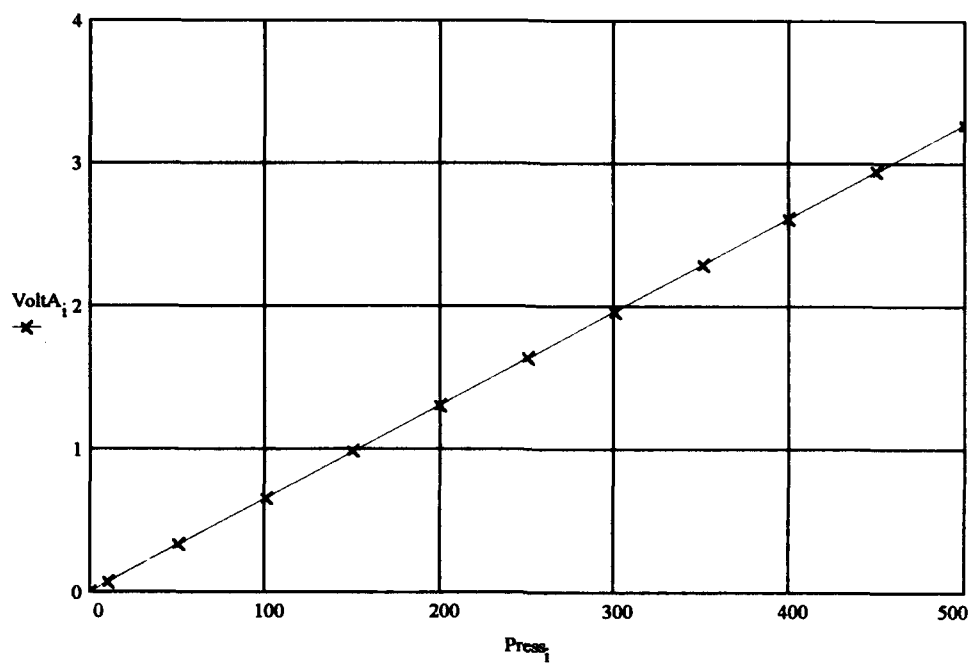
$$P_A = 152.9 \left(\frac{psi}{V} \right) + (Constant) \quad (A.1)$$

Rear Pressure Transducer (PressB), Gain = 10

$$P_B = 179.5 \left(\frac{psi}{V} \right) + (Constant) \quad (A.2)$$

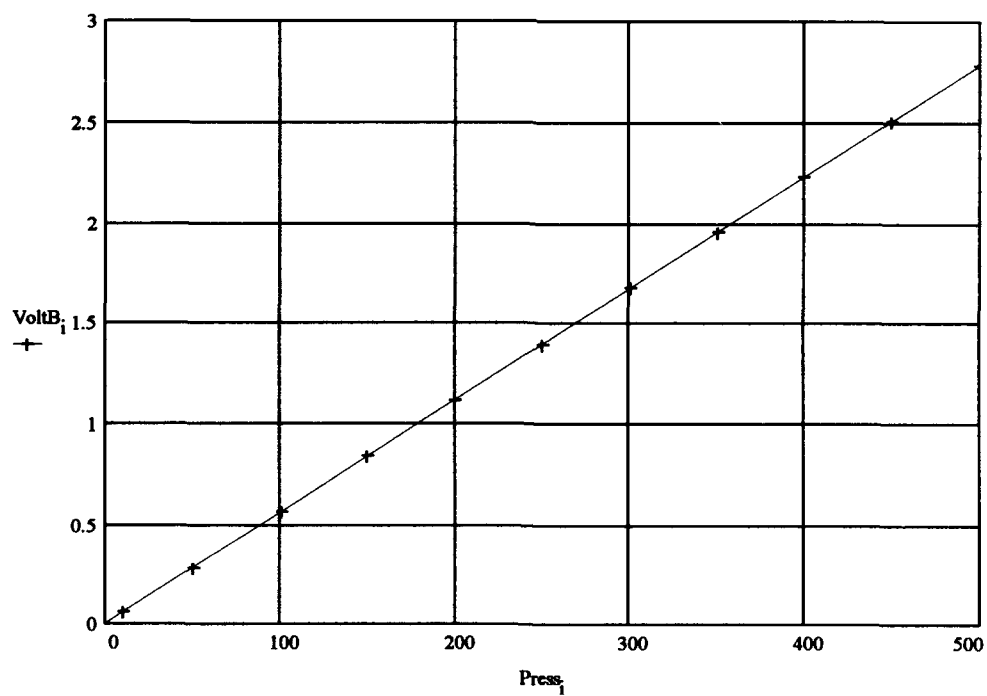
Driver Section Pressure Transducer (Press4), Gain = 10

$$P_4 = 7944.1 \left(\frac{psi}{V} \right) + (Constant) \quad (A.3)$$



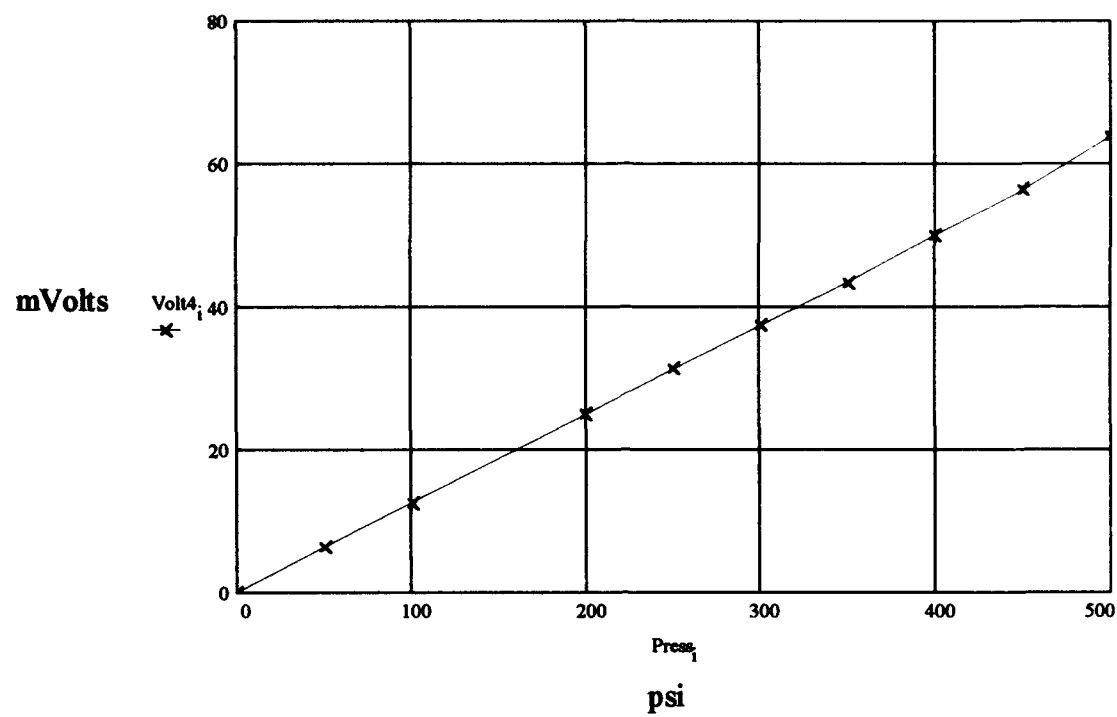
$$\text{slope}(\text{Press}, \text{VoltA}) = 0.00654$$

Figure A.1. Pressure Gauge A



$$\text{slope}(\text{Press}, \text{VoltB}) = 0.00557$$

Figure A.2. Pressure Gauge B



$\text{slope}(\text{Press}, \text{Volt4}) = 0.12588$

Figure A.3. Pressure Guage 4

Appendix B: Thermocouple Voltage to Temperature Conversion

Voltage cannot be obtained directly from a thermocouple. Connecting any measuring device to a thermocouple creates a new thermoelectric circuit which changes voltage and adds error. Hardware and software compensation are two methods which correct for these errors. This experiment uses hardware compensation in the form of Electronic Ice Point References to calibrate thermocouple voltages. Electronic Ice Point References ensure that the voltage read by a measuring device is the actual voltage from the thermocouple. A detailed discussion of thermocouple measurements, compensation techniques, and voltage-to-temperature conversions is found in *The Temperature Handbook* (Omega, 1992:Z-12).

Once compensation is used to calibrate thermocouple voltage, the next step is to convert the output reading to a temperature. Unfortunately, the temperature to voltage relationship is non-linear. If output voltages are plotted versus temperature, the slope of the resulting curve is called the Seebeck coefficient. The Seebeck coefficient varies as a function of temperature range. The National Bureau of Standards (NBS) uses thermocouple conversion equations to obtain the proper temperature from a voltage. These equations are polynomials that approximate the variation of the Seebeck coefficient. Type K thermocouples use an eighth order polynomial model to fit this relationship. The temperature conversion equation is of the form:

$$T = a_0 + a_1 V + a_2 V^2 + a_3 V^3 + \dots + a_8 V^8 \quad (\text{B.1})$$

where T is temperature in degrees centigrade, V is output voltage (in volts), and a_n

through a_8 are NBS polynomial coefficients. Table B.1 (Omega 1992.Z-12) lists polynomial coefficients for type K thermocouples.

Table B.1

NBS Polynomial Coefficients - Type K

(Temperature Range - 0°C to 1370°C)

a_0	.226584602	a_5	4.83506×10^{10}
a_1	24152.109	a_6	-1.18452×10^{12}
a_2	67233.4248	a_7	1.38690×10^{13}
a_3	221034.682	a_8	-6.33708×10^{13}
a_4	-860963914.9		

Figure B.1 is a graph of thermocouple temperature verses output voltage using equation B.1 and NBS polynomial coefficients.

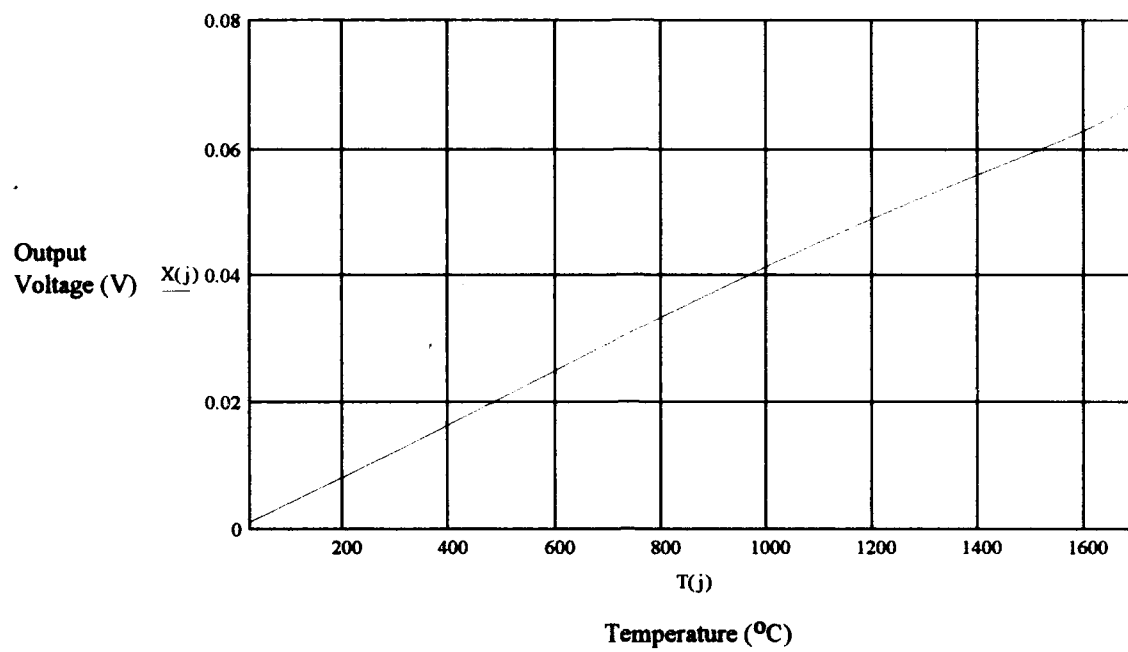


Figure B.1. Thermocouple vs. Output Voltage

Appendix C: Surface Temperature to Heat Flux FORTRAN Program

The program FLUXMC was written using FORTRAN 77, and compiled using Microsoft® FORTRAN 5.1 on a 80486-33, MS-DOS, personal computer. The program was used to convert a surface temperature data series into surface heat flux information. The program runs inside the DADiSP operating environment using the DSP Pipeline function. Pipeline allows the use of external programs to run as if they were built into DADiSP. Listed are procedures to load data series, access FLUXMC, and import converted data back into DADiSP. The DADiSP macro HEATFLX.DSP is listed next, followed by the FORTRAN program FLUXMC.

Heat Flux Macro Procedures.

1. From the DADiSP worksheet environment select a temperature data series window.
2. TYPE: **LOAD('HEATFLX.DSP')**
3. FORTRAN program will ask for initial surface temperature, total test time (of data series), and number of data steps.
4. After completion of FLUXMC, DADiSP worksheet environment is returned.
5. HFLUX.DAT is imported into DADiSP for data reduction.

DADiSP Macro HEATFLUX.DSP

```
! THIS COMMAND FILE AUTOMATES SAVING WINDOW DATA TO
! ASCII FILE AND RUNNING FLUXMC.EXE (TEMPERATURE TO HEAT
! FLUX).
WRITEA("C:\DSP\TEMPS.DAT") @CR
! WRITES WINDOW DATA TO TEMPS.DAT (ASCII FILE)
RUN("C:\DSP\FLUXMC") @CR
! CONVERTS TEMPERATURE DATA TO HEAT FLUX DATA
! AND OUTPUTS TO HFLUX.DAT ASCII FILE.
@HIGHLIGHT_MESSAGE("HFLUX.DAT FILE COMPLETED")
! ALL DONE
```

FORTRAN Program FLUXMC

```
C
C Program FLUXMC - Determines Heat Transfer on a surface using
C      raw temperature data time history from a
C      surface mounted thermocouple. This program
C      is imbedded in the DaDisp Heat Flux macro
C      ("HEATFLX.DSP"). See HTFLUXW (Windows Ver)
C      or HTFLUXD (DOS Ver) for stand alone programs.
C      This program requires a ASCII data file TEMPS.DAT
C      as an input.
C
C*****
C
C This program was written by Capt Doug High
C Date: 1 July 1993
C Sources: Cook, W.J. and E.J. Felderman, "Reduction of Data
C      from Thin-film Heat Transfer Gages: A Concise Numerical
C      Technique," AIAA Journal, 4(3): 561-562 (March 1966).
C
C      Bonafede, Joseph A., "A Numerical Investigation of Thin
C      Film Heat Transfer Guages," Thesis: AFIT/GA/AA/88M-1
C
C*****
C Begin Declarations and Set Constants and Dimensions
C      DIMENSION TM(0:4200)
C      DIMENSION TEMP(0:4200)
C      DIMENSION QFLUX(0:4200)
C      REAL ALPHA,K,PI,TOTTM,TERM,SUM,QFLUX,AA,BB,CC,TM
C      OPEN (7,FILE = "FLUX.DAT", STATUS = "UNKNOWN")
C      OPEN (9,FILE = "HFLUX.DAT", STATUS = "UNKNOWN")
C      OPEN (8,FILE = "TEMPS.DAT",STATUS = "OLD")
C      Set value of thermal diffusivity for thermocouple substrate
C      (Chromel in m**2/sec)
C      ALPHA = .000004903
C      Set value of thermal conductivity for Chromel (Watt/m K)
C      K = 19.0377
C      PI = 3.14159
C      M = 1
C      I = 1
C      Set initial time
C      TM(0) = 0.0000
C      WRITE(6,*)" ENTER INITIAL TEMPERATURE OF OBJECT (000.0)"
C      READ(5,*) TEMP(0)
11  FORMAT('*****')
```

```

12  FORMAT(' TEMP(0) = ',F6.1,' K')
    WRITE(6,11)
    WRITE(7,11)
    WRITE(6,12) TEMP(0)
    WRITE(7,12) TEMP(0)
C   Enter in total test time and # of time steps of temp data file
    WRITE(6,*)" ENTER TOTAL TEST TIME AND # TIME STEPS
(00.0000,0000)"
    READ(5,*) TOTTM,ISTEP
13  FORMAT(' TOTTM = ',F8.4,' SEC')
14  FORMAT(' #TMSTEP = ',I5,' STEPS')
    WRITE(6,13) TOTTM
    WRITE(7,13) TOTTM
    WRITE(6,14) ISTEP
    WRITE(7,14) ISTEP
C   Calculate time step increment
    TMSTEP = TOTTM/ISTEP
C   Read in temperature data file into array TEMP
    DO 20 I = 1,ISTEP
        TM(I) = TMSTEP*I
        READ(8,*) TEMP(I)
20  CONTINUE
    J = 1
    DO 40 M = 1,ISTEP
        N = 1
        SUM = 0
        DO 30 N = 1,J
            NMO = N-1
            AA = TEMP(N)-TEMP(NMO)
            BB = (TM(J)-TM(N))**.5
            CC = (TM(J)-TM(NMO))**.5
            TERM = AA/(BB+CC)
            SUM = SUM+TERM
30  CONTINUE
            QFLUX(M) = (2*K/(PI*ALPHA)**.5)*SUM
            J = J+1
40  CONTINUE
C OUTPUT RESULTS
    WRITE(7,11)
41  FORMAT('TEMPERATURE DATA',/)
45  FORMAT(F6.1)
    WRITE(7,41)
    I = 1
    DO 43 I = 1,ISTEP
        WRITE(7,45) TEMP(I)

```

```
43  CONTINUE
42  FORMAT(/, 'HEAT FLUX ARRAY, QFLUX(M) M = 1, ', I5, /)
46  FORMAT(F11.1)
    WRITE(7,42) ISTEP
    I = 1
    DO 44 I = 1, ISTEP
        WRITE(7,46) QFLUX(I)
        WRITE(9,46) QFLUX(I)
44  CONTINUE
    END
```

Appendix D: Data Reduction Procedures (Sample Case)

Calculations for test run GP3MH2TH3A are included in this appendix to detail procedures used in data reduction. Figure D.1 shows voltage data collected by the DL1200 and input into the DADiSP software program. Inputs include measurements from each pressure transducer and surface temperatures from each thermocouple sensor location.

The first step in reducing data was to convert pressure voltages into units of pressure (Pascals). Equations derived in Appendix A (Equations A.1, A.2, and A.3) were used in this transformation. Figures D.2 and D.3 show gauge A and gauge B data converted to units of pressure. Next, surface temperature data was converted from voltage to degrees Kelvin through use of the temperature conversion equation found in Appendix C (Equation C.1). Figures D.4, D.5, and D.6 show reference point, gap wall, and gap floor surface temperature time histories converted to units Kelvin. Relevant information was extracted from each surface temperature data series (Figure D.7) and then converted to heat flux through use of the FLUXMC FORTRAN program listed in Appendix C. A heat flux graph was obtained for each sensor location. Figure D.8 presents heat flux data for the reference point sensor location. Figure D.9 provides the same information after undergoing a 20 point moving average technique. This procedure reduces the noise of each heat flux data series.

The next step was to obtain convective heat transfer coefficients (h 's) from heat flux data series. Equation 2.9, along with Equation 2.19, was used with heat flux and

surface temperatures as inputs. Free stream temperature (T_∞) was obtained using extracted P_2 data (Figure D.10). Assuming a perfect gas, the T_2 data series was obtained using the following equation:

$$T_2 = \frac{P_2}{\rho_2 R} \quad (D.1)$$

where ρ_2 is Region 2 air density and R is the gas constant for air. T_∞ is assumed to equal T_2 . A Mathcad[®] Pressure to Temperature Conversion Worksheet was used to convert pressures to temperatures. This worksheet was also used to calculate shock speed, pressure ratio, and Region 2 properties. A sample worksheet is presented on pages D.13 thru D.14. A converted T_2 graph is presented in Figure D.11. T_2 is converted to adiabatic temperature (T_{aw}) using Equation 2.19. Figure D.12 shows adiabatic temperature information. Figure D.13 is a graph of the reference point convective heat transfer coefficient.

The final step in test run data reduction was converting the heat transfer coefficients to Nusselt numbers. Equation 2.10 was used to find Nu , with D being the diameter of the cylinder. k was obtained from the reference temperature defined in Equation 2.20, and tables listing the thermophysical properties of air. Figure D.14 presents reference point Nu data. Similar calculations were performed for gap wall and gap floor locations. A combined Nu graph is shown in Figure D.15.

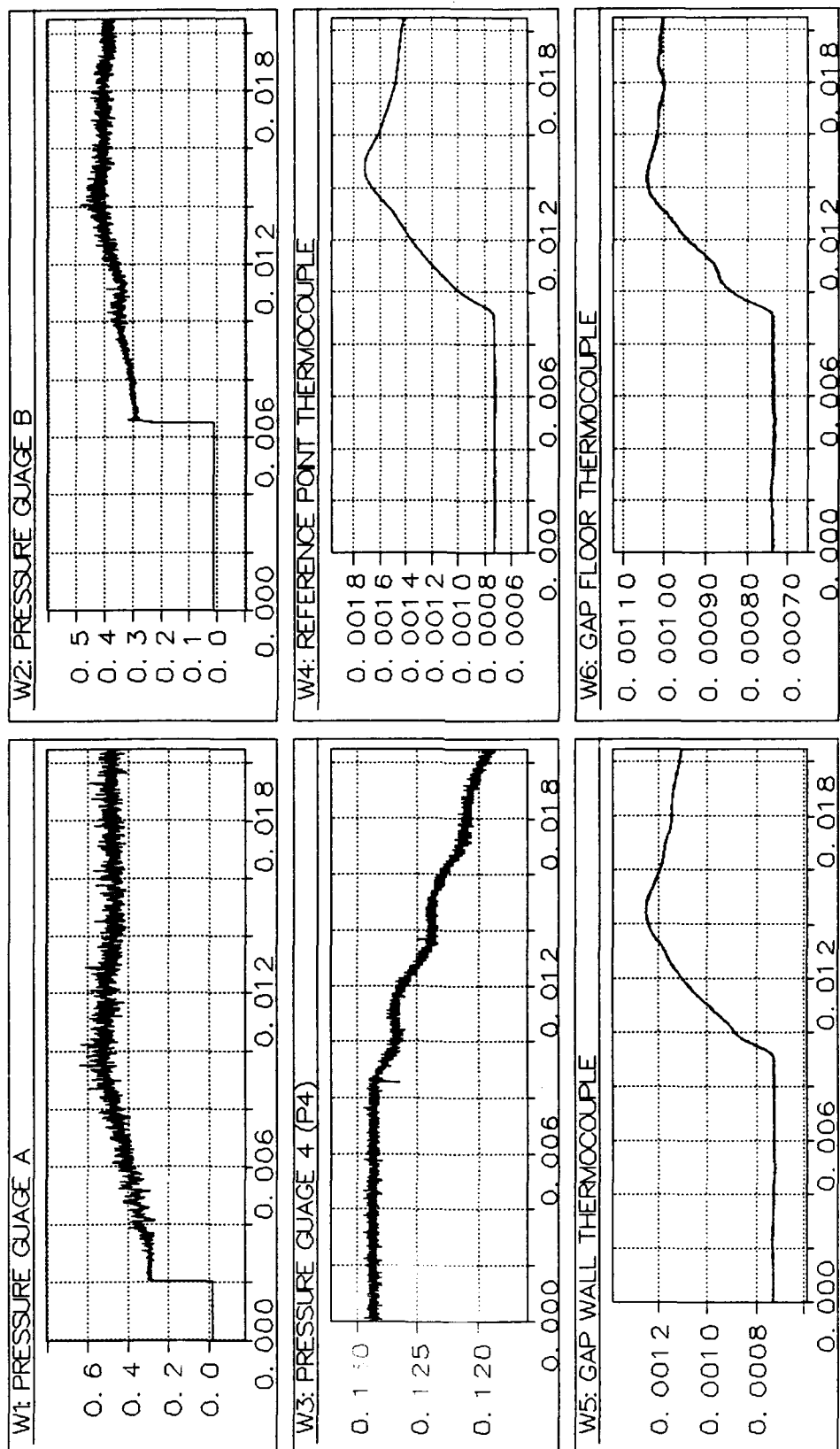


Figure D.1. Input Voltage Data

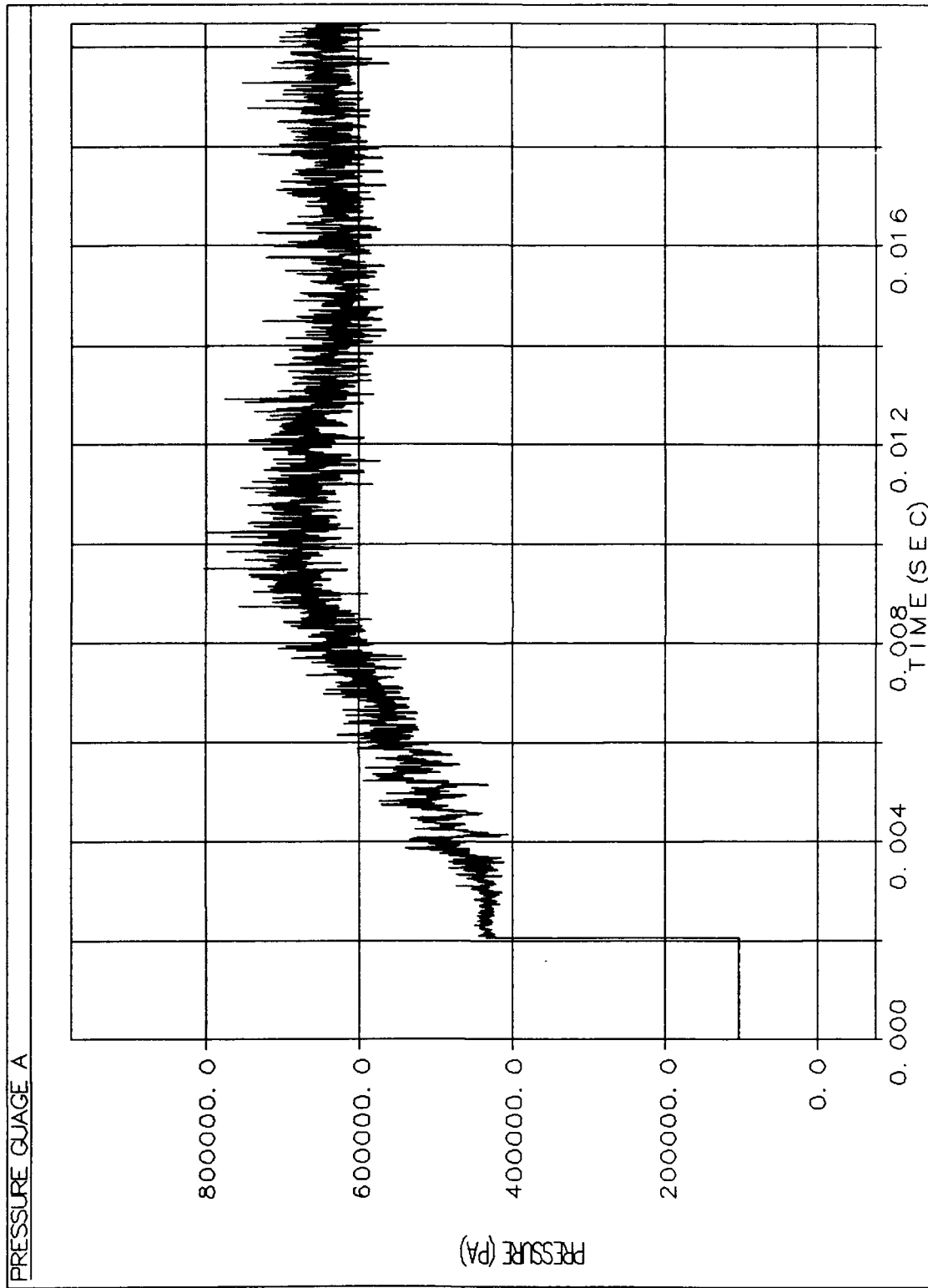


Figure D.2. Gauge A Pressure History

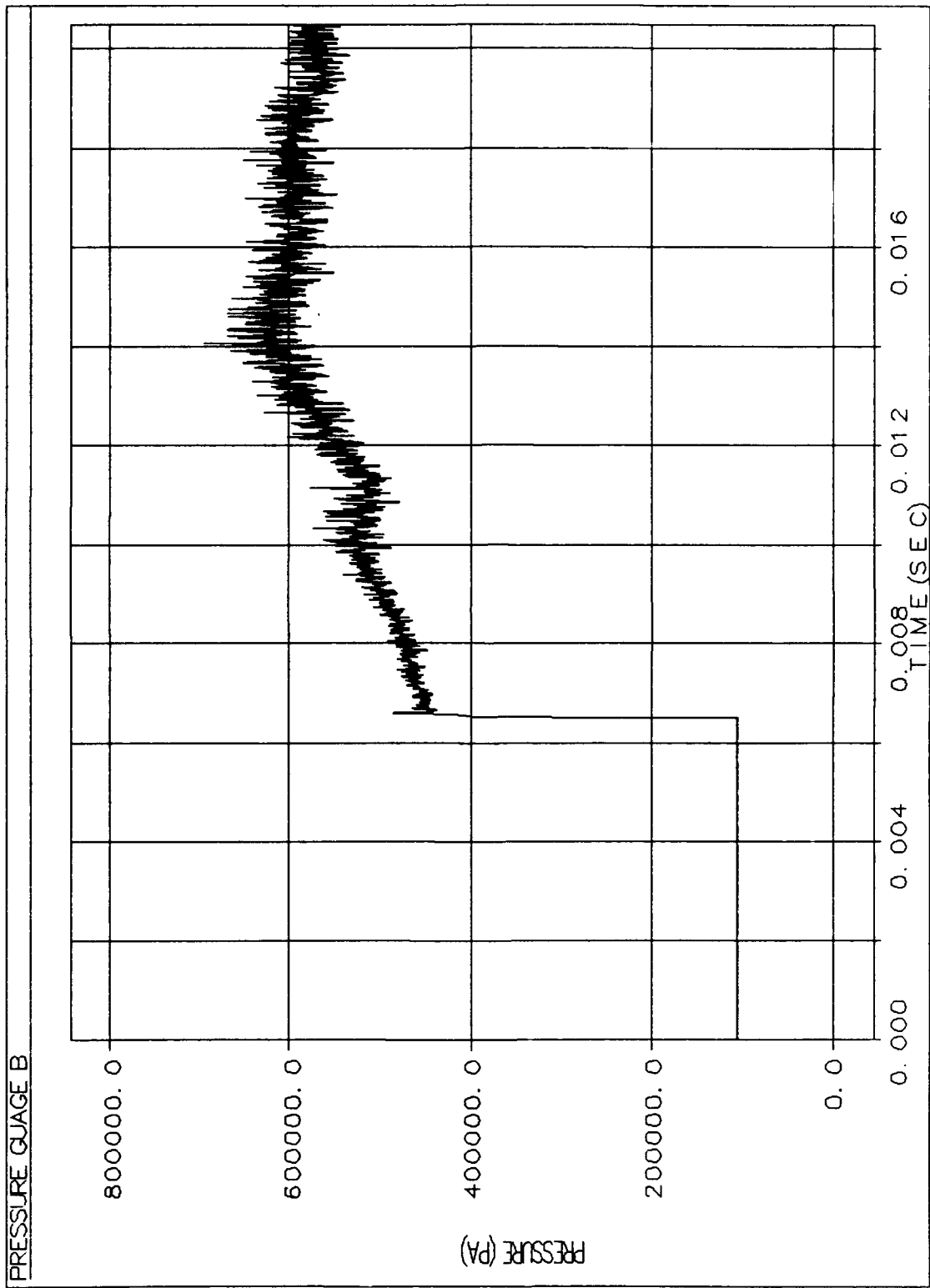


Figure D.3. Gauge B Pressure History

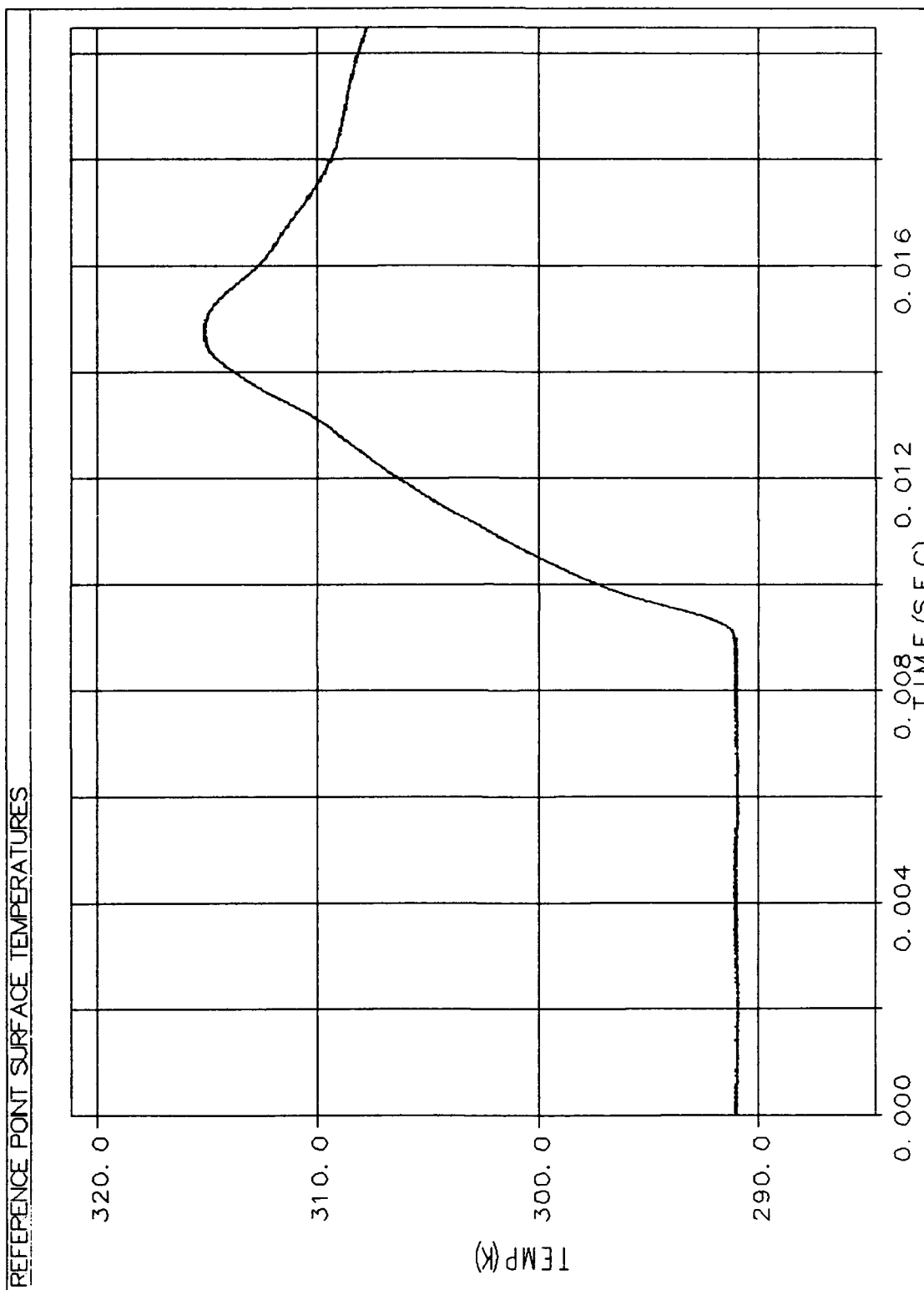


Figure D.4. Reference Point Surface Temperature History

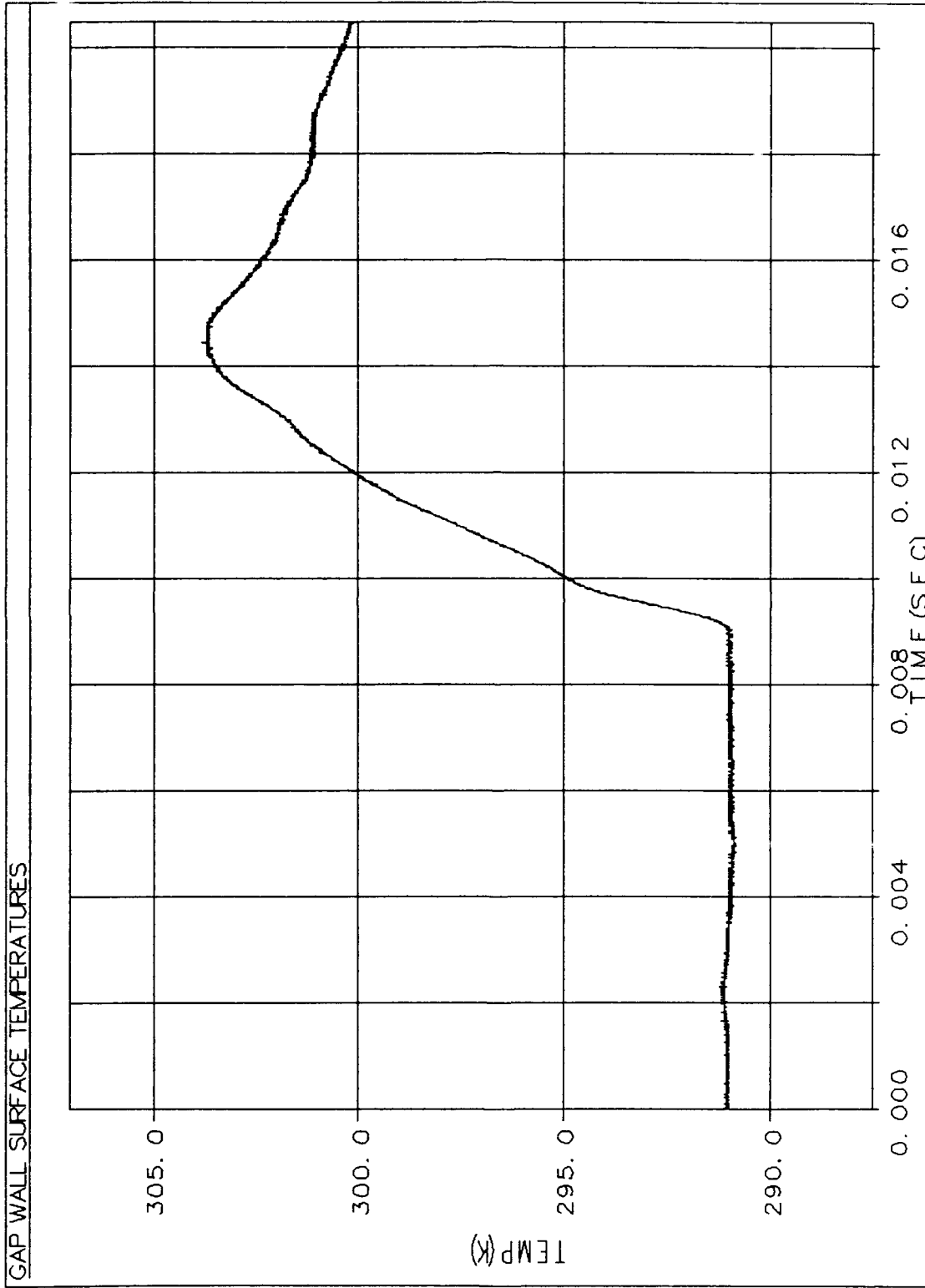


Figure D.5. Gap Wall Surface Temperature Time History

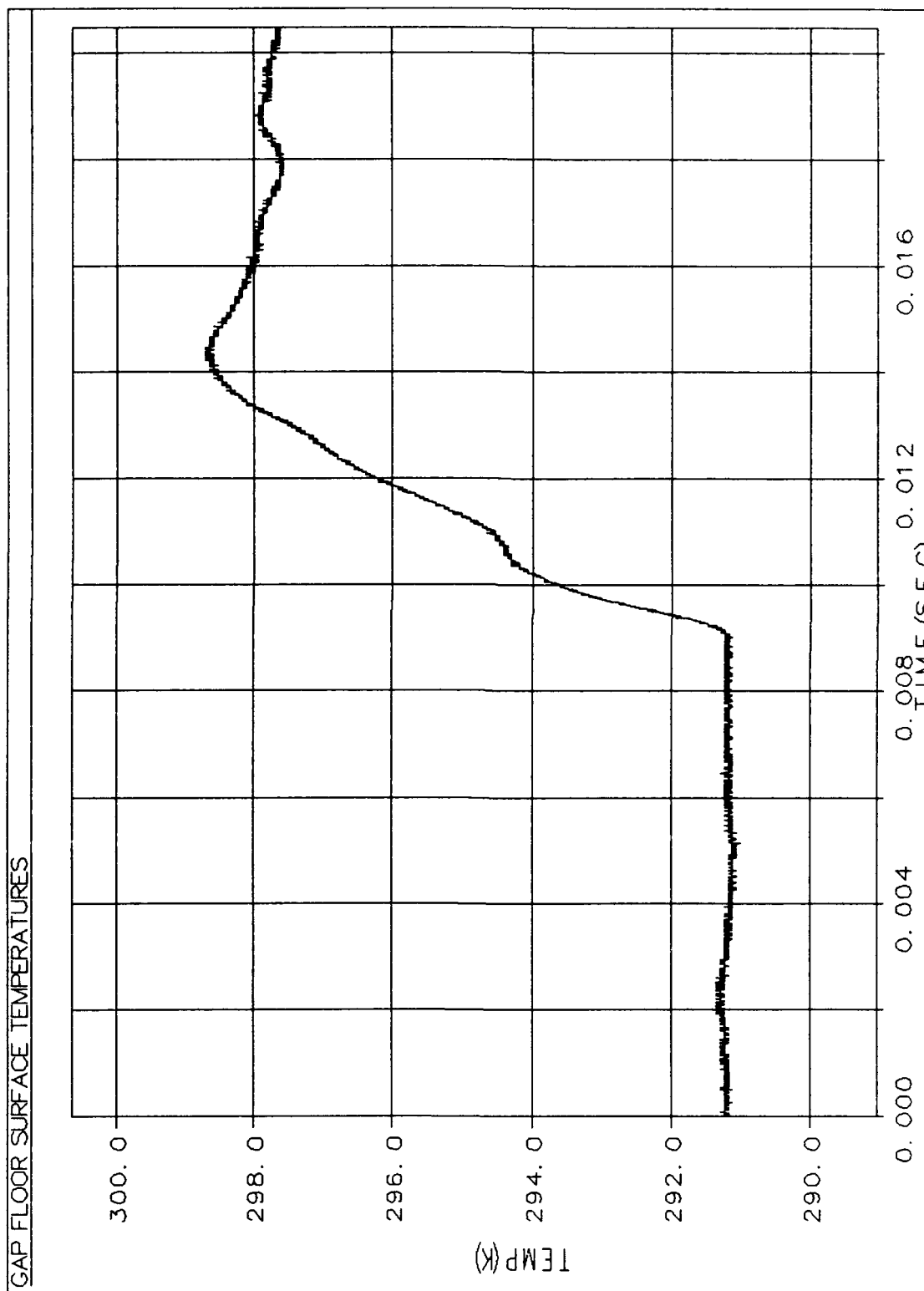


Figure D.6. Gap Floor Surface Temperature Time History

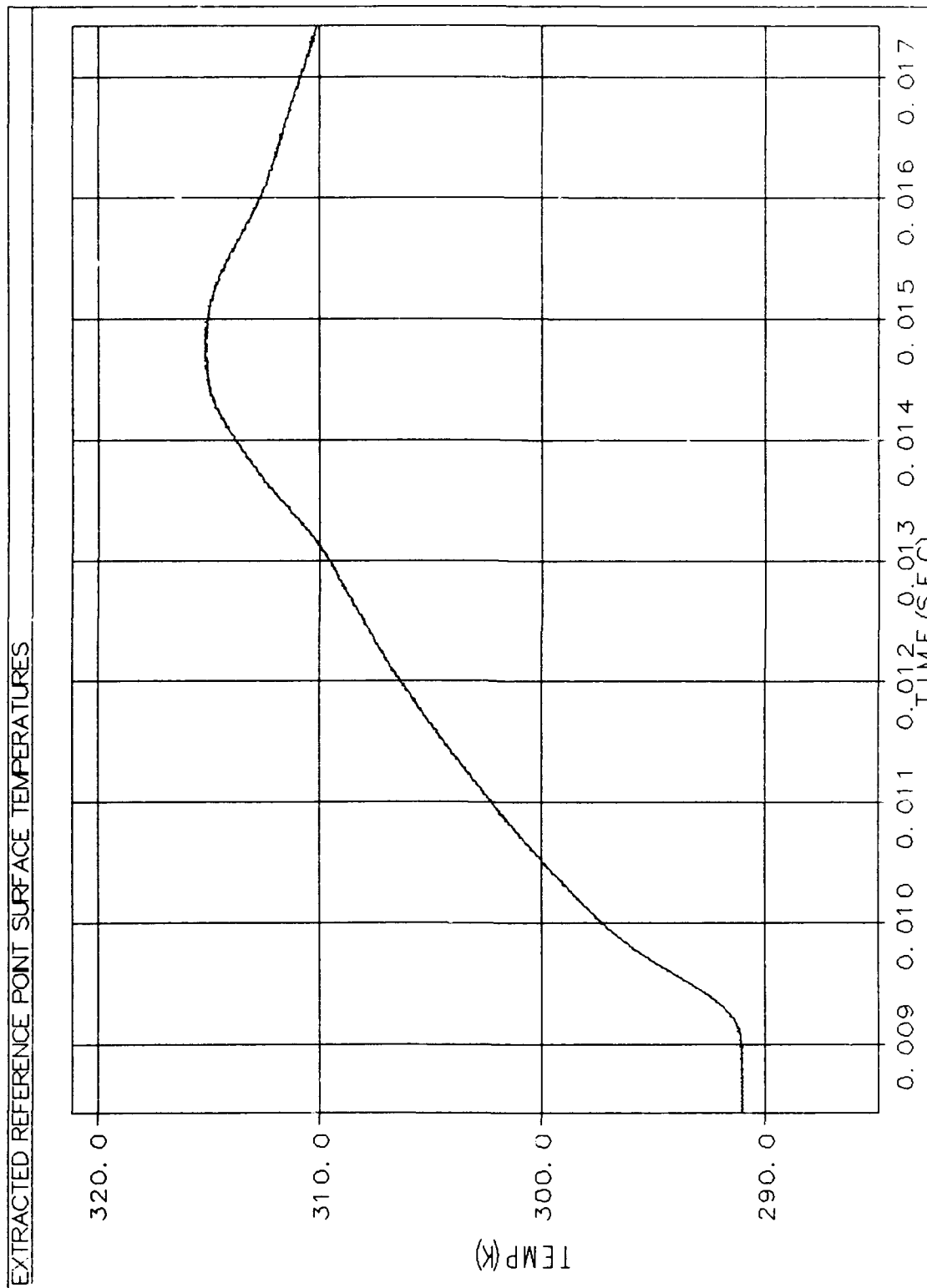


Figure D.7. Extracted Reference Point Surface Temperatures

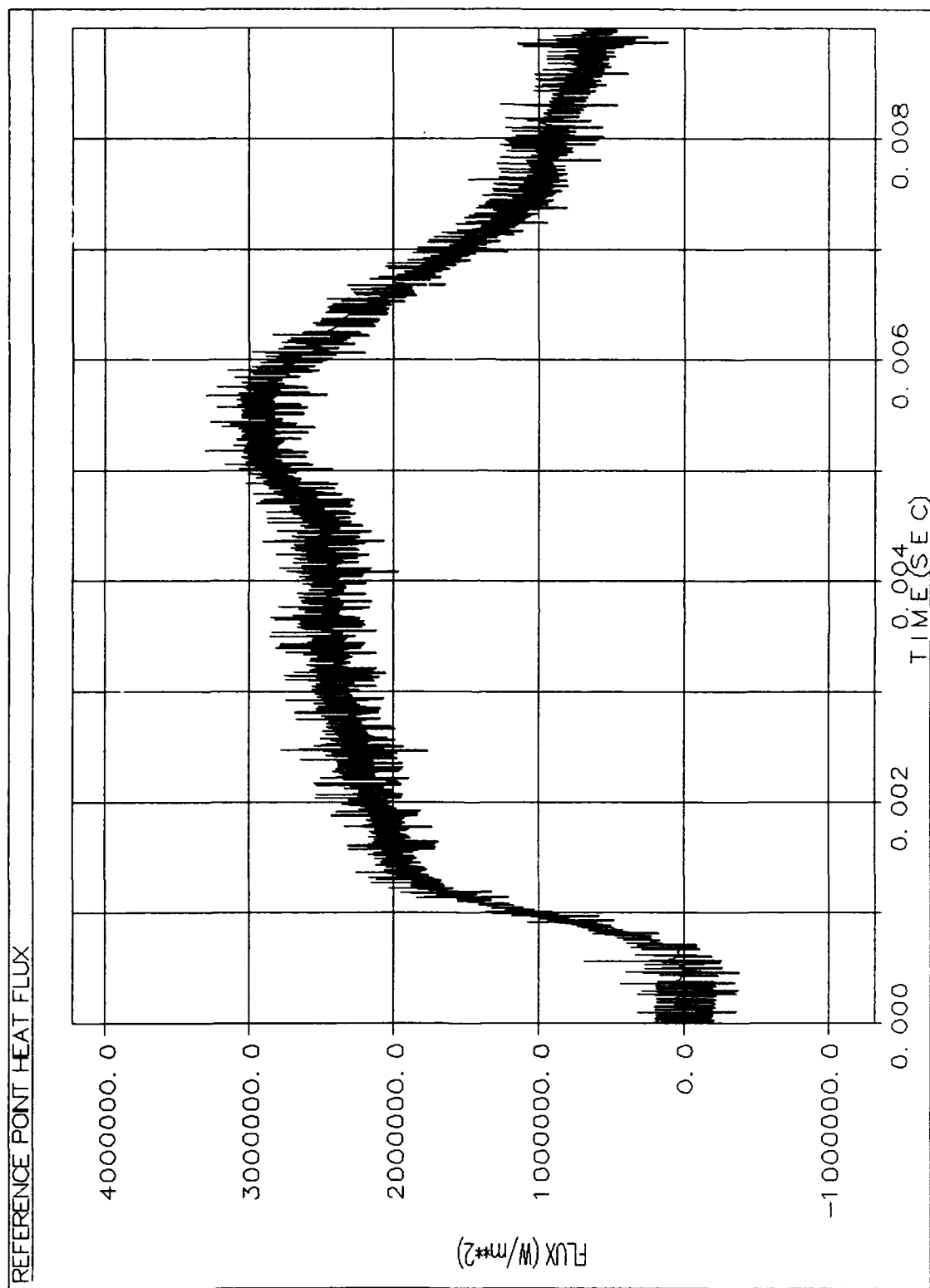


Figure D.8. Reference Point Heat Flux

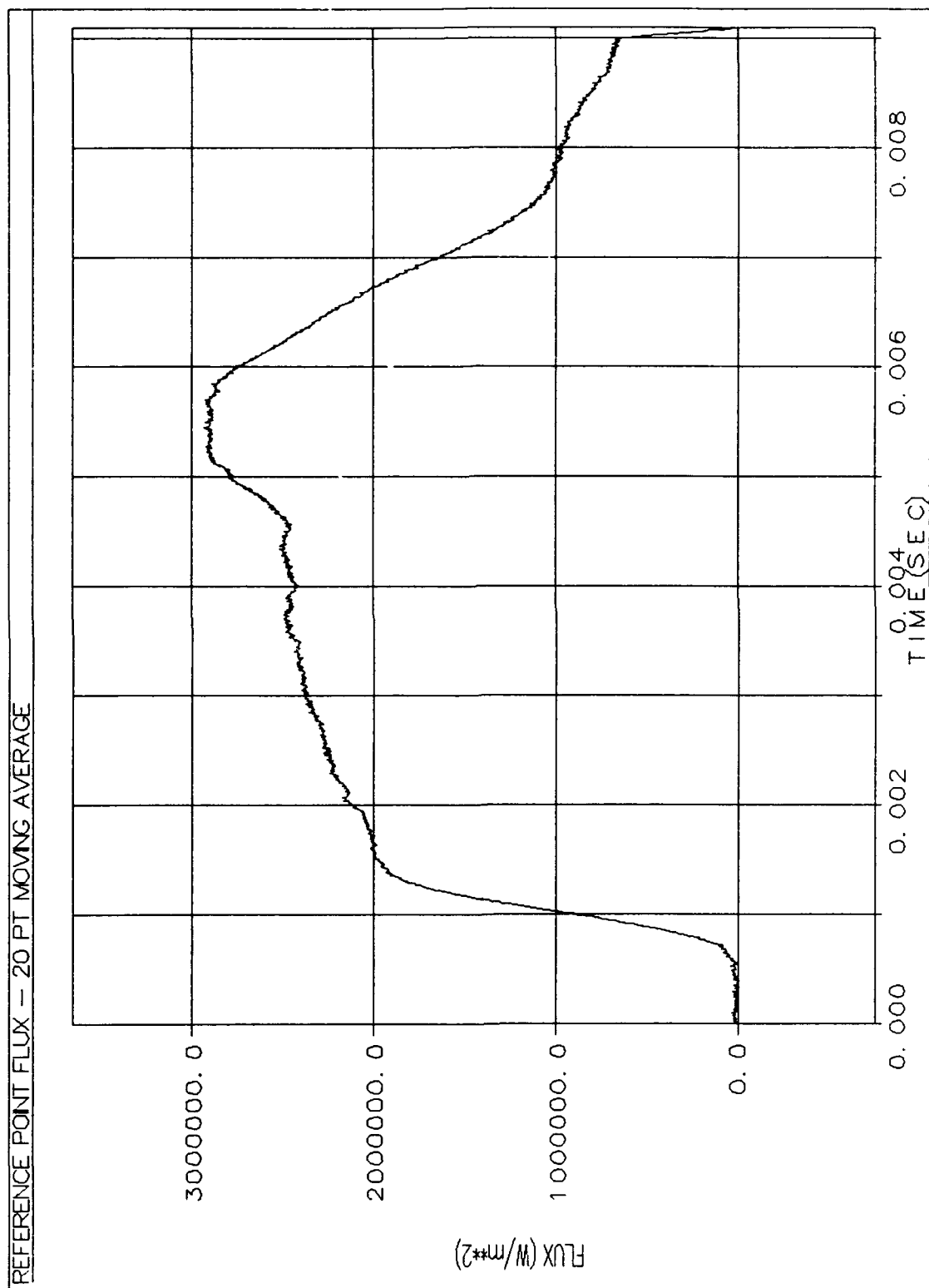


Figure D.9. Reference Point Heat Flux with 20 Point Moving Average

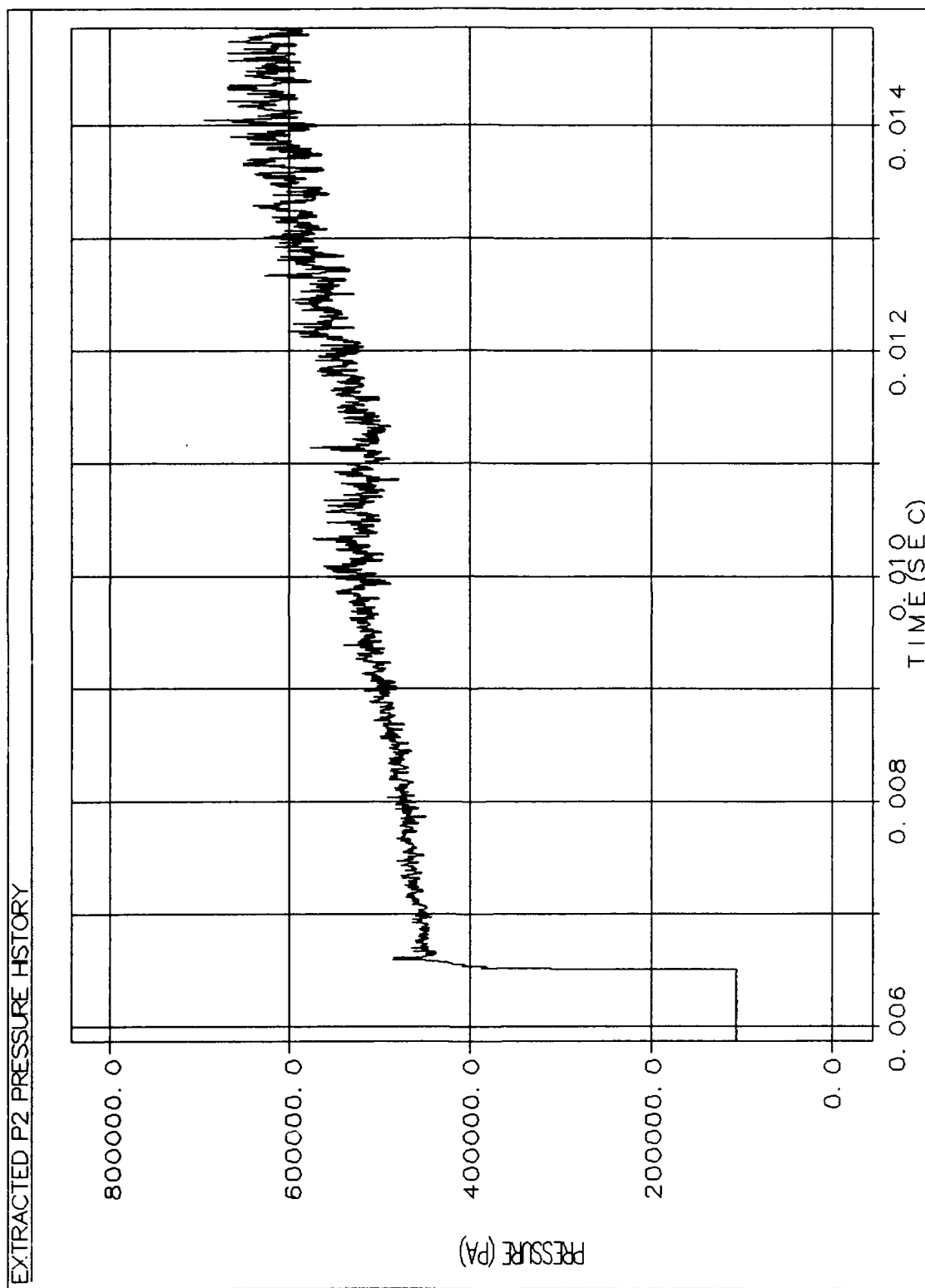


Figure D.10. Extracted P_2 Pressure History

PRESSURE TO TEMPERATURE CONVERSION WORKSHEET: **(P₂ TO T₂)**

This Worksheet calculates the proper conversion factor from P₂ to T₂ given a M₁ input.

$$\begin{array}{llll} m = 1 \cdot m & kg = 1 \cdot kg & sec = 1 \cdot sec & K = 1 \cdot temperature \\ N := kg \cdot \frac{m}{sec^2} & Pa := \frac{N}{m^2} & J := N \cdot m & kgmole = 1 \cdot coul \end{array}$$

Given:

$$\begin{array}{ll} P_1 := 99508 \cdot Pa \text{ (14.43 psi - 500' press alt)} & \gamma_1 := 1.4 \text{ Assume constant} \\ & \gamma_4 := 1.4 \text{ specific heats} \\ \rho_1 := 1.207 \cdot \frac{kg}{m^3} & \gamma_{air} := 1.4 \\ R_{bar} := 8314.3 \cdot \frac{J}{kgmole \cdot K} & molwt_{air} := 28.952 \cdot \frac{kg}{kgmole} \end{array}$$

Calculate gas constant for air:

$$R := \frac{R_{bar}}{molwt_{air}} \quad R = 287.17532 \cdot \frac{J}{kg \cdot K}$$

Calculate Speed of Sound:

$$\begin{array}{ll} a_1 := \sqrt{\frac{\gamma_1 \cdot P_1}{\rho_1}} & a_4 := 1 \cdot a_1 \end{array} \quad \begin{array}{l} \text{Note: } a_1 \text{ is obtained from ICAO tables} \\ \text{at 500 feet. Since we assume } T_1 \\ \text{equals } T_4, a_1 \text{ equals } a_4. \end{array}$$

$$a_1 = 339.73 \cdot \frac{m}{sec} \quad a_4 = 339.73 \cdot \frac{m}{sec}$$

Calculate Shock velocity from pressure gauge data:

$$TimeShock_A := .00204 \cdot sec \quad TimeShock_B := .0065 \cdot sec$$

$$W_s := \frac{1}{TimeShock_B - TimeShock_A} \cdot \left(\frac{10}{3.2808} \cdot m \right) \quad W_s = 683.4 \cdot \frac{m}{sec}$$

$$M_1 := \frac{W_s}{a_1} \quad M_1 = 2.01$$

$$Press_{ratio} := \frac{2 \cdot \gamma_1 \cdot M_1^2 - (\gamma_1 - 1)}{\gamma_1 + 1} \cdot \left[1 - \left(\frac{\gamma_4 - 1}{\gamma_1 + 1} \right) \cdot \frac{a_1}{a_4} \cdot \left(M_1 - \frac{1}{M_1} \right) \right]^{\frac{2 \cdot \gamma_4}{\gamma_4 - 1}}$$

$$Press_{ratio} = 34.9$$

Find T2 and P2 using shock equation from Gaylor:

$$T_1 := 294 \cdot K \quad 690 \cdot F$$

$$T_2 := T_1 \cdot \left[\frac{\left(\gamma_{\text{air}} \cdot M_1^2 - \frac{\gamma_{\text{air}} - 1}{2} \right) \cdot \left(\frac{\gamma_{\text{air}} - 1}{2} \cdot M_1^2 + 1 \right)}{\left(\frac{\gamma_{\text{air}} + 1}{2} \right)^2 \cdot M_1^2} \right]$$

$$T_2 = 498.9 \cdot K$$

$$P_2 := P_1 \cdot \left[\frac{2 \cdot \gamma_{\text{air}} \cdot M_1^2 - (\gamma_{\text{air}} - 1)}{\gamma_{\text{air}} + 1} \right]$$

$$P_2 = 4.53198 \cdot 10^5 \cdot \text{Pa}$$

Calculate density of region 2:

$$\rho_2 := \rho_1 \cdot \left[\frac{(\gamma_{\text{air}} + 1) \cdot M_1^2}{(\gamma_{\text{air}} - 1) \cdot M_1^2 + 2} \right]$$

$$\rho_2 = 3.2394 \cdot \frac{\text{kg}}{\text{m}^3}$$

Calculate M2 (Speed of contact surface):

$$\gamma_2 := \gamma_1$$

$$v_2 := \frac{2 \cdot a_1}{\gamma_1 + 1} \cdot \left(M_1 - \frac{1}{M_1} \right) \quad (\text{For a shock into a gas initially at rest})$$

$$u_2 := W_s - v_2 \quad v_2 = 428.8 \cdot \frac{\text{m}}{\text{sec}} \quad u_2 = 254.6 \cdot \frac{\text{m}}{\text{sec}}$$

$$a_2 := \sqrt{\frac{\gamma_2 \cdot P_2}{\rho_2}} \quad M_2 := \frac{u_2}{a_2} \quad M_{v2} := \frac{v_2}{a_2}$$

$$M_2 = 0.575$$

$$M_{v2} = 0.969$$

Using the perfect gas assumption, find conversion factor (T2 = P2/ρ2R)

ρ2R is the P2/T2 conversion factor. Divide P2 by ρ2R to obtain T2.

$$\rho_2 R := \rho_2 \cdot R \quad \rho_2 R = 930.27529 \cdot \frac{\text{J}}{\text{m}^3 \cdot \text{K}}$$

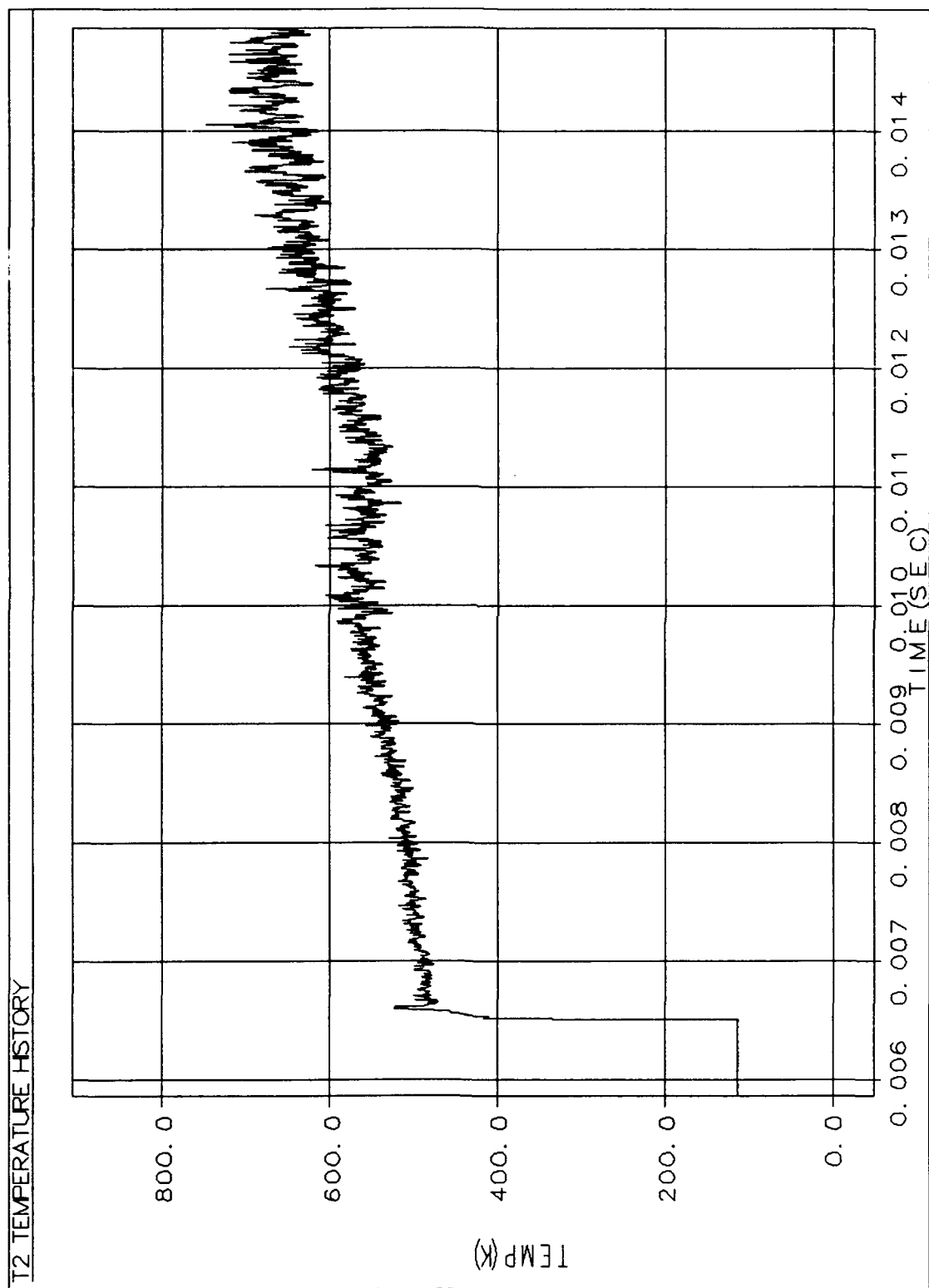


Figure D.11. Extracted T_2 Temperature History

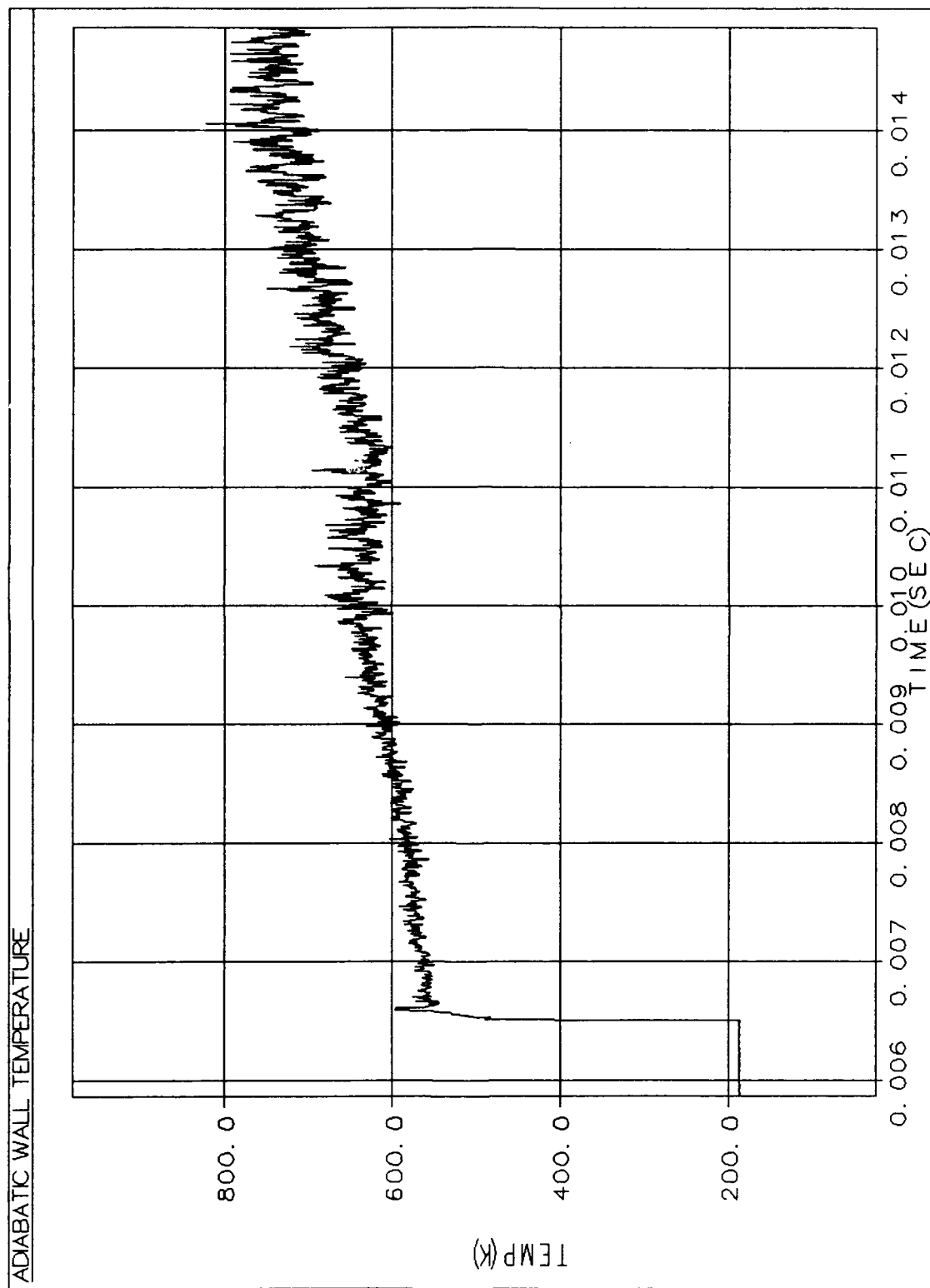


Figure D.12. Adiabatic Wall Temperatures

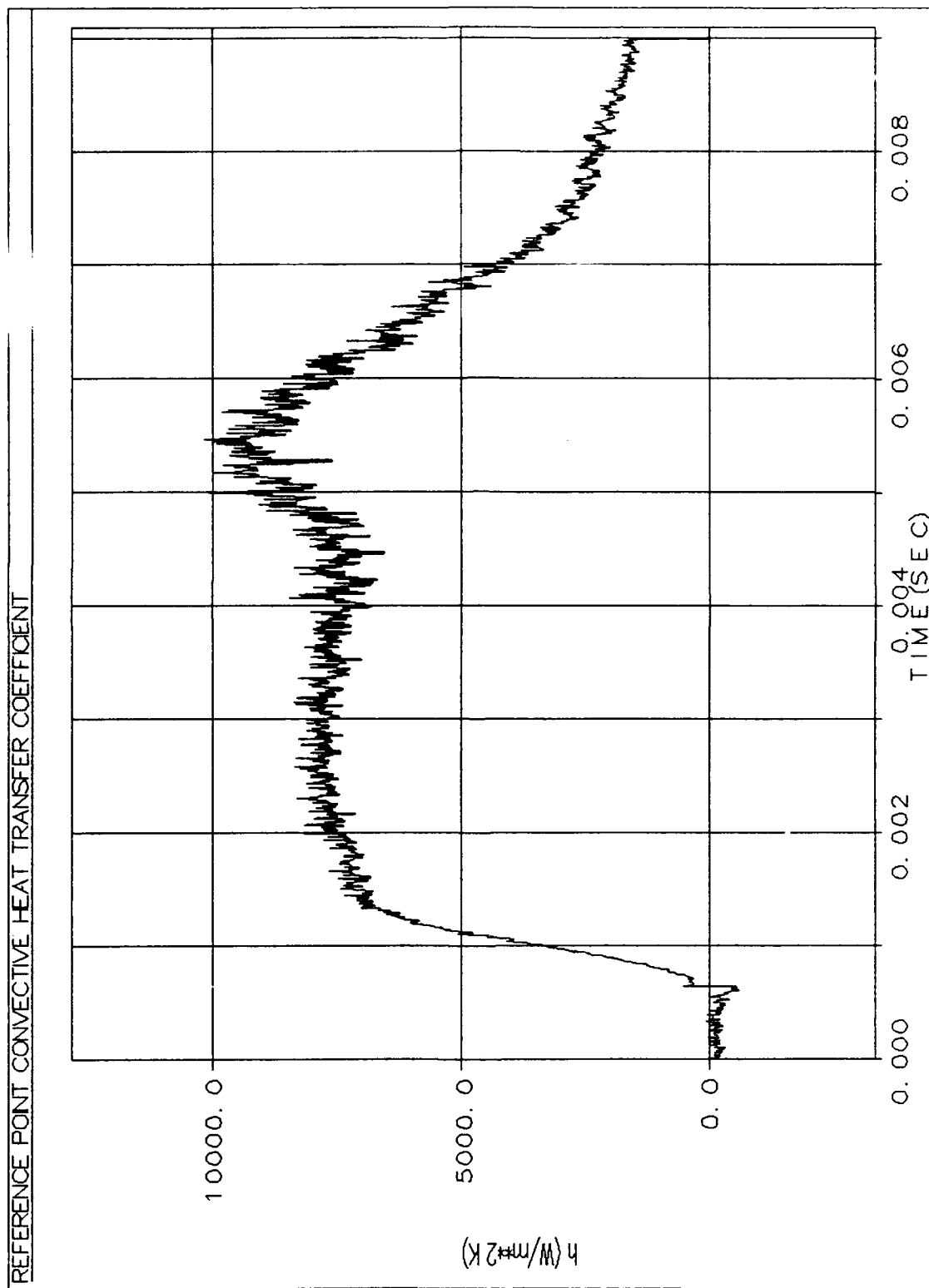


Figure D.13. Reference Point Convective Heat Transfer Coefficient

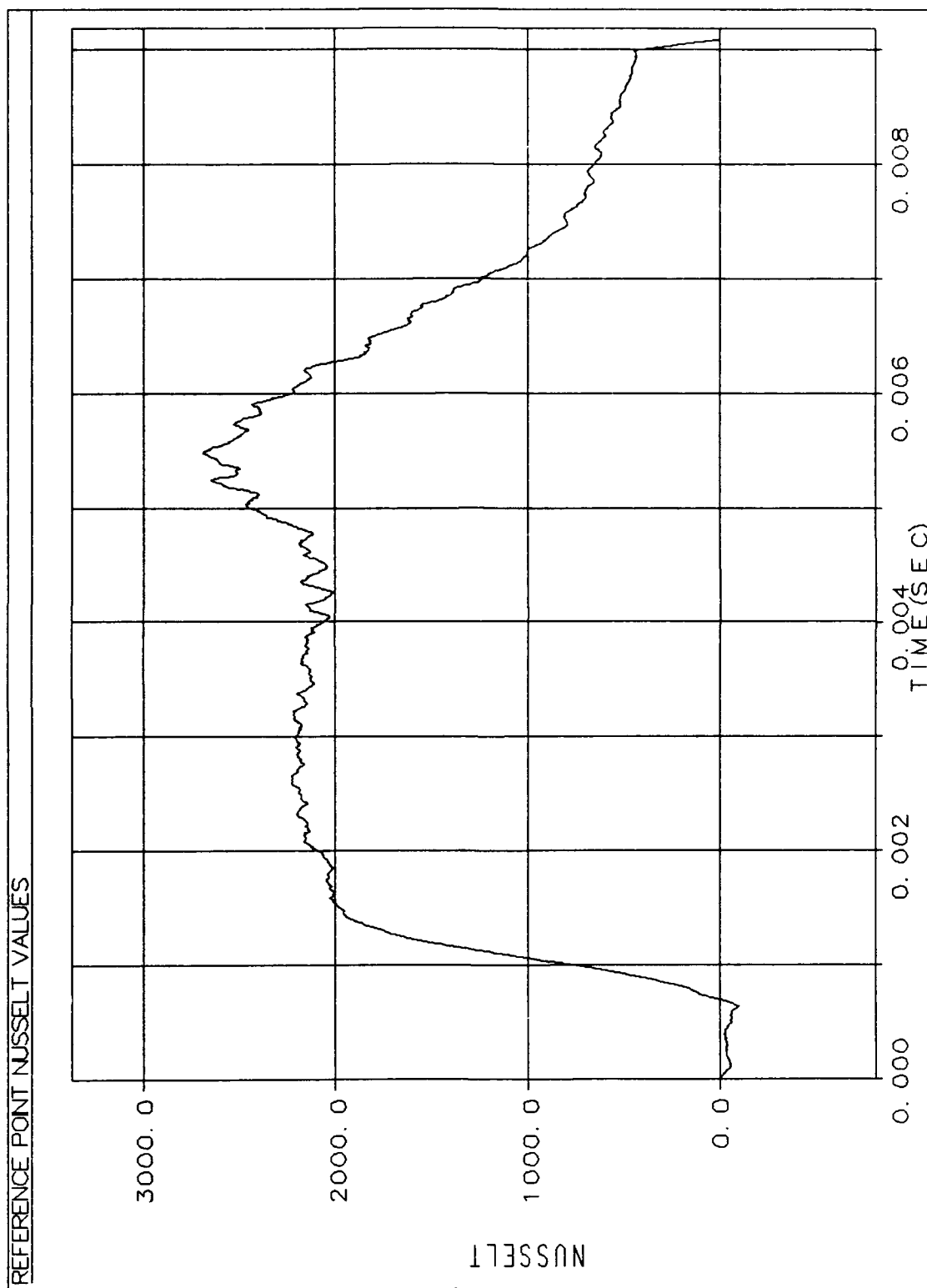


Figure D.14. Reference Point Nusselt Values

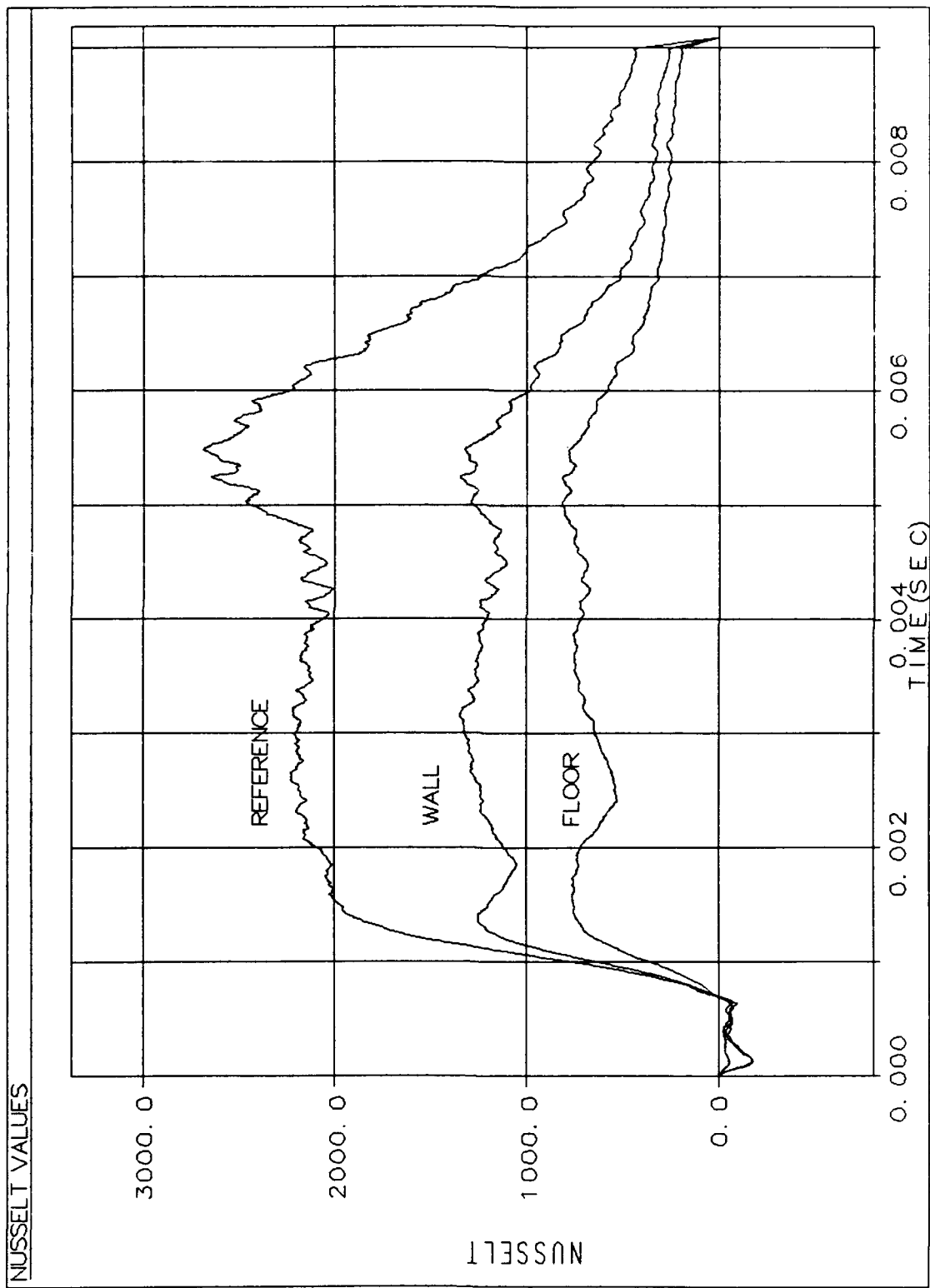


Figure D.15. Combined Nusselt Values

Appendix E: Shock Tube Wall Calculations/Flat Plate Calculations

Appendix E presents results from test run TGTA32171 and calculations used in obtaining heat transfer coefficient data from the shock tube wall position. This information was compared with an empirical model of turbulent flow over a flat plate (Incropera, 1985:367).

Measured pressure and temperature voltage data were converted to units of pressure and temperature using procedures detailed in Appendix D. Figure E.1 presents surface temperatures obtained from the wall of the shock tube (sensor location). The data was adjusted to simulate an instantaneous temperature jump as the shock wave passes over the sensor position (Figure E.2). This modification corrects for a lag in thermocouple response time in capturing instantaneous temperature rises. Surface temperature was converted to heat flux using the HEATFLX FORTRAN program listed in Appendix C. Figure E.3 presents heat flux information.

Using procedures described in Appendix D, Region 2 pressure history (P_2) was transformed into Region 2 temperatures (T_2). A Pressure to Temperature Conversion Worksheet was presented on page E.6, and the transformed T_2 information was shown in Figure E.4. The convective heat transfer coefficient (h) was calculated using Equation 2.9. Results are shown in Figure E.5.

Heat transfer coefficient data was compared with an empirical correlation (Equation 4.1) used to find the local heat transfer coefficient for a flat plate in turbulent flow. A Mathcad₆ Worksheet (page E.10) evaluates the correlation and

calculates the local heat transfer coefficient present at different locations along the flat plate. For experimental data, distance along the plate was represented by the transformation ($x = v_2 t_{sp}$). Both experimental data and empirical values are compared in Figure E.6.

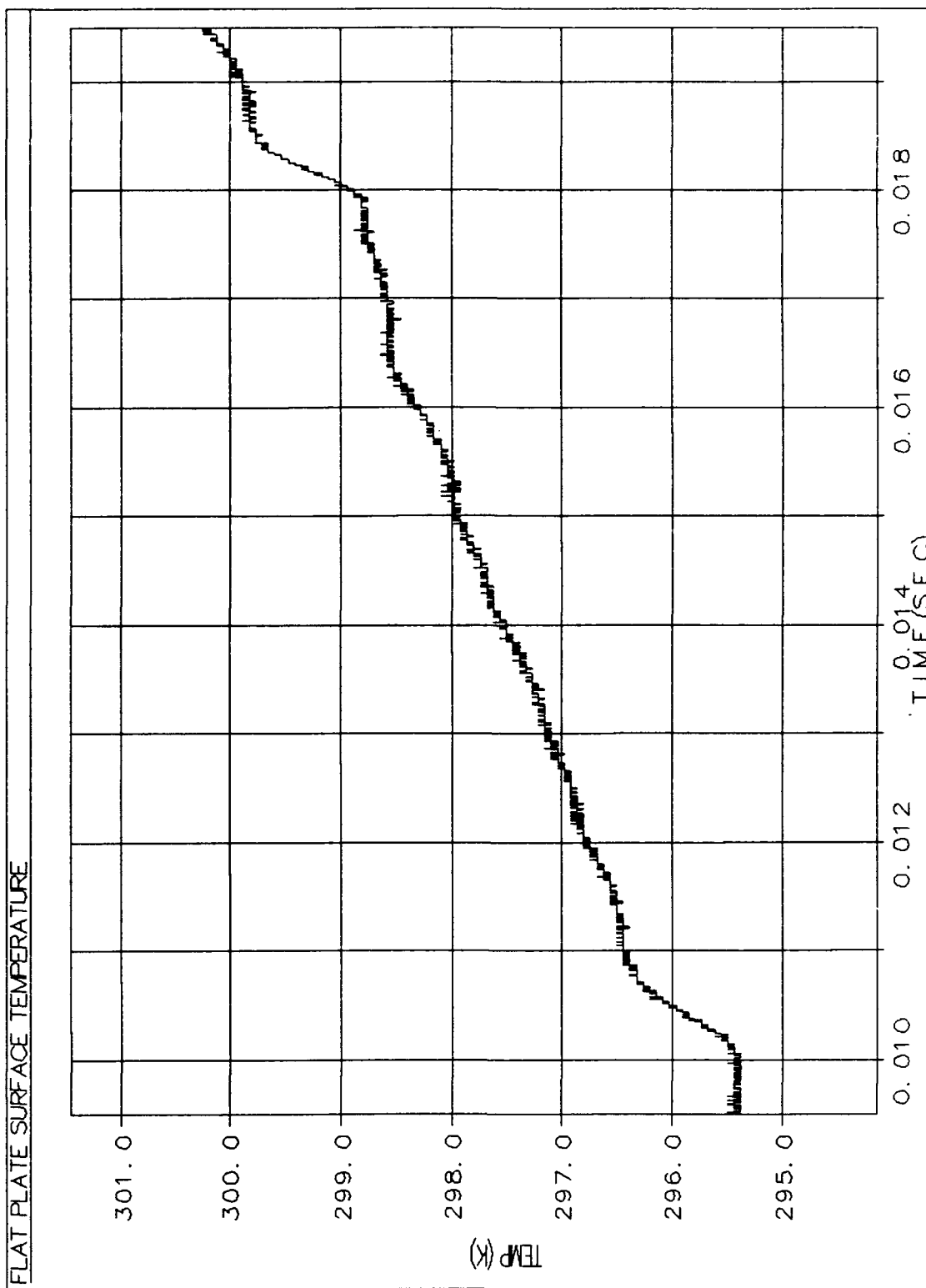


Figure E.1. Shock Tube Wall Surface Temperatures

SURFACE TEMPERATURE WITH INSTANTANEOUS JUMP

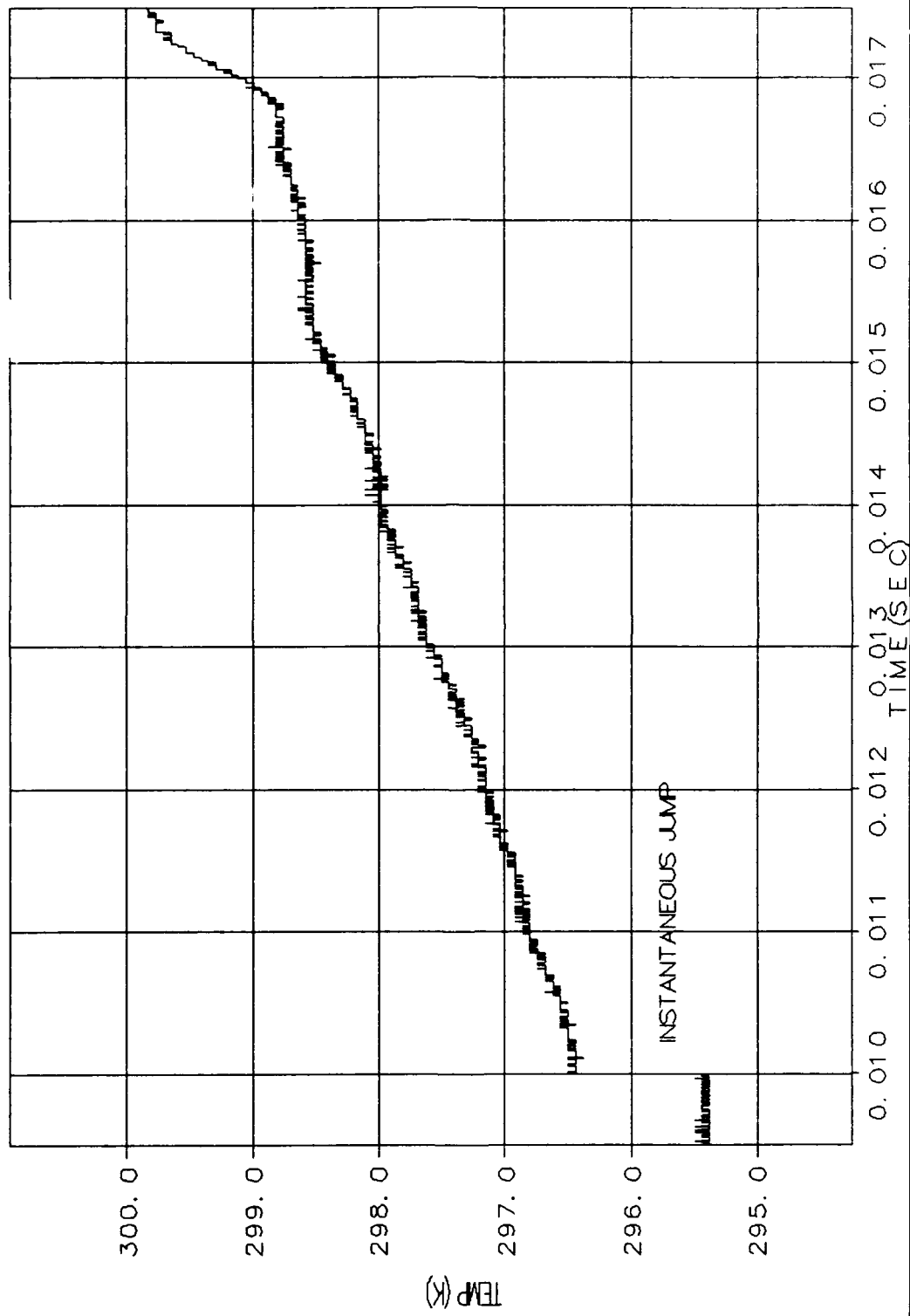


Figure E.2. Surface Temperatures with Instantaneous Jump

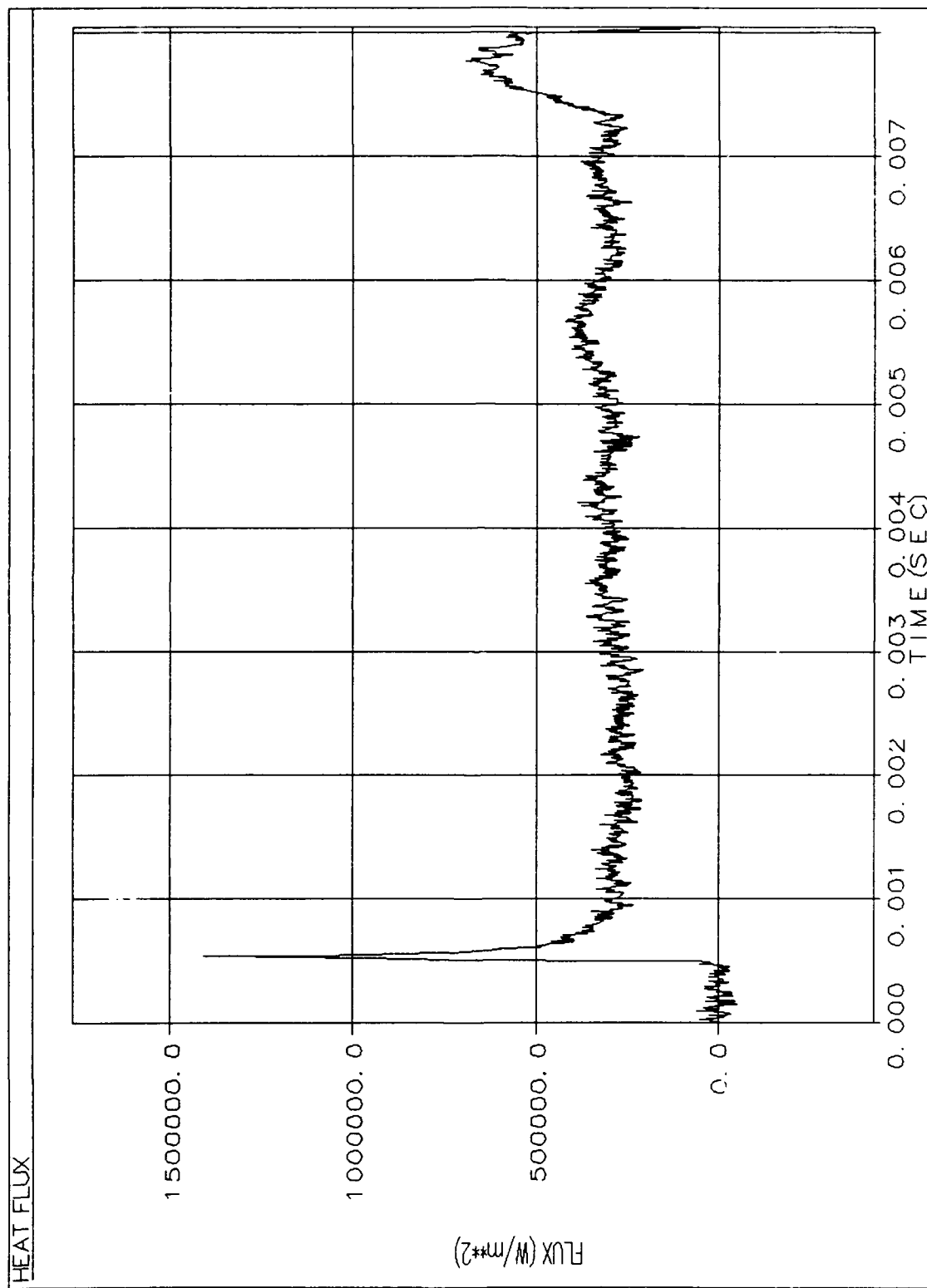


Figure E.3. Heat Flux, Shock Tube Wall

PRESSURE TO TEMPERATURE CONVERSION (P₂ TO T₂):

TEST RUN: TGTA32171

This Worksheet calculates the proper conversion factor from P₂ to T₂ given a M1 input.

$$m = 1 \cdot m \quad kg = 1 \cdot kg \quad sec = 1 \cdot sec \quad K = 1 \cdot temperature$$

$$N := kg \cdot \frac{m}{sec^2} \quad Pa := \frac{N}{m^2} \quad J := N \cdot m \quad kgmole = 1 \cdot coul$$

Given:

$$P_1 := 101325 \cdot Pa$$

$$\gamma_1 := 1.4 \quad \text{Assume constant}$$

$$\gamma_4 := 1.4 \quad \text{specific heats}$$

$$\rho_1 := 1.225 \cdot \frac{kg}{m^3}$$

$$\gamma_{air} := 1.4$$

$$R_{bar} := 8314.3 \cdot \frac{J}{kgmole \cdot K}$$

$$molwt_{air} := 28.952 \cdot \frac{kg}{kgmole}$$

Calculate gas constant for air:

$$R = \frac{R_{bar}}{molwt_{air}} \quad R = 287.17532 \cdot \frac{J}{kg \cdot K}$$

Calculate Speed of Sound:

$$a_1 := \sqrt{\frac{\gamma_1 \cdot P_1}{\rho_1}} \quad a_4 := 1 \cdot a_1$$

$$a_1 = 340.29 \cdot \frac{m}{sec} \quad a_4 = 340.29 \cdot \frac{m}{sec}$$

Calculate Shock velocity from pressure gauge data:

$$TimeShock_A := .00204 \cdot sec \quad TimeShock_B := .00718 \cdot sec$$

$$W_s := \frac{1}{TimeShock_B - TimeShock_A} \cdot \left(\frac{10}{3.2808} \cdot m \right) \quad W_s = 593 \cdot \frac{m}{sec}$$

$$M_1 := \frac{W_s}{a_1} \quad M_1 = 1.74$$

Calculate density of region 2:

$$\rho_2 := \rho_1 \cdot \left[\frac{(\gamma_{air} + 1) \cdot M_1^2}{(\gamma_{air} - 1) \cdot M_1^2 + 2} \right] \quad \rho_2 = 2.77724 \cdot \frac{kg}{m^3}$$

Using the perfect gas assumption, find conversion factor ($T_2 = P_2/\rho_2 R$)

$\rho_2 R$ is the P_2/T_2 conversion factor. Divide P_2 by $\rho_2 R$ to obtain T_2 .

$$\rho_2 R = \rho_2 \cdot R \qquad \rho_2 R = 797.6 \cdot \frac{\text{J}}{\text{m}^3 \cdot \text{K}}$$

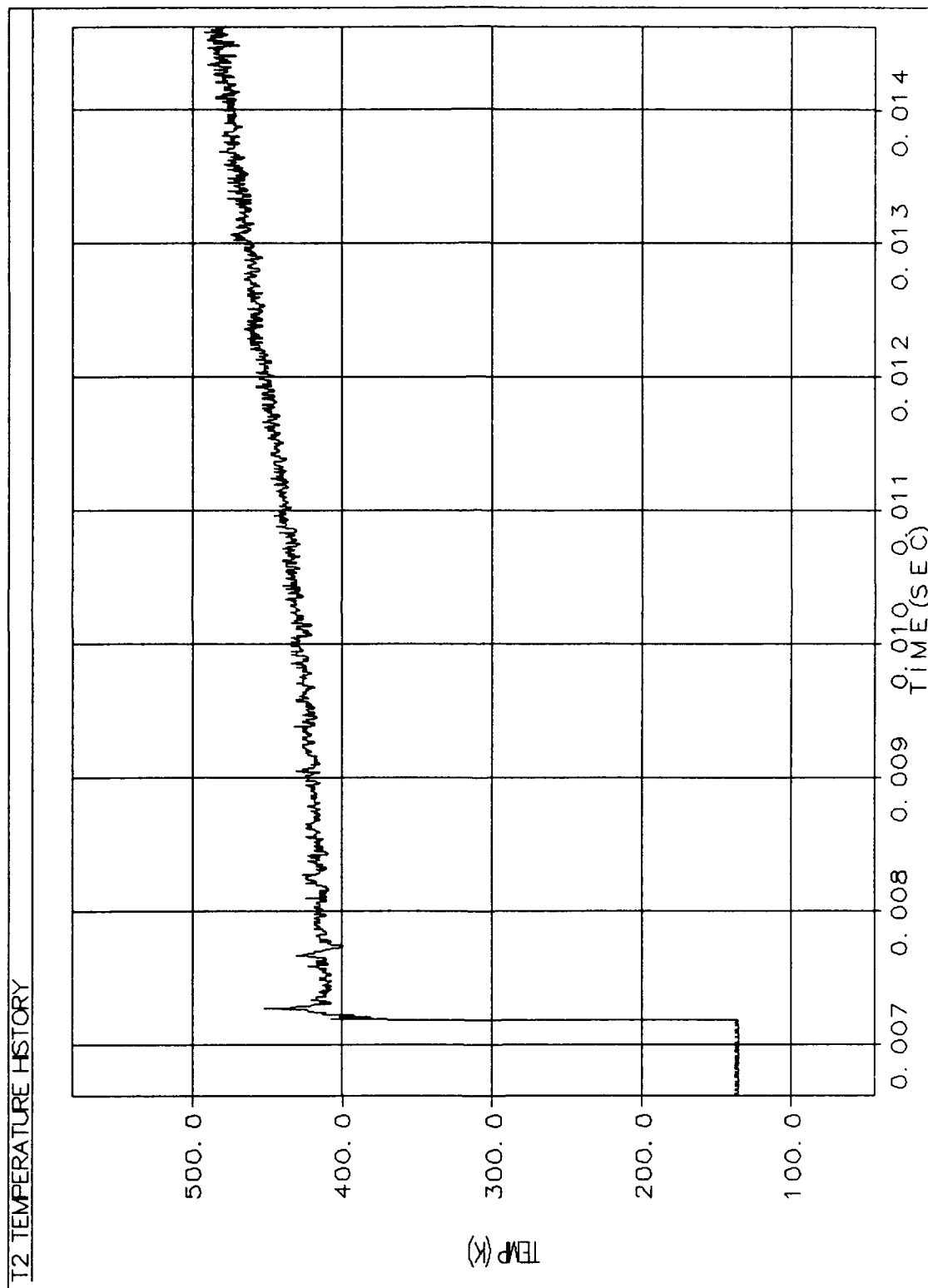


Figure E.4. Extracted T_2 Temperature History

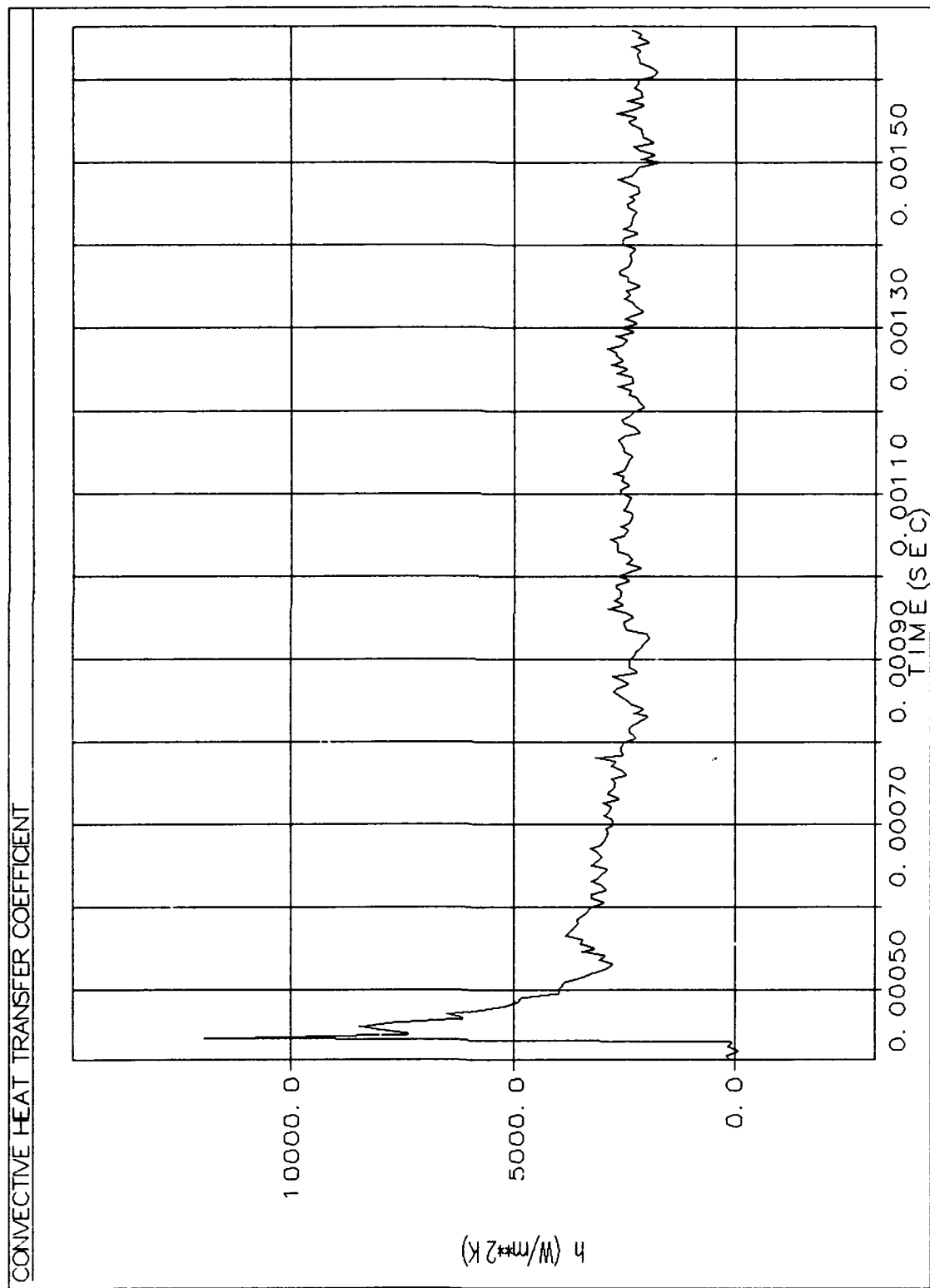


Figure E.5. Convective Heat Transfer Coefficient

EMPIRICAL MODEL WORKSHEET

Calculate heat transfer coefficient for a flat plate in turbulent flow:

Use correlation in "Incropera" p. 367. Local Nusselt number for turbulent flow.

$$T_{\text{inf}} := 450 \quad \rho_2 := 2.777 \quad \text{Re}_{\text{cr}} := 5 \cdot 10^5$$

$$T_s := 298 \quad u_{\text{inf}} := 593$$

$$T_{\text{film}} := \frac{T_{\text{inf}} + T_s}{2} \quad T_{\text{film}} = 374$$

From table A.4 in Incropera:

$$\mu = 220 \cdot 10^{-7}$$

$$k = 32 \cdot 10^{-3}$$

$$\text{Pr} := .695$$

Find x critical (transition from laminar to turbulent):

$$x_{\text{cr}} := \frac{\text{Re}_{\text{cr}} \cdot \mu}{\rho_2 \cdot u_{\text{inf}}} \quad x_{\text{cr}} = 0.00668 \quad \text{Flow on flat plate in turbulent}$$

Use flat plate turbulent correlation. page 367.

$$i := 1, 2, \dots, 50$$

$$x(i) := i \cdot 0.01$$

$$\text{Re}_{x(i)} := \frac{\rho_2 \cdot u_{\text{inf}} x(i)}{\mu}$$

$$\text{Nu}_{x(i)} := .0296 \cdot \text{Re}_{x(i)}^{\frac{4}{5}} \cdot \text{Pr}^{\frac{1}{3}}$$

$$h_{x(i)} := \frac{\text{Nu}_{x(i)} \cdot k}{x(i)}$$

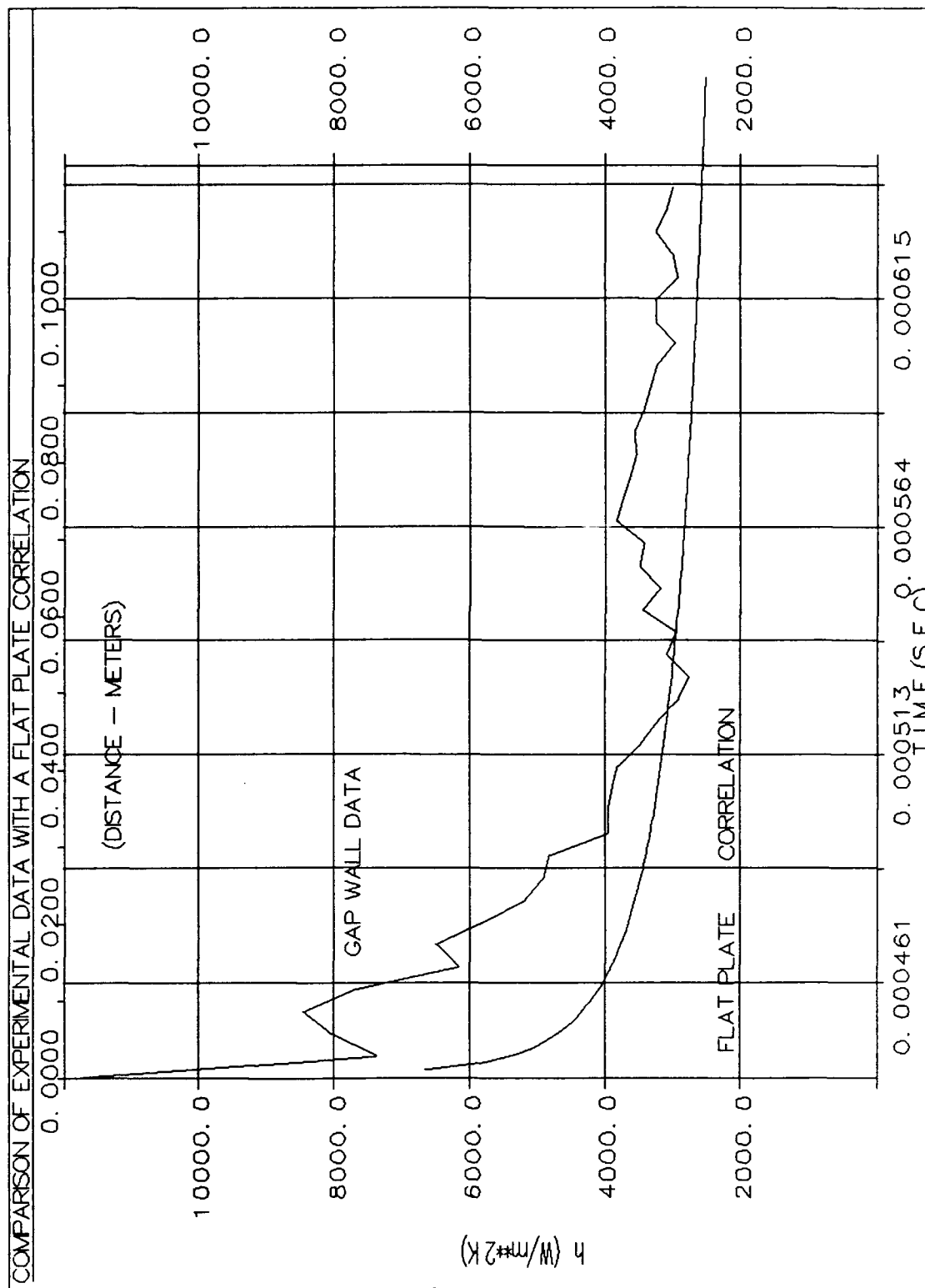


Figure E.6. Comparison of Experimental Data with a Flat Plate Correlation

Appendix F: Test Run Data

Data summary worksheets for measured and calculated parameters, used in the presentation of data, are included in Table F.1. This table is followed by tabulated heat transfer values (**Nu**) for each test run (Table F.2). Results include averaged Nusselt values from each sensor location. Finally, Nusselt graphs for each test run are presented in Figures F.1 thru F.49. Nusselt values are plotted versus time with sensor locations overlaid to display different heating rates between locations.

Data files and graphs use the following nomenclature to distinguish individual test runs:

GP(#)MH(#)TH(#)(LTR)

GP(#) - Gap width number. 1 = 5 mm, 2 = 2.5 mm, 3 = 7 mm.

MH(#) - Incident shock Mach number. 1 = 1.8 Mach, 2 = 2.0 Mach, 3 = 2.3 Mach.

TH(#) - Theta angle (θ) setting. 1 = 0°, 2 = 30°, 3 = 60°, 4 = 90°, 5 = 120°.

(LTR) - Sequence number if repeat runs were performed. A = 1st, B = 2nd, X,Y = additional runs.

Example: **GP1MH3TH3B** is the data file for a test run using a gap width of 5 mm, shock Mach number of 2.3 Mach, and theta setting of 60°. This is the second test run accomplished.

Table F.1

Measured and Calculated Parameters
Used in Reducing Data

Filename	Shock Mach (M_1)	v_2 (m/s)	$\rho_2 R$ (J/kgK)	T_{ref} (K)	k ($\times 10^{-3}$) (W/mK)
GP1MH4TH1A	1.81	356	810	380	32.28
GP1MH1TH1A	2.06	446	955	435	36.25
GP1MH1TH1B	2.06	446	955	435	36.25
GP1MH1TH1X	2.06	446	955	440	36.60
GP1MH1TH1Y	1.92	396	882	425	35.55
GP1MH3TH1A	2.47	585	1143	475	39.00
GP1MH1TH2A	2.06	446	955	440	36.60
GP1MH2TH2A	1.80	352	818	440	36.60
GP1MH3TH2A	2.25	511	1046	500	40.70
GP1MH1TH3A	2.00	424	924	420	35.20
GP1MH2TH3A	2.01	428	929	425	35.55
GP1MH3TH3A	2.20	494	1023	475	39.00
GP1MH1TH4A	2.03	435	940	425	35.55
GP1MH1TH4B	1.99	421	919	425	35.55
GP1MH2TH4A	1.95	407	898	415	34.85
GP1MH3TH4A	2.25	511	1047	500	40.70
GP1MH1TH5A	2.04	439	945	430	35.90
GP1MH2TH5A	1.81	356	823	450	37.30
GP1MH3TH5A	2.29	525	1065	485	39.68
GP2MH1TH1A	1.66	299	739	365	31.14
GP2MH2TH1A	1.79	349	812	450	33.8
GP2MH3TH1A	2.30	528	1069	490	40.02
GP2MH1TH2A	1.73	326	779	380	32.28

Table F.1

(Continued)

Filename	Shock Mach (M_1)	v_2 (m/s)	$\rho_2 R$ (J/kgK)	T_{ref} (K)	k ($\times 10^{-3}$) (W/mK)
GP2MH2TH2A	2.00	425	924	430	35.90
GP2MH3TH2A	2.25	511	1046	475	39.00
GP2MH1TH3A	1.76	337	796	360	30.76
GP2MH2TH3A	2.04	439	945	435	36.25
GP2MH3TH3A	2.28	521	1060	500	40.70
GP2MH1TH4A	1.77	341	801	390	33.04
GP2MH2TH4A	1.93	400	888	415	34.85
GP2MH3TH4A	2.25	511	1046	470	38.66
GP2MH1TH5A	1.66	299	739	355	30.38
GP2MH2TH5A	1.97	414	909	425	35.55
GP2MH3TH5A	2.11	463	980	490	40.02
GP3MH1TH1A	1.75	334	790	385	32.66
GP3MH2TH1A	2.00	425	924	430	35.90
GP3MH3TH1A	2.26	515	1051	490	40.02
GP3MH1TH2A	1.75	334	790	380	32.28
GP3MH2TH2A	2.04	439	945	430	35.90
GP3MH3TH2A	2.29	525	1065	480	39.43
GP3MH1TH3A	1.71	319	767	370	31.52
GP3MH2TH3A	2.01	428	929	435	36.25
GP3MH3TH3A	2.24	507	1042	500	40.70
GP3MH1TH4A	1.70	315	762	375	31.9
GP3MH2TH4A	2.07	449	960	440	36.60
GP3MH3TH4A	2.22	501	1032	480	39.34

Table F.1

(Continued)

Filename	Shock Mach (M_1)	v_2 (m/s)	$\rho_2 R$ (J/kgK)	T_{ref} (K)	k ($\times 10^{-3}$) (W/mK)
GP3MH1TH5A	1.76	337	796	385	32.66
GP3MH2TH5A	2.01	428	929	435	36.25
GP3MH3TH5B	2.22	501	1032	465	38.35

Table F.2

Test Run Averaged Nusselt Values

Filename	Reference (Nu)	Gap Wall (Nu)	Gap Floor (Nu)
GP1MH4TH1A	900	1000	1200
GP1MH1TH1A	1500	1200	1500
GP1MH1TH1B	1500	1150	1450
GP1MH1TH1X	1250	900	1800
GP1MH1TH1Y	950	750	1300
GP1MH3TH1A	3000	1900	2600
GP1MH1TH2A	1600	1500	2400
GP1MH2TH2A	850	1100	1400
GP1MH3TH2A	2600	2200	3500
GP1MH1TH3A	1200	1500	600
GP1MH2TH3A	1000	1600	500
GP1MH3TH3A	2200	2050	1500
GP1MH1TH4A	na	1700	100
GP1MH1TH4B	750	1500	350
GP1MH2TH4A	600	1400	150
GP1MH3TH4A	1900	2000	400
GP1MH1TH5A	250	900	400
GP1MH2TH5A	200	700	300
GP1MH3TH5A	450	1250	500
GP2MH1TH1A	800	850	1000
GP2MH2TH1A	1200	900	1250
GP2MH3TH1A	2500	1500	2600
GP2MH1TH2A	800	1200	1000

Table F.2

(Continued)

Filename	Reference (Nu)	Gap Wall (Nu)	Gap Floor (Nu)
GP2MH2TH2A	1450	1600	1950
GP2MH3TH2A	1850	2600	3150
GP2MH1TH3A	650	1350	1100
GP2MH2TH3A	1400	1900	2250
GP2MH3TH3A	2900	2650	3450
GP2MH1TH4A	300	125	100
GP2MH2TH4A	500	150	100
GP2MH3TH4A	1150	200	400
GP2MH1TH5A	400	300	475
GP2MH2TH5A	350	230	280
GP2MH3TH5A	380	260	200
GP3MH1TH1A	1130	1220	1070
GP3MH2TH1A	1500	1600	1300
GP3MH3TH1A	2700	2400	2000
GP3MH1TH2A	1500	1050	900
GP3MH2TH2A	2000	1400	1100
GP3MH3TH2A	3200	2100	1500
GP3MH1TH3A	1500	900	575
GP3MH2TH3A	2100	1250	725
GP3MH3TH3A	2950	2000	1100
GP3MH1TH4A	675	625	200
GP3MH2TH4A	1150	1000	250
GP3MH3TH4A	1400	1700	400

Table F.2

(Continued)

Filename	Reference (Nu)	Gap Wall (Nu)	Gap Floor (Nu)
GP3MH1TH5A	250	400	400
GP3MH2TH5A	300	530	400
GP3MH3TH5B	360	750	480

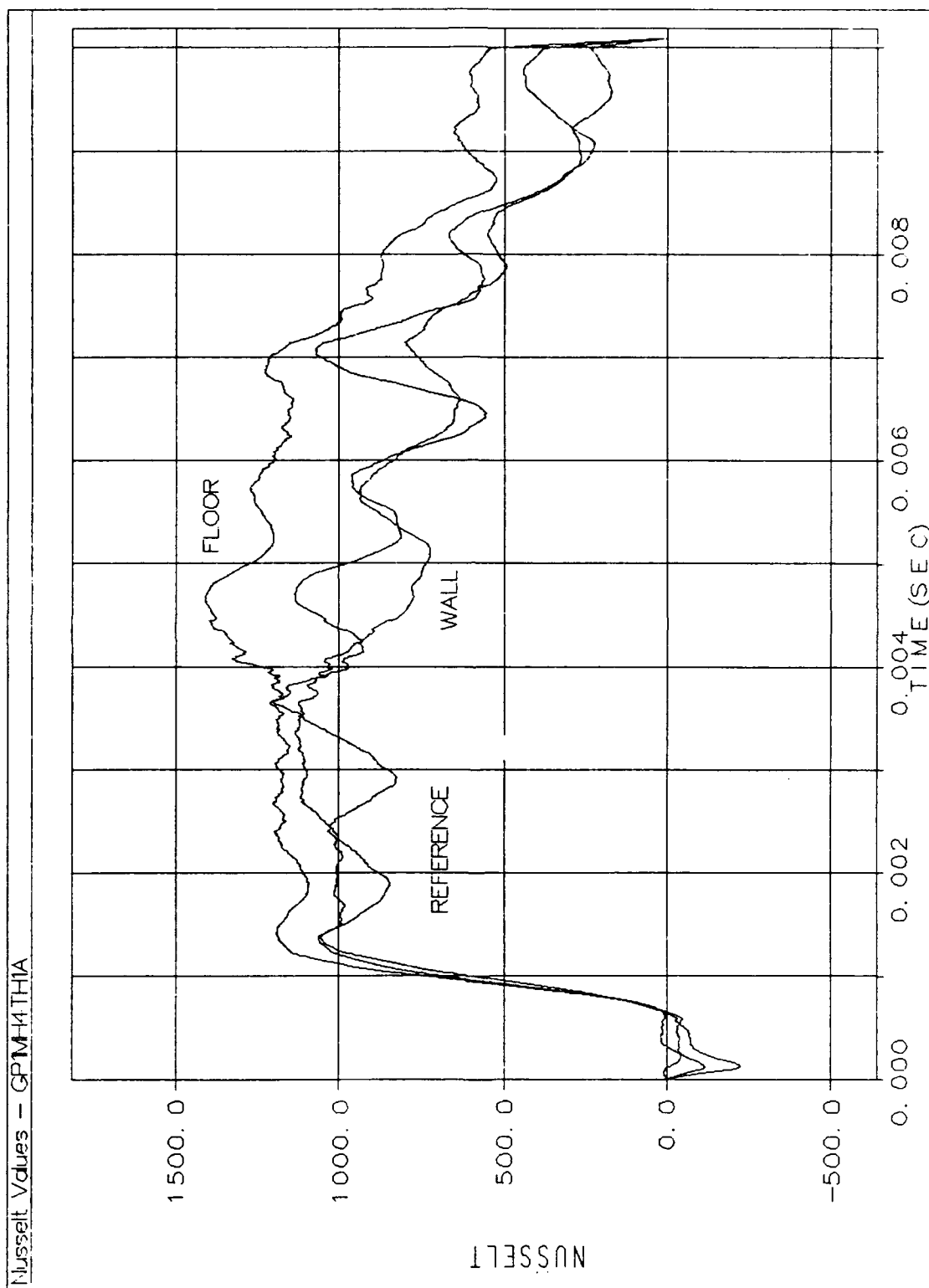


Figure F.1. Test Run Nusselt Values

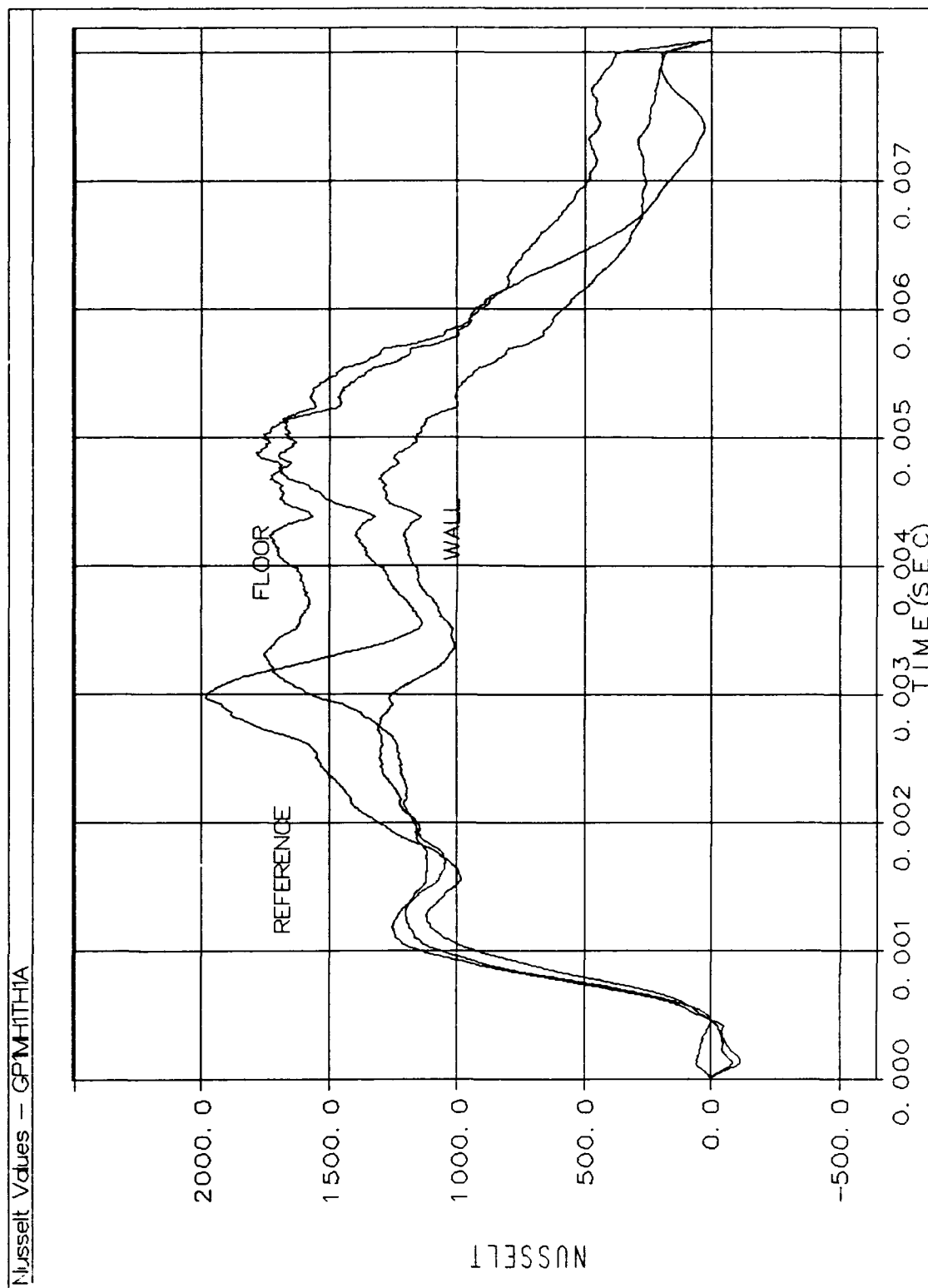


Figure F.2. Test Run Nusselt Values

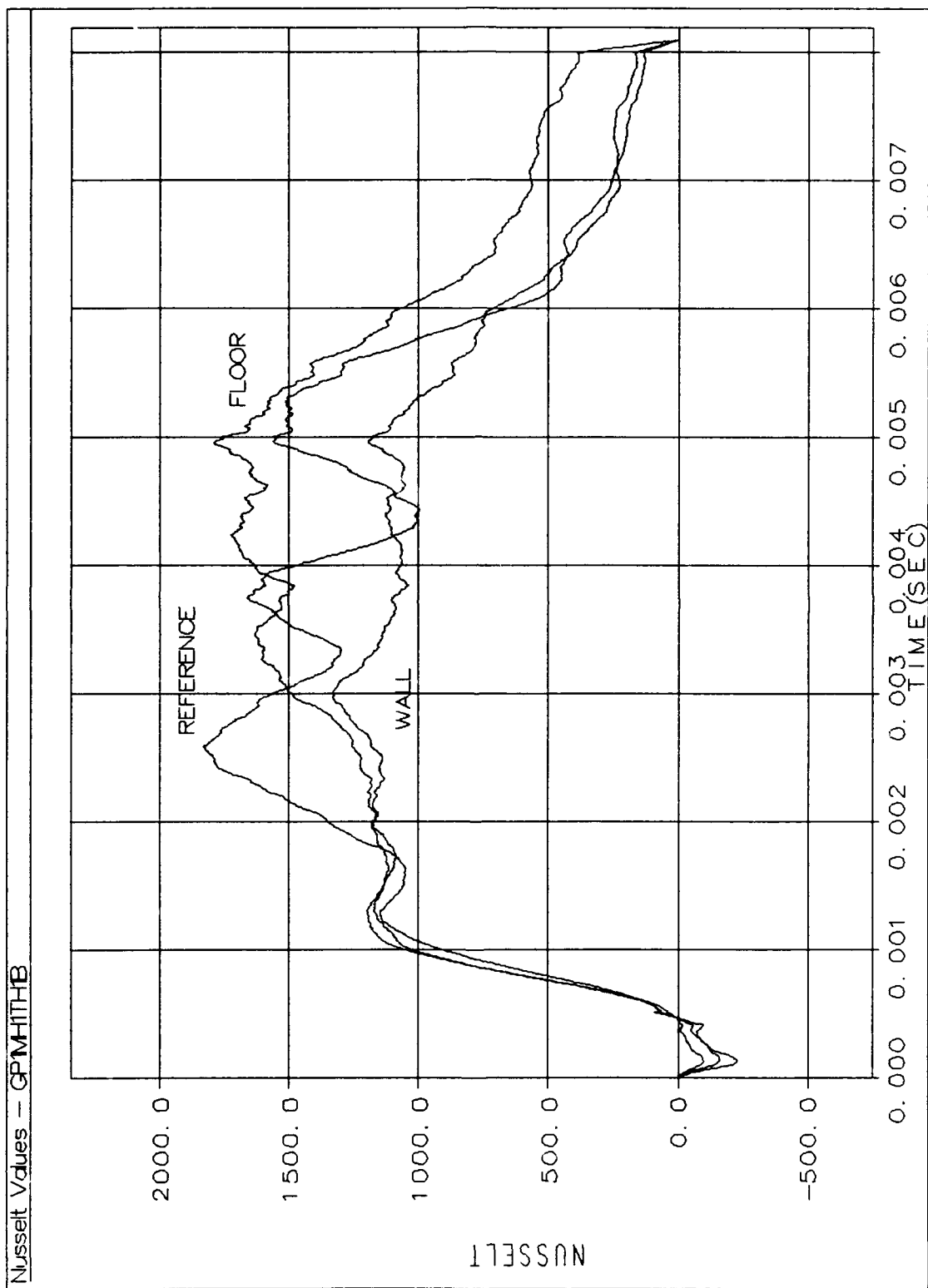


Figure F.3. Test Run Nusselt Values

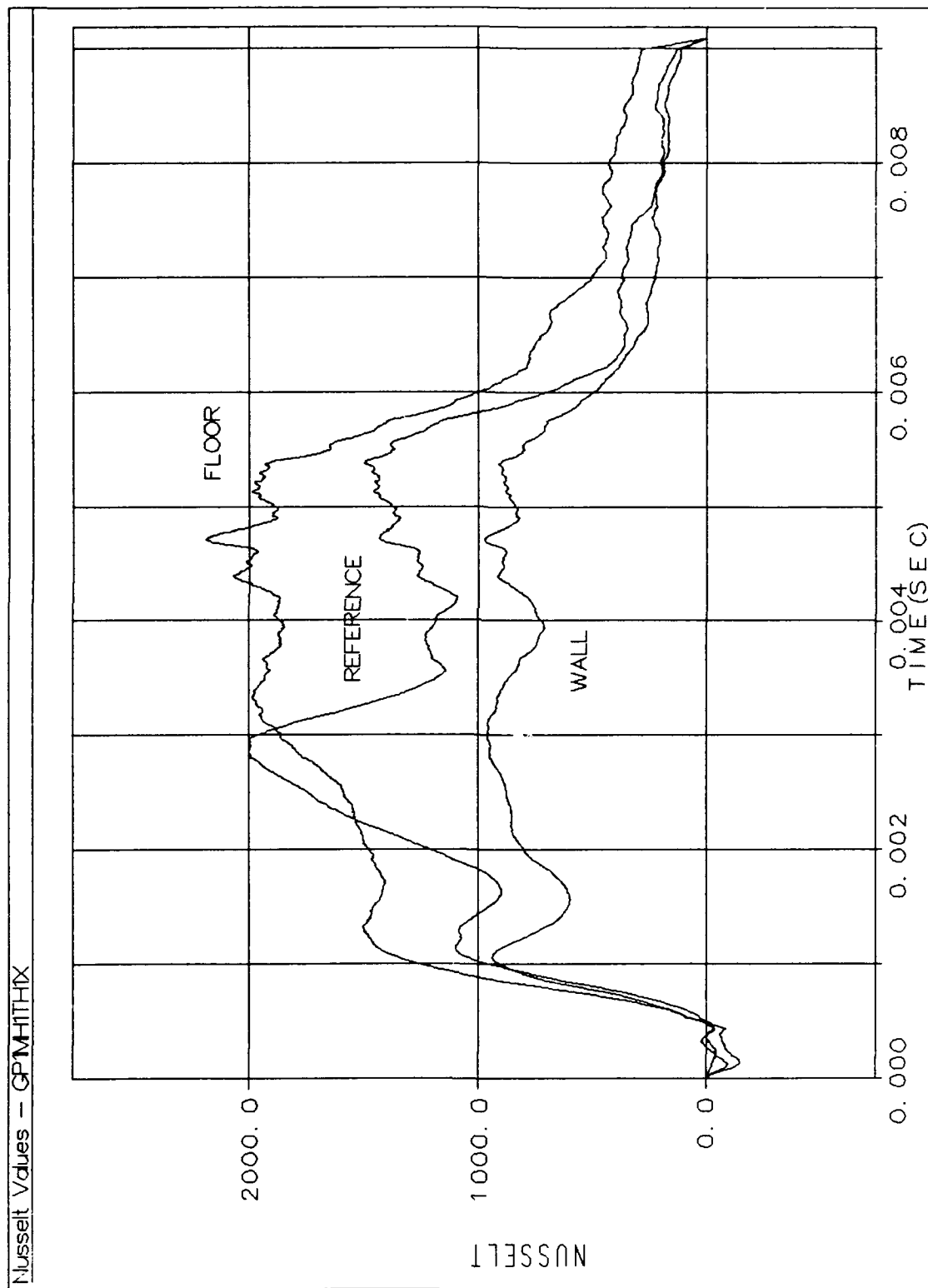


Figure F.4. Test Run Nusselt Values

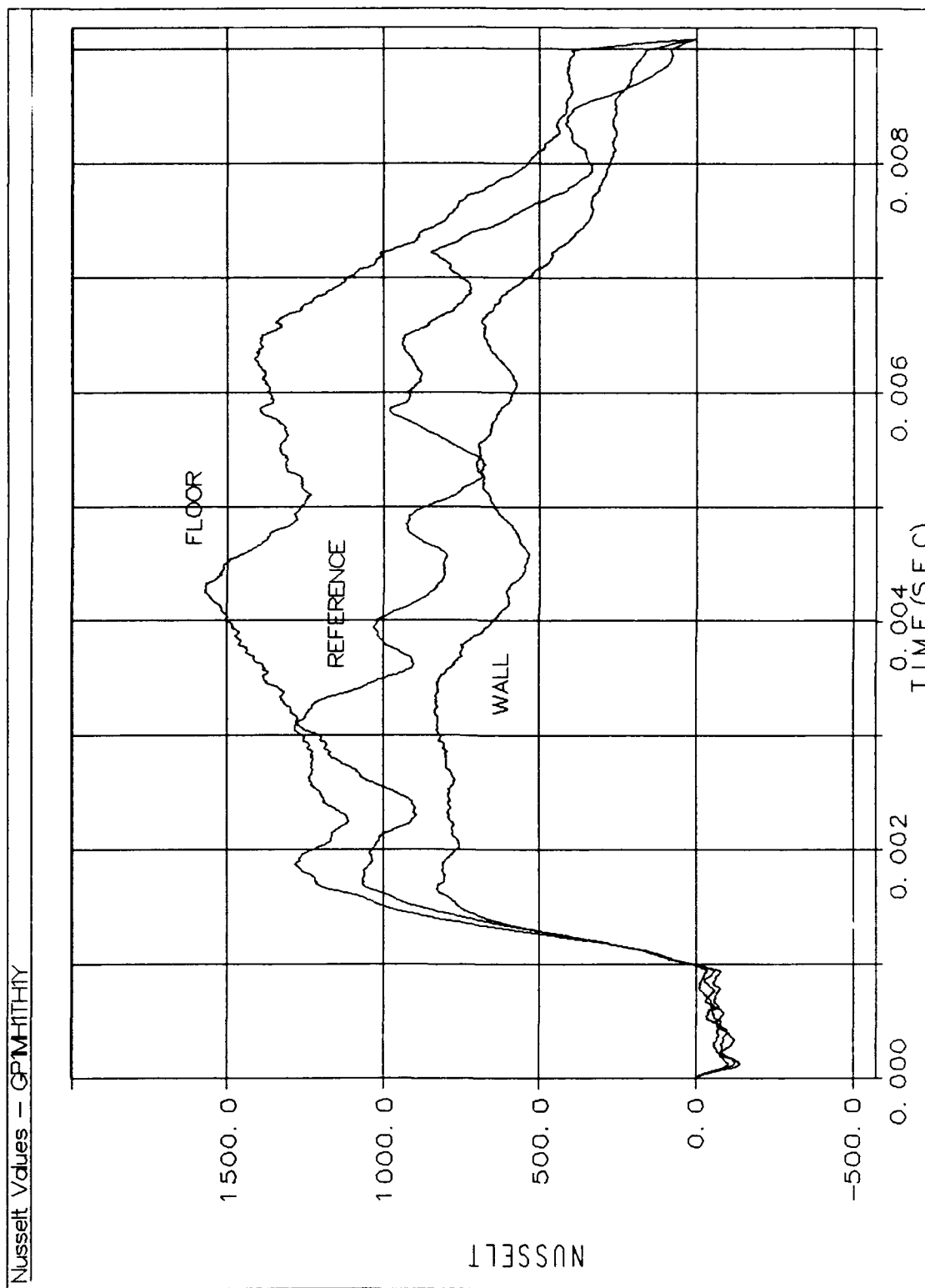


Figure F.5. Test Run Nusselt Values

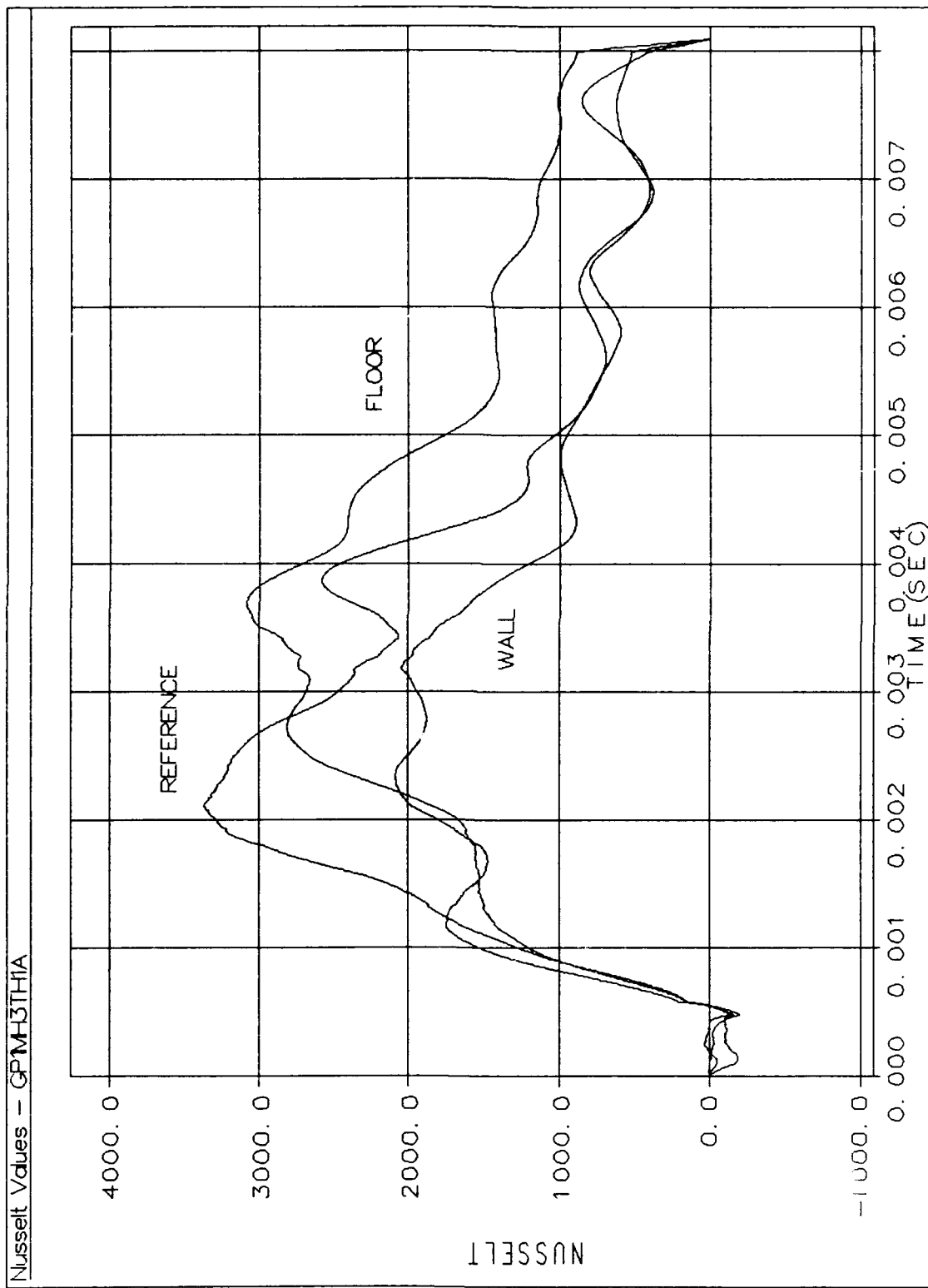


Figure F.6. Test Run Nusselt Values

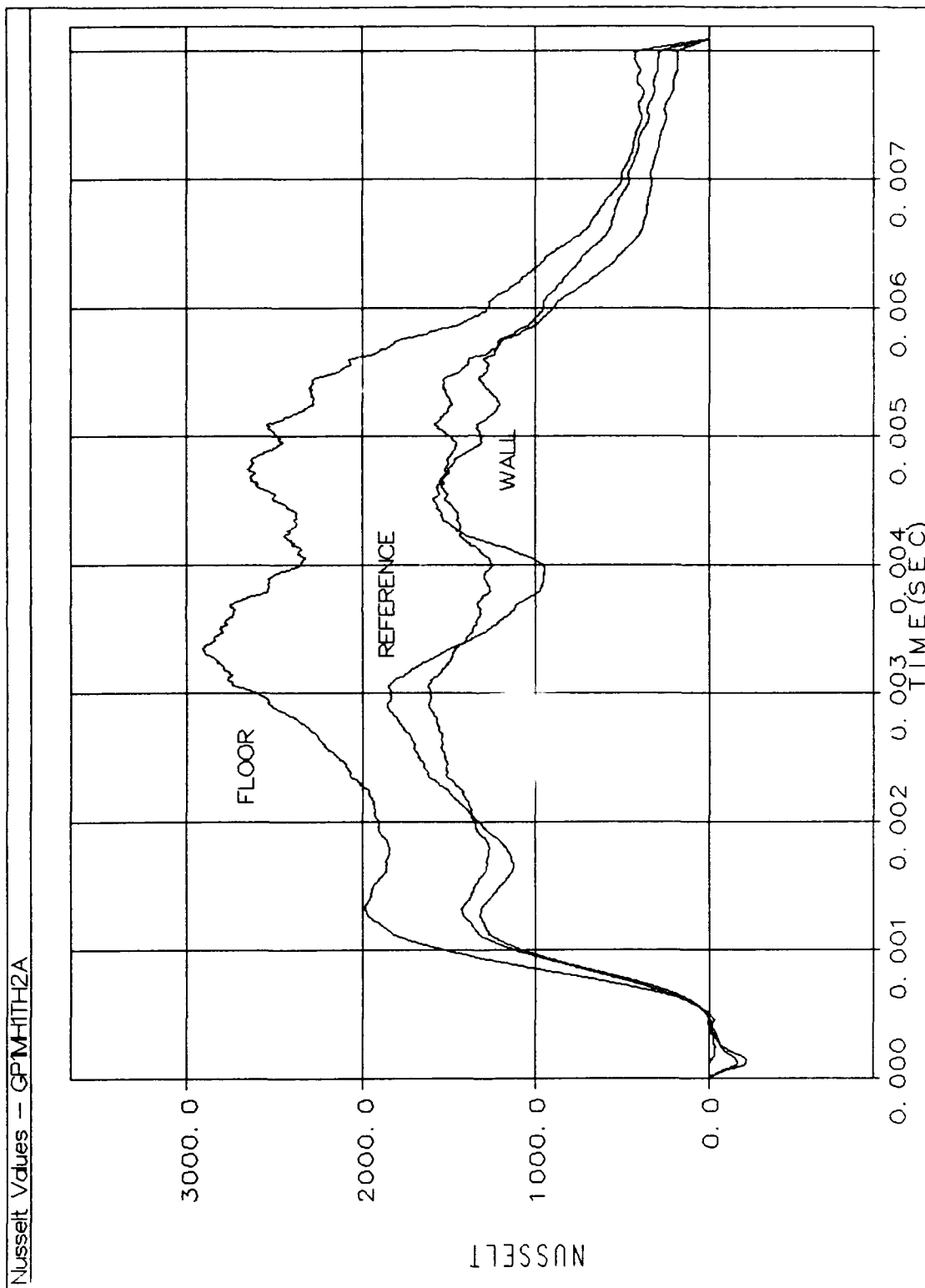


Figure F.7. Test Run Nusselt Values

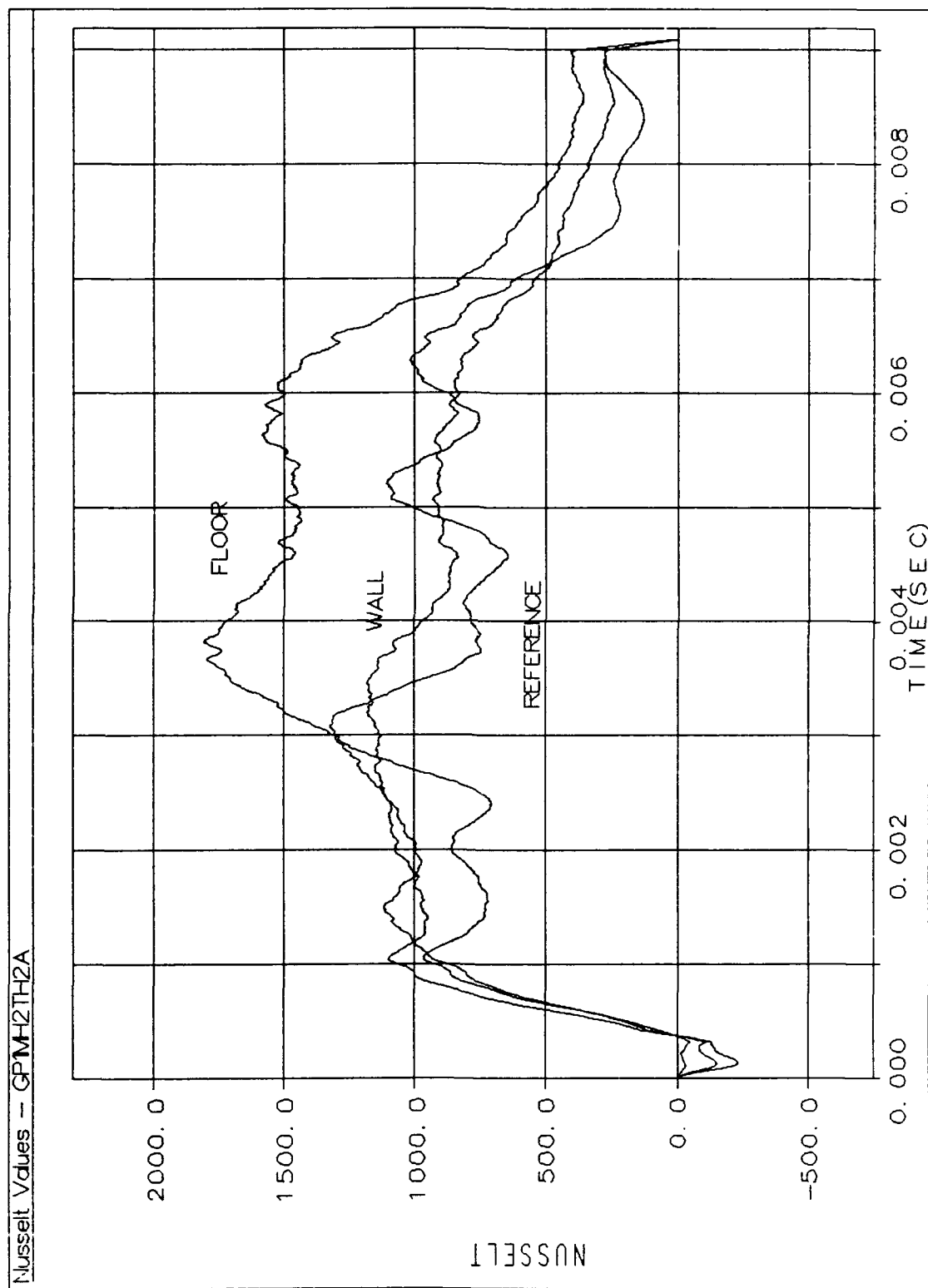


Figure F.8. Test Run Nusselt Values

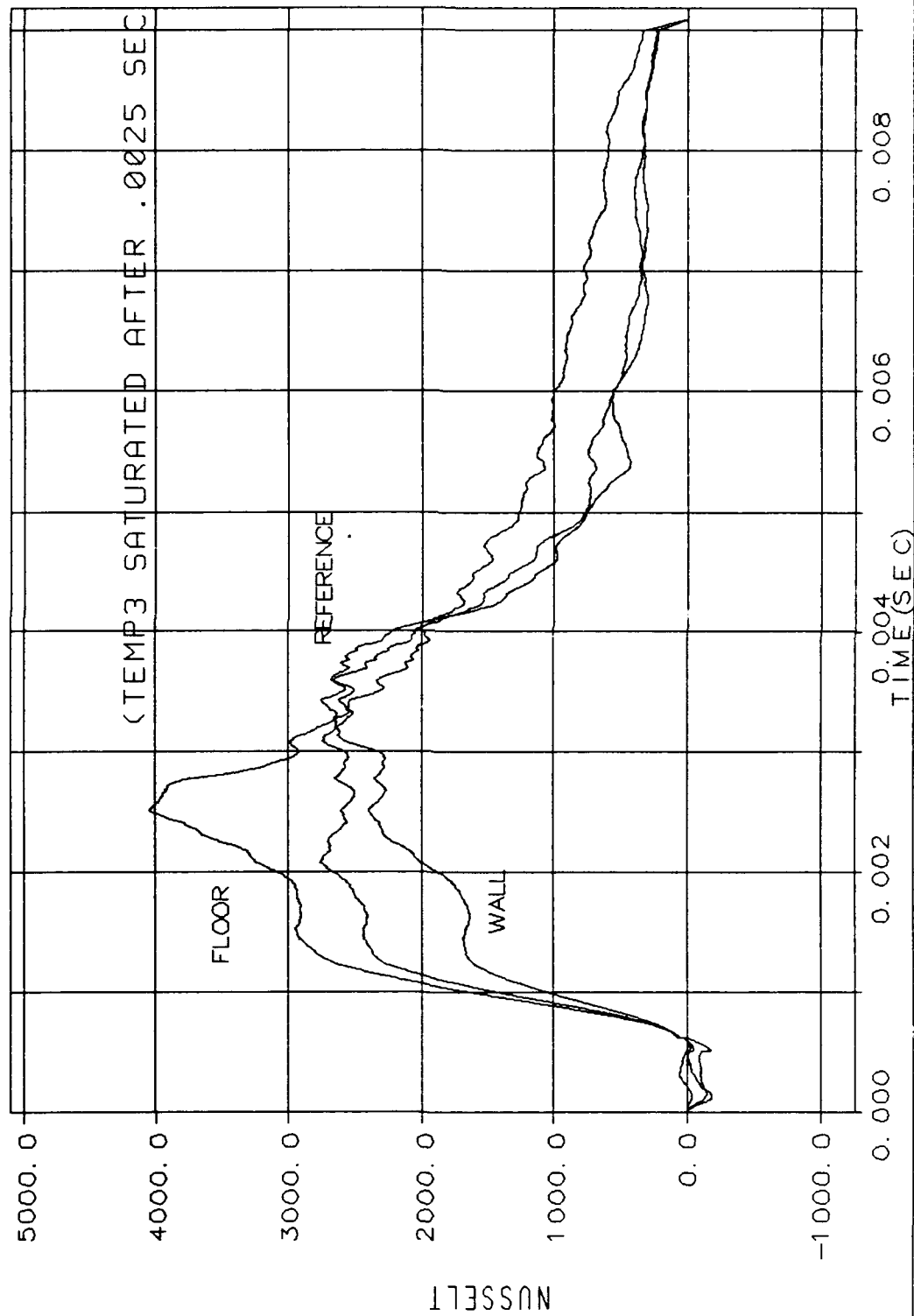


Figure F.9. Test Run Nusselt Values

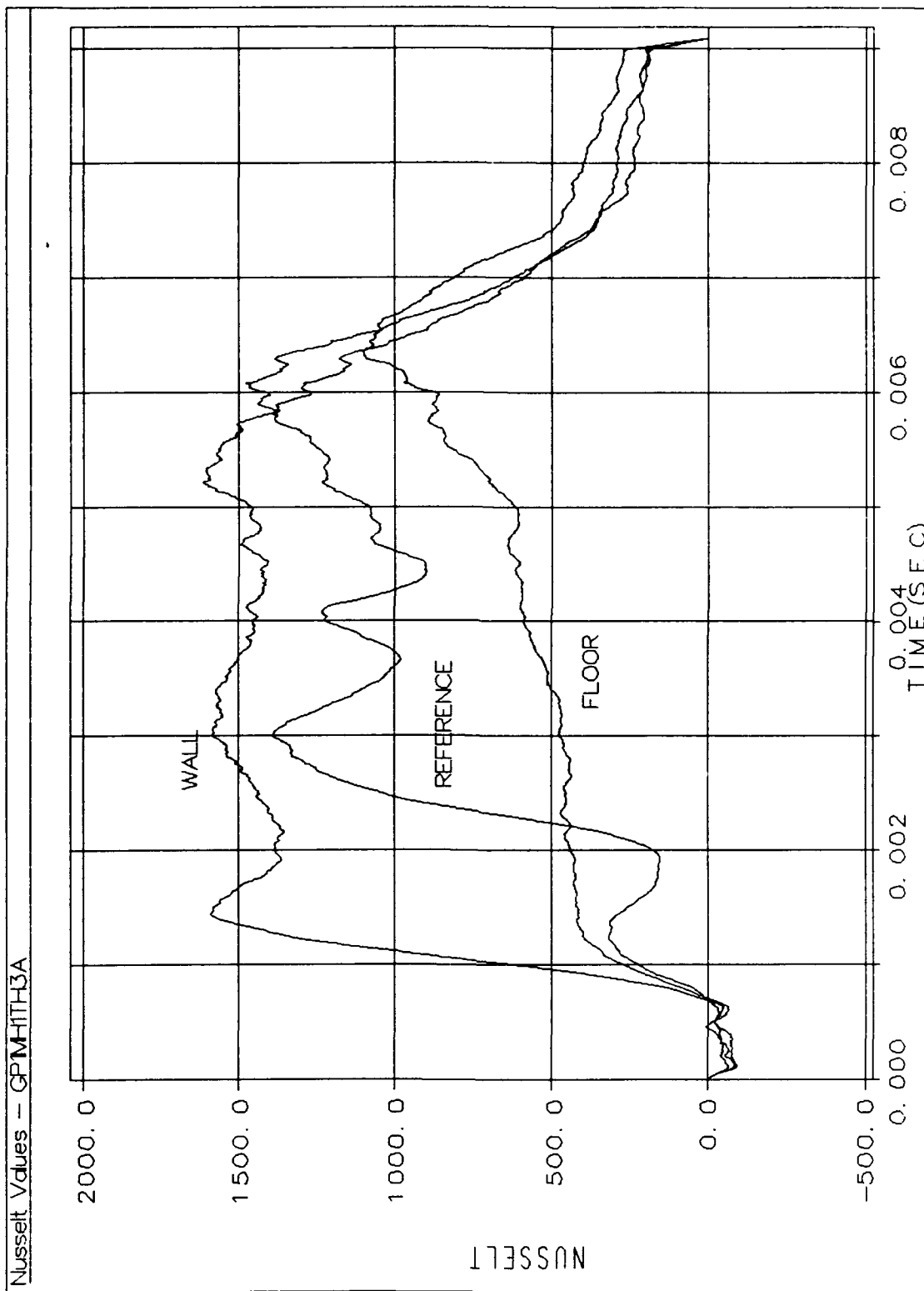


Figure F.10. Test Run Nusselt Values

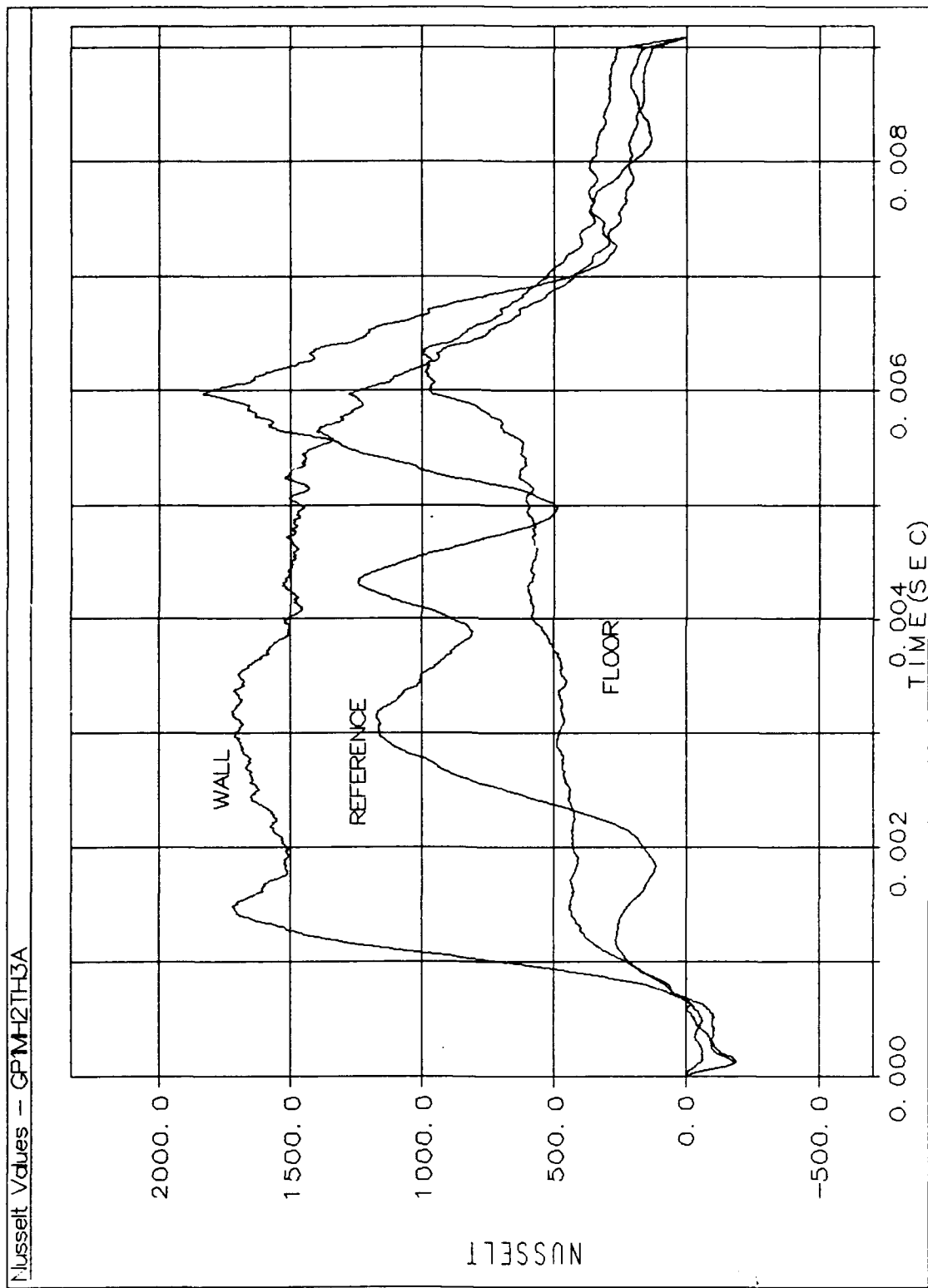


Figure F.11. Test Run Nusselt Values

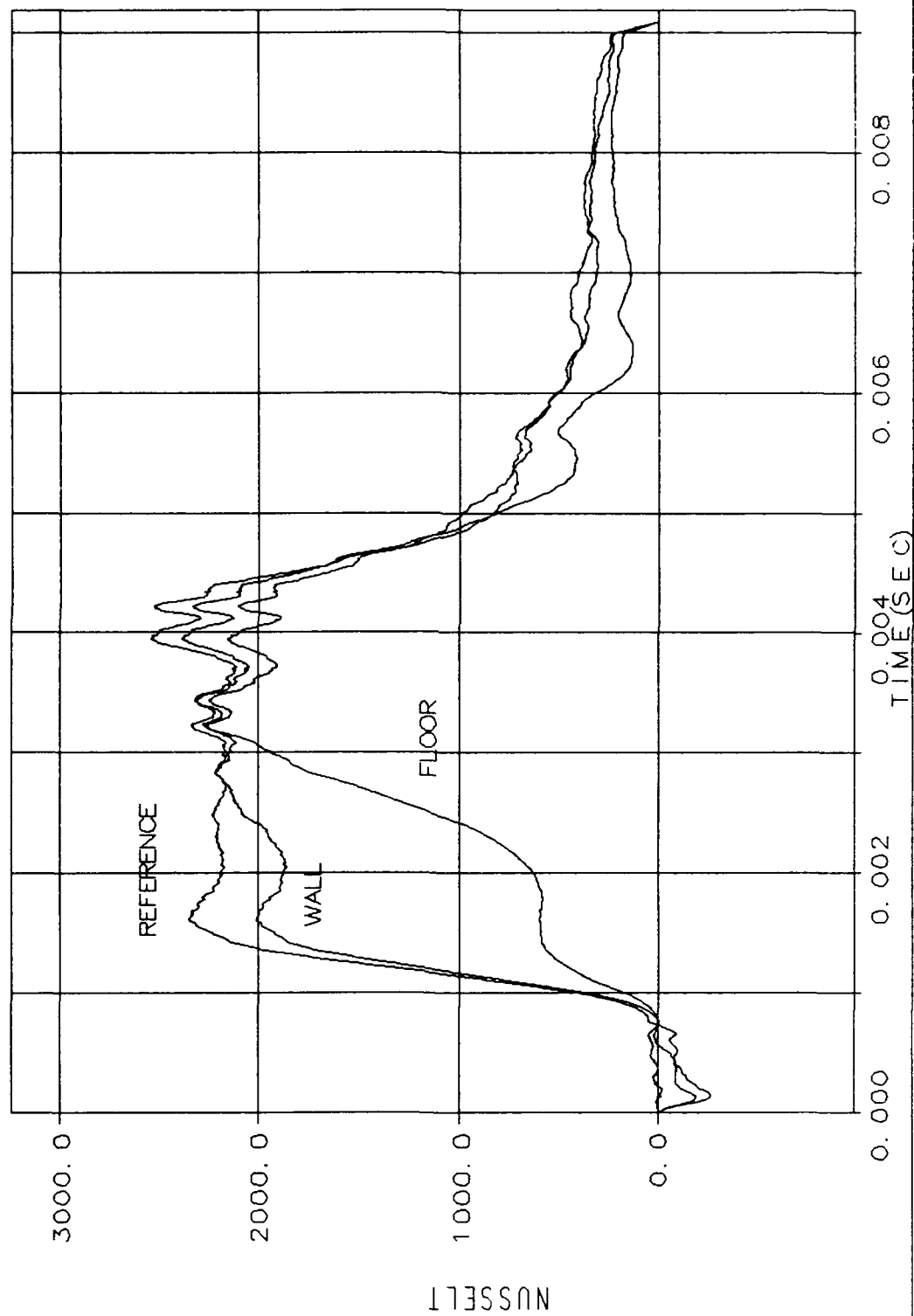


Figure F.12. Test Run Nusselt Values

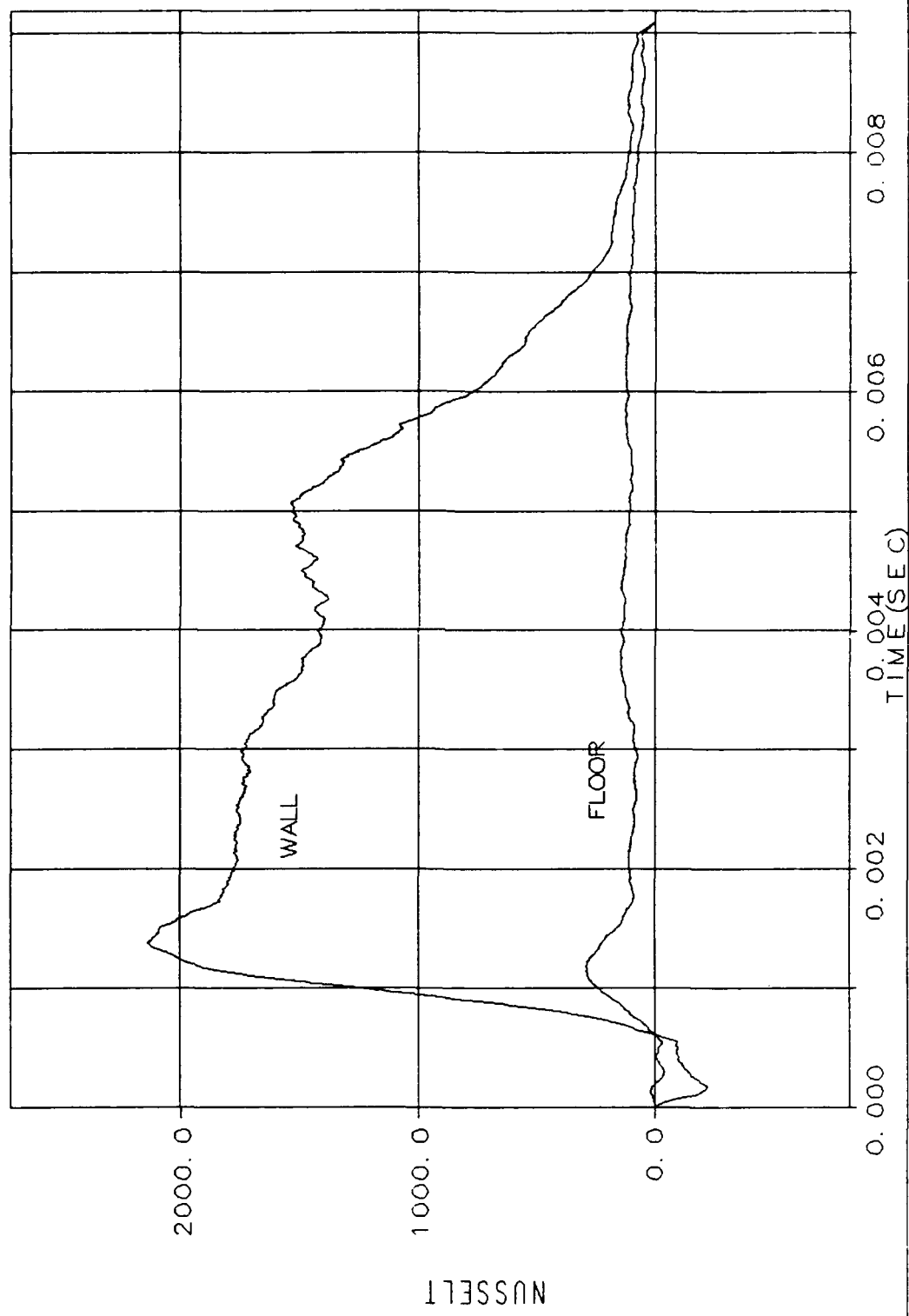


Figure F.13. Test Run Nusselt Values

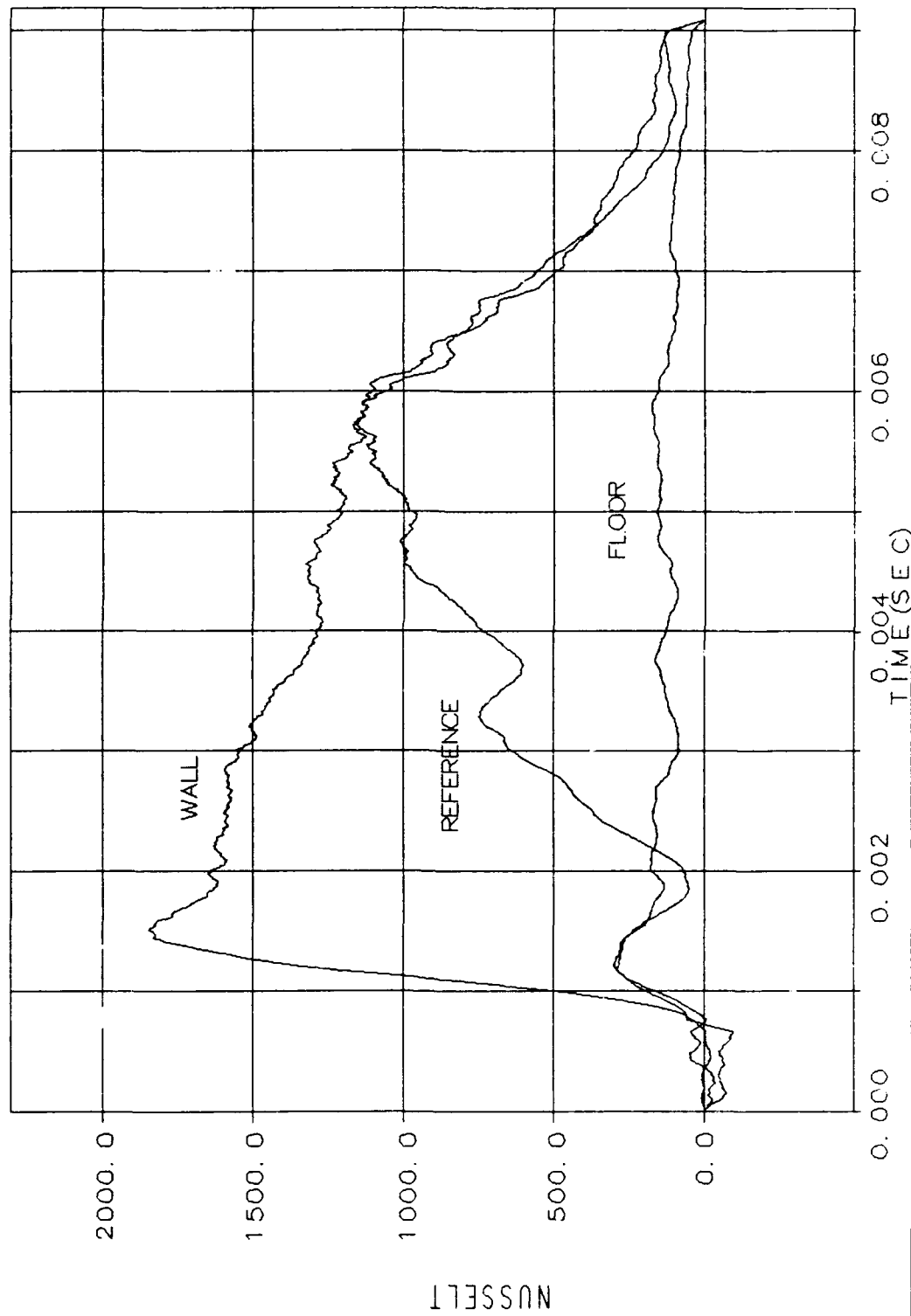


Figure F.14. Test Run Nusselt Values

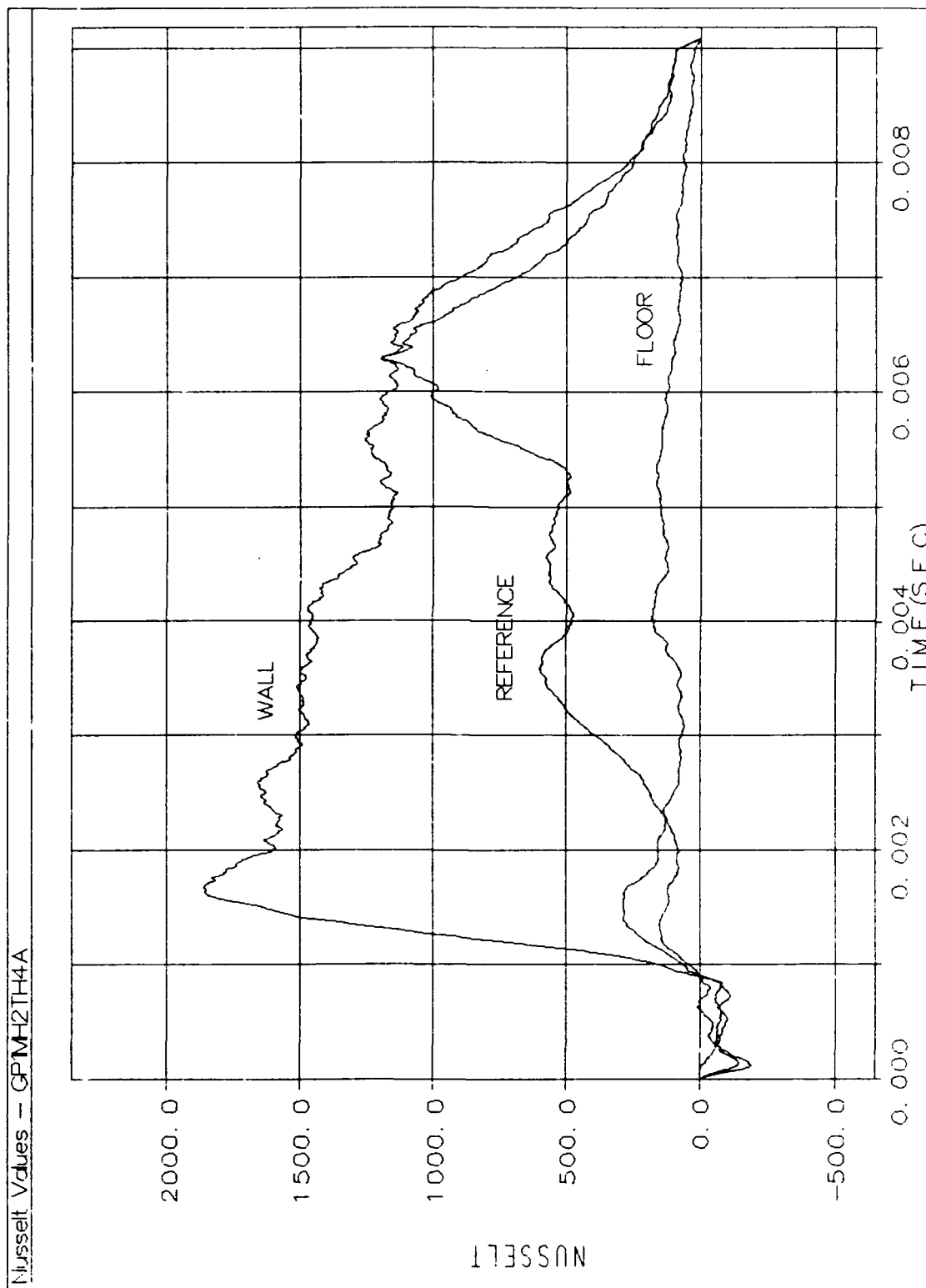


Figure F.15. Test Run Nusselt Values

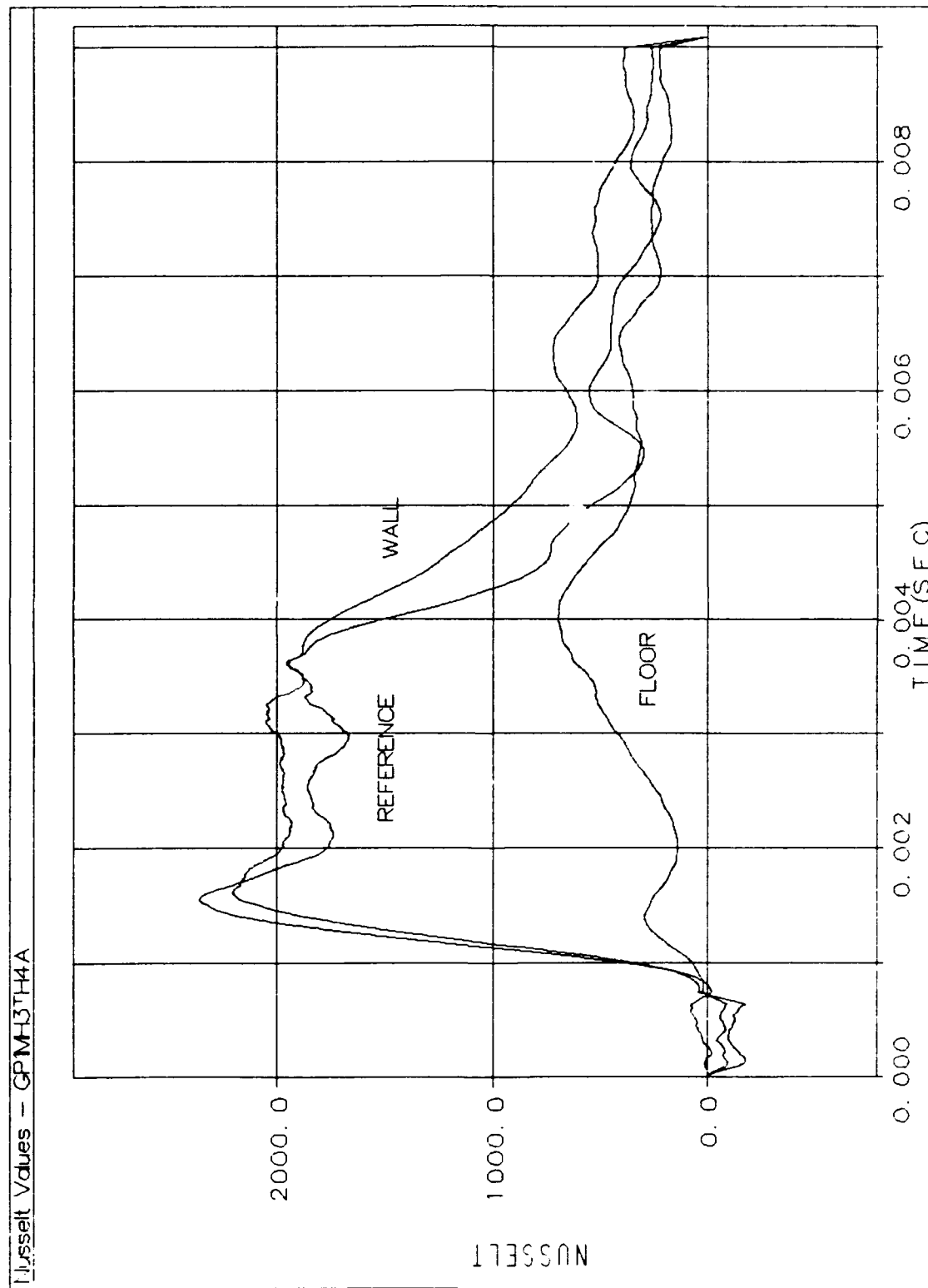


Figure F.16. Test Run Nusselt Values

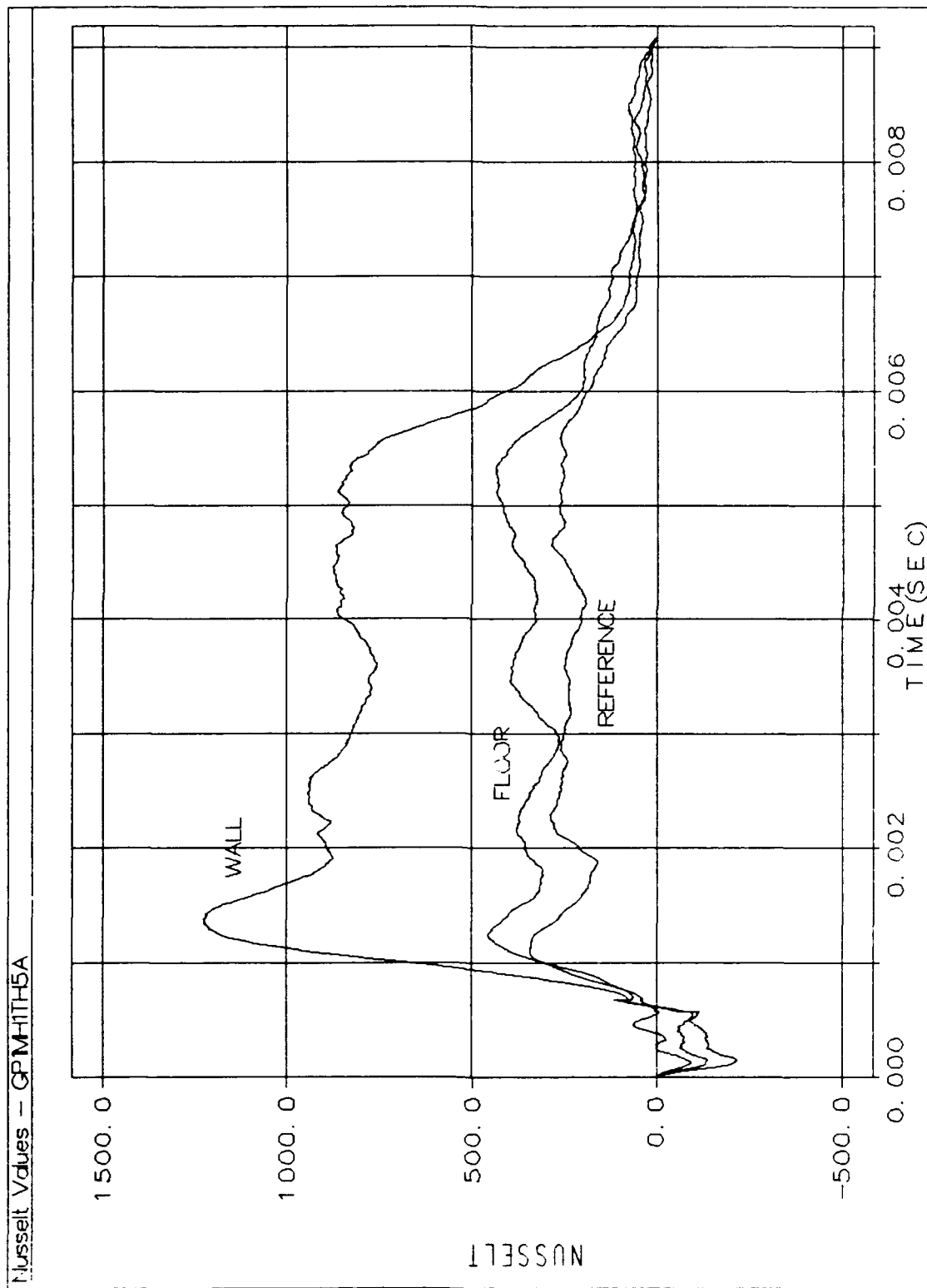


Figure F.17. Test Run Nusselt Values

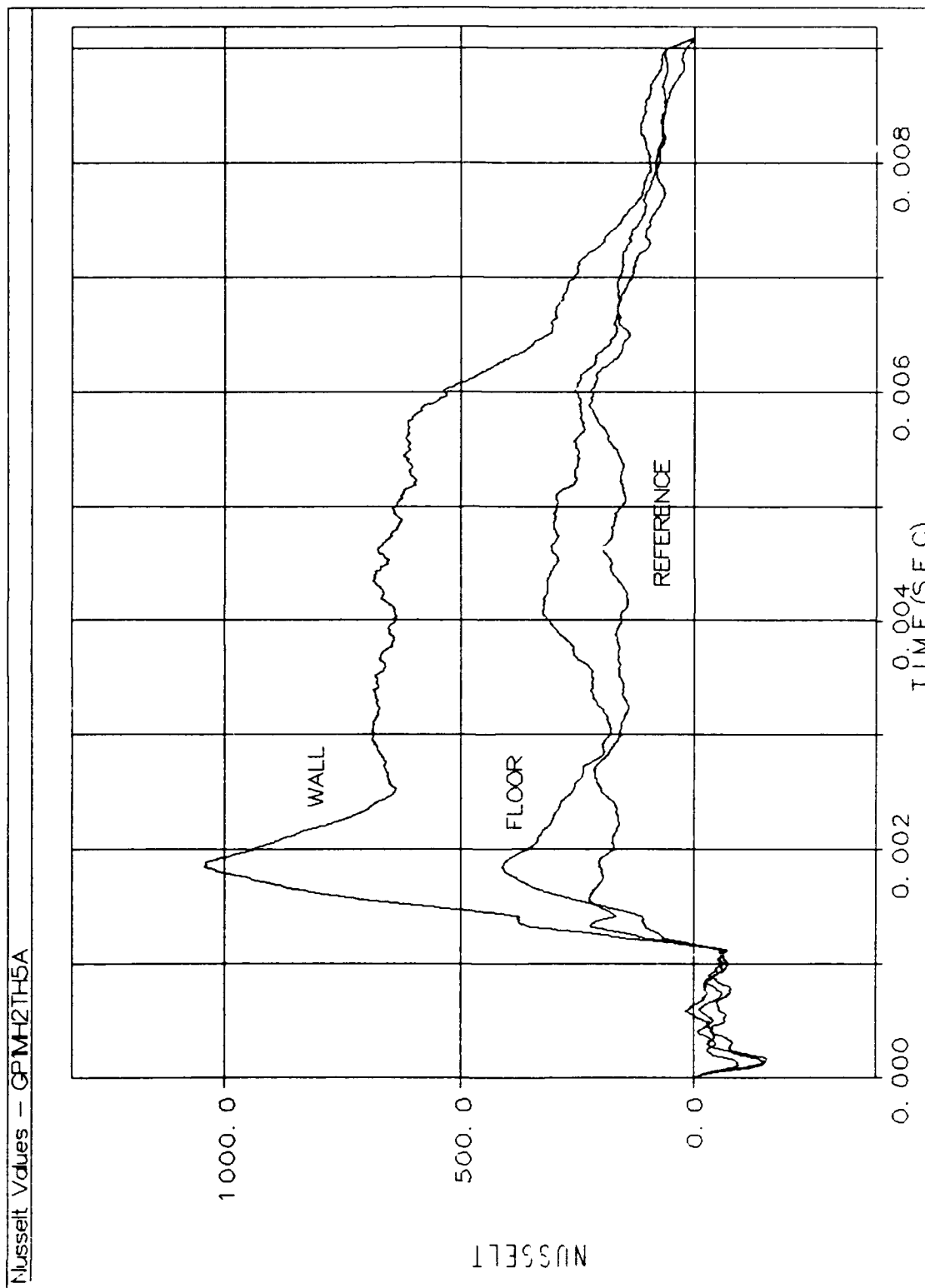


Figure F.18. Test Run Nusselt Values

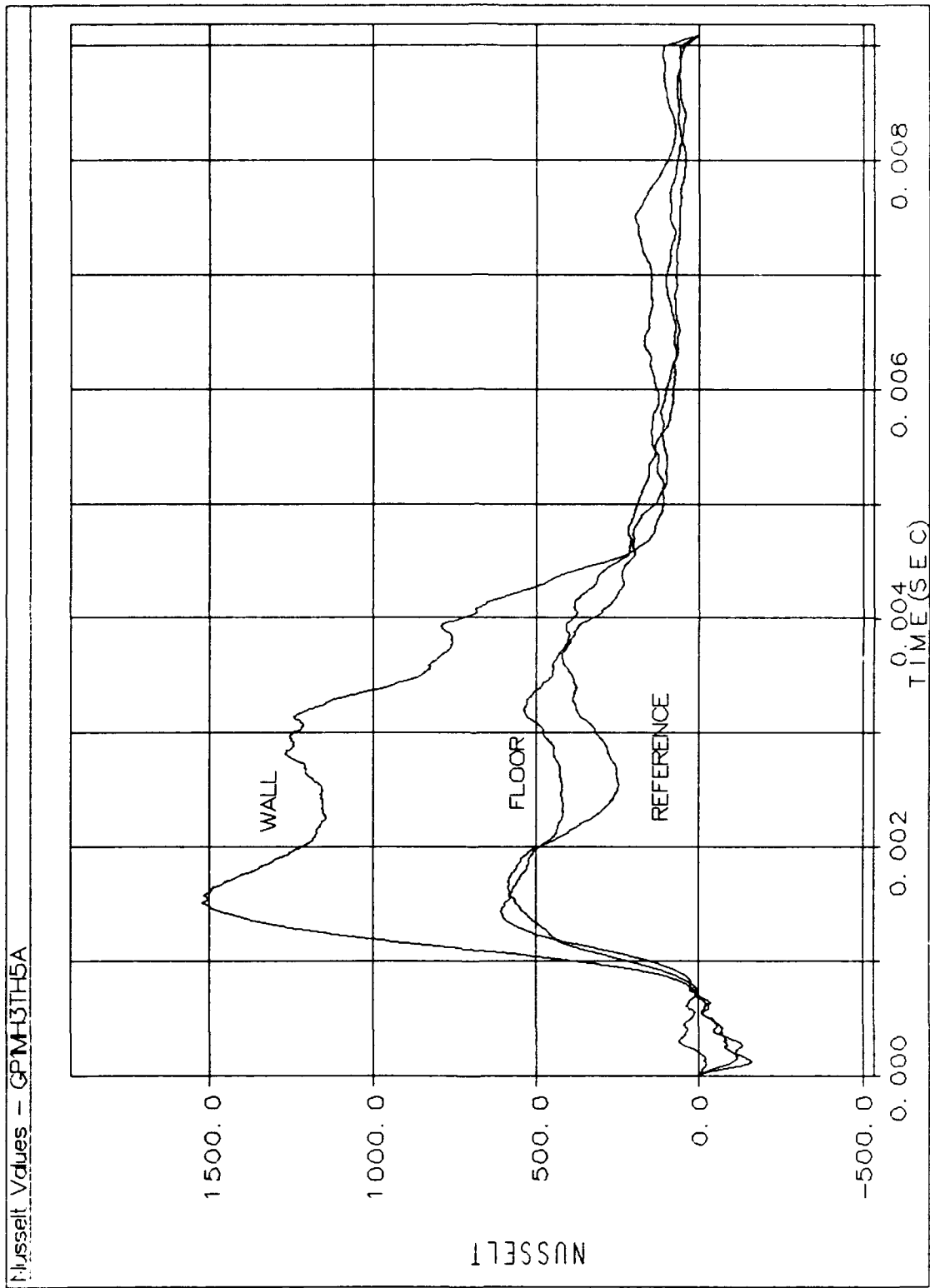


Figure F.19. Test Run Nusselt Values

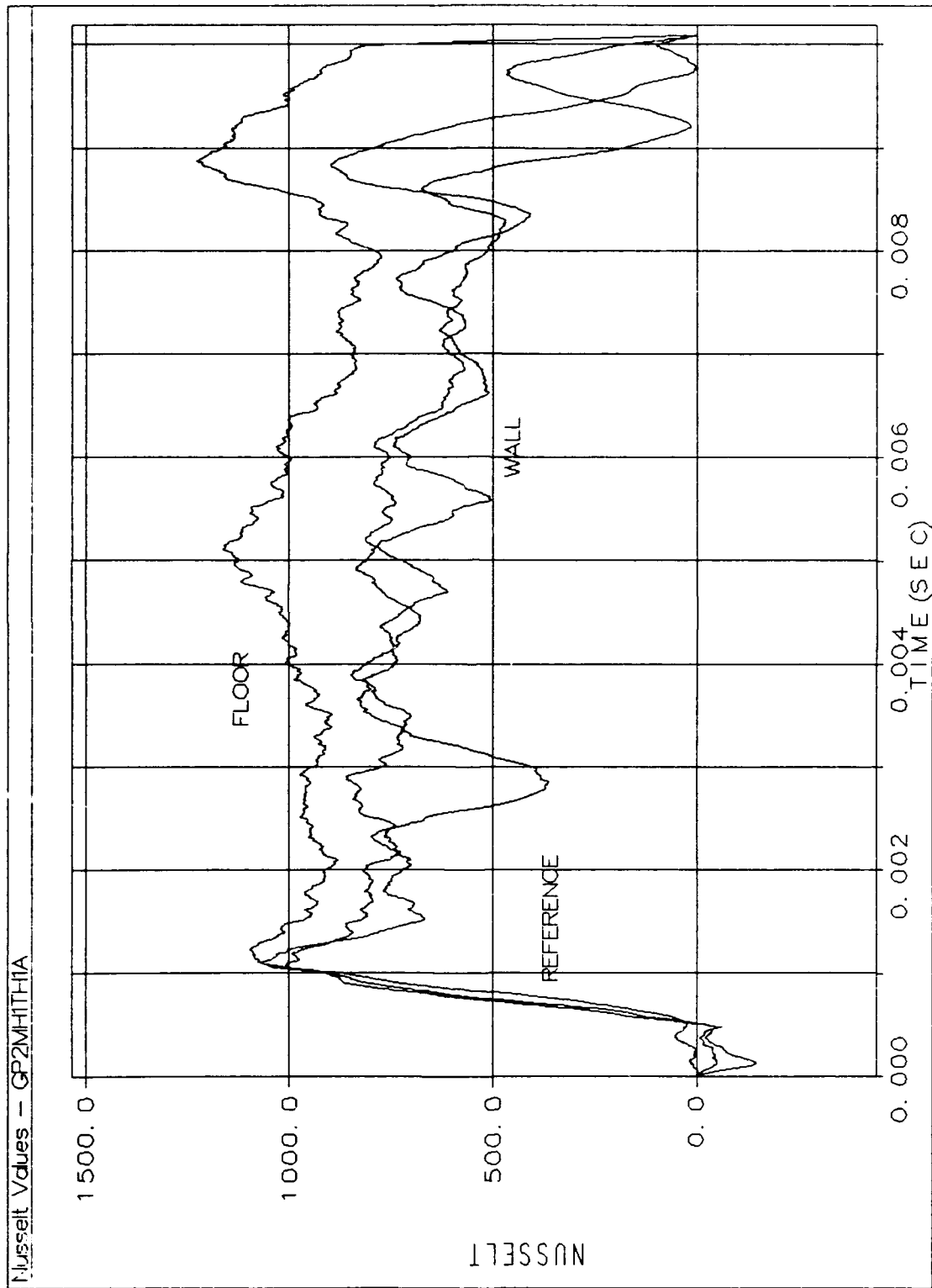


Figure F.20. Test Run Nusselt Values

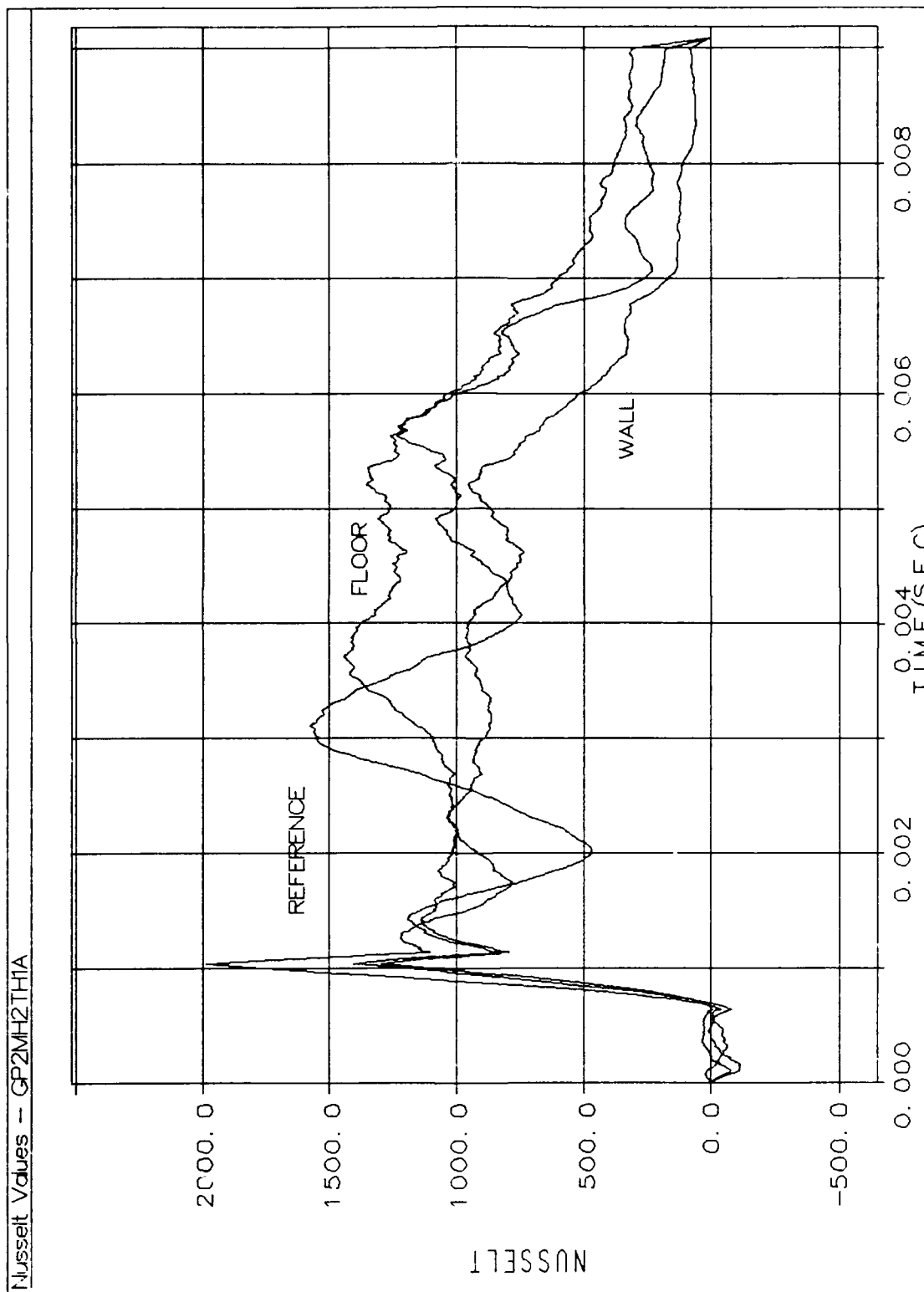


Figure F.21. Test Run Nusselt Values

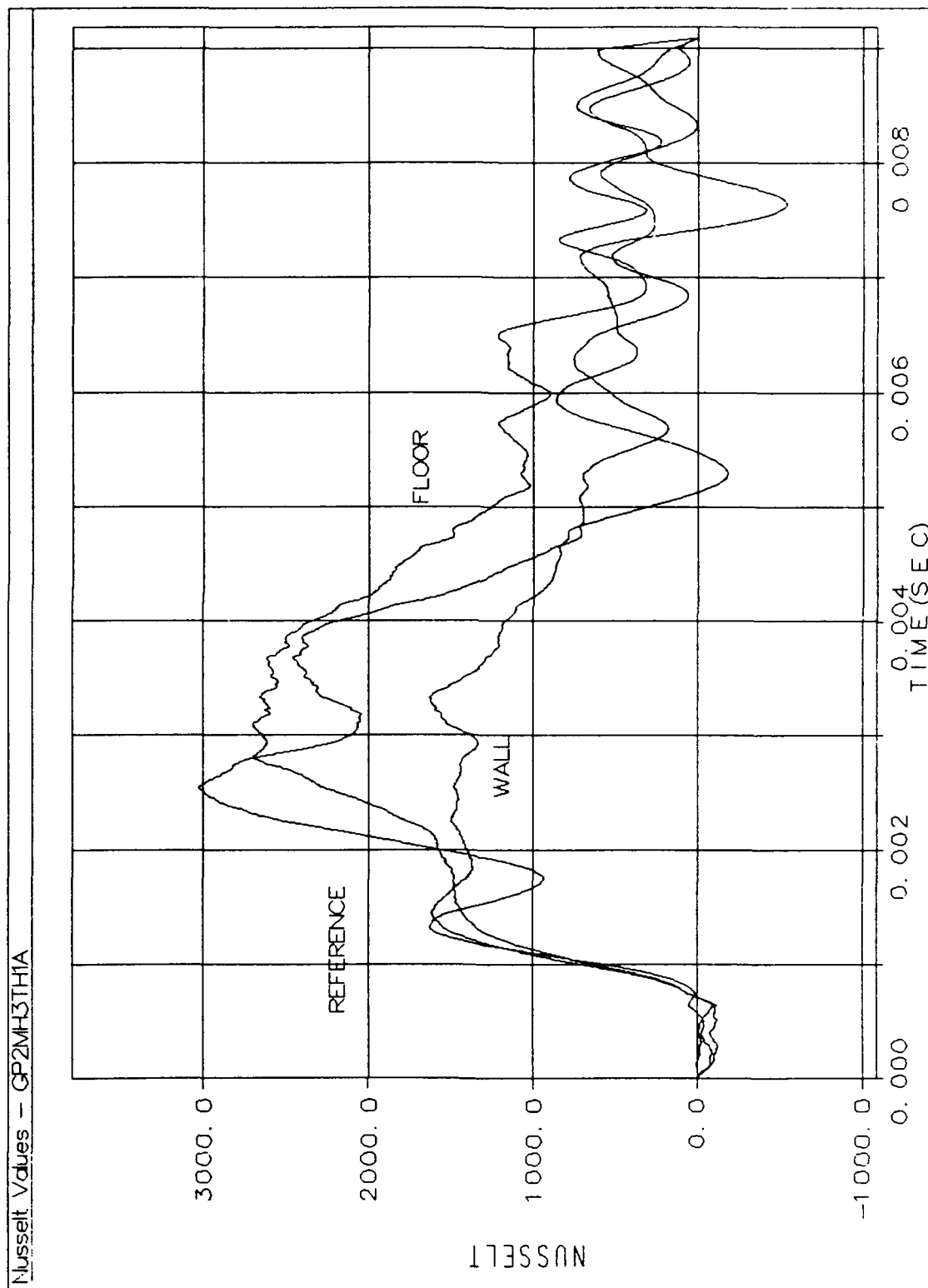


Figure F.22. Test Run Nusselt Values

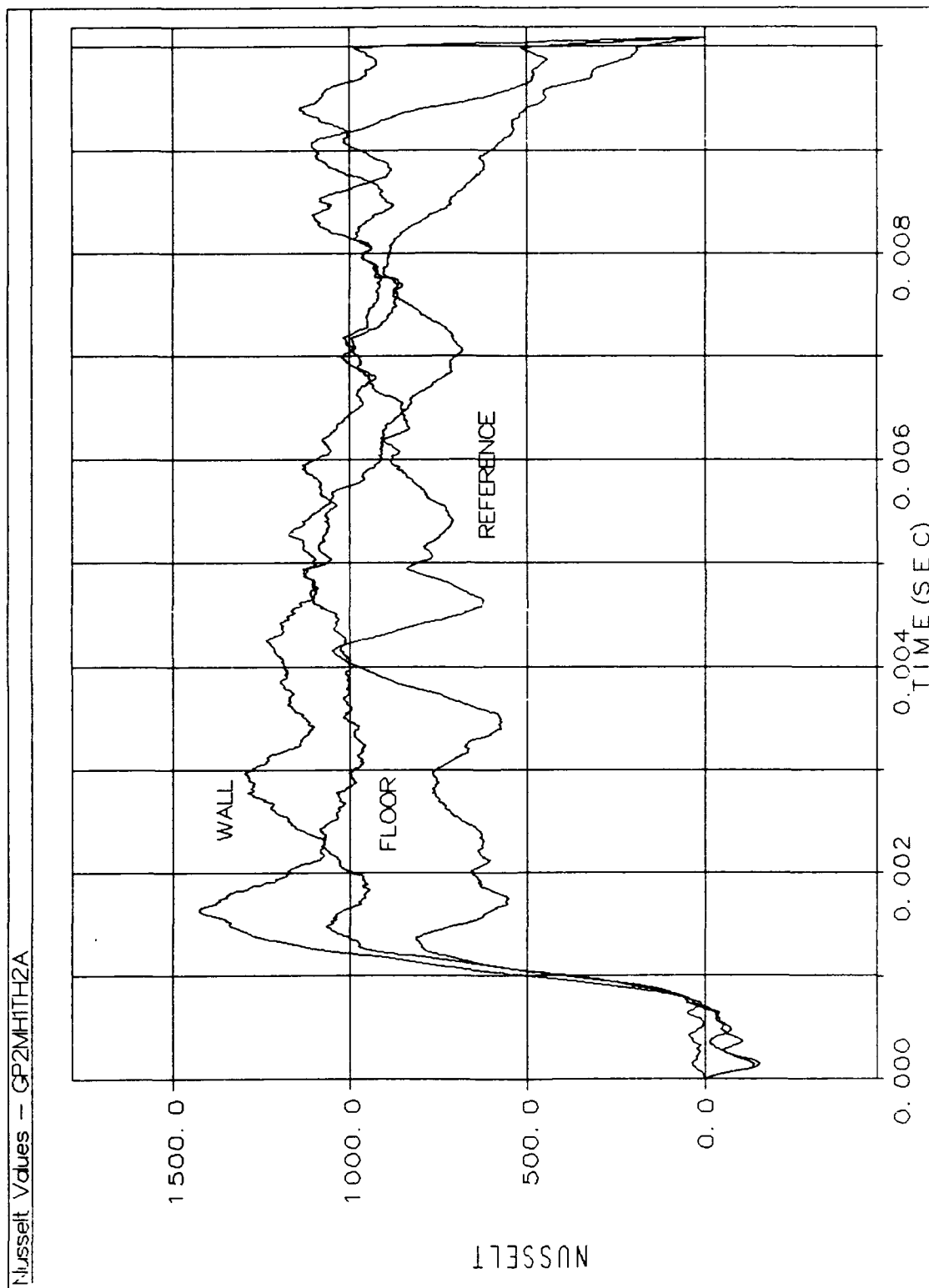


Figure F.23. Test Run Nusselt Values

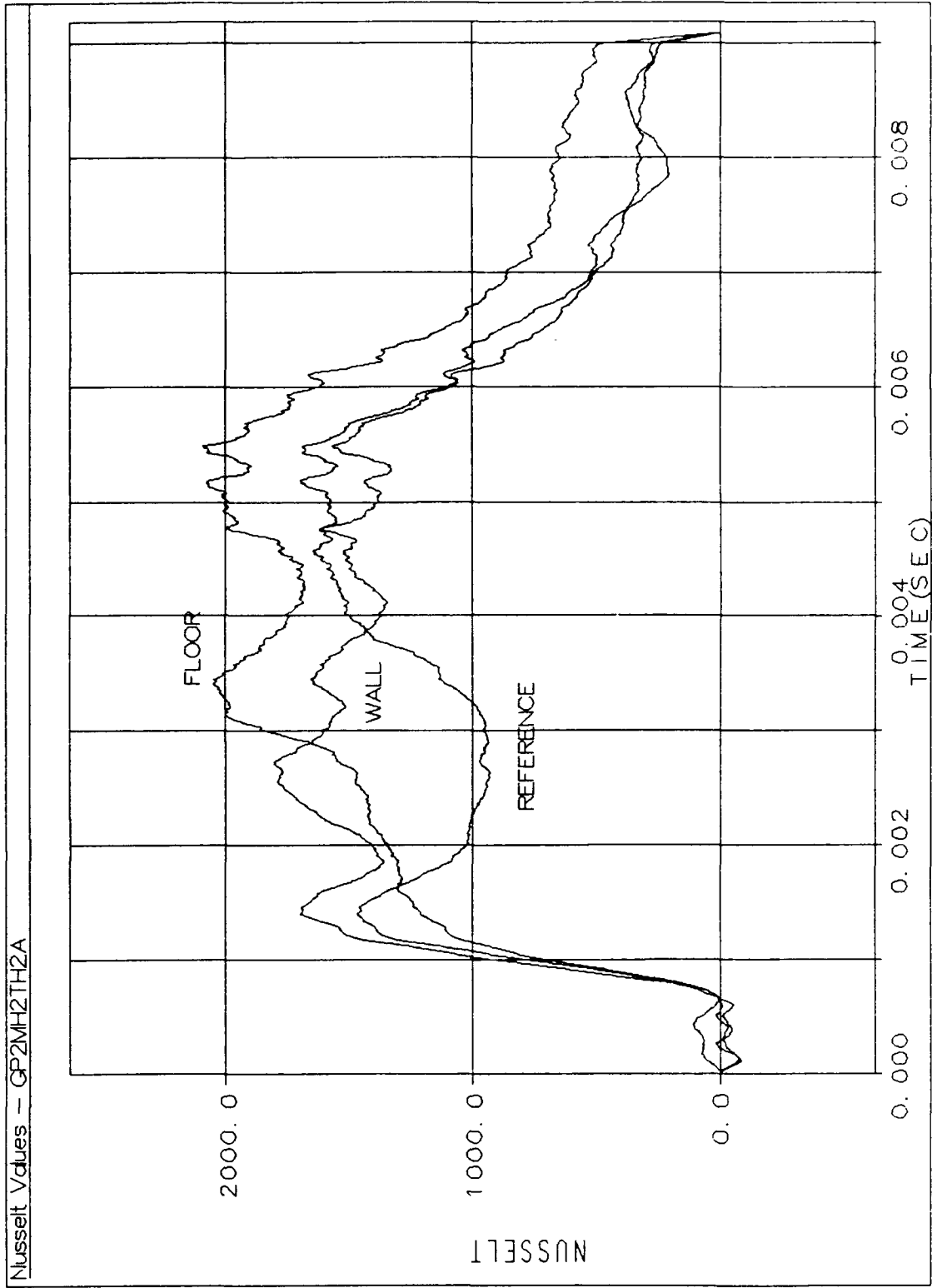


Figure F.24. Test Run Nusselt Values

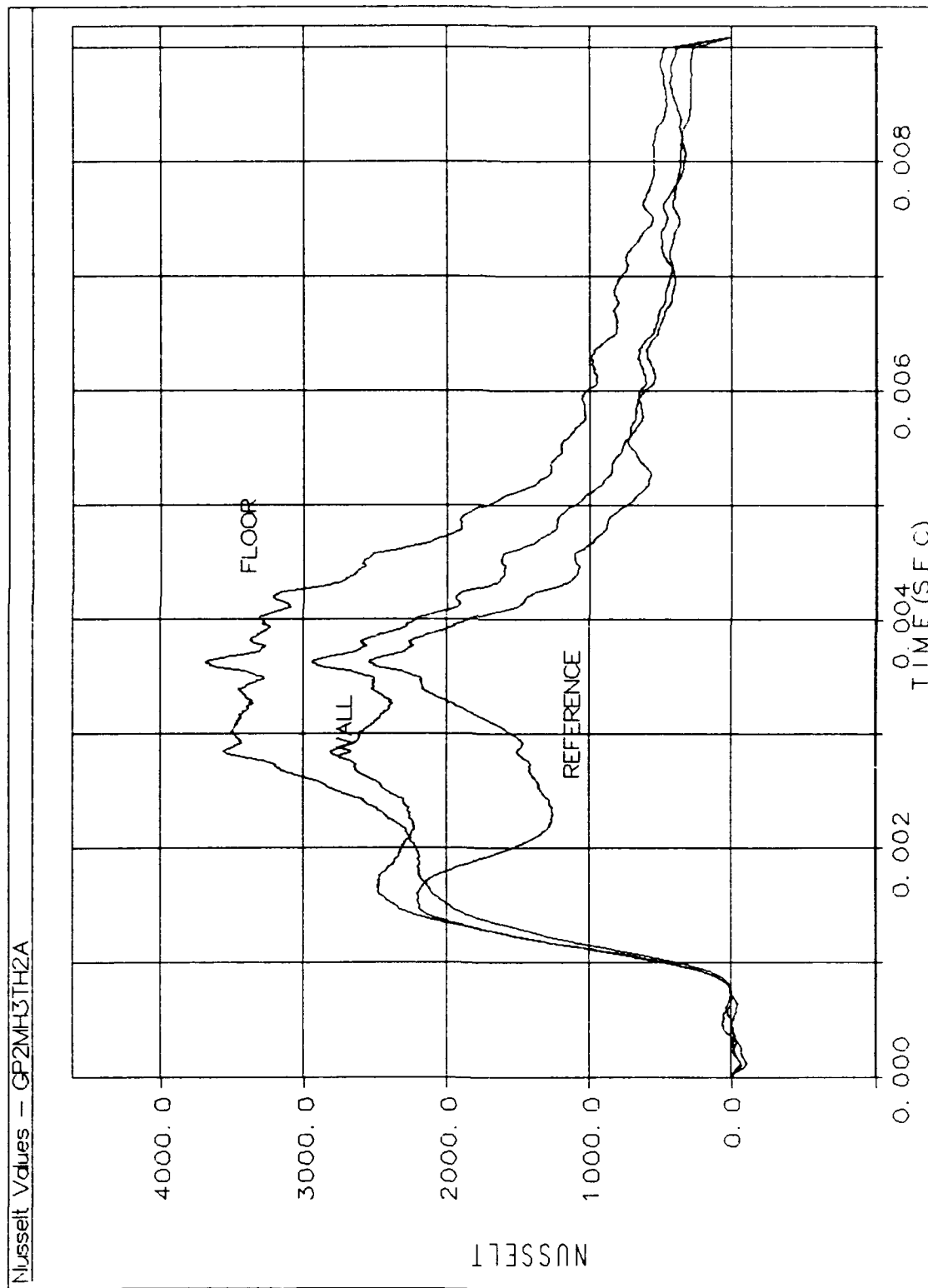


Figure F.25. Test Run Nusselt Values

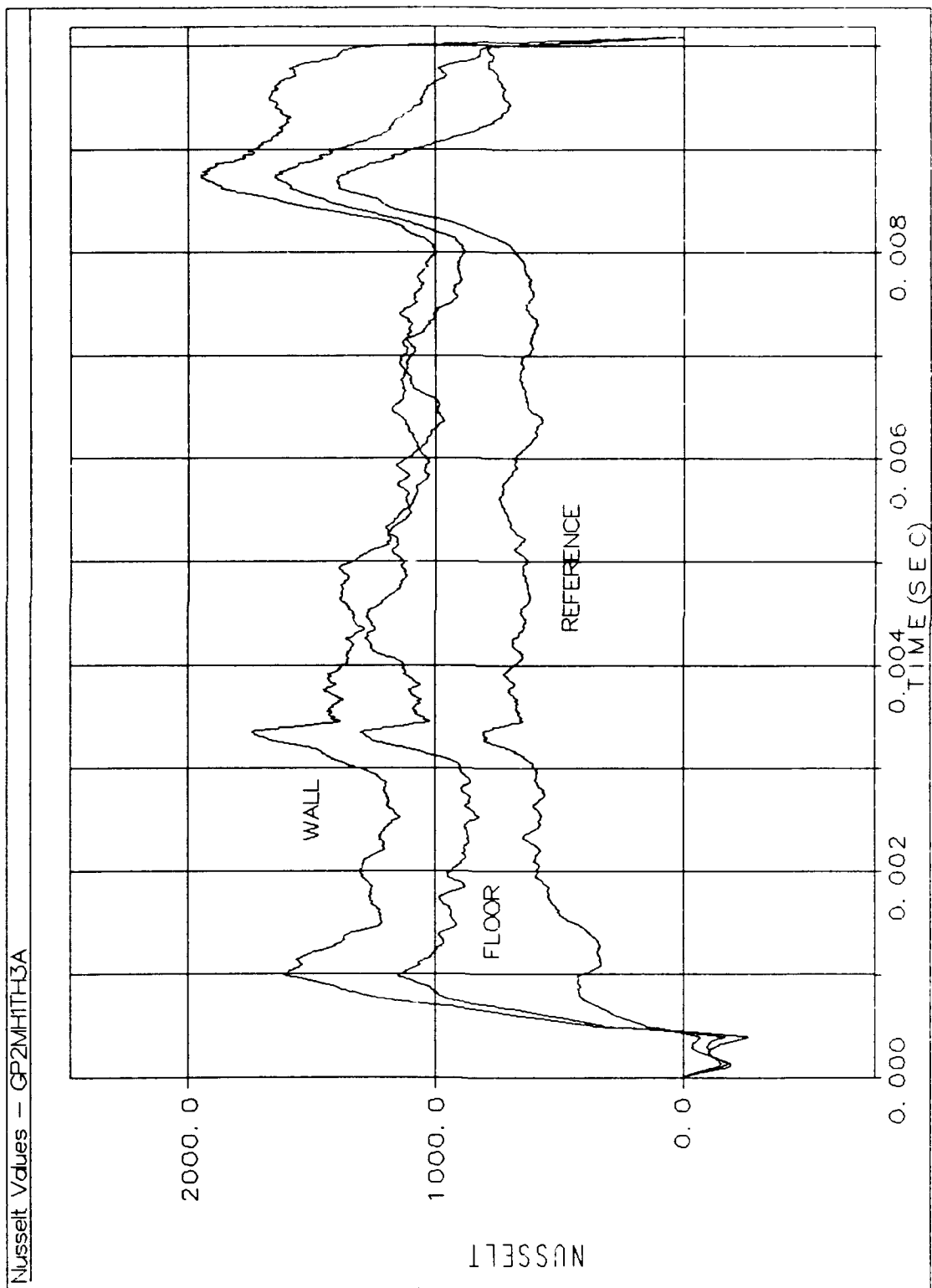


Figure F.26. Test Run Nusselt Values

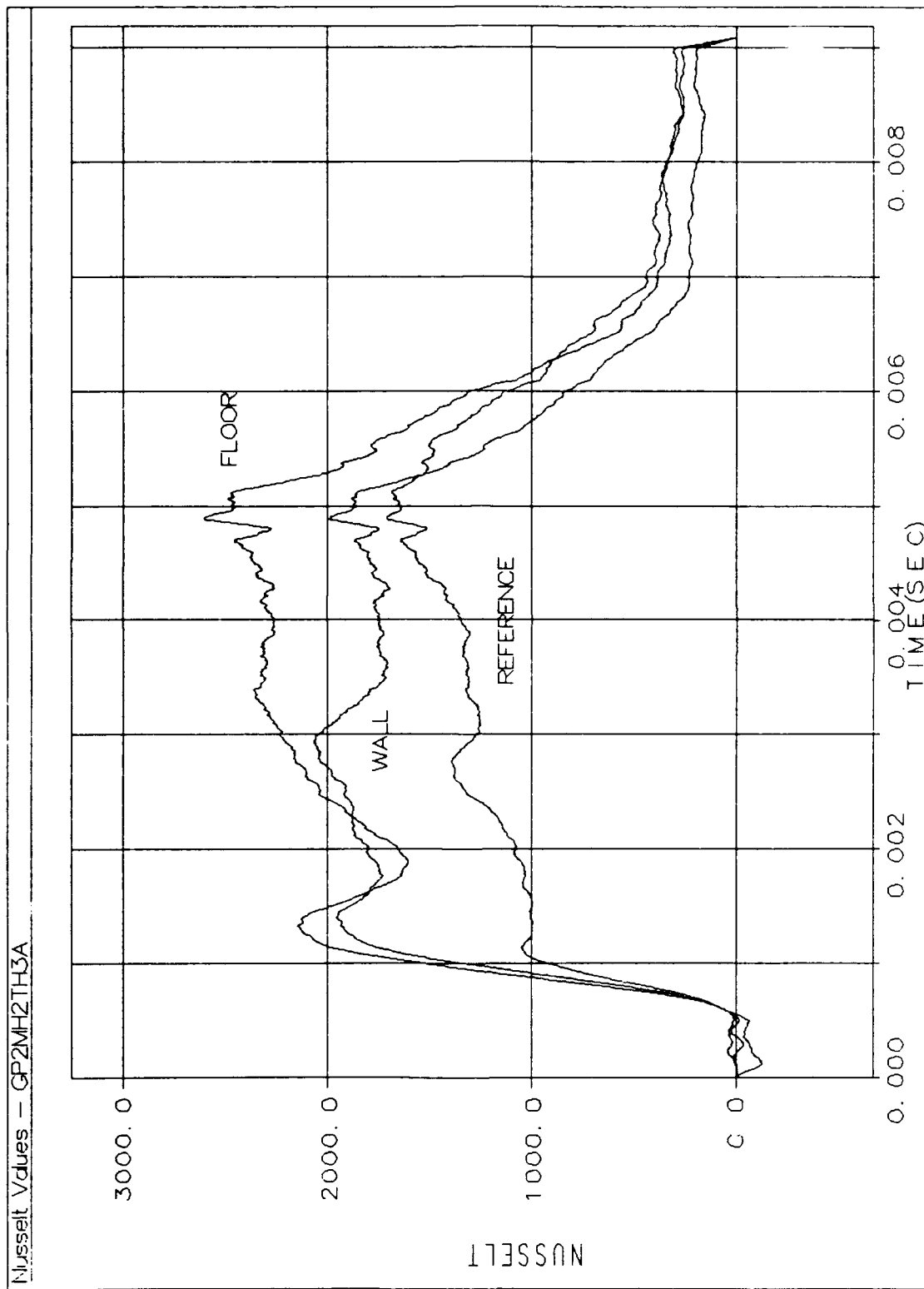


Figure F.27. Test Run Nusselt Values

Nusselt Values - GP2MH3TH3A

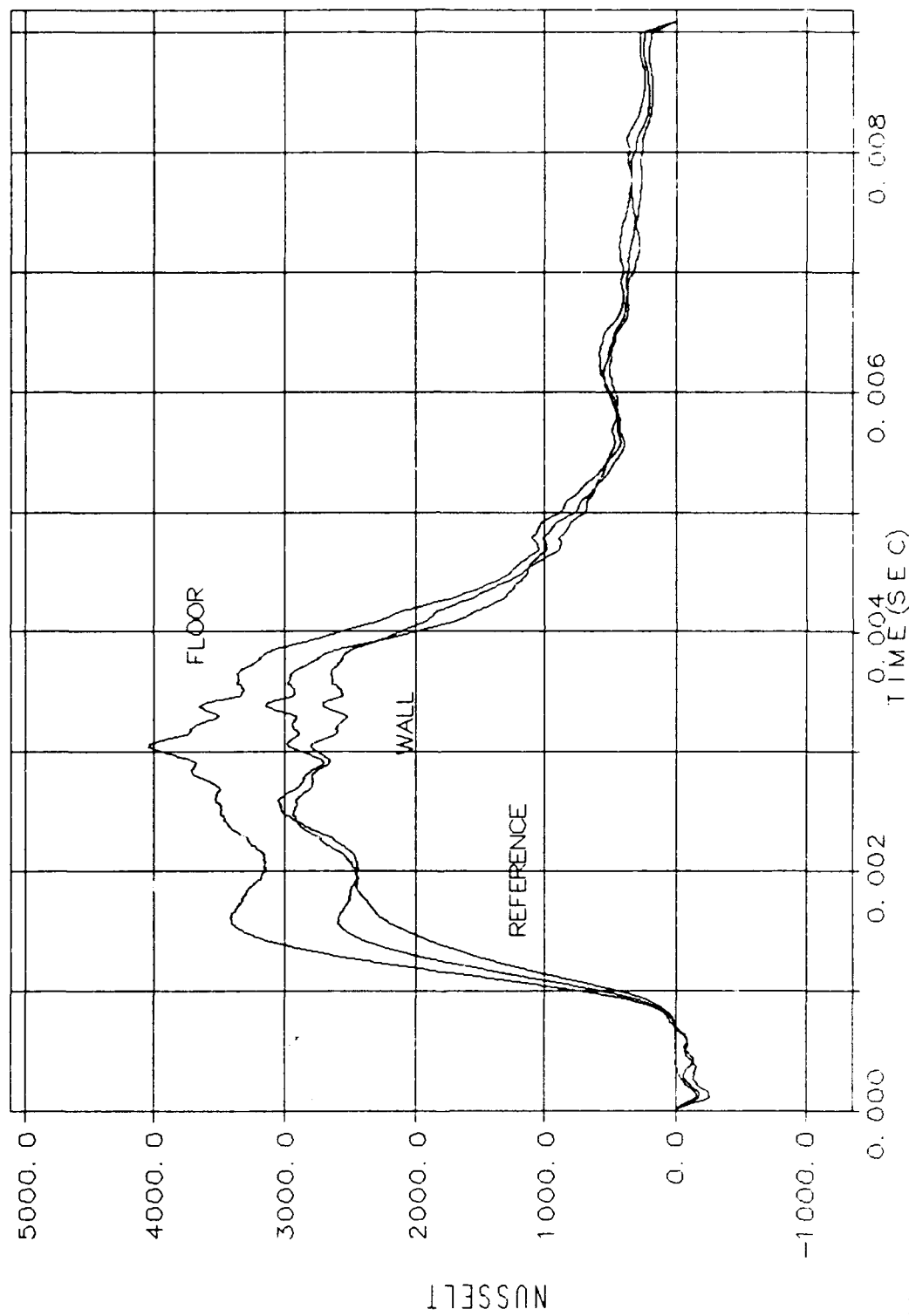


Figure F.28. Test Run Nusselt Values

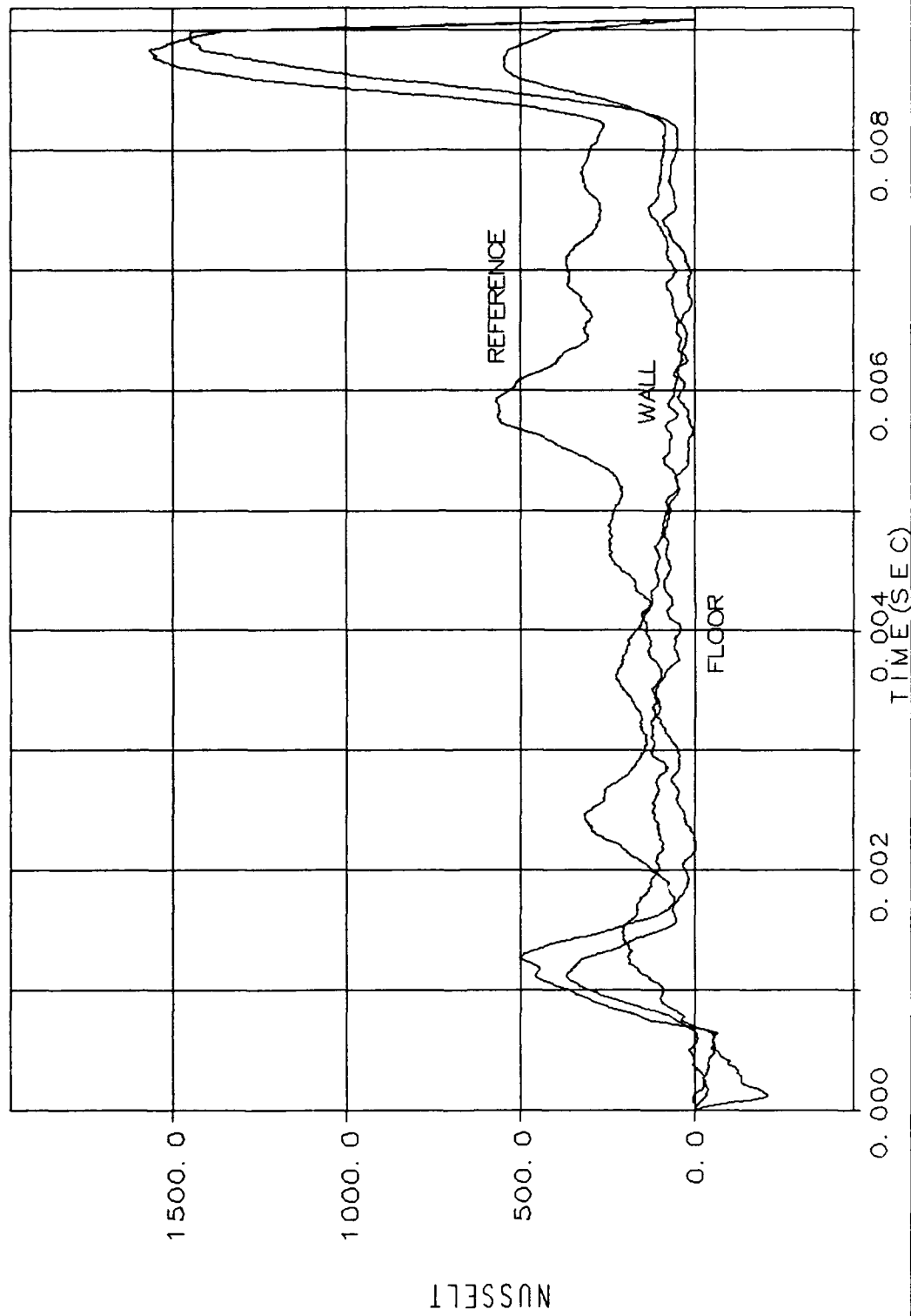


Figure F.29. Test Run Nusselt Values

Nusselt Values - GP2MH2TH4A

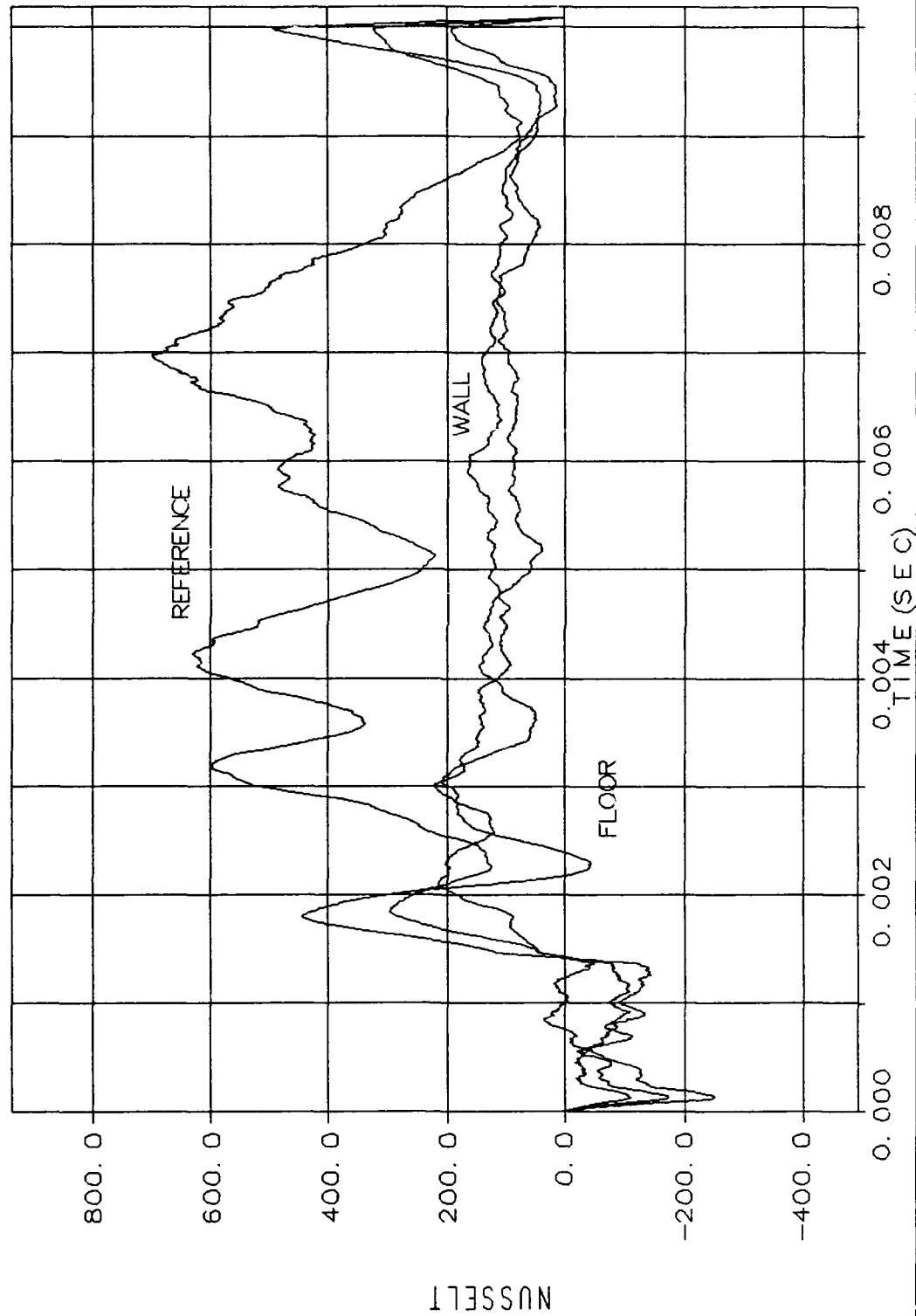


Figure F.30. Test Run Nusselt Values

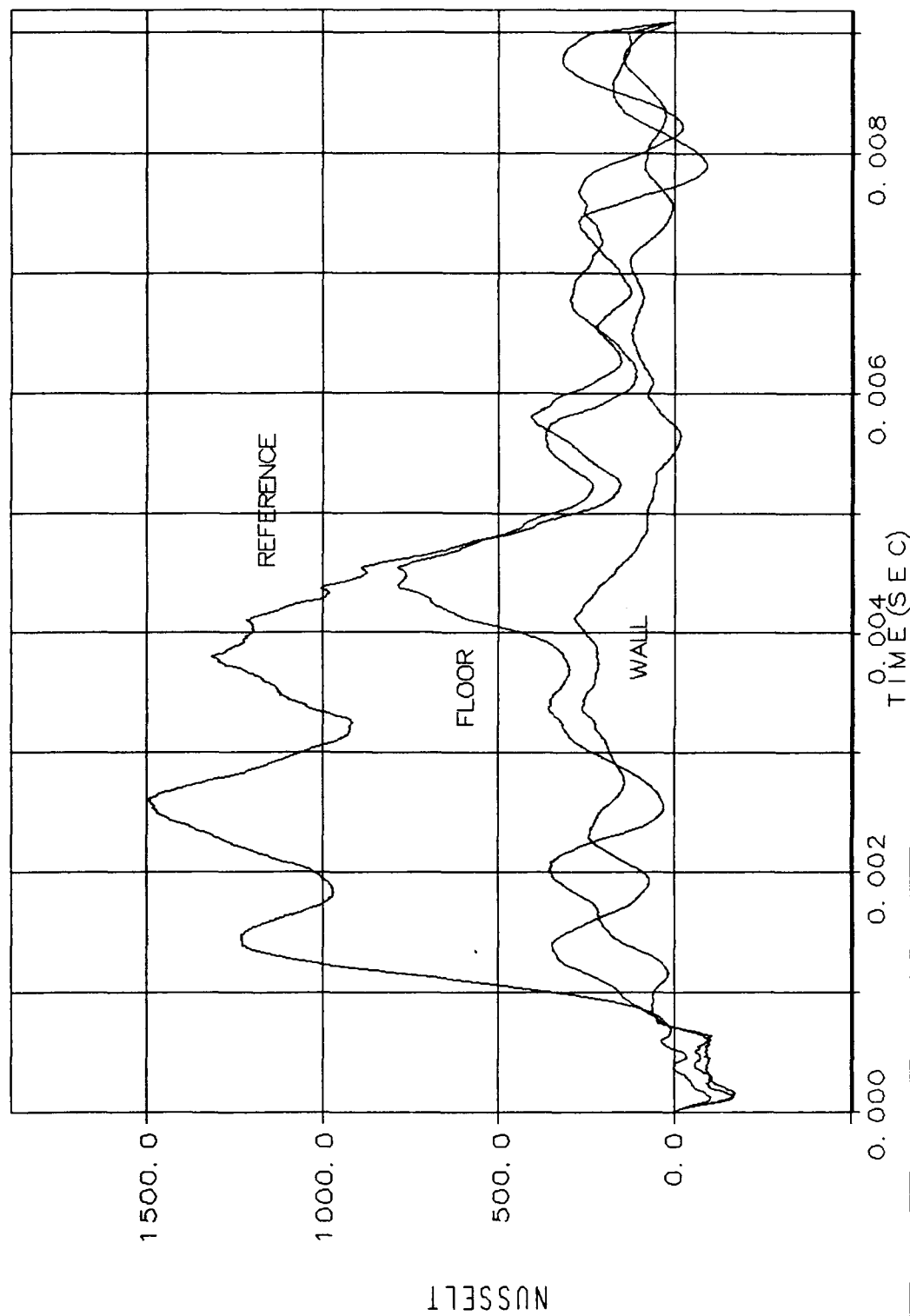


Figure F.31. Test Run Nusselt Values

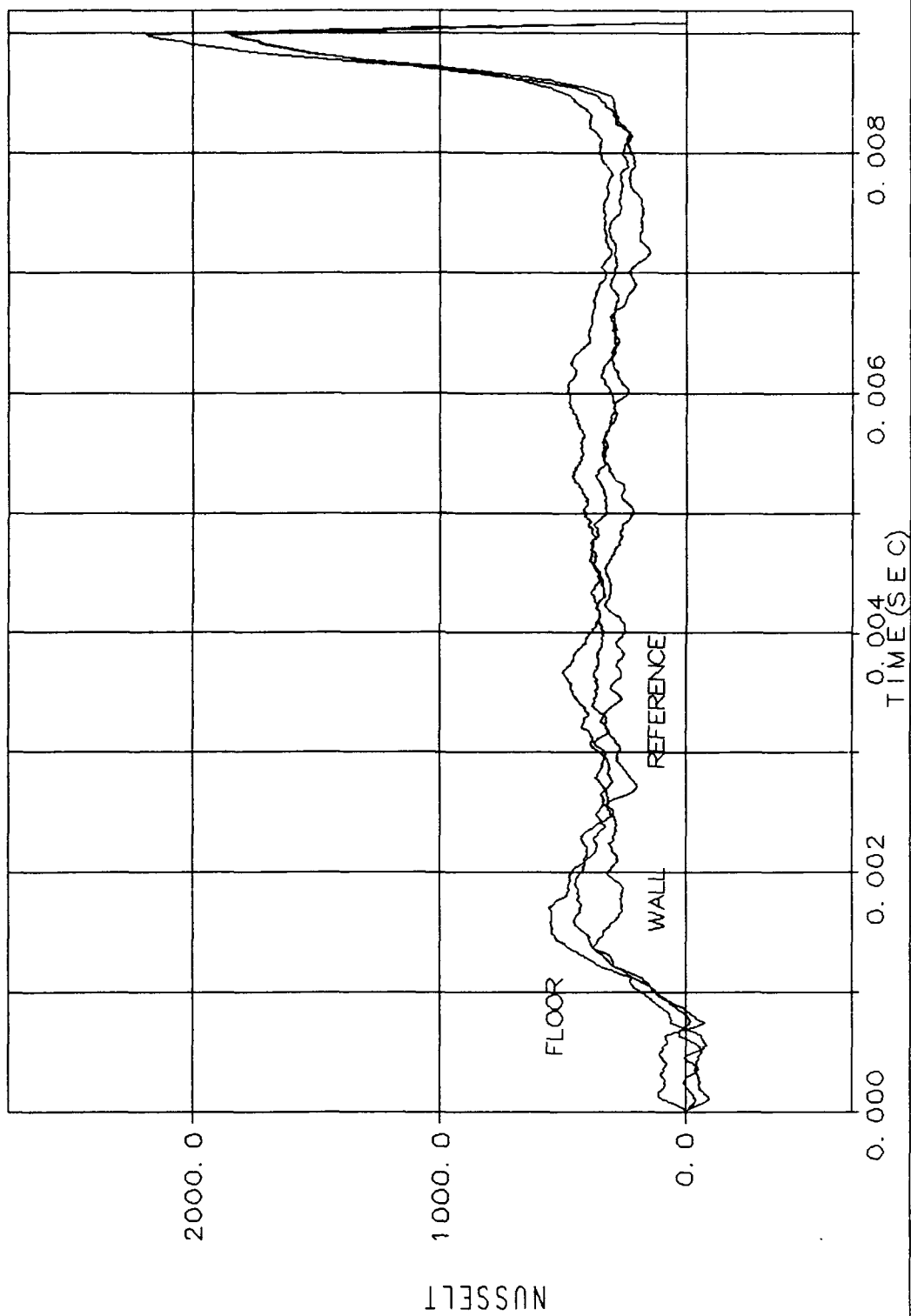


Figure F.32. Test Run Nusselt Values

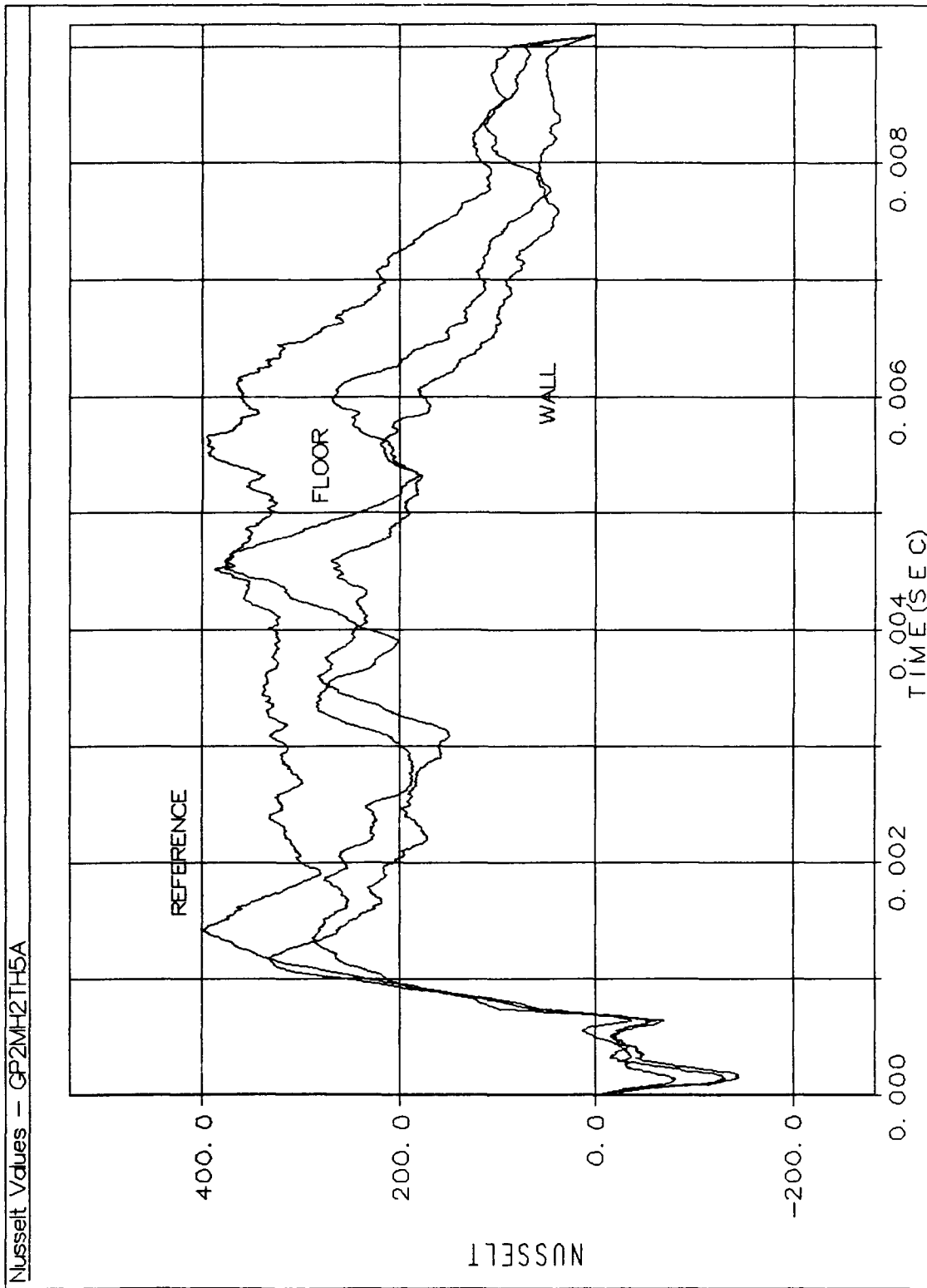


Figure F.33. Test Run Nusselt Values

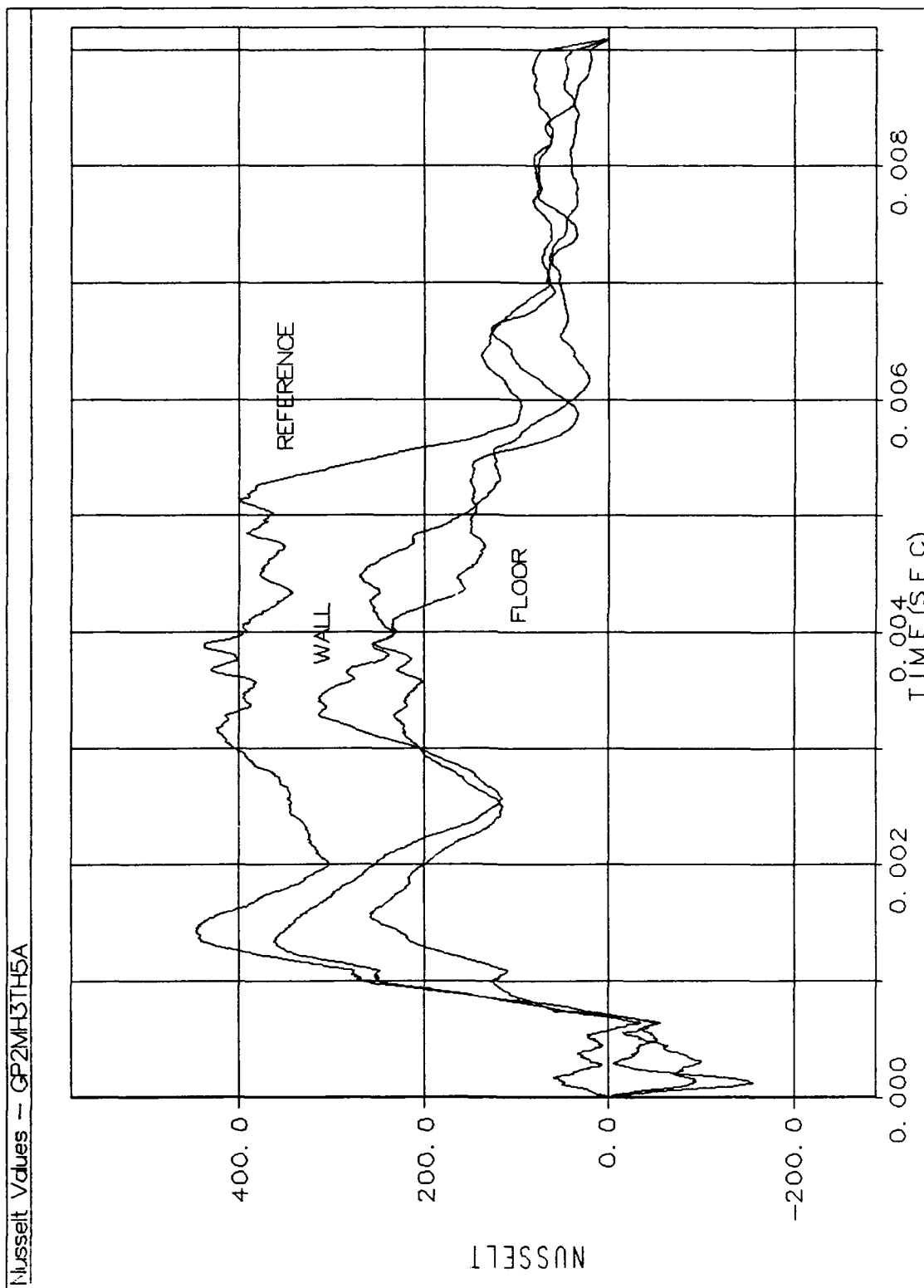


Figure F.34. Test Run Nusselt Values

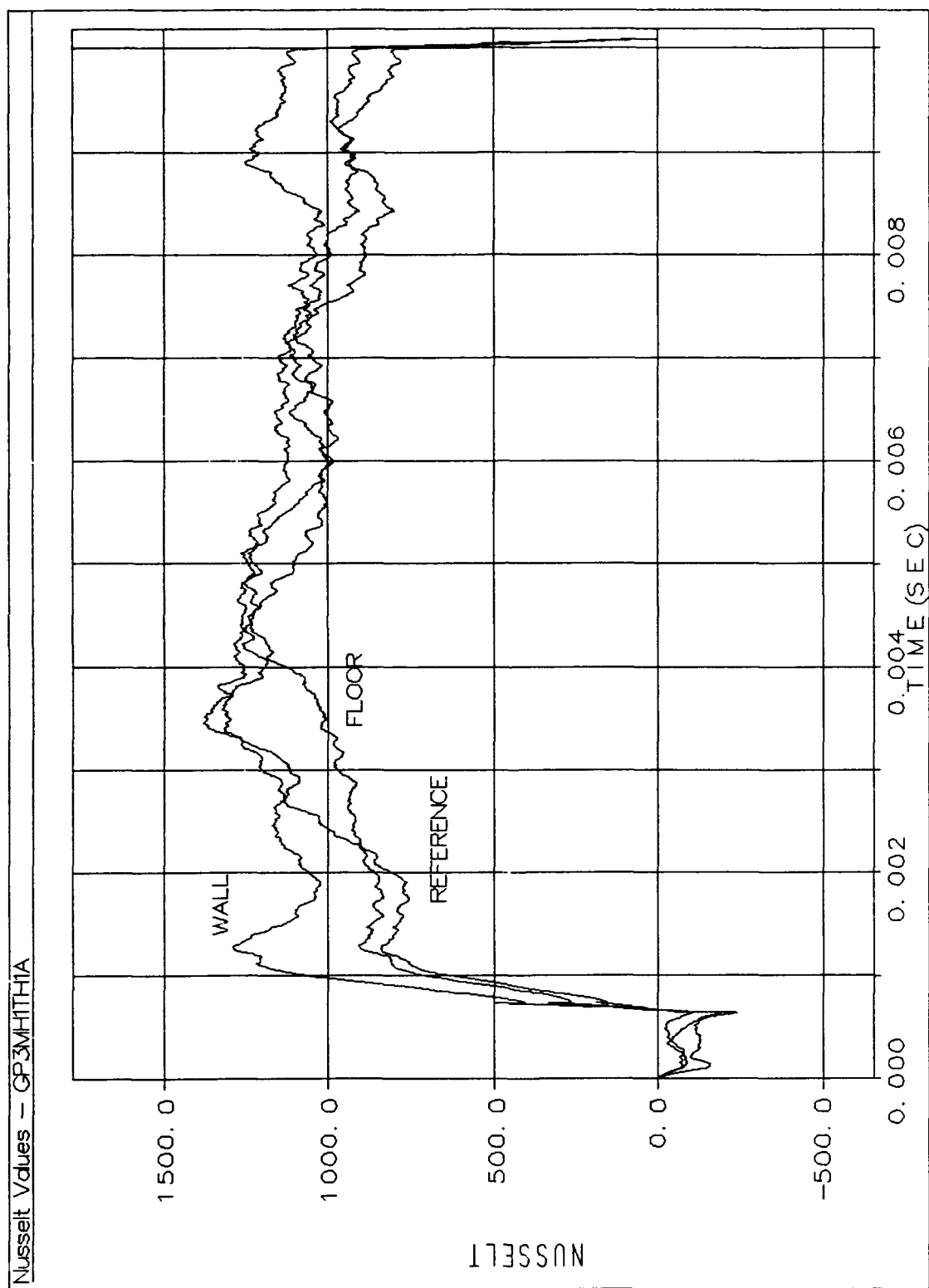


Figure F.35. Test Run Nusselt Values

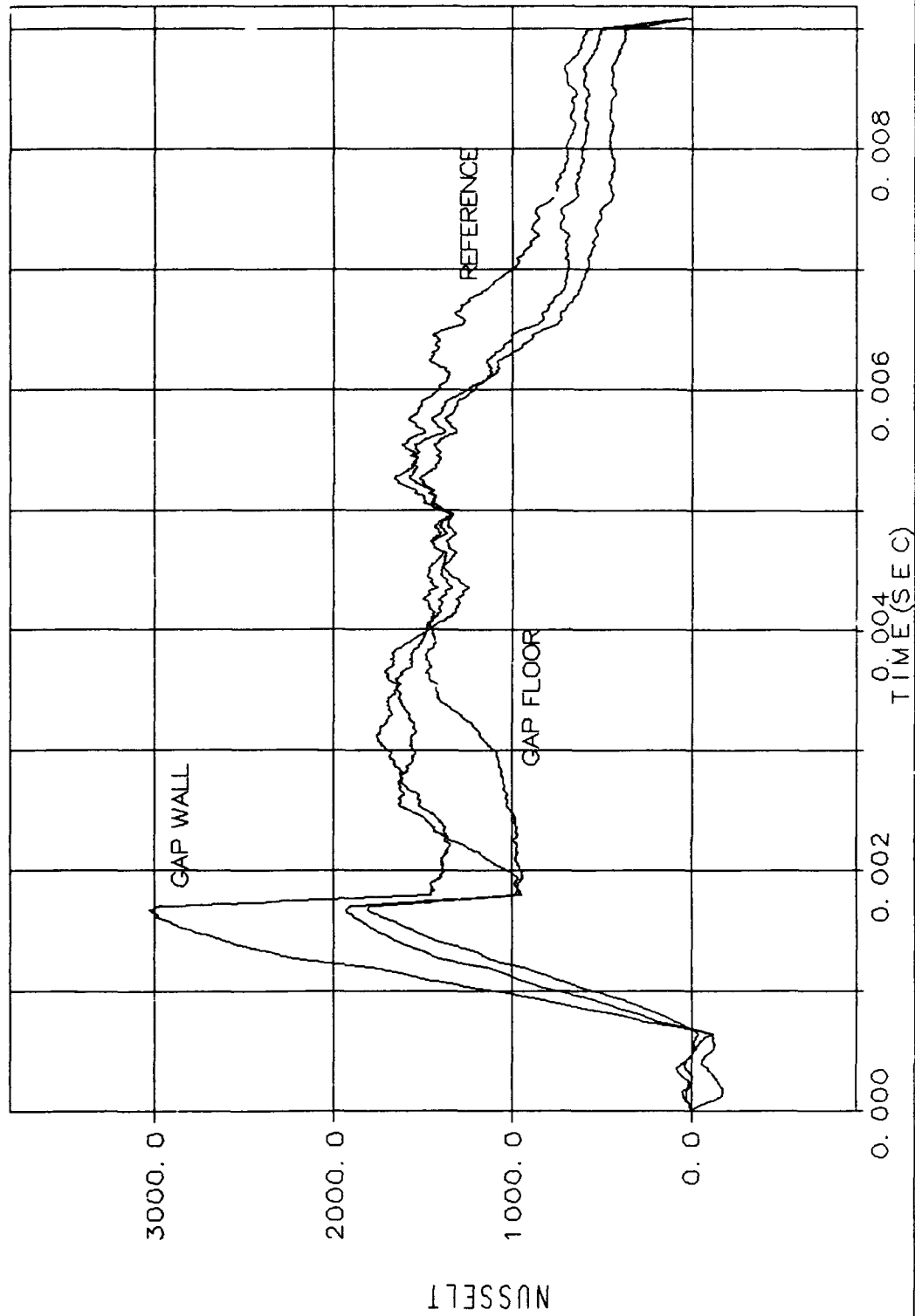


Figure F.36. Test Run Nusselt Values

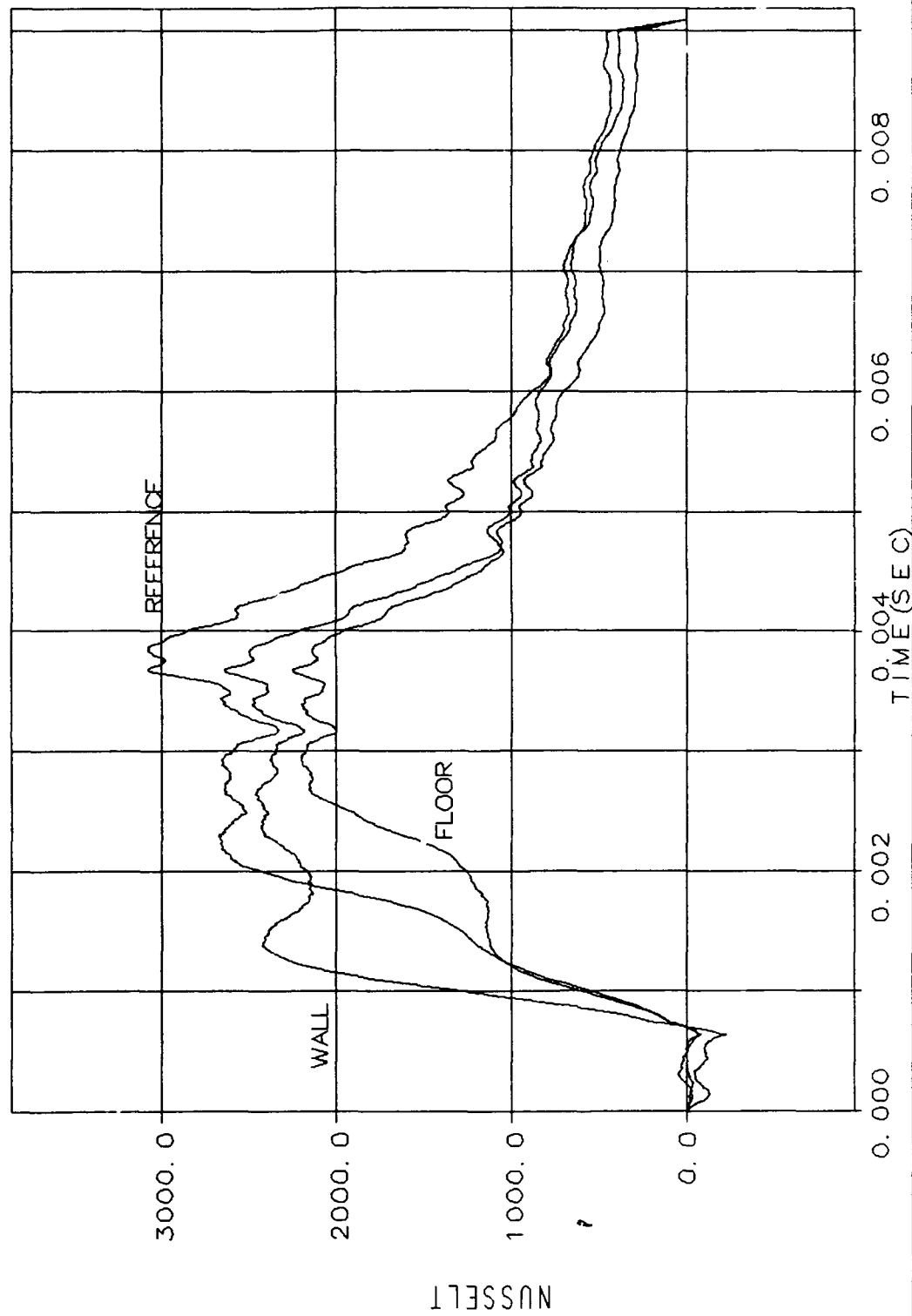


Figure F.37. Test Run Nusselt Values

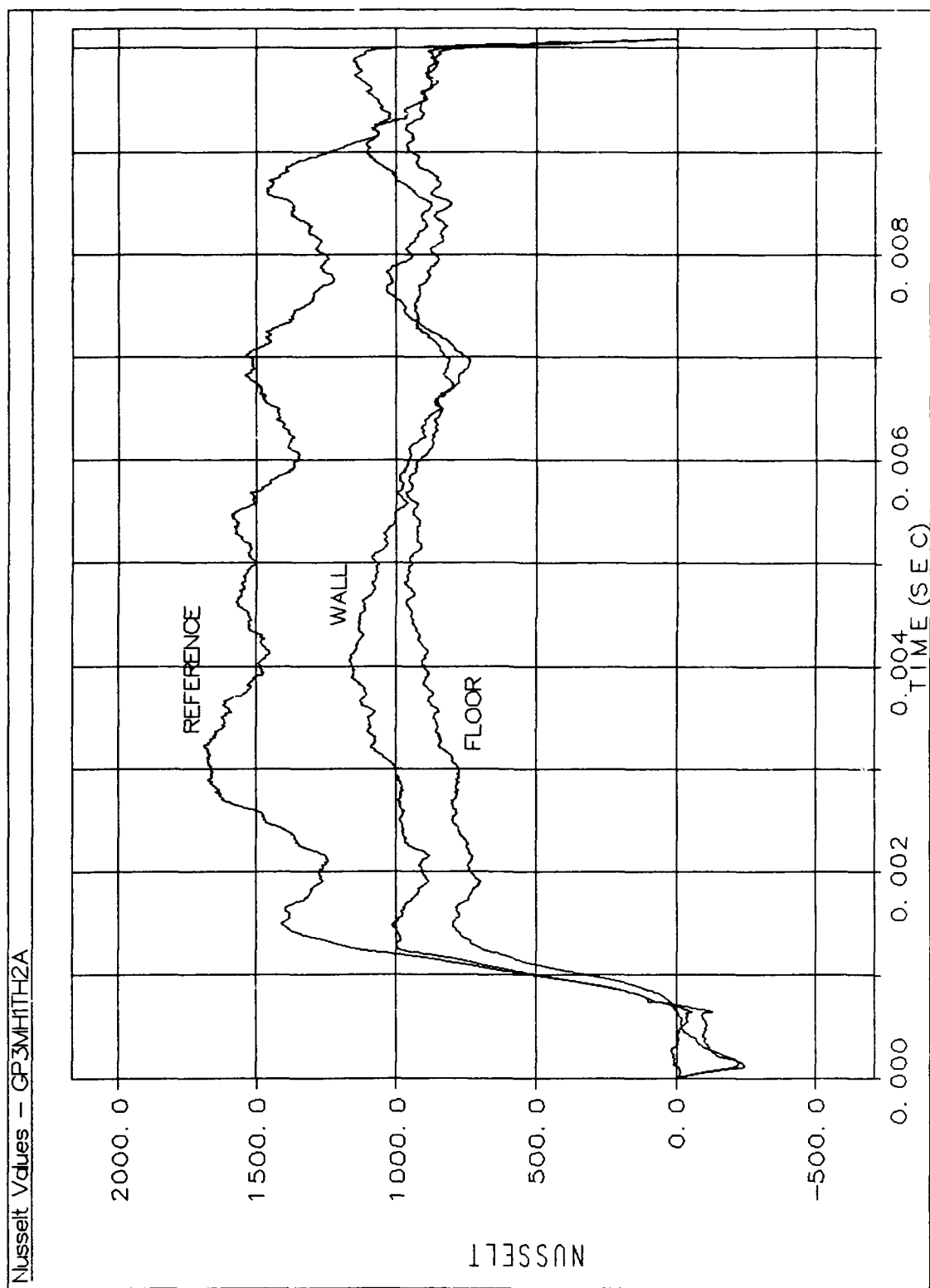


Figure F.38. Test Run Nusselt Values

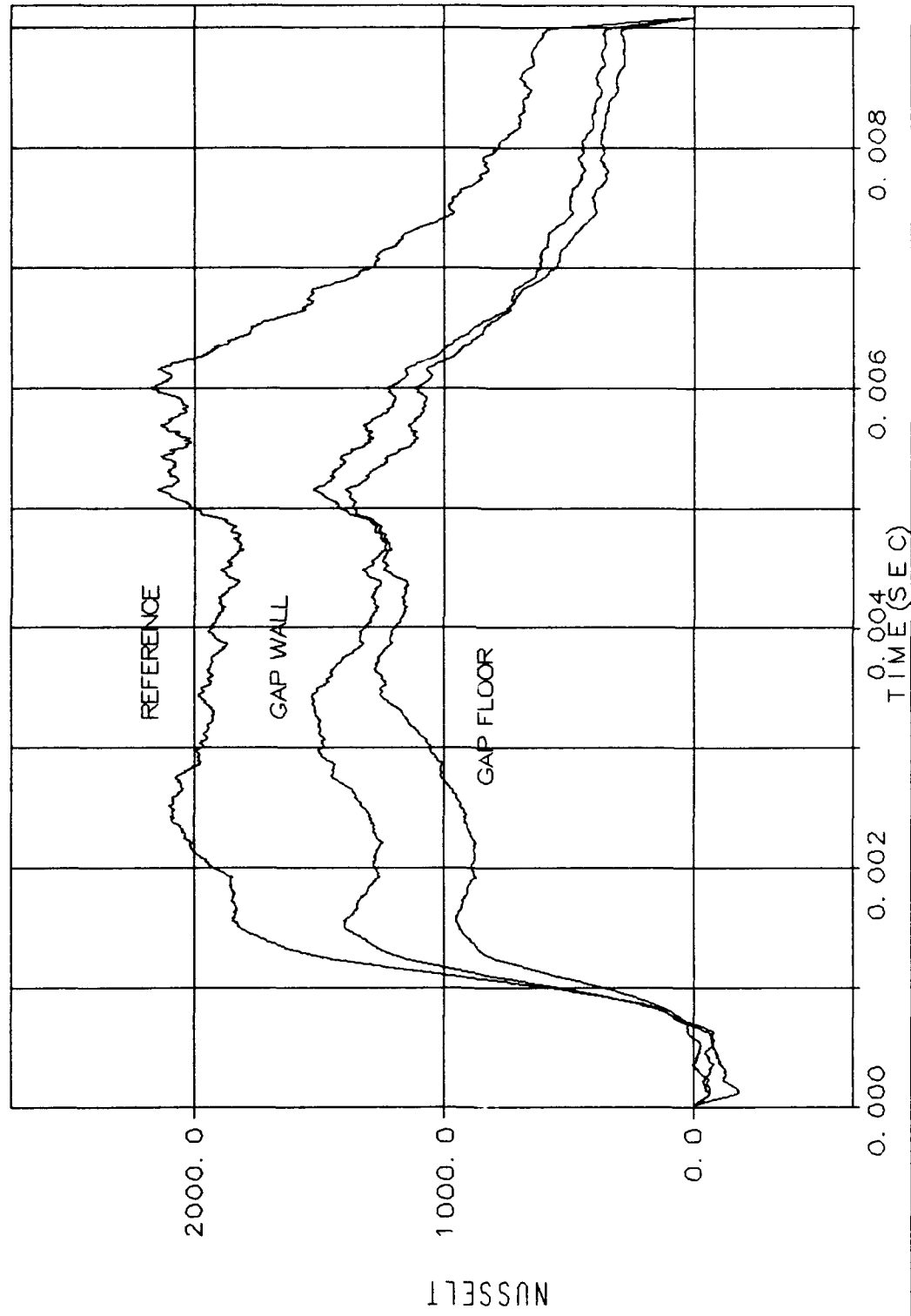


Figure F.39. Test Run Nusselt Values

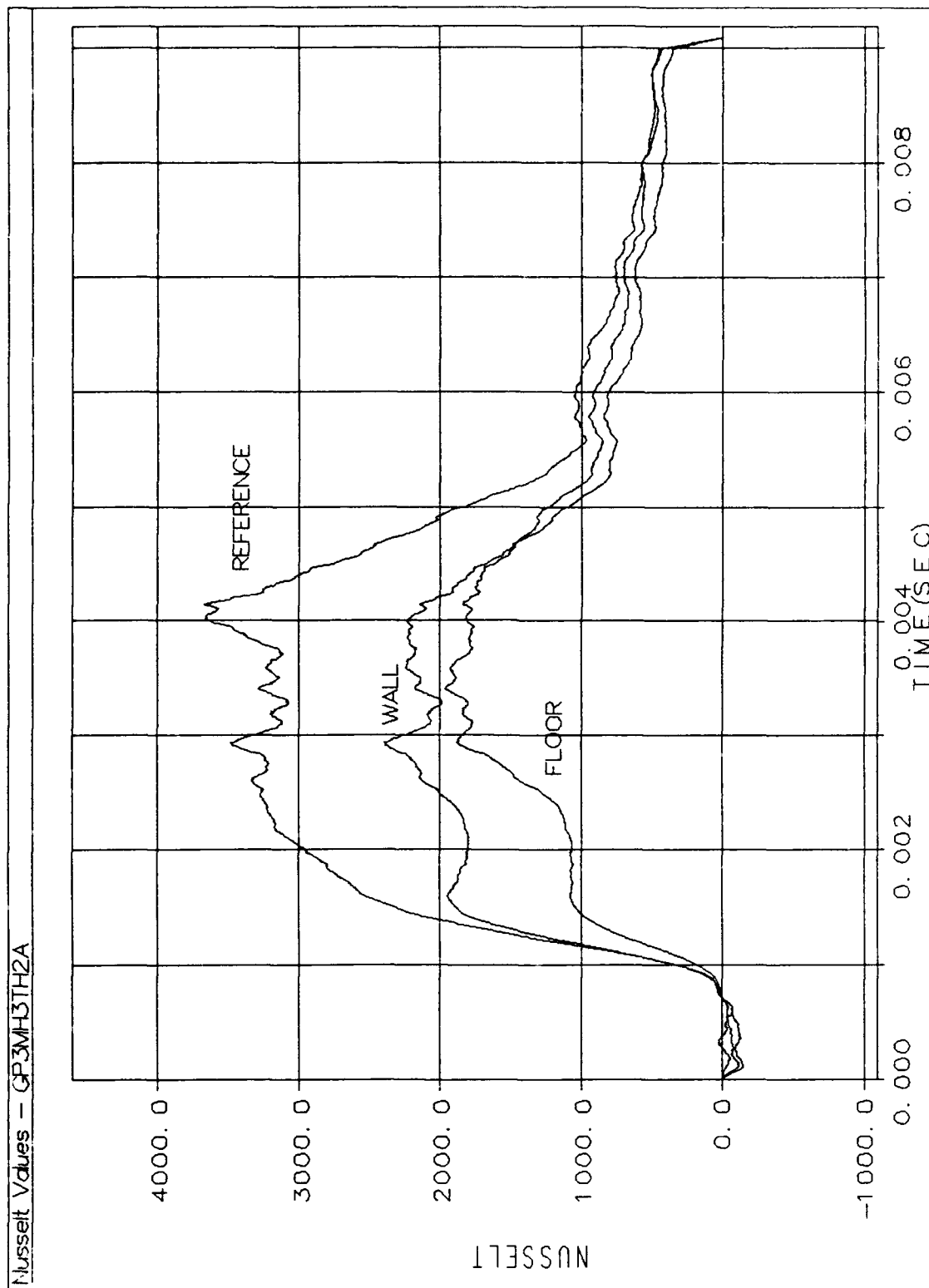


Figure F.40. Test Run Nusselt Values

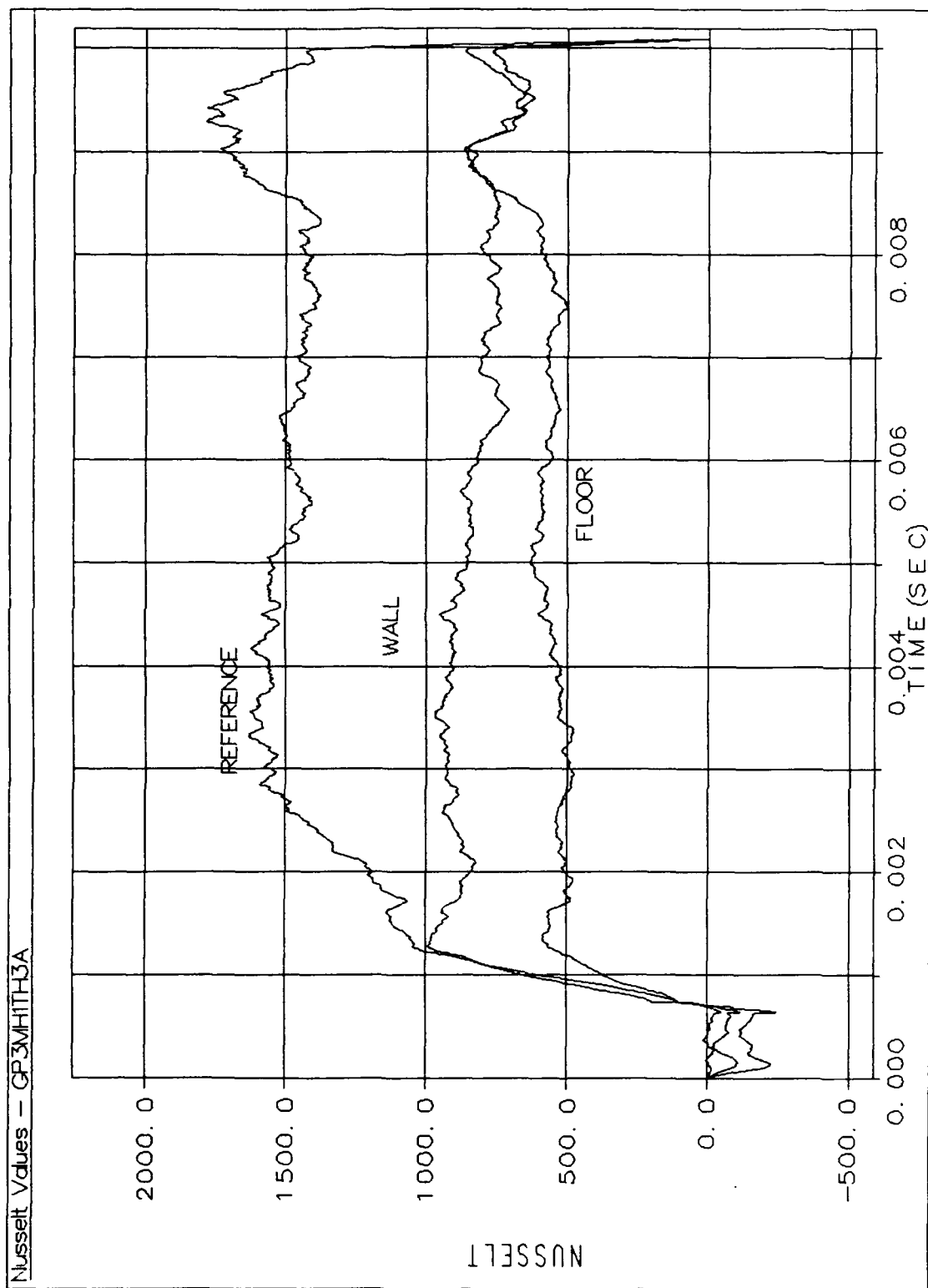


Figure F.41. Test Run Nusselt Values

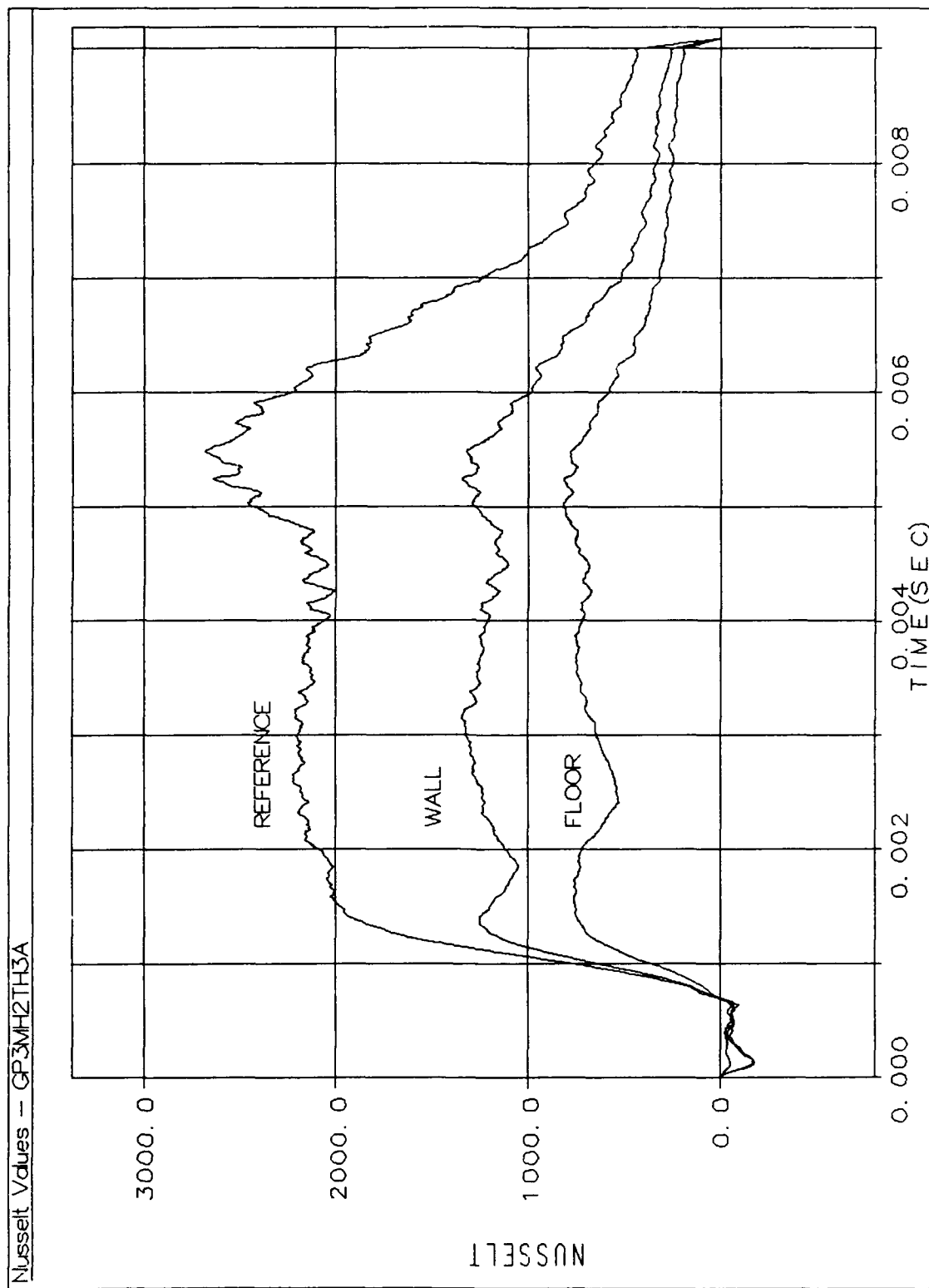


Figure F.42. Test Run Nusselt Values

Nusselt Values -- GP3MH3TH3A

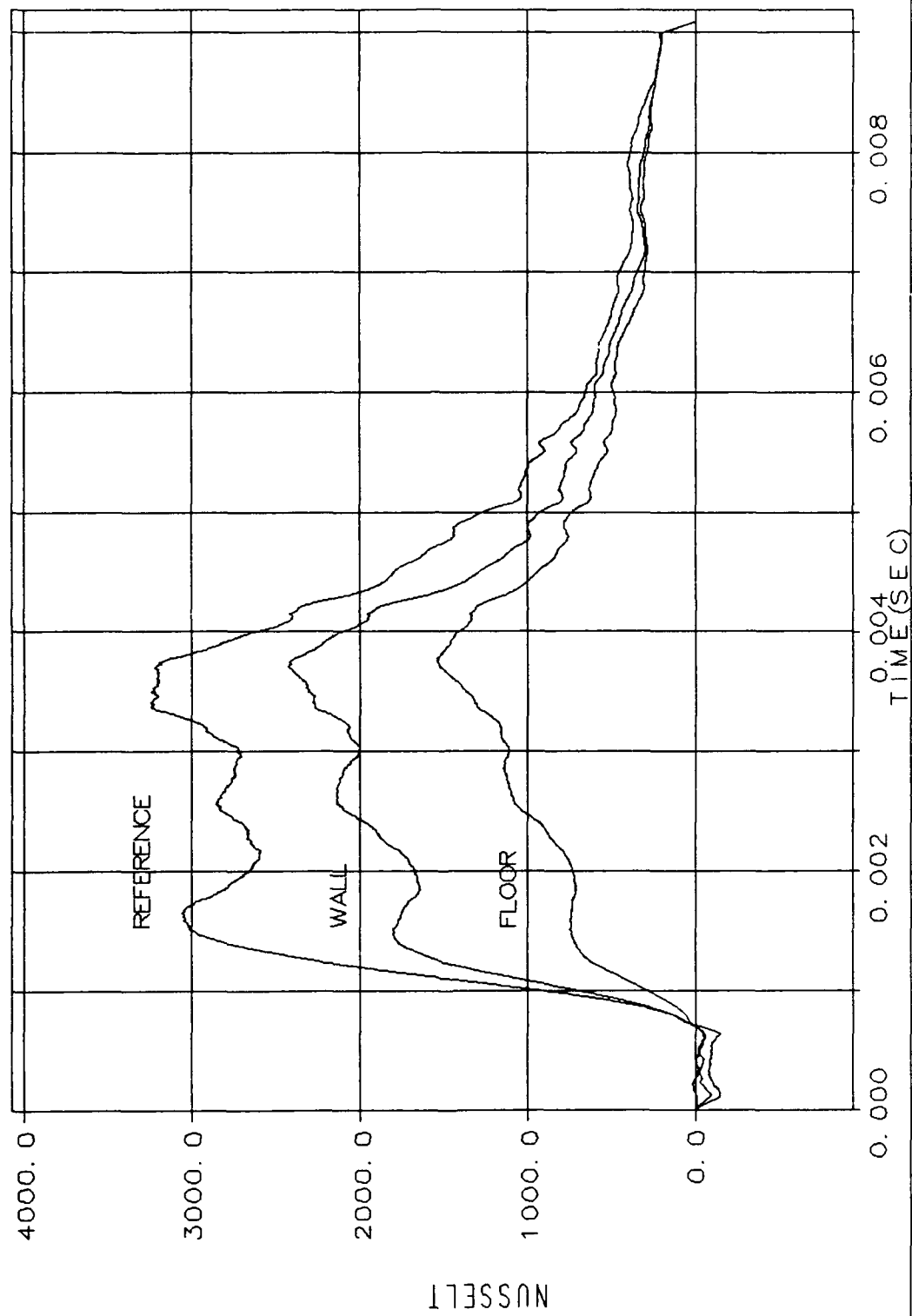


Figure F.43. Test Run Nusselt Values

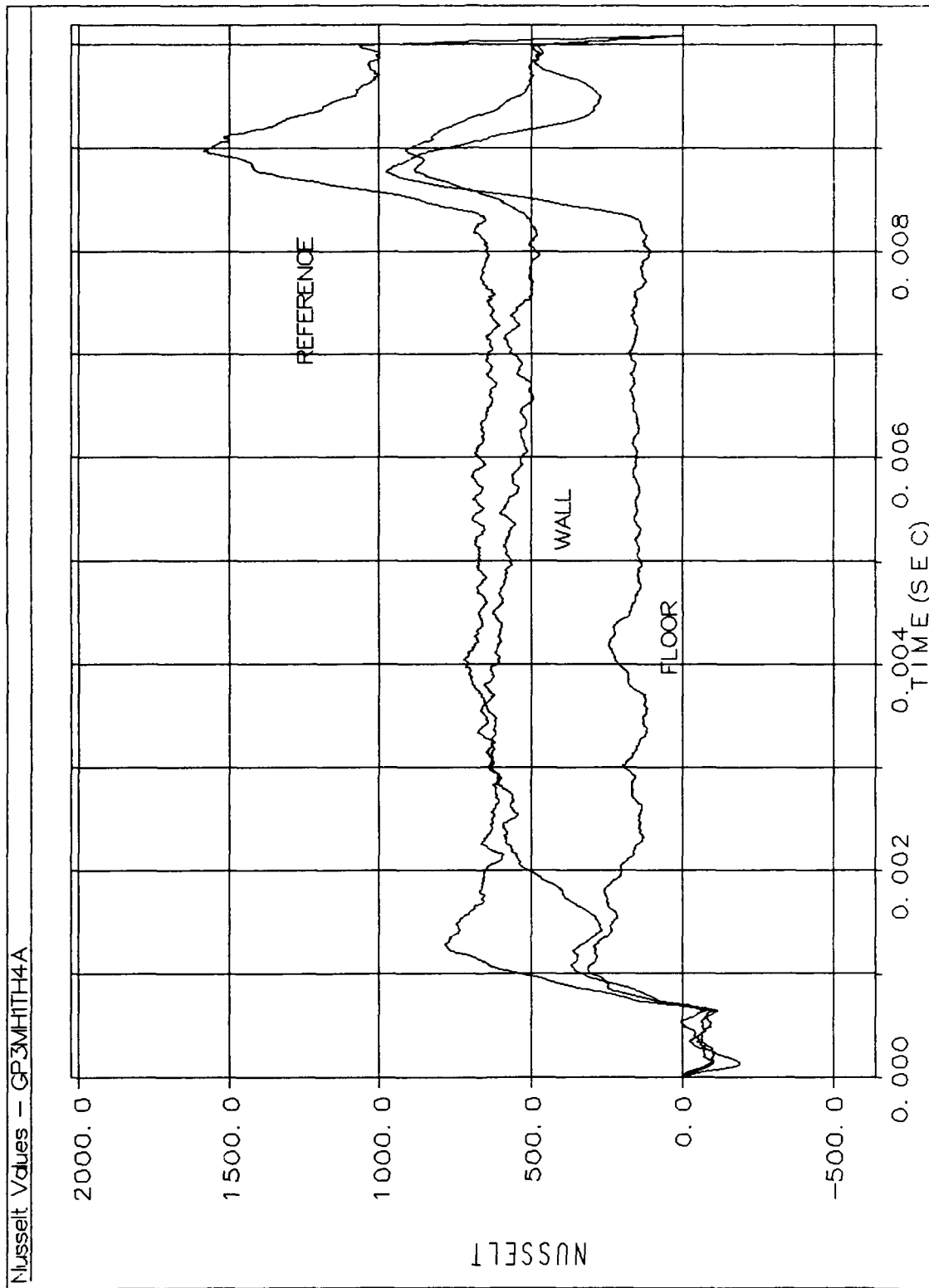


Figure F.44. Test Run Nusselt Values

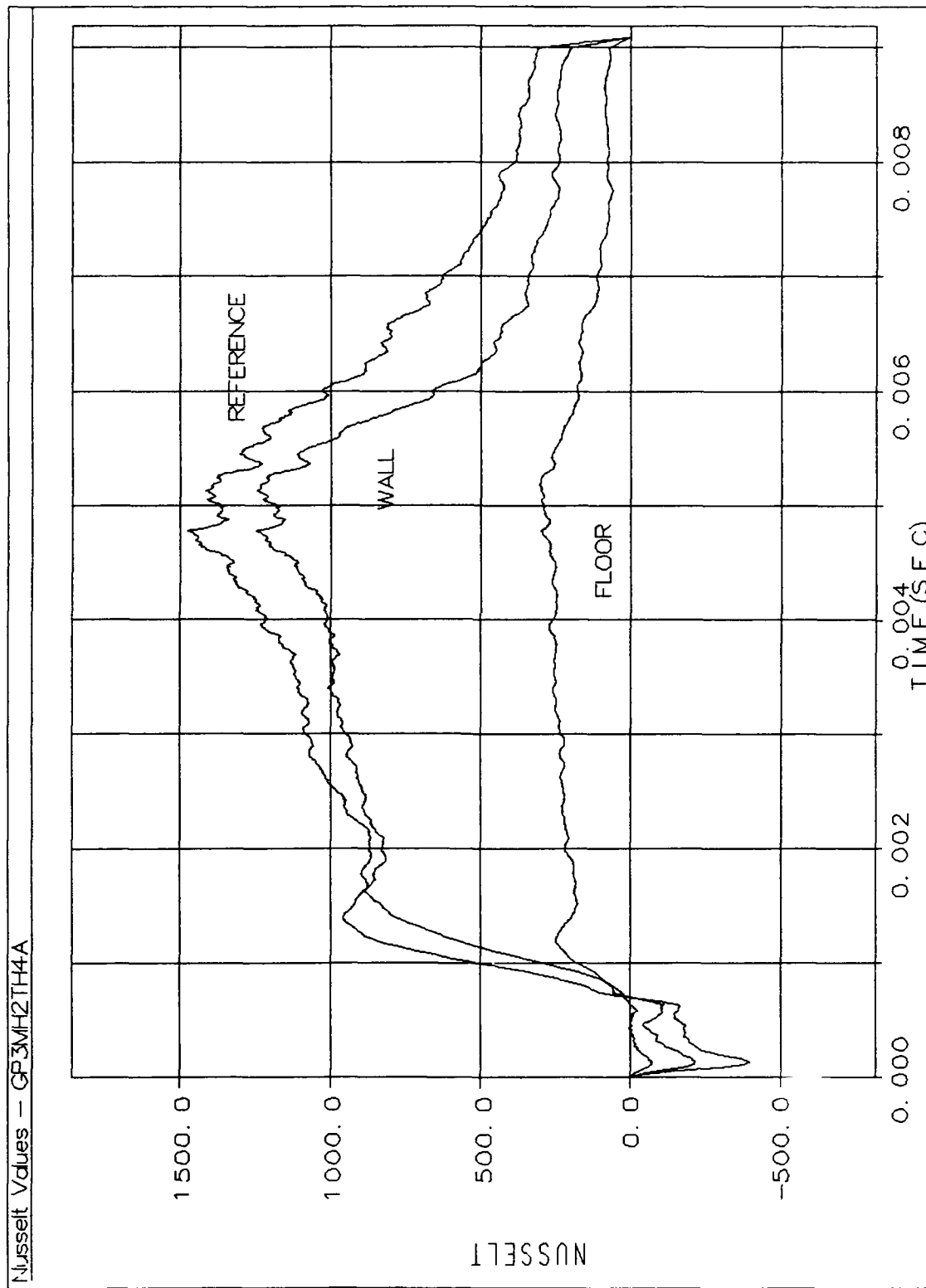


Figure F.45. Test Run Nusselt Values

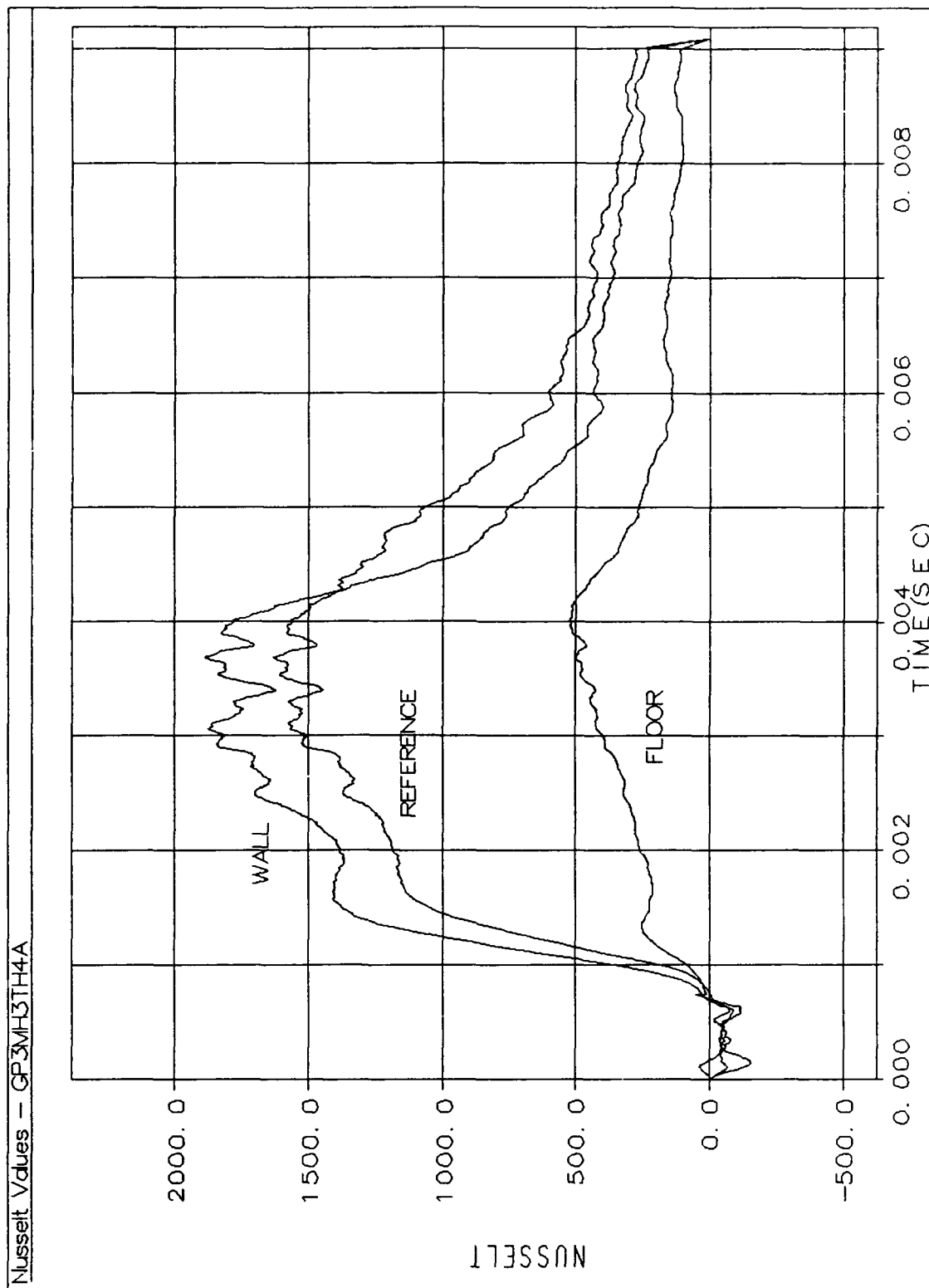


Figure F.46. Test Run Nusselt Values

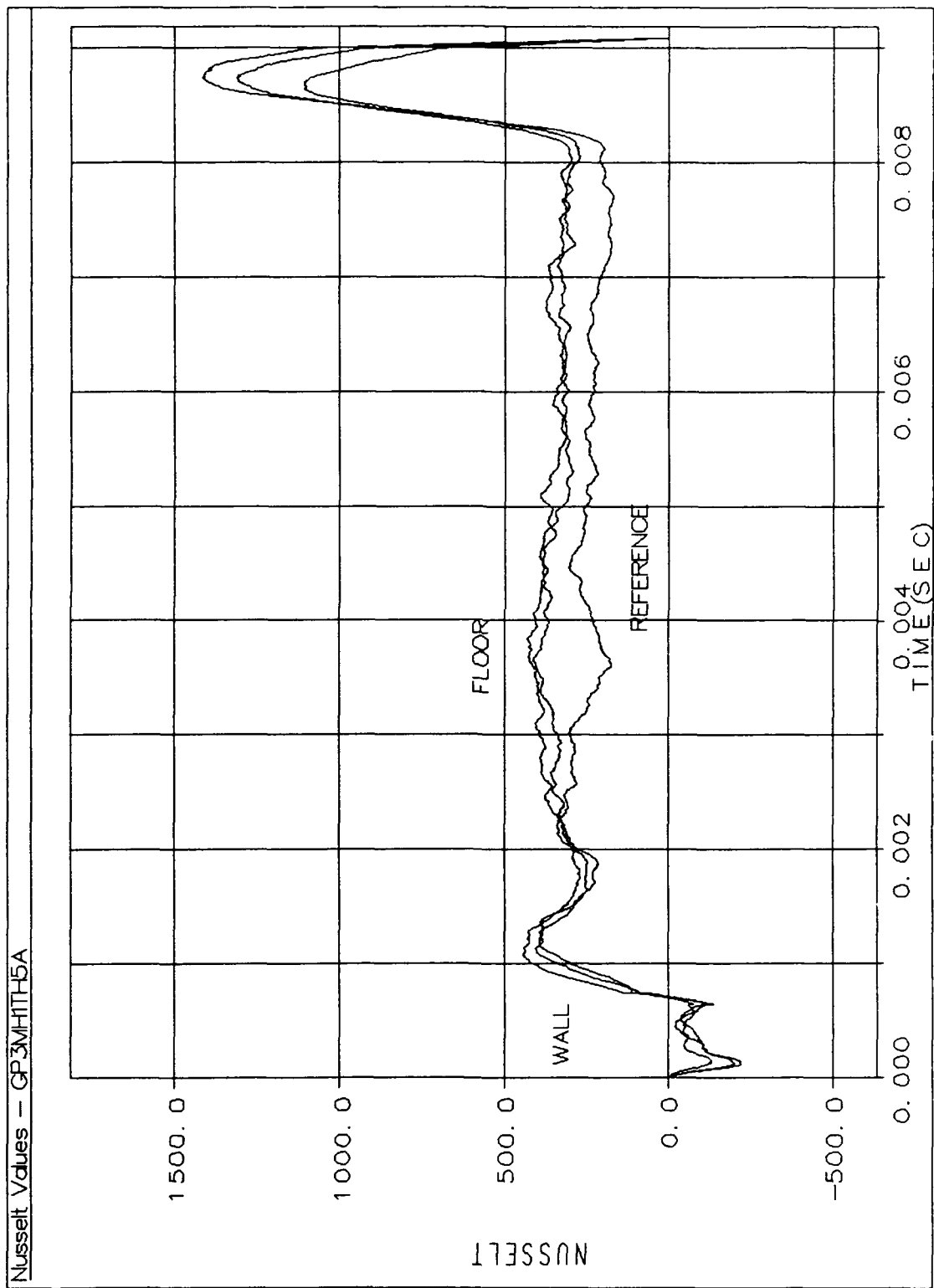


Figure F.47. Test Run Nusselt Values

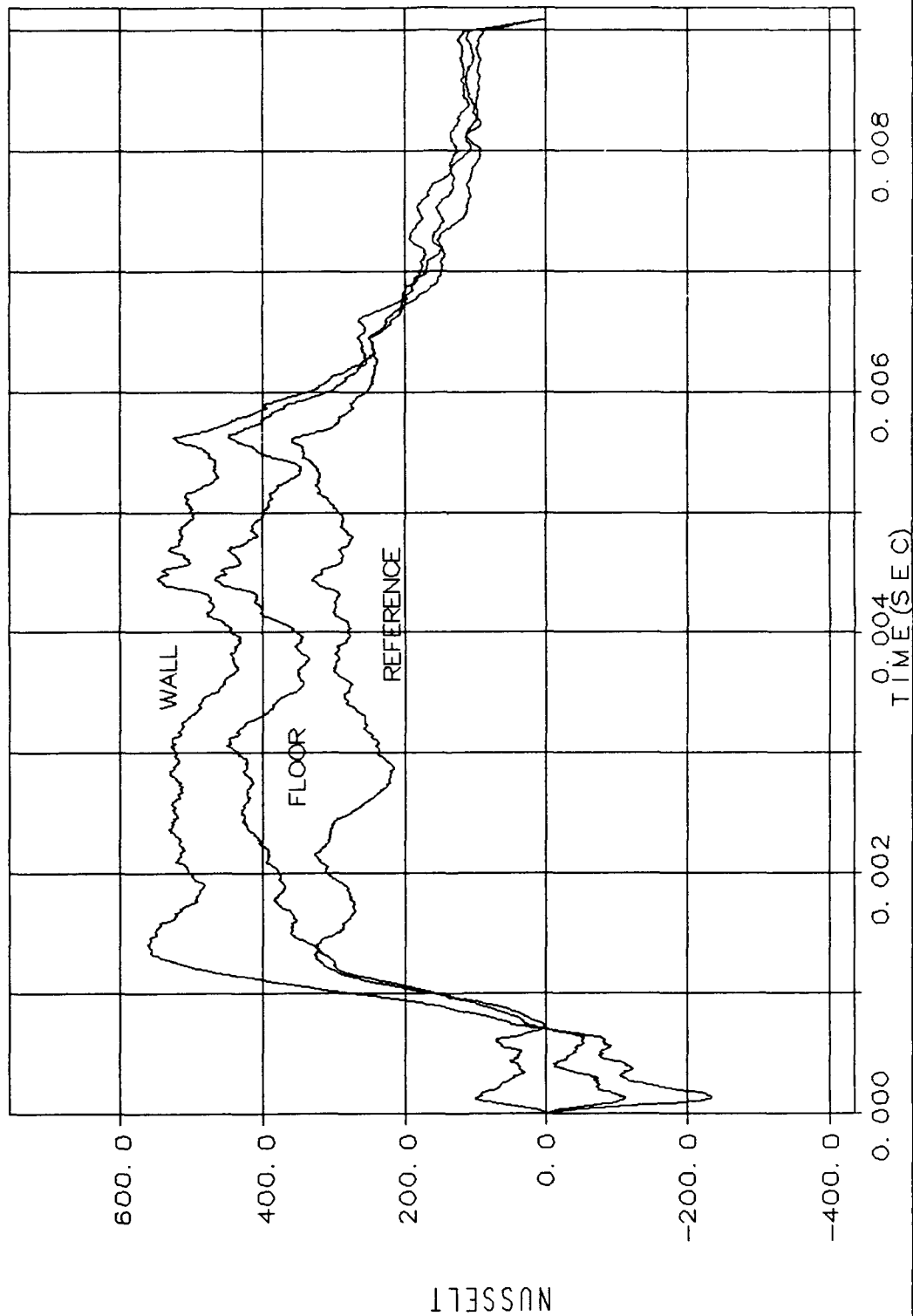


Figure F.48. Test Run Nusselt Values

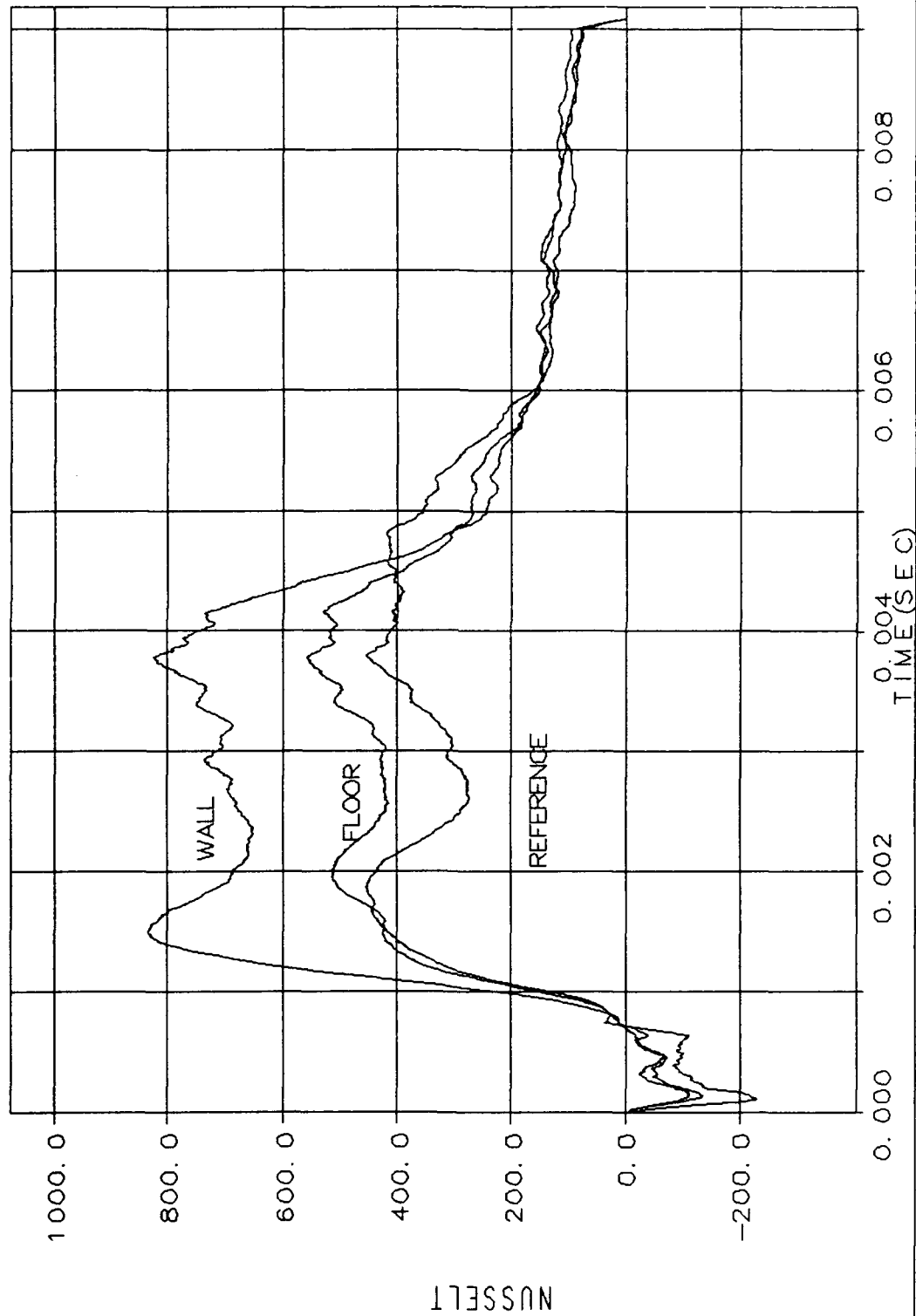


Figure F.49. Test Run Nusselt Values

Bibliography

- Anderson, John D. Jr. *Introduction to Flight*. New York: McGraw-Hill, Inc., 1978.
- Anderson, John D. Jr. *Modern Compressible Flow, With Historical Perspective*. New York: McGraw-Hill Publishing Company, 1990.
- Bertin, J.J. and Goodrich, D. "Aerodynamic Heating for Gaps in Laminar and Transitional Boundary Layers," *AIAA 18th Aerospace Sciences Meeting*. AIAA-80-0287. New York: AIAA Press, 1980.
- Bevington, Philip R. *Data Reduction and Error Analysis for the Physical Sciences*. New York: McGraw-Hill Book Company, 1969.
- Bonafede, Joseph A. *A Numerical Investigation of Thin-Film Heat Transfer Gages*. MS thesis, AFIT/GA/AA/88M-1. School of Engineering, Air Force Institute of Technology (AU), Wright-Patterson AFB OH, March 1988.
- Cook, W.J. and Felderman, E.J. "Reduction of Data from Thin-Film Heat-Transfer Gages: A Concise Numerical Technique," *AIAA Journal*, Vol. 4, No. 3. 561-562. March 1966.
- DADiSP Worksheet, Data Analysis and Display Software*. User Manual. Cambridge: DSP Development Corporation, November 1992.
- DL1200 Multichannel Waveform Recorder*. Operating Manual, Doc. No. 0M0010. Surrey, England: Data Laboratories Limited, April 1984.
- Eads, Thomas A. *Shock Tube Study of the Effects of Large Density Differences and Blowing Ratio on Heat Transfer to a Film-Cooled Flat Plate*. MS thesis, AFIT/GAE/ENY/92D-25. School of Engineering, Air Force Institute of Technology (AU), Wright-Patterson AFB OH, December 1992.
- Elrod, William C. Professor of Aerospace Engineering, Air Force Institute of Technology, Wright-Patterson AFB OH. Personal interview. September 1993.
- Gaydon, A.G. and Hurle, I.R. *The Shock Tube in High-Temperature Chemical Physics*. New York: Reinhold Publishing Corporation, 1963.
- Glass, I.I. *Shock Tubes, Part I: Theory and Performance of Simple Shock Tubes*. UTIA Review No. 12, Part I. Toronto Canada: University of Toronto Institute of Aerophysics, May 1958.

Hall, J. Gordon. *Shock Tubes, Part II: Production of Strong Shock Waves; Shock Tube Applications, Design, and Instrumentation*. UTIA Review No. 12, Part II. Toronto Canada: University of Toronto Institute of Aerophysics, May 1958.

Hermann, D. and others. "Measurements of Heat Transfer and Vortex Shedding Frequency of Cylinders in Shock Tube Cross Flow," in *Shock Tubes and Waves, Proceedings of the 16th International Symposium on Shock Tubes and Waves*, Ed. Hans Grönig. Aachen, West Germany: VCH, 1987.

Hill, Philip G. and Peterson, Carl R. *Mechanics and Thermodynamics of Propulsion*. Reading: Addison-Wesley Publishing Company, 1992.

Incropera, Frank P. and Dewitt, David P. *Introduction To Heat Transfer, 2nd Edition*. New York: John Wiley & Sons, 1990.

Jones, Jim J. *Shock-Tube Heat-Transfer Measurements on Inner Surface of a Cylinder (Simulating a Flat Plate) for Stagnation-Temperature Range 4,100° to 8,300° R*. NASA Technical Note D-54. Langley Field, VA: Langley Research Center, National Aeronautics and Space Administration, September 1959.

Jones, Larry. President, MEDTHERM Corporation, Huntsville Alabama. Personal Correspondence. 15 July 1993.

Kays, W.M. and Crawford, M.E. *Convective Heat and Mass Transfer*. New York: McGraw-Hill, Inc., 1993.

Kendall, David N. and Dixon, Paul W. "Heat Transfer Measurements in a Hot Shot Wind Tunnel," *Presented at the IEEE Aerospace Systems Conference*. Seattle, Washington: McDonnell Aircraft Corporation, 11-15 July 1966.

Lowder, J.E., Mooney, D.L., and O'Neil, R.W. *Laser Heating of Metallic Surfaces*. ESD-TR-75-107. Lexington: Lincoln Laboratory, Massachusetts Institute of Technology, 1974.

MathSoft. *Mathcad® 4.0*. User's Guide, Windows Version. Cambridge: MathSoft Inc., 1993.

MEDTHERM. *Measure Surface Temperature with a Response Time as Little as 1 Microsecond*. Bulletin 500. Huntsville: MEDTHERM Corporation, no date.

MEDTHERM. *Rifle Barrel Internal Bore Surface Temperature Measurements with the MEDTHERM Coaxial Thermocouple*. TN-371. Huntsville: MEDTHERM Corporation, 15 April 1977.

- Nestler, D.E., Saydah, A.R., and Auxer, W.L. "Heat Transfer to Steps and Cavities in Hypersonic Flow," *AIAA Fluid and Plasma Dynamics Conference*. No. 68-673. New York: AIAA Press, 1968.
- Omega Engineering, Inc. *The Temperature Handbook*. Product Catalog, Vol. 28. Stanford: Omega Engineering, Inc., 1992.
- Özişik, M. Necati. *Heat Transfer, A Basic Approach*. New York: McGraw-Hill Book Company, 1985.
- Pacific Instruments. *60A-2,A17,B6,F412-G1 Differential Data Amplifier*. Operation and Maintenance Manual 7A7800. Concord: Pacific Instruments, Inc., December 1987.
- Savage, Dick. *Aerodynamic Heating in a NASP Wing Leading Edge Expansion Slot: Draft Report, 19 September 1991*. 2-3635-RTS-00/91. September 1991.
- Vidal, R.J. and others. *Investigation of Stagnation Point Heat Transfer in the C.A.L.Hypersonic Shock Tunnel*. Report No. AA-966-A-1. Cornell Aeronautical Laboratory, Inc., November 1955.
- Vidal, R.J. *A Resistance Thermometer for Transient Surface Temperature Measurements*. ARS Meeting, Buffalo, New York, September 24-26, 1956.
- Žukauskas, A. "Heat Transfer from Tubes in Crossflow," in *Advances in Heat Transfer*, Volume 8. Ed. James P. Hartnett and Thomas F. Irvine, Jr. New York: Academic Press, 1972.
- Žukauskas, A. "Convective Heat Transfer in Cross Flow," in *Handbook of Single-Phase Convective Heat Transfer*, Ed. Sadik Kakaç, Ramesh K. Shah, and Win Aung. New York: John Wiley & Sons, 1987.

Vita

Captain Douglas D. High was born on 23 May 1961 in Twin Falls, Idaho. He graduated from Twin Falls High School in 1979, and attended the United States Air Force Academy at Colorado Springs, Colorado from which he received the degree of Bachelor of Science in Civil Engineering in June 1983. Upon graduation, he attended Undergraduate Navigator Training at Mather AFB, California and completed RF-4C replacement training as a Distinguished Graduate. Stationed at Bergstrom AFB, Texas he served as an RF-4C Weapon Systems Officer and later as an instructor. While at Bergstrom AFB, he was winner of the General Jerome F. O'Malley Award for top reconnaissance aircrew member in the USAF and Air Force nominee for the Norman P. Hayes Award, honoring outstanding management and support in the advancement of navigation. Captain High also served overseas tours in Japan and Korea flying in the RF-4C and was a 1989 graduate of the United States Air Force Fighter Weapons School and RF-4C Fighter Weapons Instructor Course. After serving overseas, he returned to Bergstrom AFB, where he served as Flight Commander and Wing Supervisor of Flying. He entered the Graduate School of Engineering, Air Force Institute of Technology, in May 1992.

Permanent Address: 1242 Lawndale Drive

Twin Falls, ID 83301

REPORT DOCUMENTATION PAGE			Form Approved OMB No. 0704-0188	
<small>Public reporting burden for this collection of information is estimated to average 1 hour per response, including the time for reviewing instructions, searching existing data sources, gathering and maintaining the data needed, and completing and reviewing the collection of information. Send comments regarding this burden estimate or any other aspect of this collection of information, including suggestions for reducing this burden, to Washington Headquarters Services, Directorate for Information Operations and Reports, 1215 Jefferson Davis Highway, Suite 1204, Arlington, VA 22202-4302, and to the Office of Management and Budget, Paperwork Reduction Project (0704-0188), Washington, DC 20503.</small>				
1. AGENCY USE ONLY (Leave blank)		2. REPORT DATE March 1994		3. REPORT TYPE AND DATES COVERED Master's Thesis
4. TITLE AND SUBTITLE A SHOCK TUBE STUDY OF AERDYNAMIC HEATING OF GAPS IN A CYLINDER SUBJECTED TO SUPERSONIC CROSSFLOW			5. FUNDING NUMBERS	
6. AUTHOR(S) Douglas D. High, Captain, USAF				
7. PERFORMING ORGANIZATION NAME(S) AND ADDRESS(ES) Air Force Institute of Technology, WPAFB OH 45433-6583			8. PERFORMING ORGANIZATION REPORT NUMBER AFIT/GA/ENY/94M-2	
9. SPONSORING / MONITORING AGENCY NAME(S) AND ADDRESS(ES)			10. SPONSORING / MONITORING AGENCY REPORT NUMBER	
11. SUPPLEMENTARY NOTES WL/FIBEB, WPAFB OH				
12a. DISTRIBUTION / AVAILABILITY STATEMENT Approved for public release; distribution unlimited			12b. DISTRIBUTION CODE	
13. ABSTRACT (Maximum 200 words) The effects of localized aerodynamic heating in cylinder expansion gaps positioned in cross flow were investigated in a shock tube. For this study, Mach number and Reynolds number were varied from 1.04 to 1.38 and 5×10^5 to 9×10^5 , respectively. The cylinder was instrumented with quick response time thermocouples positioned on the surface of the cylinder, the wall of the gap, and the gap floor. Gap aspect ratios varied from 1.23 to 3.69. Pressure gauges were used to measure wave shock speeds, pressure ratios, and transient pressure conditions. Surface temperatures were measured and converted to heat fluxes using a one-dimensional semi-infinite slab model. Adiabatic wall temperatures were obtained from pressure measurements and ideal gas law relationships. Local nondimensional heat transfer coefficients, Nusselt numbers, were calculated from experimental surface and adiabatic wall temperatures. The present study found a direct dependence on Nusselt number values with Mach number. Peak heating inside the gap was determined to be a function of gap width and location on the cylinder. As gap width was reduced, the location of peak heating on the cylinder varied and Nusselt number values on the floor of the gap dominated.				
14. SUBJECT TERMS Shock Tubes, Aerodynamic Heating, Cylinder Heat Transfer, Heat Transfer in Gaps, Cylinder in Cross Flow			15. NUMBER OF PAGES 261	
			16. PRICE CODE	
17. SECURITY CLASSIFICATION OF REPORT Unclassified	18. SECURITY CLASSIFICATION OF THIS PAGE Unclassified	19. SECURITY CLASSIFICATION OF ABSTRACT Unclassified	20. LIMITATION OF ABSTRACT UL	